ISAS - INTERNATIONAL SCHOOL FOR ADVANCED STUDIES

DYNAMICAL AND RADIATIVE EVOLUTION OF A FIREBALL

Thesis submitted for the degree of
"Doctor Philosophiæ"

International School for Advanced Studies
Via Beirut 2-4, 34014 Trieste, Italy.
Astrophysics Sector.

Candidate: Vanessa Mangano
E-mail: *mangano@sissa.it*

Supervisors: A. Celotti, J.C. Miller

June 2002

SISSA - SCUOLA NTERNAZIONALE SUPERIORE STUDI AVANZATI
TRIESTE
Via Beirut 2-4

TRIESTE

Contents

List of Figures

Chapter 1

Introduction

Gamma-ray bursts (GRBs) are bright and short high energy flashes of extra galactic origin, isotropically distributed in the sky. Though GRBs are very difficult to localize with the accuracy required for a follow up, counterparts GRBs at longer wavelengths are now routinely detected. The long lasting emission detected after the gamma–ray flash, named afterglow, spans the whole electromagnetic spectrum from X–rays to the radio band. The observed flux in any fixed energy band initially grows to a peak and then decays, higher frequency light curves peaking earlier than lower frequency ones. The peak frequency of the spectrum is softening with time.

The observed afterglow emission has been naturally interpreted, within the framework of the fireball model, as synchrotron emission from relativistic electrons of the medium surrounding the explosion site which are swept up and heated by the relativistic shock at the leading edge of the expanding fireball. Standard fireball models are usually based on spherical or jet–like geometry. Predictions for the afterglow light curves are generally in agreement with the observations although unusually steep temporal decay slopes and breaks are still a matter of debate and there are competing interpretations for them. Recently, the possibility of explaining some GRB and afterglow observational features with an anisotropic fireball having a smooth angular distribution in baryon loading, expansion Lorentz factor and gamma–ray luminosity viewed from different directions have been considered. Models assuming GRBs to be the result of collapse of rotating massive stars would naturally channel the emitted energy along the rotation axis, which is also the most baryon free direction, and give rise to a fireball with a smooth spread in ejected energy and baryon loading in directions far from the axis. Recently a growing amount of indirect evidences in favour of the

GRB–massive star collapse connection is being collected. So, theoretical investigations concerning the class of smooth anisotropic fireballs are very appealing.

The final aim for the present work is the detailed calculation of afterglows and spectra emitted from smooth anisotropic fireballs viewed by different directions. Our detailed calculation of the observed radiation is intended to fully take into account the interior emission of the fireball, the relativistic beaming, the light travel delays of radiation emitted by different volume elements of the fireball and the effect of cooling via synchrotron radiation and adiabatic volume expansion on the emitting electrons. Thus, light curves and spectra have been calculated through whole integration of lab frame boosted emissivity over the volume delimited by the place of points from which radiation emitted by the post–shock fluid arrives simultaneously to the observer (Equal–T surface).

We have modeled the anisotropic fireball interior assuming that the fluid evolution along any fixed direction is not affected by the adjacent directions and resembles a portion of a spherically symmetric expanding fireball having the same baryon loading as the anisotropic fireball in that direction, and a total energy equal to 4π times the total energy per unit solid angle of the anisotropic fireball in that direction.

It has already been shown that for ultrarelativistically expanding spherical fireballs results of afterglow calculation with the procedure described above qualitatively agree with rough estimations based on the fact that because of relativistic beaming, and because of the post–shock particle distribution highly concentrated close to the shock (almost shell shaped), radiation that reaches the observer at each given time mostly comes from the fluid just behind the shock along the line of sight. A calculation as precise as the one we perform is important for predictions on timescales at which the flow (or the shock front) becomes marginally relativistic, lateral portions of the fireball can contribute significantly to observed radiation and the fireball internal structure is no longer approximable as a thin shell. But it is also important to show that, even in case of ultra-relativistic shocks, realistic afterglow calculation produces light curves and spectra much more smooth and far from simple broken power laws than rough approximations, suggesting that broken power law fits actually performed on afterglow data might appear to be too simple as soon as better quality and more complete data sets will be acquired.

The complete hydrodynamical evolution of a spherical fireball, from the time of explosion to non relativistic Sedov expansion, has been described, along any given direction, by matching the analytic laws characterizing the different known evolutionary

stages. In order to have a consistent and smooth global evolution from the initial relativistic expansion to the late Newtonian one, it has been necessary to use generalized jump conditions at shocks and generalized energy conservation law and to derive a set of analytical approximations allowing either for a good match between different laws and a relatively easy and fast calculation of the comoving time. As far as the radiation process is concerned, once verified that within the ranges of intrinsic fireball parameters used synchrotron radiation from shock accelerated electrons dominates over other possible radiation mechanisms, we have performed the exact calculation of the comoving synchrotron emissivity of the shocked fluid. The cooling of the emitting electrons due to synchrotron energy losses and adiabatic expansion has been carefully taken into account thanks to the knowledge of the whole fireball structure and evolution, and different hypotheses about the magnetic field strength evolution have been tested.

The detailed afterglow light curve and spectra from spherical fireballs that have been calculated so far with comparable accuracy have always concerned fireballs with a very low degree of baryon pollution (i.e. baryon loading parameter $\eta \gtrsim 100$, see section 3.2 for the definition of η), because this value, though not directly measurable, seems to be always compatible with observed data in spherical geometry and is suggested by the high value of the lower limit on the bulk Lorentz factor of the flow needed to solve the compactness problem [Fenimore, Epstein & Ho 1993, Woods & Loeb 1995]. Under this assumption the observed X–ray, optical and radio afterglows should always be emitted during the Blandford & McKee stage, the relativistic self–similar expansion stage that is expected to start when the mass of the swept–up external medium becomes high enough to decelerate the fireball. Thus, this has always been considered to be the most relevant stage for afterglow predictions and light curve and spectra detailed calculation have been restricted to it.

Since the spherical fireball evolution is determined by the values of the baryon loading parameter η and the total energy, and the start times of different evolutionary stages depend on these parameters, in an anisotropic model with smooth angular distribution of baryon loading and "isotropic" energy spanning two decades in values, the radial evolution will go on with different timescales in different directions. The start time of each evolutionary stage will depend on the direction, and stages before the Blandford & McKee one must be taken into account for a consistent description of the whole fireball evolution and proper definition of its shape.

For this reason we have built an approximated but complete and realistic version of the hydrodynamical evolution of a spherical fireball with arbitrary baryon loading

parameter value, valid at least for η as low as 3 (i.e. quite high baryon pollution).

We have developed a single code for the numerical calculation of afterglow light curves and spectra from either an anisotropic fireball or a spherical fireball with intrinsic parameters varying in the ranges required for the corresponding anisotropic calculation.

To date, we have fully tested the code calculating afterglows for all the spherical models of interest both neglecting and taking into account the cooling on the evolution of the emitting particle distribution.

Since the code is complete, the forthcoming development of the project will be the full calculation of afterglows in the anisotropic case at varying viewing angles.

1.1 Plan of the thesis

In chapter 2 we introduce the observational properties of GRBs and afterglows, describing the main features of these events and summarizing the currently proposed interpretations within the framework of the fireball model.

In chapter 3 we introduce the complete theoretical treatment of the hydrodynamics of a spherical fireball and the whole set of analytical approximations we have derived and used (sections from 3.2 to 3.5), the general procedure for the detailed calculation of afterglow light curves and spectra (section 3.6) and of the comoving emissivity of shocked matter according to the theory of synchrotron radiation and the fireball hydrodynamics (sections 3.7 and 3.8).

The anisotropic fireball model we have developed, based on spherical hydrodynamics with a direction dependent baryon loading, is introduced in chapter 4.

Finally, in chapter 5 we present the results of the calculation of afterglows and spectra from spherical fireballs with intrinsic parameters varying in the range required for building an anisotropic fireball. After presenting (standard) approximated predictions about afterglows from spherical fireballs (section 5.2), we show the results of calculations performed neglecting the cooling of emitting electrons (section 5.3.1), and then the results of calculations performed taking into account the cooling of electrons (section 5.3.2).

1.2 Results

We present only results regarding afterglows from spherical fireballs.

The spherical fireball afterglows we have calculated under the same approximations of the similar estimate performed by [Granot, Piran & Sari 1999c] are consistent with their results over the time interval corresponding to the Blandford & McKee stage, if the fireball intrinsic parameters (baryon loading parameter η, total energy E_T, degree of equipartition of the electron energy ϵ_e, and of the magnetic energy ϵ_B) and the observation frequency ν satisfy the relation (5.25), i.e.

$$\eta > 80 \left(\frac{\nu}{10^{16}}\right)^{1/4} \left(\frac{\epsilon_B}{0.01}\right)^{-1/8} \left(\frac{\epsilon_e}{0.1}\right)^{-1/2} \left(\frac{E_T}{10^{52}}\right)^{1/24} \tag{1.1}$$

This relation corresponds to the condition that the peak time of the light curve occurs during the Blandford & McKee stage. The extension outside this range has not been performed before this work. Furthermore, even in the range determined by equation (1.1) we extend the results to before and after the Blandford & McKee stage.

From an observational point of view, at very early time after the explosion ($\lesssim 100s$) the light curves we calculate would be probably out-shone by the GRB emission (in the soft γ–rays and X–rays) or by the reverse shock emission (in the optical/NIR), and would be probably undetectable because of the low flux in the radio. The early part of the light curve we predict might be observed only for fireball parameters that imply the Blandford & McKee stage beginning after the first $\sim$ 100 s. The late part of the light curves we calculate (after $\sim$ 1 year) should always be difficult to be observed at frequencies from the X–rays to the infrared because of the low flux compared to the flux coming from the host galaxy or, possibly, the remnant of the progenitor.

The main result we find is that if the fireball parameters and the observed frequency do not satisfy (1.1), the qualitative behaviour of the peak of the afterglow light curve changes. Light curve peaks always occur during the early deceleration stage, after the fireball has stopped the coasting stage (i.e. expanding at constant speed), and have a different shape. The peak times are frequency independent, but energy and baryon loading dependent exactly like the Blandford & McKee's phase start time. Thus, at moderately low baryon loading parameter values ($\eta \sim 20$, corresponding to a relatively large baryon pollution) and standard total energy values ($E_T \sim 10^{52}$ ergs) we expect the afterglow peak to fall just on timescale of real afterglow detections. The second important characteristic of peaks of this second family, arising when (1.1) is not satisfied, is that the peak height (i.e. the maximum detectable flux) scales as $\propto E_T\, \eta^{10/3}\, \nu^{-\frac{(p-1)}{2}}$,

unlikely the "standard" peak heights scaling as $\propto E_T$. This makes, for instance, X–ray afterglows significantly dimmer than optical at the maximum, allowing for the occurrence of GRB events with an intrinsically faint X–ray afterglow as compared to the optical.

The afterglow light curve calculation including effects of electron cooling via synchrotron and adiabatic expansion energy losses reflects the same general peaking behaviour we have just described, with the second family of afterglow peaks just having a peak time value different within 20% from the corresponding peak time calculated without electron cooling. Comparison of absolute values of peak heights with or without accounting for the electron cooling is delicate in all cases, but the scaling laws with the fireball intrinsic parameters are roughly the same.

The most relevant result in this case is that both light curves and spectra are difficult to be well approximated by broken power laws. Spectral peaks and breaks are very broad and smooth, and curve segments far from peaks or breaks are definitely not straight lines in a log–log plot. This is not surprising, and should be considered as a warning to observers for future analysis of better quality afterglow data.

Chapter 2

Gamma–Ray Bursts and Afterglows

2.1 GRBs observational features

Gamma–Ray Bursts (GRBs) are bright, irregular, transient events in the gamma–ray sky, unpredictable in time and location, with a typical duration of a few tens of seconds though possible durations span from a fraction of second to minutes (for reviews, see [Fishman 1995, Fishman 1999, Fishman & Meegan 1995, Meegan 1998]). The brightest bursts have gamma–ray fluences of order 10^{-4} erg cm^{-2}, but they have been detected down to limiting fluxes of $\sim 10^{-7}$ erg cm^{-2}s^{-1} or fluences of 10^{-6} erg cm^{-2}. This cutoff is determined primarily by the threshold of the sensitivity of the detectors combined with the trigger method. GRBs are currently detectable at a mean rate of $\sim 10^3$ per year.

Most of energy of the bursts is released in the 0.1–1 MeV range. Spectra generally display featureless smooth continua well fitted by the classical spectral model by [Band *et al* 1993] consisting of a low energy power law with an exponent α, being exponentially cut off at $E \sim E_0$, and by a high–energy power law with the exponent β. Though the values of (α, β, E_0) can be different for individual bursts, they usually are in the ranges $\alpha \sim [-2, 0.5]$, $\beta \sim [-3.5, -1]$, $E_0 \sim [100, 200]$ keV* [Preece 2000]. Moreover, quite irregular spectral evolution (i.e. evolution of the parameters (α, β, E_0)) is observed during all bursts [Ford 1995]. All these spectra, integrated or time resolved, are definitely far from a black body, so it is widely believed that the source of gamma radiation is optically thin, i.e. the photon mean free path is larger than the emitting

*Remind that the exponents α and β usually refer to the photon number spectrum, i.e. we write $N(E) \propto E^{-\alpha}$ at low energy and $N(E) \propto E^{-\beta}$ at higher energy.

plasma cloud. Yet the spectra are not always described by nonthermal emission in a simple synchrotron shock model (see e.g. [Crider 1997, Preece 2000]). Especially their low energy tails are sometimes incompatible with pure synchrotron emission since such a radiation mechanism would forbid spectral slopes $\alpha > -1/3$ [Katz 1994] as those observed for instance in GRB 970111 [Frontera *et al.* 2000].

The time profiles of pulses of gamma–ray radiation show a great variety. There are single–pulse bursts, bursts showing a few of prominent spikes and bursts showing many pulses (even hundreds). The variability timescale in GRB light curves can be very short, usually significantly smaller than the total duration of the burst, the shortest rise time of a luminosity peak ever detected being of 0.2 ms (GRB 910711) [Bath *et al.* 1992]. It is hard to observe any regularity in the time profiles of bursts though [Stern & Svensson 1996] claim that they find scale–invariant properties in the light curves of GRBs.

It is most probable that the source of gamma radiation, moves towards us with extreme relativistic speed, corresponding to a Lorentz factor $\gamma \sim 100$. This was originally deduced as the only reasonable solution to the compactness problem, that is a paradox due to the simultaneous presence of variability timescales as short as $\delta t \sim 10^{-2}$ seconds and non thermal gamma–ray spectra [Guilbert, Fabian & Rees 1983]. The compactness problem arises because of the conflict of the naive estimate of the source size $R \sim \delta t\ c \sim 3 \times 10^3$ km with the observed nonthermal GRB spectra: a number of gamma photons as large as the observed one confined within such a small region would imply an optical depth for e^+e^- pair production that large to unavoidably thermalize radiation and produce a black body spectrum. The conflict can be resolved if one supposes that the emitting region moves towards the observer with an extreme relativistic speed, i.e. a very high value of the Lorentz factor γ. Then, the actual size of the emitting region would be $R \sim \gamma^2\ \delta t\ c \sim 3 \times 10^{12}$ cm, and the optical depth would become correspondingly smaller allowing non thermal emission in an optically thin environment [Paczyński 1986, Goodman 1986, Krolik & Pier 1991, Rees & Mészáros 1992].

Now-days relativistic motion in GRBs is widely accepted because of the apparent superluminal expansion measured during the radio afterglow of GRB 970508 thanks to interstellar scintillation [Goodman 1997, Waxman, Kulkarni & Frail 1998] (see fig. 2.5 and its caption).

The nature of the GRB progenitors is still unsettled, though it now appears likely that at least some of them originate in explosions of very massive stars or occur in or near the regions of massive star formation in other galaxies.

We have already noticed that their duration (0.1–100 s) and intrinsic variability timescale (10^{-3} s) suggest a spatial scale comparable to that of stars and dense stellar remnants, i.e. Black Holes (BHs) or Neutron Stars (NSs).

Actually, though many new ideas continue to be generated, after the establishment of the cosmological distance scale of the GRBs and therefore the energetic scale (see next section) the debate about progenitors has focussed on two types of models: explosions of very massive ($> 30\ M_\odot$?) stars (also known as "collapsar" or "hypernova" type models [Paczyński 1998, MacFadyen & Woosley 1999]), and mergers of compact stellar remnants [Eichler, Livio, Piran & Schramm 1989] (NS, BH, or even white dwarfs; but with at least one merger being a NS or a BH).

In both cases, the end product is a stellar mass scale BH, surrounded by a rapidly rotating torus, whose orbital kinetic energy can be extracted via magneto hydrodynamical (MHD) processes and used to power the GRB. If the BH itself is threaded by a magnetic field (which has to be amplified to $\sim 10^{15}$ G), its spin energy can be extracted via the Blandford–Znajek mechanism [Blandford & Znajek 1977]. Both mechanisms can extract $\sim 10^{54}$ ergs, and both provide a natural collimation (spin) axis, for energy release via Poynting jets. Additional energy ($\sim 10^{51}$ ergs) can be provided by thermal neutrino cooling, $\nu\bar{\nu} \rightarrow e^{\pm}, \gamma$. The gravitational wave component is strongly model–dependent and is highly uncertain at this point; hopefully it will be settled observationally with LIGO and LISA. Regardless of the exact model for GRBs, it appears highly likely that black holes are involved.

The evidence for the collapsar/hypernova type of models is becoming increasingly compelling, at least for the well–studied long bursts, but the case is still not closed. It is entirely possible that more than one physical model is at work, where very different physical mechanisms lead to a roughly comparable observed phenomenology. This can happen because after a while fireballs loose memory about the initial explosion mechanism they were produced by.

We will not refer to any particular GRB progenitor model because the physics of the afterglows is reasonably well understood, and has been tested and confirmed very well by the observations regardless detailed knowledge on the GRB origin.

2.2 A bit of history

The first GRB was recorded with the *Vela* satellites on July 2, 1967 [Klebesadel, Strong, & Olson 1973, Strong, Klebesadel, & Olson 1974]. More than

2000 bursts were detected by numerous space–based experiments in the following 30 years, but for all the three decades, the nature of GRBs have remained mysterious. The main reason for the missing identification of the burster population was that prior to 1997 no small, arcmin–sized GRB error boxes were available for rapid follow–up observations. This unsatisfactory observational situation led to an enormous flood of publications and culminated in more than 100 theories about the nature of the bursters. GRB distance were absolutely uncertain: their distance D from the earth could vary in different models from tens of astronomical units (1 AU $\approx 1.5 \times 10^{13}$ cm), up to Gigaparsecs (1 Gpc $\approx 3{\times}10^{27}$ cm). So, for a typical fluence $F \sim 10^{-6}$ ergs cm^{-2} the total energy emitted in gamma–rays under assumption of isotropic emission, $E_{\gamma,iso} = 4\pi F D^2$, could be as low as $\sim 10^{24}$ ergs for the nearest locations, and go up to $\sim 10^{50}$ ergs for 1 Gpc. And if F is 4 orders of magnitudes higher (as e.g. for GRB 990123), and/or the distance is larger than 1 Gpc, then the energy release in gamma photons becomes correspondingly higher.

An indirect evidence for cosmological location of GRBs, i.e. on the Gpc distance scale and on the luminosity scale as a consequence, is their isotropic distribution on sky [Prilutskii & Usov 1975].

The 1990's have seen two observational breakthroughs in GRB research. The first came with the *Burst and Transient Source Experiment* (BATSE)
on the *Compton Gamma-Ray Observatory* (CGRO)
[Fishman 1981],[Fishman *et al.* 1993],[Fishman *et al.* 1994]. It characterized the period from 1991 to 1996. During this period several GRB experiments aboard various satellites were carried out, but BATSE was most successful. In operation since 1991, BATSE detected about 1 burst/day, corresponding to a full sky rate of about 800 a year [Meegan *et al.* 1992]

The method of checking with high precision the angular isotropy of the bursts on the sky worked very well with the large sample of BATSE detected bursts in spite of the very large error boxes ($\approx$ tens of degrees), and, based on BATSE gamma–ray data alone, over the years it became more and more difficult to postulate a Galactic halo origin of all bursts [Briggs *et al.* 1996, Hakkila *et al.* 1994, Tegmark *et al.* 1996b].This included constraints on burst repetition [Meegan *et al.* 1995, Tegmark *et al.* 1996a].

This evidence represented substantial progress. However the missing item was the direct observational proof of an extra galactic origin of the bursts. This second observational breakthrough was initiated by the Italian–Dutch gamma–ray/X–ray satellite *Beppo–SAX* launched in 1996 [Boella *et al.* 1997, Costa *et al.* 1998, Frontera 1998]

and later it included successful GRB localizations with RXTE [Bradt & Smith 1999, Smith *et al.* 1999] and HETE [Price, Kulkarni *et al.* 2002].

Contrary to BATSE, Beppo–SAX can provide an arcmin–sized GRB error box within hours after the GRB trigger, though only about ten bursts a year because of its small field of view.

Beppo–SAX has both a gamma–ray detector (GRBM) and a wide field ($\sim 40° \times 40°$) soft X–ray camera (WFC). It could for the first time find an X–ray transient in the same field where a GRB flashed, provide X–ray positions with accuracy of a few arc minutes and re-point them with the Narrow Field Instruments (NFI, imaging instruments orthogonal to both the GRBM and the WFC axes) after a delay of only 4–6 hours for processing. The technique led to the discovery by Beppo–SAX [Costa *et al.* 1997] of the first X–ray transient associated with GRB 970228. This allowed follow–ups in X–rays (by Beppo–SAX itself), in visual light [van Paradijs *et al.* 1997] as well as at radio wavelengths [Frail *et al.* 1997]. The transient counterparts to GRBs are called X–ray, optical (i.e. visual light) and radio *Afterglows*. X–ray afterglows usually become undetectable in a day, optical afterglows last a few days and radio afterglows last some weeks. For some of them the observations last many months [Zharikov *et al.* 1998]. The number of discovered GRB afterglows is growing continuously and much has been learned about GRBs based on multi–wavelengths observations of afterglows.

The breakthrough in proving that at least some of GRBs are at cosmological distances occurred when absorption lines with redshift $z = 0.835$ were measured in the spectrum of the optical transient counterpart of GRB 970508 [Metzger *et al.* 1997]. Since the absorption was seen in the light of the afterglow, the source could be only more distant. Thus $z = 0.835$ is a lower limit to the redshift of the transient and the GRB that induced it. Later, in some cases, the identification of candidate host galaxies was suggested. Spectroscopy of the likely host galaxy generally shows that the absorption redshift measured during the afterglow coincides with the redshift of the galaxy emission lines, confirming the association of the GRB with the proposed host. An outstanding example is the galaxy associated with GRB 971214, its redshift probably being $z = 3.418$ [Kulkarni *et al.* 1998]. The correctness of this value has been matter of debate, since there is only one emission line discernible above the noise level of the spectrum of this very distant galaxy, and the identification relies heavily on the assumption that the line is a Lyman–α. For GRB 000301C and GRB 000131 the lower limit to the afterglow redshift has been determined through identification of absorption edges with the Lyman limit and in-

tervening Lyman–α forest [Smette, Fruchter *et al.* 2001, Masetti, Bartolini *et al.* 2000, Garnavich, Loeb & Stanek 2000, Andersen, Hjorth *et al* 2000]. The obtained redshifts are actually higher than the average: $z = 2.033$ the former and $z = 4.5$ the latter. Much more convincing is the observation of a system of absorption lines with $z = 1.6$ in the spectrum of the afterglow of the very bright burst GRB 990123 [Kulkarni *et al.* 1999] followed by host identification [Fruchter, Thorsett *et al.* 1999]. An energy output in gamma–rays $E_{\gamma,iso}$ of at least 3.4×10^{54} ergs is implied by such a redshift if emission is isotropic. Moreover, the sub–sample of GRBs with reported spectroscopic redshift shows estimated values of the isotropic energy output between 10^{51} and 10^{54} ergs, with the only exception of the very special burst GRB 980425, maybe coming from the local universe because it has been suggested for an association with the anomalous Type Ic Supernova SN1998bw at redshift z=0.0085. If such an association were correct, GRB 980425 would have $E_{\gamma,iso} \sim 10^{47}$ ergs, quite less than the average.

The huge energy release in some of the bursts implied by their extra galactic origin poses extremely hard questions to theorists who try to explain these super powerful events. Even if the beaming is invoked, which reduces the energy budget by a couple of orders of magnitude (if emission were confined within a cone of half–opening ϑ_b pointing to us the total emitted energy would be $E_\gamma \sim 4E_{\gamma,iso}/\vartheta_b^2$), this is still too high for conventional models that involves collapses or mergers of objects with masses on the solar mass scale.

2.3 The Afterglows

The occurrence of broad–band afterglows following GRBs was expected on theoretical grounds ([Rees 1998], and references therein). Compared to the duration of the bursts, afterglows in the long–wavelengths bands were expected to be long–lived, making the precise localization of the bursters possible and extending GRB research into international multi–wavelength observing campaigns.

According to the currently most accepted theoretical GRB model, the afterglows are due to external shocks when a relativistically expanding fireball released by a compact source sweeps up matter from the "interstellar" medium surrounding the burster (for an introduction into this subject and/or a review, see Mészáros 1997, Mészáros 2000; Piran 1997, Piran 1999, Piran 1999a; Rees 1999). This medium could be, for example, the ordinary interstellar medium in a spiral galaxy, or the stellar wind environment from the GRB progenitor [Chevalier & Li 2000, Halpern *et al.* 1999]. The afterglow

emission process is most likely synchrotron radiation (see, e.g., Sari, Piran, & Narayan 1998; Wijers, Rees, & Mészáros 1997, and references therein).

At the date of submission of this thesis, long–lasting optical afterglows have been observed from about 25 GRBs, and about 20 radio afterglows have been discovered. In three cases (GRB 970828, GRB 981226, and GRB 990506) the radio afterglow has been detected in spite of the lack of optical counterparts. Evidence for a short–lived afterglow in the gamma–ray band has been reported in the case of GRB 980923 [Giblin *et al.* 1999]. About 60% of all GRB afterglows seen in the X–ray band show no detectable optical emission, whereas almost all well localized GRBs detected by Beppo–SAX exhibited an X–ray afterglow [Costa 1999].

Then, X–ray afterglow emission appears to be ubiquitous. The failure to find radio afterglow is most likely due to lack of sensitivity (see section 2.4.3), but the discussion on failed detection of optical afterglows, i.e. the problem of the "dark" GRBs, is more delicate. Many causes can concur to make optical searches unsuccessful (see also [Djorgovski, Frail *et al.* 2001]). First of all, as we will explain in section 2.4.2, optical afterglows show a larger range of decay rates with respect to other afterglows, and have a rather wide range of magnitudes measured at equal times from the GRB, so they might be intrinsically faint, rapidly decaying, or dim because of the large redshift, causing the Lyman–α break to affect the optical spectrum. This, together with the lack of a straightforward correlation between optical emission and gamma–ray brightness of the prompt event, makes it difficult to predict the detection level and to devise an optimal observing strategy. Therefore, in some cases, the lack of an optical detection may be due to the insufficient sensitivity of the search [Taylor, Bloom *et al.* 2000, Fynbo, Jensen *et al.* 2001, Frail, Kulkarni *et al* 1999].

Moreover, to date, there are about 23 reported redshift measurements of GRB afterglows and/or host galaxies [Bloom, Kulkarni & Djorgovski 2002]. The redshifts measured so far either with spectroscopy or broad–band photometry span the range $\sim$0.4 to $\sim$4 (excluding the peculiar case of GRB 980425). The data seem to indicate that the redshift distribution of the bursters peaks around 1, with a long tail towards higher redshifts (for model fits see, e.g., [Schmidt 1999]).

Precise localization of the GRBs via afterglow detection and redshift measurements is very important in constraining the progenitor model. The statistical study of the offsets of GRBs from their apparent host galaxy centers performed by [Bloom, Kulkarni & Djorgovski 2002], for instance, provides strong observational evidence for the connection of GRBs to star–formation and allows to rule out at the

2×10^{-3} level the compact objects binary merger model for GRB progenitors.

But just the large number of successful host galaxy identifications within the subsample of GRBs showing an optical counterpart simply suggests that GRBs usually occur inside galaxies. So optical afterglows may be affected by absorption in their host galaxies as well as by extinction in the plane of our Galaxy (which is instead transparent to gamma–rays, to hard X–rays and to radio wavelengths) and this makes their detection largely more difficult than detection at other wavelengths. The further evidence of association of GRBs to star forming regions found by [Bloom, Kulkarni & Djorgovski 2002] can only strengthen the idea that many optical afterglows might be simply undetectable because highly absorbed.

By simulating the absorption experienced at the center of a dense dust clump, similar to those found in star forming regions in our Galaxy and in external ones, in a number of directions randomly distributed, Lamb determined that in only 35% of the lines of sight the optical depth is $\tau \lesssim 1$ (i.e. optical radiation from a GRB afterglow might escape the dust clump and reach the observer), while in the remainder it is $\tau \gg 1$ [Lamb 2001]. This statistic is consistent with the percentage of dark GRBs, supporting the idea that local dust absorption may hamper or completely prevent optical detection of the GRB afterglow and strengthening the importance of infrared observations to verify the presence of substantial quantities of dust at the burst explosion site and confirm the association of GRBs with star forming regions. Although the result of this test would relate all dark GRBs to the effect of dust extinction, perhaps this is only one of the possible causes for a failed optical detection.

An alternative view [Lazzati, Covino & Ghisellini 2001] is that dark GRBs can be heavily extincted only if dust sublimation by the strong UV/optical [Waxman & Draine 2000] and X–ray radiation [Fruchter, Krolik & Rhoads 2001] following the explosion does not play a significant role. If dust destruction around the burst site is important [Galama & Wijers 2001], then dark GRBs should belong to a distinct population with respect to GRBs with detected optical afterglows.

Anyway the basic questions if all GRBs have the same kind of progenitor and if all GRBs produce afterglows (X–ray afterglows at least) are still open mainly because the Beppo–SAX GRB sample [Frontera *et al.* 2000] is entirely composed of long bursts (i.e. bursts with duration longer than 10 s). No short (i.e. lasting less than 1 s) GRB has been localized accurately enough for multi wavelength follow–ups and hence for afterglow and host galaxy detection. The GRB 000301C, which was detected by the Interplanetary Network (IPN) with a 2 s duration and exhibited a bright variable coun-

terpart, cannot be unambiguously classified as long, sub–second hard, or intermediate GRB [Jensen, Fynbo *et al.* 2001].

2.4 Multi wavelength Afterglow Properties

The time–dependent flux density of a detected afterglow generally follows a power-law decay, $F_\nu(T) \propto T^{-\beta}\nu^{-\alpha}$ in accordance with fireball models and synchrotron emission from shock accelerated electrons [Sari, Piran & Narayan 1998, Wijers, Rees, & Mészáros 1997]. Since afterglows have been detected only associated to long GRBs, we refer only to this class of GRB.

Higher frequency afterglows are detected and are seen to fade earlier than lower frequency afterglows. X–ray afterglows are usually detected a few hours after the GRB, likely starting even earlier, maybe during the burst itself, and lasting a few tens of hours. Optical afterglows are usually detected within a day from the GRB and last a few days. Radio afterglows are usually detected within a few days or weeks from the GRB and last a few weeks or months.

2.4.1 X–ray afterglows

X–ray afterglows detected by Beppo–SAX have time slope β in the range 1.1–1.5 [Frontera *et al.* 2000] and typical 2–10 keV fluence[†] of the order of 10^{-6} ergs cm^{-2}, comparable to the GRB fluence in the 2–10 keV band and also to the GRB fluence in the 40–700 keV band. (Beppo-SAX usually detects X–ray emission simultaneous to gamma-ray emission from the main burst). The X–ray afterglow fluence ranges from 0.4% to 1% of the GRB fluence in the 2–10 keV band and from 0.4% to 20% of the GRB fluence in the 40–700 keV band, but the three quoted fluences are not strictly related. Thus, it seems that the total amount of energy emitted in gamma-rays and/or X–rays during the burst is comparable, on average, with the total amount of energy emitted in X–rays during the afterglow. Anyway how the X-ray emission observed during the burst connects to the X-ray afterglow is uncertain. The 2–10 keV afterglow spectral slope α is in the range 0.7–1.4 [Frontera *et al.* 2000]. In a few cases the X-ray afterglow light curve presents some evidence of steepening (see section 2.4.2).

[†]According to [Frontera et al. 2000] for X–ray afterglow 2–10 keV fluence we mean the integral of X–ray afterglow radiation from the end of the GRB up to 10^6 s, integral obtained by extrapolating the observed fading law.

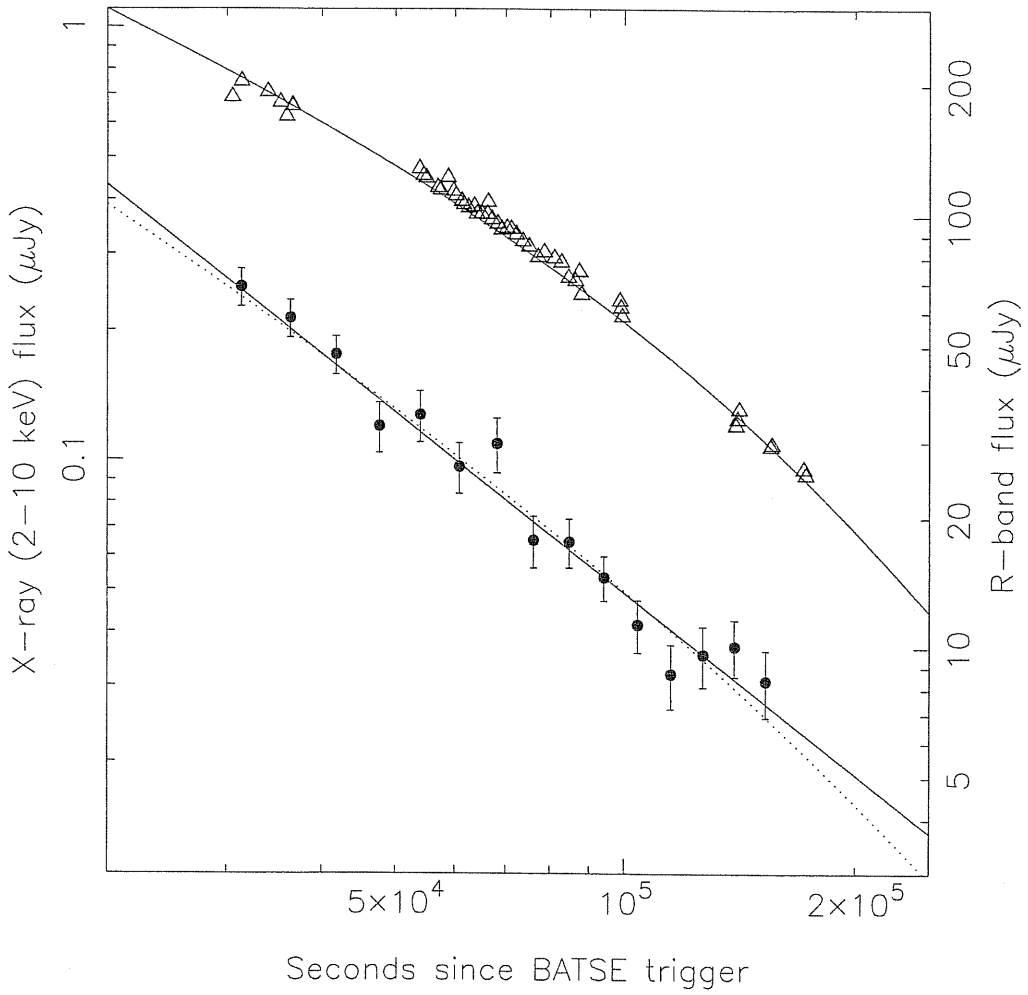

Figure 2.1: *Figure extracted from [Kuulkers, Antonelli et al. 2000]. X-ray (filled circles) and optical R-band (open triangles) light curves of the afterglow of GRB 990510. The R-band measurements (Stanek, Garnavich et al. 1999, Harrison, Bloom & Frail 1999, Covino, Lazzati et al. 1999) have been corrected for reddening ($A_R = 0.54$, Harrison, Bloom & Frail 1999) and reduced to the same photometric system. For the R-band we also show the corresponding fit to a steepening power-law (solid curve) as given in the literature (Harrison, Bloom & Frail 1999, Stanek, Garnavich et al. 1999, Israel, Marconi et al. 1999). The X-ray light curve can be satisfactorily described by a single power law (solid line) or a steepening power law similar to that describing the R-band data, but with parameter values appropriate for the X-ray data.*

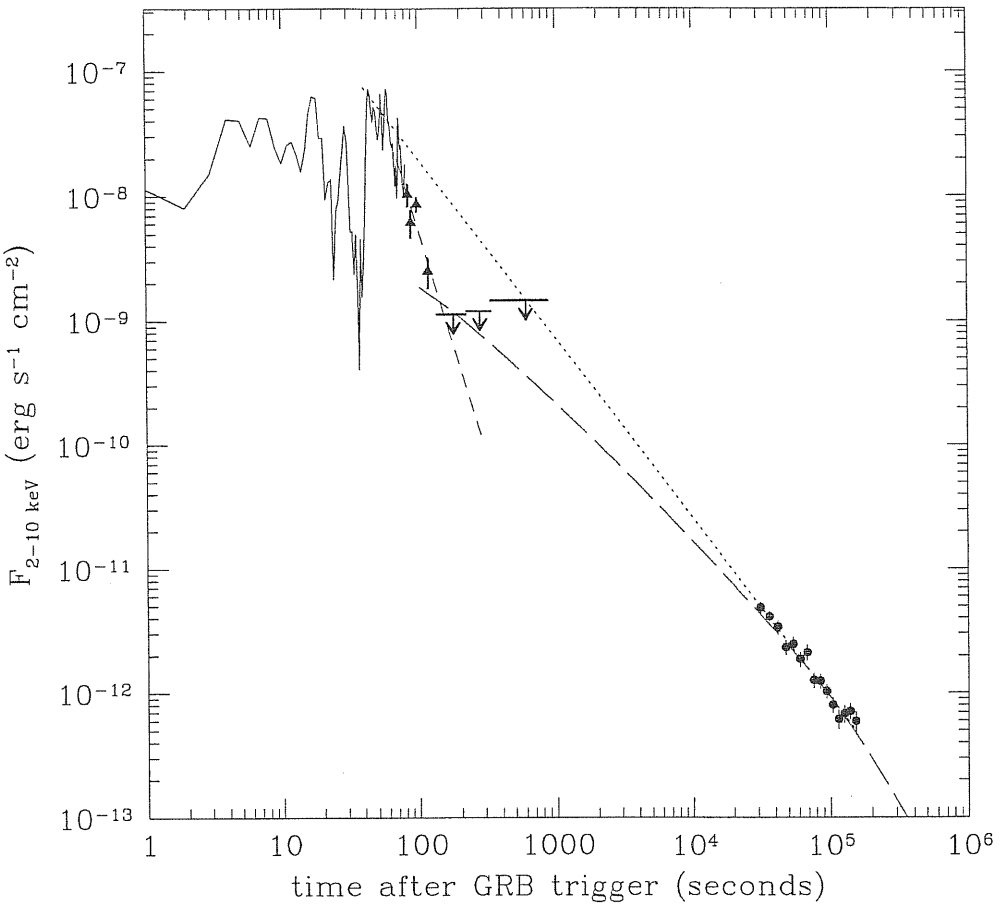

Figure 2.2: *Figure extracted from [Pian, Soffitta et al. 2001]. Beppo–SAX light curves of GRB 990510 in the 2–10 keV range: WFC temporal profile (solid curve, filled triangles and 3–σ upper limits) and afterglow NFI measurements (filled circles). Also shown are the single power–law $f(t) \propto t^{-1.42}$ (dot) fitted to the afterglow by [Kuulkers, Antonelli et al. 2000] (see fig.2.1), the power–law $f(t) \propto t^{-3.7}$ (short dash) which best–fits the last four points of the WFC profile, and the double power–law of indices $\alpha_1 \simeq 1$ and $\alpha_2 \simeq 2$ (long dash) required for the afterglow to fit the jet model by [Panaitescu & Kumar 2001a]. The extrapolation of the single power–law $t^{-1.42}$ backward to the time of the prompt event is not consistent with the WFC latest points and upper limits, while the double power–law matches well the last WFC point and upper limits.*

2.4.2 Optical Afterglows

At epochs between a few hours and ~1 day after the GRB the afterglow decays following approximately a temporal power–law $t^{-\alpha}$ with an index α ranging from ~1 to ~2. These slopes are sometimes steeper than the corresponding ones at other wavelengths (see discussion in section 2.5). Moreover, rapid fading ($\alpha > 2$) has been observed in GRB 980326 [Groot *et al.* 1997] and GRB 980519 [Halpern *et al.* 1999, Vrba *et al.* 2000] and GRB 991208 [Castro-Tirado *et al.* 2001].

For GRB 970508 a "plateau" ($\alpha = 0$) has been observed between 3 hours and 1 day from the bursts [Pedersen *et al.* 1998, Castro-Tirado *et al.* 1998]. The optical light curve reached a peak in two days [Djorgovski *et al.* 1997, Galama *et al.* 1998] and was followed by a power law decay with $\alpha = 1.2$. Another plateau was detected in the near infrared light curve of GRB 971214 between 3 and 7 hours from the burst [Gorosabel *et al.* 1998].

Usually the optical transient following a GRB has an R–band magnitude of about 18–23 when it is detected some hours after the burst [Pian 2001], provided that no strong extinction occurs in the GRB host galaxy or in our Galaxy. Such initial luminosities of GRB optical afterglows are two orders of magnitudes larger than maximum supernova luminosities (GRB 980425, possibly associated to SN1998bw, was an exception [Galama *et al.* 1998]) and obviously out-shine their parent galaxies, which become visible weeks or months after the main burst. This can make the optical transient detectable to 1–m class telescopes. When the flux of the transient subsides under the brightness of the host galaxy, the optical light curve levels off. This allows a photometric estimate of the host magnitude, which is generally confirmed or refined by successive direct HST imaging. The afterglow magnitudes reported by [Pian 2001] have been obtained from a fit with a single or double power–law after subtraction of the host galaxy flux, and in some cases after decomposition of a possibly underlying supernova using SN1998bw as a template, appropriately redshifted. Actually, the still debated association of GRB 980425 to the peculiar TypeIb/c Supernova SN1998bw [Galama *et al.* 1998] coincident with a galaxy at redshift $z = 0.0085$ suggested to interpret bumps observed in the late light curves of GRB 970228 [Reichart 1999], [Galama *et al.* 2000], GRB 970508 [Sokolov *et al.* 2001], GRB 980326 [Castro-Tirado & Gorosabel 1999], [Bloom *et al.* 1999], GRB 980703 [Holland *et al.* 2001], GRB 991208 [Castro-Tirado *et al.* 2001] and GRB 000418 [Klose *et al.* 2000, Lazzati *et al.* 2001] as contributions from a SN1998bw–like Su-

pernova. But alternative explanations for the existence of such bumps in the Optical Afterglow light curves exist, like, for instance, scattering of a prompt optical flash by 0.1 $M_{\odot}$ dust located beyond the sublimation radius (0.1–1 pc from the main burst origin) producing an echo after 20–30 days as observed [Esin & Blandford 2000]; delayed energy injection by late shell collision [Kumar & Piran 2000], [Kumar & Piran 2000a], or finally, axially symmetric jet surrounded by a less energetic outflow [Panaitescu, Mészáros & Rees 1998]. In any case, to complicate further the picture, the afterglow of GRB 990712 provides a firm evidence that no underlying Supernova was present [Hjorth *et al.* 2000].

In a large fraction of the best monitored optical and/or near–infrared afterglows the initial power–law decline steepens at times ranging from ∼0.5 to ∼5 days after the GRB explosion. The first break deviating from a power–law decay was observed 1.5 days after the burst in GRB 990123. Further breaks have been reported in other GRBs: GRB 990123 [Castro-Tirado, Zapatero-Osorio *et al.* 1999], [Fruchter, Thorsett *et al.* 1999], [Kulkarni *et al.* 1999], GRB 990510 [Harrison, Bloom & Frail 1999], [Stanek, Garnavich *et al.* 1999], [Israel, Marconi *et al.* 1999], GRB 991208 [Castro-Tirado *et al.* 2001], GRB 991216 [Halpern, Uglesich *et al.* 1999], GRB 000301C [Masetti, Bartolini *et al.* 2000], [Jensen, Fynbo *et al.* 2001], [Rhoads & Fruchter 2001], [Bhargavi & Cowsik 2000], GRB 000926 [Fynbo, Gorosabel *et al.* 2001], [Rol, Wijers *et al.* 2000], [Price, Harrison *et al.* 2001], GRB 010222 [Stanek, Garnavich *et al.* 2001], [Masetti, Palazzi *et al.* 2001]. Fig.2.3 illustrates the achromatic break in the light curves observed in different visual bands for this last GRB. The effect is clearly seen as a smooth increase of the flux decay rate and is suggested also by the X-ray data in a few cases: GRB 990510 [Pian, Soffitta *et al.* 2001], GRB 000926 [Harrison, Yost *et al.* 2001], [Piro, Garmire *et al.* 2001], GRB 010222 [Zand, Kuiper *et al.* 2001].

A very special case is the case of GRB 990123, where an astonishingly bright optical flash was detected for the first (and still unique) time when the burst was still in progress in the gamma–ray band [Akerlof *et al.* 1999]. The detection was due to ROTSE–I, a robotic optical telescope consisting of a two–by–two array of 35 mm lenses performing automatic follow–ups of just detected GRBs. The optical flash of GRB 990123 was detected in 22 seconds from the trigger and peaked about 45 sec after the onset of the burst at a mean V-band magnitude of about 9 on a frame with a 5 sec exposure [Akerlof *et al.* 1999]. The (minimum) redshift of the burster was found to

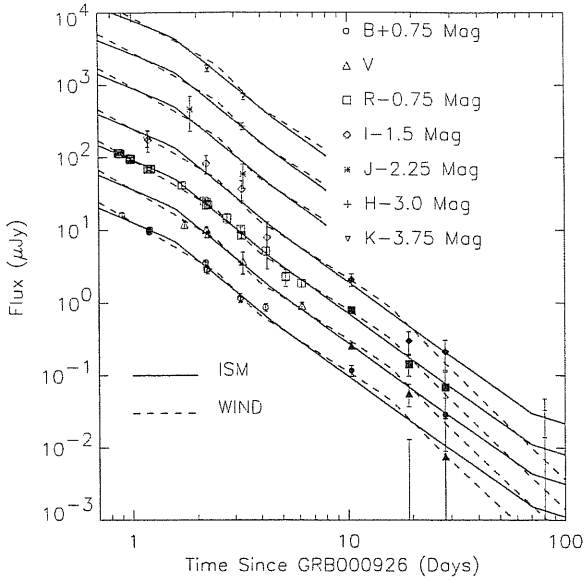

Figure 2.3: *The BVRIJHK light-curves of the afterglow of GRB 000926, from 8 hours to 80 days after the GRB, with model fits corresponding to an isotropic ISM and an* $\rho \sim r^{-2}$ *(i.e., simple stellar wind) medium [Harrison, Yost et al. 2001]. Also evident is a break in the light-curve at* $t \sim 1.5$ *days, interpreted as evidence for collimation of the ejecta [Price, Harrison et al. 2001]. Fluxes from the underlying host galaxy and another contaminating galaxy have been subtracted using late-time HST observations.*

be 1.60 [Andersen *et al* 1999, Kulkarni *et al.* 1999], so that the optical flash translates into an ultraviolet rest–frame luminosity of about $3 \times 10^{16}\ L_{\odot}$ [Kulkarni *et al.* 1999]. This early optical peak seems to be uncorrelated with gamma–ray peaks of the burst, and the ROTSE–I light curve is fitted by a steeper temporal power law than the afterglow points, indicating a different radiation mechanism (see fig. 2.4). Prompt emission at optical and near–infrared wavelengths simultaneous with a GRB, or delayed by a few seconds, was predicted from theory (see [Mészáros, Rees & Papathanassiou 1994, Mészáros & Rees 1997, Mészáros 2000, Sari & Piran 1999b], and references therein; for a phenomenological approach, see [Ford & Band 1996]). It is expected to take place as a consequence of a reverse shock propagating into the explosion ejecta, and is therefore distinct from the afterglow, which should be produced by the interaction of the forward shock with the external medium. The estimated power output in the optical flash of GRB 990123 of about 1% of that gamma–ray energies [Galama, Briggs *et al.* 1999], seems to be in agreement with the reverse shock interpretation and allows an estimate of the plasma initial Lorentz factor [Sari & Piran 1999b].

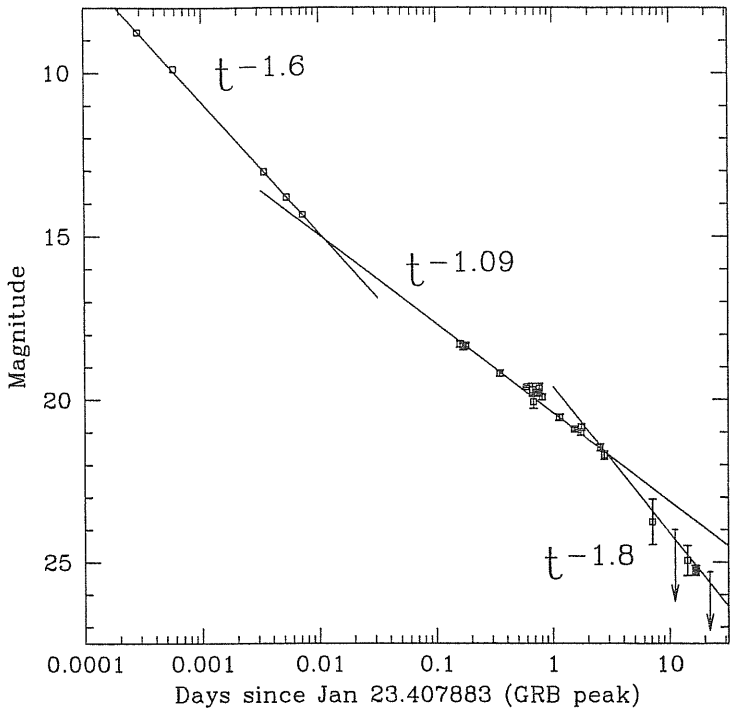

Figure 2.4: *Figure extracted from [Fruchter, Thorsett et al. 1999] illustrating the R-band light curve of the GRB990123 afterglow. ROTSE-I data are reported (from immediately after the light maximum to* $\sim$ *10 minutes after the GRB) along with the measurements of successive afterglow taken at bigger telescopes. All points, except for the HST point (rightmost filled square), represent measurements taken from the ground and are reduced to a common flux standard with the galaxy flux subtracted. Error bars (1* σ*) are shown where available, and arrows indicate 95% confidence upper limits.*

The last important observational campaign regarding GRB afterglows in the visual band is polarimetry. We have already said that the multi wavelength afterglow spectrum is thought to be primarily produced by synchrotron radiation from a relativistic plasma expanding in the interstellar medium or in a wind pre–ejected by the GRB stellar progenitor [Piran 1999, Chevalier & Li 1999]. Besides the approximately good agreement of the relation between temporal and spectral slopes of observed afterglows with the predictions of synchrotron emission based afterglow models, that has long been considered a convincing argument in favor of the model itself (see discussion in the following section) also linear polarization, measured in the optical afterglows of GRB 990510 and GRB 990712 at

the level of a few percent [Wijers, Vreeswijk *et al* 1999, Covino, Lazzati *et al.* 1999, Rol, Wijers *et al.* 2000], represents a good test of the synchrotron mechanism [Loeb & Perna 1998, Gruzinov & Waxman 1999]. In the case of GRB 000301C, near–infrared polarimetry yielded only an upper limit of 30%. Although not very constraining, this is consistent with a synchrotron origin of the continuum in a relativistic jet [Stecklum, Fischer *et al.* 2001].

2.4.3 Radio afterglows

The first radio afterglow detection came following the localization of GRB 970508 [Frail *et al.* 1997]. The radio afterglow of GRB 970508 is famous for several reasons: it was the first radio detection, it gave the first direct demonstration of relativistic expansion (see the caption of fig. 2.5), and it remains the longest–lived afterglow [Frail, Waxman & Kulkarni 2000].

The more extended international collaboration for radio afterglow detection [Frail *et al* 1999] uses the interferometer facilities of the Very Large Array (VLA), the Australia Telescope Compact Array (ATCA), the Very Long Baseline Array (VLBA) and the Owens Valley Radio Observatory (OVRO) Interferometer. At high frequencies, single dish telescopes which include the James Clerk Maxwell Telescope (JCMT) and the OVRO 40-m Telescope are used. All afterglow searches begin as quick as possible with the VLA in the northern hemisphere (dec.$> -45°$, $\sigma_{\rm rms} = 45$ μJy in 10 min., FOV$\simeq 5'$) and the ATCA in the southern hemisphere (dec.$< -45°$, $\sigma_{\rm rms} = 45$ μJy in 240 min., FOV$\simeq 5'$), typically at a frequency of 8.5 GHz, which provides a balance between sensitivity and field–of–view. Follow–up programs at the other radio facilities are begun after a VLA or ATCA transient is discovered.

Since 1997 only for 40% of the GRBs observed with the VLA a radio afterglow has been detected. Usually the rising to a peak followed by power law decay is observed (see e.g. GRB 980703 in fig. 2.5) [Frail *et al* 1999, Kulkarni *et al.* 2000]. In contrast, at optical and X–ray wavelengths, most of the times we see only the decaying portion of the light curve (as expected, the higher frequency afterglow light curve peaks on shorter timescales). The peak fluxes of the radio afterglow detections range from 1200 μJy to 150 μJy. This small range of values suggests that our ability to detect radio afterglows is severely limited by the sensitivity of the telescope. The brightest radio afterglow to date is that from GRB 991208 with a peak flux of 2 mJy, a 60-σ detection (at centimeter wavelengths) whereas the weakest afterglow is typically around 5σ. In

contrast, at optical and X-ray wavelengths, afterglow emission is routinely detected at hundreds of sigma.

The "lifetime" of the radio afterglows is signal–to–noise limited but it is clear, at least among bursts of comparable brightness, that it varies substantially. Of special note are the three GRBs (970828, 981226, and 990506) which have no optical counterparts. These may represent an important group of GRBs whose optical emission is extincted by dust.

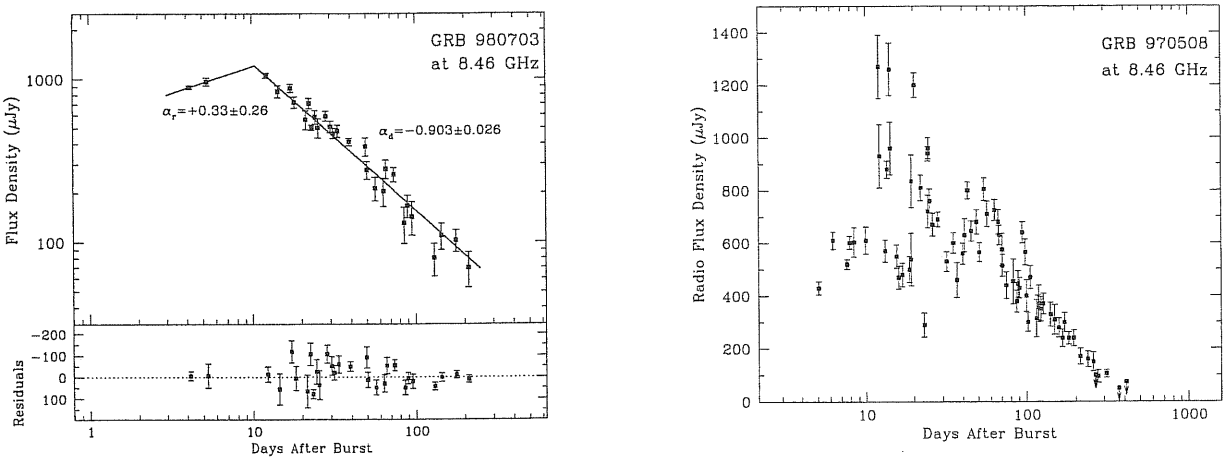

Figure 2.5: *Figure extracted from [Kulkarni et al. 2000]. Left: The radio light curve of GRB 980703. This is a typical afterglow, a rise to a peak followed by a power law decay. Right: The radio light curve of GRB 970508 [Frail, Waxman & Kulkarni 2000]. The wild fluctuations of the light curve in the first three weeks are chromatic. At later times, the fluctuations become broad–band and subdued. These fluctuations are a result of multi–path propagation of the radio waves in the Galactic interstellar medium. As the source expands the scintillation changes from diffractive to refractive scintillation. According to the theory of interstellar scintillation, the time at which oscillations stop gives a measure of the source linear size and consequently allows to estimate the average expansion speed of the source. This speed appears to be superluminal, and relativistic expansion must be invoked to explain the observations.*

2.5 Discussion

The classical fireball model we will illustrate in detail in the following chapter (under the assumptions of spherical symmetry and impulsive energy ejection) has specific predictions for the temporal evolution of the broad–band spectral shape of afterglows [Sari, Piran & Narayan 1998]. This has been modified to include the detectable effects of the presence of a jet [Sari, Piran & Halpern 1999].

The basic model assumes that electrons are accelerated by the shock into a power–law distribution $N(\gamma_e) \sim \gamma_e^{-p}$ for $\gamma_e > \gamma_m$. The lower cutoff of this distribution is assumed to correspond to an electron energy density equal to a fixed fraction ϵ_e of the total internal energy density of the plasma. It is also assumed that a considerable magnetic field is being built behind the shock and that it is again characterized by a certain fraction ϵ_B of the internal energy density of the plasma. The relativistic electrons then emit synchrotron radiation which is the observed afterglow. The broad band spectrum of such emission was given by [Sari, Piran & Narayan 1998] (see fig. 2.6). At each instant, there are three characteristic frequencies:

(*i*) ν_m which is the synchrotron frequency of the minimal energy electrons, having a Lorentz factor γ_m.

(*ii*) The "cooling frequency" ν_c that corresponds to the characteristic Lorentz factor γ_c, above which electrons can cool on the dynamical timescale of the system. Remind that the cooling time of an electron is inversely proportional to its Lorentz factor γ_e. Therefore, electrons with a Lorentz factor higher than the critical value γ_c for which the cooling time is equal to the dynamical timescale of the fireball, have a shorter cooling time.

(*iii*) The critical frequency ν_a below which the synchrotron radiation is self absorbed and the flux is given by the Rayleigh–Jeans portion of a black body spectrum.

The evolution of this spectrum as a function of time depends on the hydrodynamics. The simplest, which also describes the data well, is the spherical adiabatic model with a surrounding medium uniform or with a density $\propto r^{-2}$ (where r is the distance from the centre of the explosion, or the centre of the expanding spherical fireball). The rest mass collected by the shock at radius R_s is about $R_s^3 n_i m_p$ where n_i is the external medium particle density. On the average, the particles move with a Lorentz factor γ_s^2 in the observer frame, and therefore the total energy is given by $E_T \sim \gamma_s^2 R_s^3 n_i m_p c^2$.

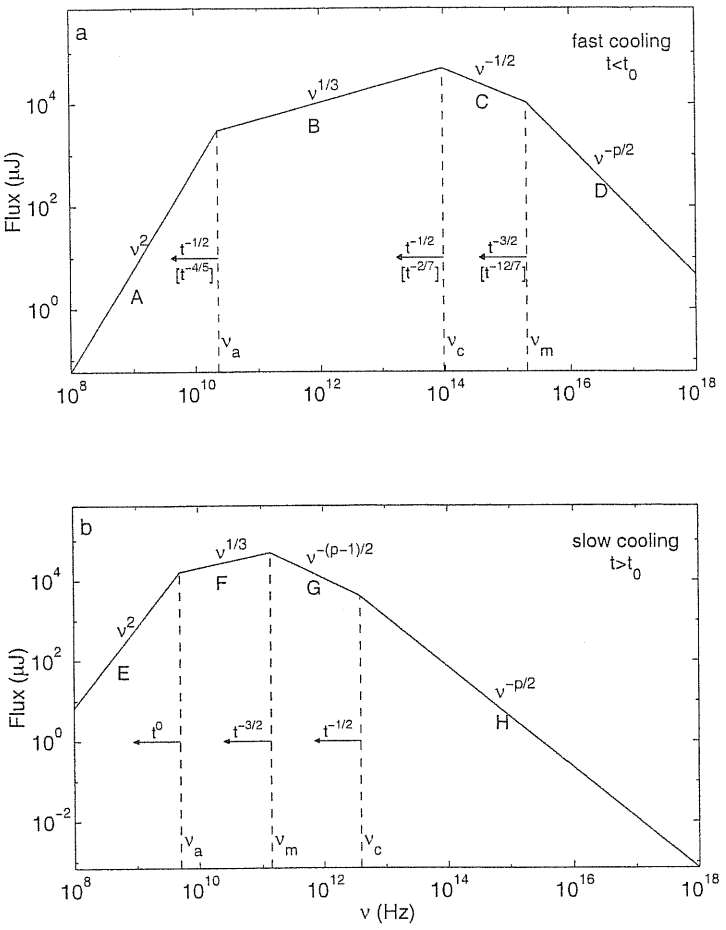

Figure 2.6: *From [Sari, Piran & Narayan 1998]. Theoretical spectra of synchrotron emission from a power–law distribution of electrons. Two different regimes are illustrated: (a) Fast cooling, which is expected at early times. In this case all the emitting electrons cool on a timescale shorter than the hydrodynamical timescale, i.e.* $\nu_c < \nu_m$. *The characteristic frequencies decrease with time as indicated; the scalings above the arrows correspond to an adiabatic evolution, and the scalings below, in square brackets, correspond to a fully radiative evolution. (b) Slow cooling, which is expected at late times. In this case* $\nu_c > \nu_m$ *and only electrons with a Lorentz factor greater than* γ_c *cool on a timescale shorter than the hydrodynamical timescale. The evolution is always adiabatic. Electron energy power–law index* $p \approx 2.2 - 2.4$ *fits well the observed spectra. The temporal scalings correspond to the case of a spherical fireball shock expanding into a constant density medium.*

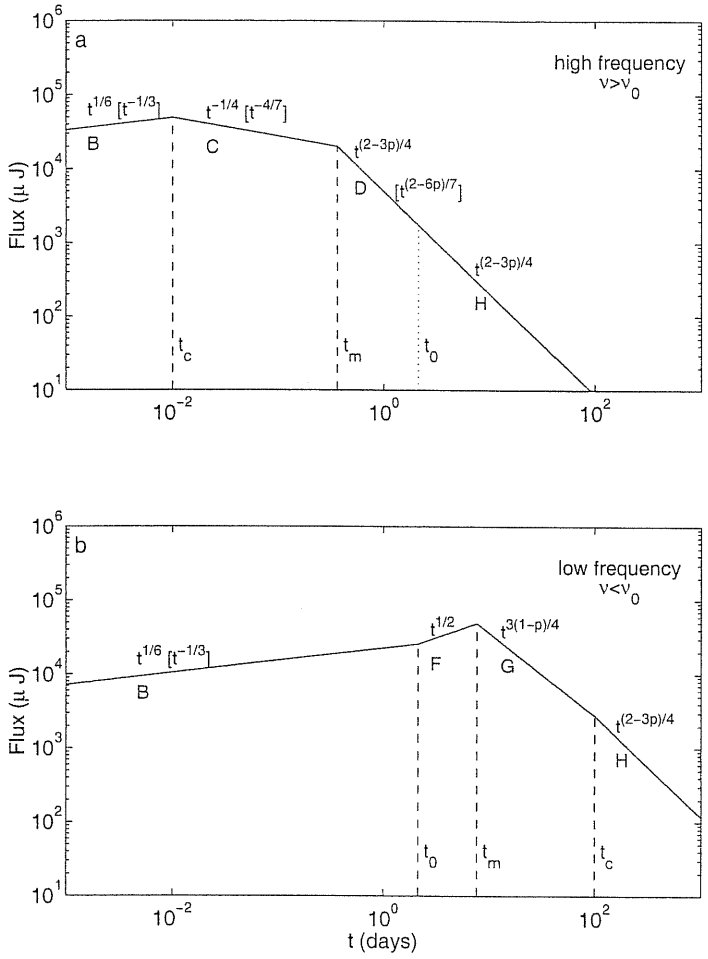

Figure 2.7: *From [Sari, Piran & Narayan 1998]. Theoretical lightcurves corresponding to the afterglow models shown in fig. 2.6, in the high frequency (a) and low frequency (b) regimes. The four segments that are separated by the critical times as labeled correspond to the spectral segments in fig. 2.6. The observed flux varies with time as indicated; the scalings within square brackets are for radiative evolution, and the other scalings are for adiabatic evolution.*

Assuming that the radiated energy is negligible compared to the flow energy, we obtain that $\gamma_s \sim R_s^{-3/2}$ or in terms of the observer time, $T = R_s/\gamma_s^2 c$ (see section 3.6.1 for a proper definition of the observer time), we get $\gamma_s \sim T^{-3/8}$. If the external particle density drops as r^{-2} (as is expected if the surrounding is a wind produced earlier by the progenitor of the burst) we get $\gamma_s \sim T^{-1/4}$. These simple scaling laws lead to the spectrum evolution illustrated in fig. 2.6.

One can then construct light curves at any given frequency. These will consist of power laws, changing from one power law to the other once the break frequencies sweep through the observed band (see fig. 2.7). These power laws are in good agreement with the observations.

According to this simple model simultaneous multi wavelength observations at various epochs during the evolution of the afterglow allow the measurement of the spectral slopes and breaks and the estimate, in principle, of the relevant physical parameters of the afterglow: total energy, ambient medium density, magnetic field energy density, electron energy density, plasma Lorentz factor (see e.g., [Wijers & Galama 1999, Panaitescu & Kumar 2001a, Panaitescu & Kumar 2001b]). The knowledge of both temporal decay slopes and spectral slopes in afterglows should allow also the measurement of the slope p of the electron energy distribution.

Afterglows typically have energies $< 10^{51}$ ergs, and power–law electron energy distributions with index $p \approx 2.3$. However, some afterglows appear to have harder electron energy distributions, with $p \approx 1.5$ and a high energy cutoff. Moreover the optical photometric observations, which are often accurate and sufficiently extended in time to make a good signal–to–noise ratio measurement of the spectral and temporal slopes possible, show that the optical spectra of some afterglows, corrected for Galactic extinction, are steeper (i.e., redder) than expected from the theory based on comparison with the temporal decay rate. This has been commonly attributed to absorption intrinsic to the source or, especially for GRBs at very high redshift, intervening along the line of sight [Ramaprakash, Kulkarni *et al.* 1998, Reichart 2001]. Reddening by dust in the GRB host galaxy has been invoked in many cases to reconcile the afterglow spectrum with its temporal decay, using extinction curves typical of our own Galaxy, of star–forming galaxies, or of the LMC and SMC [Palazzi, Pian *et al.* 1998, Vreeswijk, Galama *et al.* 1999, Dal Fiume & Amati 2000, Masetti, Palazzi *et al.* 2001,
Harrison, Yost *et al.* 2001, Lee, Tucker *et al.* 2001, Jensen, Fynbo *et al.* 2001]. While even a moderate quantity of dust at the GRB source redshift may significantly at-

tenuate the observed optical spectrum (which corresponds, at the average $z \sim 1$, to rest–frame ultraviolet wavelengths), or even completely obscure it, near–infrared data are less affected and may be more effective in determining the overall afterglow spectrum, when combined with data at other frequencies [Palazzi, Pian *et al.* 1998, Dal Fiume & Amati 2000, Lamb, Castander & Reichart 1999]. Observations in the near–infrared range are therefore critical for the study of afterglows.

The simple spherical model just described can be easily modified to allow for a non homogeneous external medium. This would allow for a wider range of possible spectral and temporal slopes of afterglows, but due to the sparseness of multi wavelengths data for individual objects it is currently difficult even to distinguish between spherical models in which the ejecta expand into a $n_i \sim r^{-2}$ wind–stratified ISM, and models in which the ejecta expand into an $n_i \sim const.$ ISM, although the latter appears to be preferred in some cases [Harrison, Yost *et al.* 2001]. Early–time measurements may help distinguish between these possibilities. There have been suggestions [Panaitescu & Kumar 2001a] that the particle density of the ISM can be very low in some cases, $\sim 10^{-3} - 10^{-4}$ cm^{-3}. While this may present difficulties for the collapsar-type models, it might be explained in terms of pre–existing super bubbles [Scalo & Wheeler 2001].

Anyway, the change in the temporal slope sometimes observed in optical and even X–ray afterglows is thought to witness the presence of a decelerating jet. Collimation of the radiation in a jet structure has been long invoked by theorists also before light curve breaks observation because it would reduce the huge energy outputs ($\sim 10^{52} - 10^{54}$ ergs) derived from the observed gamma–ray brightnesses and the measured distances of GRBs, in the assumption of isotropy (see section 2.2). It can be shown that in case of a jetted fireball pointing toward the observer, when the aperture of the radiation cone, $\sim 1/\gamma_s$, (beaming angle), which progressively increases as the relativistic plasma decelerates, becomes larger than the jet opening angle ϑ_b, the observer is expected to perceive a faster light dimming, independent of wavelength, due to the jet edge becoming visible and/or to jet sideways expansion [Mészáros & Rees 1999, Sari, Piran & Halpern 1999, Rhoads 1999]: in the first case the decreasing brightness of the shock front would not be any longer partially compensated by the increasing of the emitting area visible to the observer; in the second case the sudden lateral expansion would cause a faster deceleration of the shock front. The prediction of [Sari, Piran & Halpern 1999] is that these two effects Should happen almost simultaneously and might cause a single break in the afterglow light curve at a

time of the observer $\propto \left(\frac{E_T}{n_i}\right)^{\frac{1}{3}} (\vartheta_b)^{\frac{8}{3}}$, with the temporal decay slope *alpha* of the afterglow passing from the value $\frac{3}{4}(p-1)$ to p at frequencies below the cooling frequency ν_c and from the value $\frac{3}{4}p - \frac{1}{2}$ to p at frequencies above the cooling frequency ν_c, provided that the slow cooling regime (i.e. the $\nu_m < \nu_c$) has started as expected.

The change in fading rate should be however smooth, due to light travel time effects at the ending surface of the jet [Panaitescu & Mészáros 1999, Moderski, Sikora & Bulik 2000]. The steepening of the afterglow light curve would then be a probe of the GRB and afterglow emitting geometry.

In this scenario we would expect different GRBs to have jets with different opening angles and breaks in the optical afterglow light curve at different times. But not all afterglows do exhibit a detectable steepening in their optical light curve. This may simply be due to under sampling: when not detected, the steepening may have occurred at early, not well–sampled epochs (many afterglows are described by power–laws with temporal indices steeper than 2), or at late epochs, when the afterglow behaviour is significantly contaminated by the emerging host galaxy or supernova, so that discerning a decay rate variation is more difficult. A further complication might be that one would expect jets are not always pointing toward the observer. The effect of off axis view can be either a flattening or a steepening of the light curve [Livio & Waxman 2000]. However a complete theoretical description of afterglow emission from jets as a function of the viewing angle is still missing in the fire-cone scenario.

To date specific jet models for individual cases have been proposed
[Panaitescu 2001, Berger, Diercks *et al.* 2001, Berger, Sari *et al.* 2000],
and [Stanek, Garnavich *et al.* 2001] have noted an anti–correlation between the slope change $\Delta\alpha$ accompanying optical breaks and the isotropic gamma–ray energy of the burst, suggesting that the different jet opening angle may be responsible for it. An unambiguous interpretation of the whole set of data on afterglows, or at least its greatest part, in terms of a simple jet model is not possible yet.

This is mainly because light curve steepening cannot be uniquely ascribed to a decelerating jet, even allowing for varying viewing angle, but may be caused instead, or in addition, by the transition of a spectral break (most likely the cooling break) through the observing frequency band [Sari, Piran & Narayan 1998] or by the propagation of the external shock in a non homogeneous medium [Panaitescu, Mészáros & Rees 1998, Mészáros, Rees & Wijers 1998, Chevalier & Li 1999, Jaunsen, Hjorth *et al.* 2001] (although in these cases the steepening would be frequency dependent, as opposed to

what is usually observed; see however [Kumar & Panaitescu 2000] for detectability of a jet in a stratified medium), or by the transition of the plasma kinematic conditions from relativistic to Newtonian in a dense medium [Dai & Lu 1999, Dai & Lu 2001, Masetti, Palazzi *et al.* 2001, Huang, Dai & Lu 2000]. In some cases the interpretation is not unique [Halpern, Kemp, Piran & Bershady 1999, Li & Chevalier 2001], although simultaneous multi wavelength observations may resolve the ambiguity [Chevalier & Li 2000, Harrison, Yost *et al.* 2001, Panaitescu & Kumar 2001a, Piro, Garmire *et al.* 2001]. In summary, the data are consistent with all optical afterglows virtually undergoing a change of temporal slope, whatever the cause of such a change might be among the different possibilities theoretically devised up to now. Sideways expansion and edge viewing effects due to the presence of a jet are often quite consistent explanations for individual cases, but it is not possible to firmly conclude that a temporal steepening in the afterglow is in all cases associated with a decelerating and sideways expanding jet.

2.6 The possible role of anisotropy

A possible explanation of some observational features of GRBs (spread in the isotropic energy emitted in γ-rays) and afterglows (breaks in the lightcurves) that is now becoming popular as alternative to the uniform jet with varying opening angle model, is the existence of an axially symmetric anisotropic outflow, with smoothly varying baryon loading and initial Lorentz factor but a standard total energy reservoir, viewed from different angles.

Many GRBs are now found to be associated to with star forming regions, close to remnants of massive stellar progenitors or supernovae, and these observations give support to the idea that GRBs could origin from a special and rare kind of collapse of massive stars. The suggested model assumes a catastrophic collapse of the core of a massive rotating star to a stellar black hole of a few solar masses producing a collimated outflow, or a jet along the rotation axis of the massive star, going through the stellar envelope. Numerical simulations show that the emitted energy is preferentially channelled along the rotation axis, which is also the lowest baryon contaminated direction because angular momentum takes matter away from the axis and on axis matter (with low angular momentum) falls into the black hole [MacFadyen & Woosley 1999, MacFayden, Woosley & Heger 2001, Aloy *et al* 2000]. A broad spread of Lorentz factors of the flow, with the maximum attained along the rota-

tion axis, i.e. the direction with the lowest degree of baryon pollution, is then expected. The measured flux will be correspondingly higher for an observer with a viewing direction close to the axis, and this would give rise to the spread in the observed GRB luminosities. In any case, from the theoretical point of view a simple general law relating the directional degree of pollution of an anisotropic outflow with energy radiated via internal shocks in the same direction is still missing. Thus, the idea of explaining some puzzling spreads in observed quantities with a standard type of event viewed from different orientations is very appealing but still needs for the angular distributions of baryon loading, initial Lorentz factor and burst luminosity of the anisotropic outflow to be theoretically investigated and constrained by observations.

Also the uniform jet interpretation explains the apparent dispersion in the isotropic energy as caused by a distribution of jet opening angles at constant energy reservoir. [Frail *et al.* 2001] and [Panaitescu & Kumar 2001b] have shown that the conical opening angles derived from the presence of breaks in afterglow light curves make the gamma–ray energy release of the corresponding GRBs, corrected for geometry, narrowly clustered around 5×10^{50} erg, and suggest a standard total luminosity of GRBs very close to the standard energy release of an ordinary Supernova.

On the other hand, [Rossi *et al.* 2002] have shown that an axially symmetric anisotropic outflow with bulk Lorentz factor varying $\propto \vartheta^{-\alpha}$ with $\alpha > 0$ and luminosity varying $\propto \vartheta^{-2}$ viewed by different directions can mimic the same afterglow behaviour of uniform jets with a distribution in opening angles.

Recently [Ramirez-Ruiz & Lloyd-Ronning 2002] have shown that the anisotropic scenario may also help explaining tentative correlations of the isotropic luminosity with the degree of variability of "spikiness" of GRBs [Fenimore & Ramirez–Ruiz 2002], the differential time lags for the arrival of burst pulses at different energies [Norris, Marani & Bonnell 2000, Norris 2002], and the rest frame GRB peak energy [Lloyd–Ronning & Ramirez–Ruiz 2002].

A detailed calculation of the hydrodynamical evolution and afterglows from an anisotropic fireball with a smooth angular distribution in baryon loading, expansion Lorentz factor etc. viewed from different directions has not been performed yet and would be very important. As in the spherical case, introduction of realistic treatment of hydrodynamics and radiation is expected to smooth away simple broken power law behaviours of afterglow light curves and spectra. This makes somewhat unreliable fireball intrinsic parameters derived by fitting the observed afterglow data with broken power laws, though the use of power law fits is often adequate to the sparseness and

inhomogeneous quality of currently available data. Larger inconsistencies in these "simple" fits may occur in the future, when better quality data will be at disposal.

We have focussed our investigation on the lateral view of smooth anisotropic fireballs, aiming at the understanding of geometrical effects on decay slopes, peak times and breaks with realistic (though approximated) hydrodynamical evolution and radiation model. The fireball model which we have developed is axially symmetric (see chapter 4). It is thought of as the result of a direction–dependent energy ejection that leads to the creation of a non spherical shock front surrounding the centre of the explosion which then expands radially with different Lorentz factors in different directions, being faster where the energy output was higher. The pure radial expansion is likely satisfied up to very late times in the evolution (see section 4.4). The delays in the arrival times of simultaneously emitted photons lead to a further distortion of the fireball shape as seen by a distant observer, especially when the line of sight is not aligned with the direction of greatest energy output. Moreover, the faster traveling regions of the blast wave will accelerate electrons to a higher average Lorentz factor and emit harder synchrotron radiation which is highly beamed. At any given time, the observer will see only that part of the shock front whose emission beam is wide enough to include the line of sight. Since the fireball expansion slows down as time passes, if the line of sight were not aligned with the fireball axis it might happen that the fastest part of the blast wave, initially not visible because of the emission beam being too narrow, becomes visible after a while when the emission beam becomes wider as the expansion velocity decreases. This effect can produce an apparent re-burst at a frequency higher than the typical emission frequency of the shock front along the line of sight and change the temporal decay slopes of afterglow light curves and the timescales for detection and visibility of the afterglow in a given energy band.

All these effects should be calculated and quantified as deviations from the "standard" models in order to help the interpretation of better quality observations coming in the near future thanks to GRB and afterglow study devoted spatial missions like for instance SWIFT.

Chapter 3

Spherical Fireballs

3.1 Introduction

A simple model for GRB afterglows, still able to explain the general behaviour of detected afterglows, is the spherical fireball model. This model is based on an isotropic instantaneous explosion in a extraordinarily but not completely baryon free environment (details are coming later). It was originally formulated as a tentative model for the GRB prompt emission and discarded after a while as it cannot explain the main burst variability timescales.

Refinements of the fireball model for GRBs require wind–like and intrinsically variable energy ejection by a central engine instead of a single "explosion" to properly explain the main burst variability. An extreme case could be random expulsion of randomly sized and baryon polluted shells of energy. In this case multiple collisions among shells of plasma traveling at different relativistic speed could be at the origin of the prompt GRB radiation. The shell collisions lead anyway to a final unique "average" shell as if there had been a single explosion, so that the simple impulsive model can still be used for modeling the system after the GRB emission.

Afterglows are a natural prediction of any fireball model (impulsive or wind driven).

In a fireball model afterglows are thought to arise from the radiation emitted by the matter that surrounds the progenitor as it is shocked by the expanding blast wave at the fireball outer edge. Interaction with the surrounding matter via a shock wave cannot be avoided (see the SNR case as an example) and is likely to be independent of the impulsive or wind–like nature of the energy deposition mechanism/explosion. Thus afterglow radiation can be modeled as synchrotron radiation from relativistic electrons

accelerated at the shock with the external matter.

Because of this, impulsive and wind–like spherical fireballs predict the same afterglow properties though only the second type reasonably predicts a main burst too via the standard external shock scenario.

Since I am interested in afterglows light curves and spectra only I will use as basic model the impulsive fireball model and simply neglect possible emission from the ejecta, that in the wind–like model are the site for internal shocks and GRB emission but finally settle down in an cold single shell as in the impulsive case. I will assume that the outer shock wave that sweeps the external matter during the fireball expansion is born at the explosion, immediately starts shocking the surrounding medium and accumulates an outer thin shell of shocked matter all around the expanding ejecta cloud. I am going to calculate emission from this thin shell, i.e. from the shocked external matter only. I will neglect also radiation possibly emitted by the ejecta as they are shocked by the reverse shock associated to the outer expanding one that sweeps external matter, usually named the forward shock. Because of the finite thickness of the ejecta shell, radiation eventually emitted by ejecta at the reverse shock passage can contribute to the afterglow only for a short time interval from the GRB detection, and we are more interested in the long lasting component of afterglow emission, that can be better observed and studied.

The light curves I will obtain must be considered as a component to be added to (and observationally not distinguishable from) the GRB emission during the main burst and the reverse shock emission. They are expected to model the observable radiation only after the GRB end and/or the end of early and very short afterglow component possibly due to the reverse shock. So I will trust my calculation only after the GRB, whose time of occurrence and duration must be estimated as if internal shocks have taken place.

Now I am going to introduce the impulsive fireball model in details.

I illustrate the fireball hydrodynamics up to non relativistic expansion as it can be qualitatively predicted via physical principles.

In the quantitative hydrodynamical treatment I use an approximated analytical approach to join smoothly analytic solutions corresponding to different evolutionary stages. So I will able to describe the whole hydrodynamical evolution of the shock front radius and shocked matter distribution behind the shock from the very initial to the late stages. Then I will be able to calculate continuous light curves through all the different evolutionary stages of the fireball up to very late times from the explosion

and/or starting by very low values of the baryon loading parameter η (i.e. very high baryon pollution) as compared to the standard ones (see section 3.2 for the definition of η). I can follow smoothly, for instance, the transition to non relativistic expansion and model light curves from a fireball that is not extremely relativistic from the very beginning of its life.

I will describe how observed spectra and light curves can be calculated in a detailed way, i.e. all relativistic Doppler shifts of emitted radiation and light travel delays included, once the complete fireball hydrodynamics is known and a particular radiation mechanism is assumed.

It will be necessary to discuss how the time measured by a far observer is related to the coordinate time of the lab frame (the frame in quiescence with respect to the fireball centre of mass) and the comoving time of fireball volume elements and define the Equal-T surfaces.

I will illustrate detailed calculation of light curves due to synchrotron emission by relativistic electrons in the swept up plasma accelerated at the forward shock. Assumptions and approximations in the radiative part of the model will be discussed. I will calculate light curves and spectra also taking in account the cooling of the emitting electrons due to synchrotron radiation itself and adiabatic expansion of the fluid under the hypothesis that the only site for particle acceleration (and eventually for magnetic field amplification) is just behind the shock front and that from the hydrodynamical point of view emitting electrons are frozen in within the volume element they were injected in at the shock passage. This calculation will require an approximated estimation of the comoving time elapsed from the moment each single volume element has been shocked.

The results will be illustrated discussed and compared to rougher estimations at the end.

3.2 Impulsive Fireballs and Afterglows

An impulsive fireball is what originates from the sudden release of a large amount of energy within a small region of space polluted with relatively few cold baryons (that will represent the *ejecta*) and surrounded by a tenuous and cold external medium. For sake of simplicity we will now assume the external medium to be homogeneous and delay to future developments of the model the detailed study of implications of a non homogeneous environment. The reader can refer to [Wijers, Rees, & Mészáros 1997] for the first discussion of the problem.

The initial conditions of an impulsive fireball are

1. the total initial energy released

$$E_T = 10^{52} E_{52} \text{ erg} \tag{3.1}$$

2. the radius of the region where the energy is released

$$r_i = 10^7 r_7 \text{ cm} \tag{3.2}$$

3. the total mass of baryons entrained in this region

$$M_T = 10^{29} M_{29} \text{ g} \tag{3.3}$$

4. and the density of the external medium

$$n_i = 1 \; n_0 \text{ protons/cm}^3 \tag{3.4}$$

(and the density profile of the external medium if it is not uniform).

A useful parameter to be defined directly from the initial conditions is

5. the *baryon loading* parameter

$$\eta = \frac{E_T}{M_T c^2} \sim 1.11 \times 10^2 \frac{E_{52}}{M_{29}} \tag{3.5}$$

This parameter measures the degree of initial baryon pollution of the released energy. High values of η ($\gg 100$) correspond to low baryon contamination and vice versa.

We will be interested in spherical fireballs with baryon loading parameter η in the range $3 \lesssim \eta \lesssim 300$ and total energy E_T varying accordingly in the range 10^{50} erg $\lesssim E_T \lesssim 10^{53}$ erg for a fixed total ejecta mass $M_T = 3.6 \times 10^{28}$ g. These are the values of the fireball parameters corresponding to all the spherical models required to build an anisotropic model as described in chapter 4. We will also use a fixed initial radius $r_i = 10^7$ cm and a homogeneous ambient medium with typical interstellar matter density $n_i \sim 1$ protons/cm^3.

In what follows I will try to explain how crucial is the baryon loading in determining the fireball hydrodynamics and summarize the expected fireball evolution for the initial conditions in the range above.

3.2.1 Initial evolution and Baryon Loading role

First of all, if the initial energy density is high enough and the initial baryon contamination is low enough (i.e. high η values, $\eta \gg 1$) a radiation dominated optically thick plasma of photons, e^+e^- pairs and protons quickly develops and starts expanding isotropically. This can be easily proved to happen even if all the energy E_T were initially electromagnetic, no pairs were present at the beginning and the baryons were perfectly cold. Remember that the average optical depth for e^+e^- pair creation in a photon plasma of total energy E_T confined within a sphere of radius r_i is

$$\tau_{\gamma\gamma} = n_{\gamma\gamma}\sigma_T r_i \sim f_p \frac{E_T}{2m_e c^2}\frac{1}{\frac{4}{3}\pi r_i^3}\sigma_T r_i \sim 9.6 \times 10^{18} f_p \frac{E_{52}}{r_7}$$

where $\sigma_T = \frac{8\pi}{3}\frac{q_e^4}{m_e^2 c^4}$ is the Thomson cross section, m_e and q_e are the electron mass and charge and f_p is the fraction of photon pairs of energy E_1 and E_2 such that $\sqrt{E_1 E_2} > m_e c^2$. The value of $\tau_{\gamma\gamma}$ corresponding to typical initial energy and initial size we have chosen is expected to be really large for any reasonable initial photon energy distribution, so, even if no pairs were initially present, they would rapidly form and then these pairs would Compton scatter lower energy photons, resulting in a huge optical depth for all photons on a very short timescale. The very hot and highly opaque photon–lepton plasma cloud that forms, with its low baryonic load included, is what was originally named the *fireball*. The high radiation pressure causes the fireball to explode, i.e. to expand faster and faster, initially unimpeded by the tenuous external medium swept up and accumulated outside (*free expansion*), no matter if the external medium is not homogeneous.

The optically thick plasma of the ejecta forms a geometrically thin shell that accelerates up to relativistic velocities and acts as a piston on the surrounding medium. During the acceleration stage the Lorentz factor of the ejecta shell grows linearly with the shell radius $\gamma = R/r_i$ [Mészáros, Laguna & Rees 1993]. The acceleration stops when an expansion Lorentz factor equal to η is reached (all initial energy has been converted into bulk kinetic energy of the baryons and no radiation and pairs are left), or equivalently when the ejecta shell has expanded to a radius $r_c = r_i\eta$. From that point the expansion of the ejecta shell goes on at constant (relativistic) speed and the coasting stage begins.

No radiation can be observed from the expanding ejecta shell (or from the region it surrounds) until it becomes optically thin. The GRB radiation must be produced after optical thinning of the ejecta. If the baryon loading parameter η is lower than $\eta_{max} \sim 1.52 \times 10^5 E_{52}^{1/3} r_7^{-2/3}$, the fireball expansion velocity saturates to a constant value before optical thinning (see [Mészáros, Laguna & Rees 1993] for a more detailed discussion) i.e. no residual thermal radiation is emitted at thinning (consistently with the observation that GRB seem to show no thermal precursors nor thermal components in their spectra) and opacity just before thinning is not dominated by electron–positron pairs, whose population have already drop out of equilibrium and have almost completely annihilated, but by electrons associated to the polluting baryons.

This is why fireballs producing GRBs are thought to have baryon loading parameter spanning at most between 1 and η_{max}, with a typical value of a few hundreds suggested by the short variability timescale of the GRB observed light curves.

The ejecta shell remains optically thick out to radii as large as r_{th} such that the optical depth for Thomson scattering by the electrons associated to baryons τ_s is $\sim$ 1. So, at thinning $\tau_s = n_p \sigma_T \Delta_{ej,com} \sim \frac{M_T}{4\pi r_{th}^2 \Delta_{ej,com}\, m_p} \sigma_T \Delta_{ej,com} \sim 1$, where n_p is the comoving density of baryons and $\Delta_{ej,com}$ is the thickness of the shell of ejecta in the comoving frame. It simply comes

$$r_{th} = \left(\frac{\sigma_T}{4\pi}\frac{M_T}{m_p}\right)^{1/2} = \left(\frac{\sigma_T}{4\pi}\frac{E_T}{\eta\, m_p c^2}\right)^{1/2} \sim 5.92 \times 10^{13} \sqrt{\frac{E_{52}}{\eta_2}}\ \mathrm{cm} \qquad (3.6)$$

The time at which the ejecta become optically thin can be considered as an estimate of the time after which the non thermal GRB radiation can be produced for instance via internal shocks among different sub-shells of the ejecta expelled by the central engine if the fireball were not impulsive. A better estimate of GRB start time could be the time at which two spherical sub-shells of ejecta entering the coasting stage with

Lorentz factors close to η but differing by a factor two, catch each other. The estimate of a GRB end time is more delicate, and we will simply use an average value of some tens of seconds after the beginning (in the observer view) according to observations.

I recall anyway that, no matter how many colliding sub-shells of ejecta are expelled, no matter how long they take to catch each other and merge into a single shell, it is quite reasonable that the explosive event drives from the very beginning a blast wave in the medium surrounding the central engine, and that by the time the ejecta starts coasting this blast wave has become an ultra relativistic shock wave slightly faster than the ejecta itself that goes on sweeping the external medium.

In the very simple model consisting of a single homogeneous ejecta shell acting as a piston, I assume that from the very beginning of the expansion a second thin shell of external matter is continuously accumulated at the outer edge of the ejecta shell. This external matter is thought to have been compressed and heated by a spherical forward traveling shock wave (of radius R_s) born at the time of the explosion and moving as fast as needed to be compatible with the Rankine Hugoniot conditions (see section A). By the time of optical thinning of the ejecta the external blast wave has long become an ultra relativistic shock (note that from the r_{th} definition (3.6), thinning occurs during the coasting stage, so that the maximum possible expansion velocity has already been attained). The outer shell of shocked external matter is both geometrically and optically thin from the beginning, and it can emit radiation from the beginning. Moreover, the most reasonable nature of emitted radiation is synchrotron radiation by relativistic electrons accelerated at the shock.

After a few assumptions on the physics of shocks and shocked plasma, I will calculate synchrotron radiation emitted by the shocked external matter only, but use the resulting light curves as afterglow predicted light curves only after the time of thinning of the ejecta.

3.2.2 Deceleration

Until optical thinning, and long after, the fireball ejecta show up in a spherical homogeneous shell of external radius R, whose lab frame thickness Δ_{ej} is initially constant and equal to the initial radius r_i then starts growing ($\Delta_{ej} \sim R/\gamma^2$) when $R \sim r_b = r_i\eta^2$ (i.e. after the coasting stage has started but typically before optical thinning if $E_T > 2.8 \times 10^{46}\ r_7^2\ \eta_2^5$ erg). The broadening radius r_b is estimated as the radius

such that a velocity difference Δv between the front and the back of the ejecta shell* due to radial velocity spread would give rise to a comoving shell thickness $\Delta r \sim r\frac{\Delta v}{c}$ substantially larger than r_i, which would be the comoving shell thickness without any radial velocity spread.

The swept up matter shell, on the other hand, will have a radius R_s and a lab frame thickness Δ such that $R_s = R + \Delta$ and the comoving particle density is uniform and equal to the post–shock particle density.

The total mass of the swept up matter ($\sim \frac{4}{3}\pi R_s^3 n_i$) is negligible as compared to the total mass of the ejecta M_T during all the early evolutionary stages (free expansion and coasting) and thus the shocked matter shell travels at the same speed of the ejecta shell. During the free expansion both shells move forward with a Lorentz factor $\gamma = R/r_i$ (growing linearly with the ejecta shell radius) and during the coasting stage the shells move with a constant Lorentz factor $\gamma_c = \eta$. Only when the total mass of swept up matter has grown enough to influence the fireball hydrodynamics causing a deceleration the double shelled internal structure of the fireball starts to change. This change should begin/start when an amount of external matter as large as $\frac{M_T}{\gamma_c}$ has been swept up, i.e. at about an outer radius

$$R_d \sim \left(\frac{3E_T}{4\pi n_i m_p c^2 \eta \gamma_c}\right)^{1/3}$$

for an homogeneous external medium. At about this radius the coasting stage ends and the fireball enters a *deceleration stage* composed by an initial *transition stage* and a later self–similar relativistic expansion stage, known as *Blandford & McKee stage*, during which the swept up external matter dominates on the original fireball ejecta and the fireball interior is no more shell shaped as during the early stages of evolution.

The transition stage, because of its transient and unsteady nature, can only be properly modeled via numerical simulations. Numerical simulations presented for instance in [Panaitescu, Wen, Laguna & Mészáros 1997] show that during the transition to the Blandford & McKee stage the ejecta shell is slowed, widened and smoothed back towards the inner regions of fireball by multiple reverse shocks and rarefaction waves going back and forth and, though still denser than matter on the other side of the contact discontinuity, ejecta soon becomes substantially colder, too cold to radiate. Moreover, during all this process the contact discontinuity is continuously slowed down and migrates further and further inwards (relatively to the forward shock front) while

*If the front and the back of the ejecta shell expand respectively with Lorentz factors $\gamma_f \gtrsim \gamma_b \sim \eta$ we can estimate $\Delta v \sim \frac{c}{2}\left(\frac{1}{\gamma_b^2} - \frac{1}{\gamma_f^2}\right) \sim c\,\eta^{-2}$.

the hot external shocked matter that fill the most part of the fireball volume finally distributes according to the Blandford & McKee solution. The transition ends more or less when the post-shock matter Lorentz factor has decreased to about two thirds of its initial value and the shock radius has nearly doubled.

Before going on I must recall that together with the forward shock a second reverse blast wave should be born at the explosion. This second blast wave is expected to start traveling back through the ejecta from the beginning, causing the ejecta shell to be composed by an outer shell of shocked ejecta in pressure equilibrium with the shell of shocked external matter at the contact discontinuity and an inner shell of unshocked ejecta. According to the treatment of [Sari & Piran 1995], with the initial conditions we have chosen the internal energy and particle density of the ejecta shell are always so high as compared to the external medium that the reverse shock is not expected to become relativistic during all the coasting stage.

At the beginning of the deceleration stage the reverse shock has just shocked a tiny fraction of the total ejecta mass, and up to that moment its presence can be completely ignored. The reverse shock is expected to actually shock the whole ejecta during the early deceleration stage, ending before the Blandford & McKee stage sets in. As noted by [Mészáros & Rees 1999, Sari & Piran 1999b] the reverse shock passage through the ejecta should produce a short flash of non thermal radiation to add to the standard afterglow emission due to the forward shock (the early optical flash in the afterglow of GRB012300 has been interpreted in this way in [Mészáros & Rees 1999, Sari & Piran 1999b]) but we are not going to calculate any kind of radiation coming from the ejecta. After the reverse shock has completely burnt the ejecta once, they substantially cool by adiabatic expansion; subsequent shocks and rarefaction waves traveling back and forth as predicted by [Sari & Piran 1995, Panaitescu, Wen, Laguna & Mészáros 1997] are not expected to heat them enough to cause further observable radiation.

After the transition stage we can completely forget about the ejecta. They would at most appear as a dense and cold feature in the fireball internal structure near to the centre, the contact discontinuity now being very close to the centre, everything outside evolving as if they simply were not present.

We expect the fireball enters an evolutionary stage that is well approximated by the Blandford & McKee solution with a total mass equal to the total swept up external mass only and a total energy equal to $\sim E_T$.

Note that all the previous hydrodynamical evolution has been almost adiabatic,

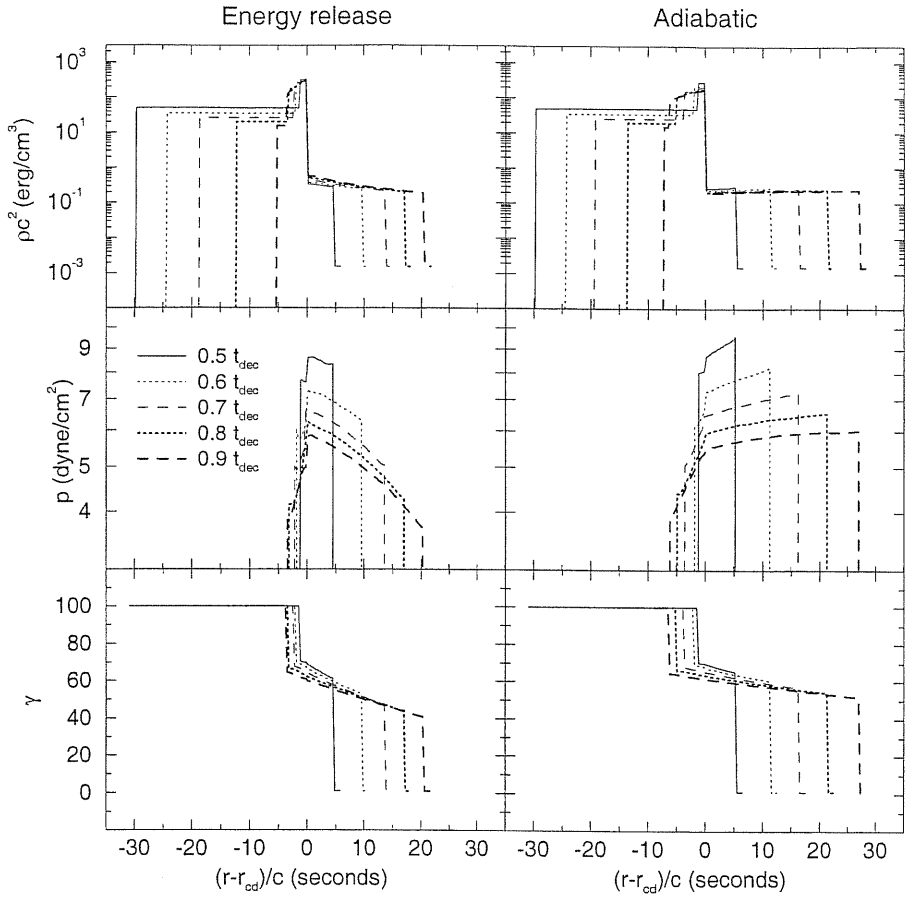

Figure 3.1: Figure extracted from [Panaitescu, Wen, Laguna & Mészáros 1997] representing density, pressure and flow Lorentz factor profiles for $\Gamma_s = 100$, $E_T = 10^{51}$ ergs, $r_i = 10^8$ cm and $n_i = 1$ cm^{-3}, at times indicated in the legend. The left column shows these profiles for non–adiabatic evolution, while the right column is for the adiabatic interaction. The time t_{dec} is the time at which the forward shock starts deceleration. The structure is much thinner than its curvature radius of the spherical fireball and the position inside it is indicated relative to the contact discontinuity, whose radius is named r_cd. Negative values correspond to the inner shell of ejecta, positive values to the outer shell of shocked external matter. Note that in the adiabatic interaction, the outer shell is less dense and more extended, and that the gradients in density, pressure and Lorentz factor are smaller. After $t = 0.9\ t_{dec}$ the reverse shock crosses the inner shell, in both cases.

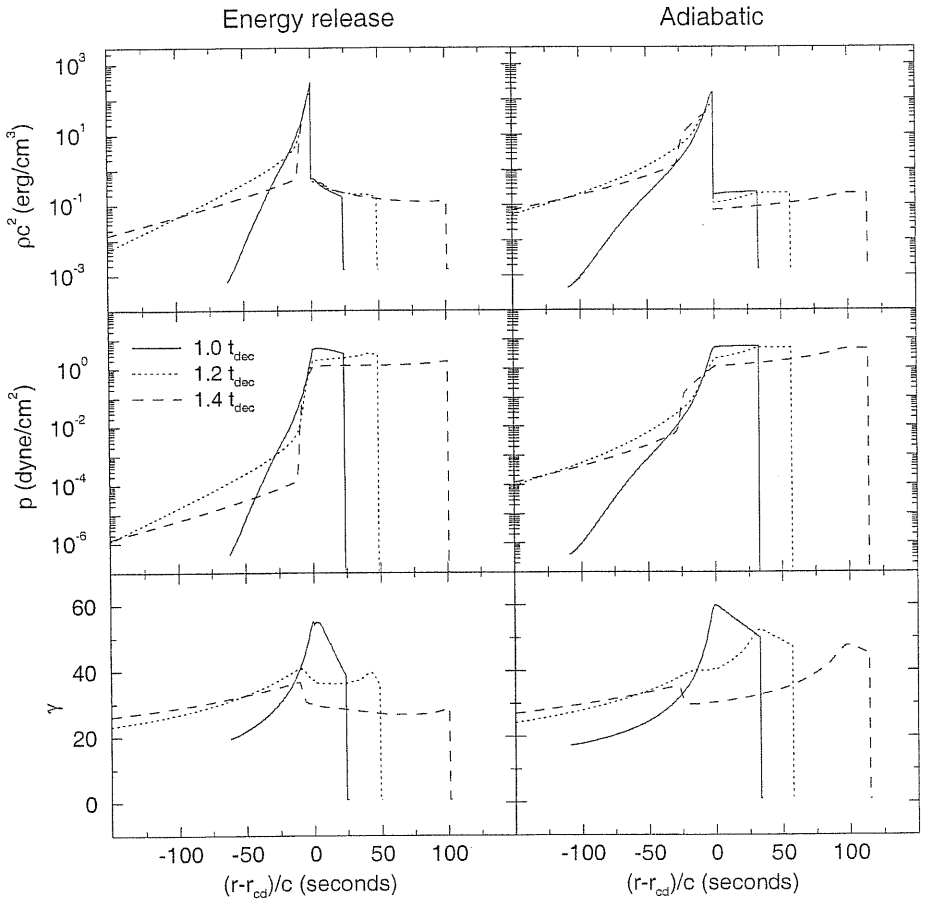

Figure 3.2: The same profiles as those shown in fig.3.1 in the radiative and adiabatic cases, after the reverse shock has crossed the ejecta shell. A second reverse shock can be seen easier in the Lorentz factor γ graph.

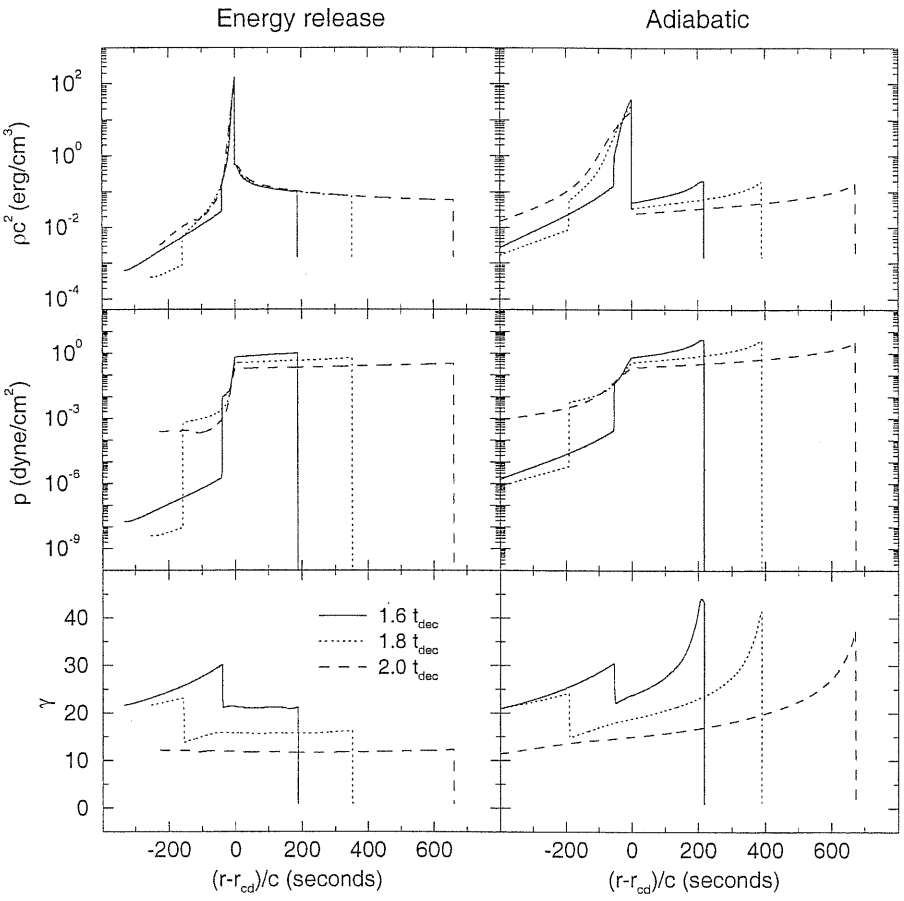

Figure 3.3: Same as in figures 3.1 and 3.2, until $t = 2.0\ t_{dec}$, when most of the initial kinetic energy has been radiated (in the non-adiabatic case) and the simulation is ended. Shortly before $t = 2.0\ t_{dec}$, the second reverse shock crosses the rarefaction fan behind the contact discontinuity.

the radiated energy was always negligible as compared to the reservoir, included the energy loss in the internal shocks, if we had considered them, since they are not efficient radiators. During the initial evolutionary stages, all the initial energy had been gradually converted into kinetic energy of the ejecta first and into internal and kinetic energy of the shocked external matter later. It can be shown that by the beginning of the deceleration the total amount of energy in the shocked matter is equal to E_T, though the mass is still η times lower than M_T.

Since I always use analytic approximations to hydrodynamical evolution laws and matter distributions, and I do not have an adequate one for the transient early deceleration stage, I simply choose to model the transition joining smoothly the known solutions in the easiest way I find. I know that during the transition stage the ejecta must become "negligible" because the final Blandford & McKee solution does not depend on them, it regards only the swept up external matter. Then, as I have decided not to calculate the possible ejecta contribution to emitted radiation even before the transition to Blandford & McKee, it seems reasonable to model the transition as if the ejecta were not present, i.e. joining the shocked matter distributions in the coasting and in the Blandford & McKee stages in a smooth way, with the total mass and energy of the shocked matter growing from the values they had at the end of the coasting stage to the values they must have at the beginning of the Blandford & McKee stage.

The Blandford & McKee solution, described in appendix B, is adiabatic as well, and in fact there are negligible radiation losses via the afterglow also during this stage.

3.2.3 Non relativistic expansion

The fireball deceleration can be driven by the Blandford & McKee solution until the expansion velocity becomes marginally relativistic ($\gamma \lesssim \sqrt{2}$). After that, a second transition should lead to a Newtonian stage of expansion resembling the Supernova Remnants expansion, i.e. well approximated by the Sedov solution. During this transition we expect the post–shock plasma too becoming non relativistic, i.e. the adiabatic index $\hat{\gamma}$ passing from the value $\frac{4}{3}$ to the value $\frac{5}{3}$ and the jump conditions for internal energy and particle density at the shock changing accordingly. The Sedov solution is an adiabatic solution as the Blandford & McKee, and also this second transition should be modeled as conserving the energy.

The Sedov Taylor self–similar expansion stage is expected to set in more or less when an amount of external matter of total rest mass as large as the initial bulk

kinetic energy $M_T c^2 \gamma_c$ has been swept up. This corresponds to a shock radius

$$R_{sed} \sim \left(\frac{3E_T \gamma_c}{4\pi n_i m_p c^2 \eta} \right)^{1/3}$$

At about this radius we will start to use not exactly the Sedov solution, but a slightly modified law having the Sedov solution as asymptotic limit. In fact physical conditions of the post-shock plasma will be far from typical SNR post-shock plasma conditions during the Sedov stage yet.

In the following sections I will illustrate in more details the shock evolution and post-shock matter distributions laws used in the different hydrodynamical stages, transitions included, and introduce all the physical quantities required for the mathematical treatment of the problem.

But before starting I need to remind some concepts that will be useful in defining all these laws.

3.3 Jump conditions at a shock

In the case of a planar collisionless shock that propagates into a cold external medium we can easily relate the comoving physical properties of the post–shock fluid to the unshocked ones.

As in appendices A and C, we will mark pressure, particle/energy densities and adiabatic index in the the unshocked fluid with and index 1 and pressure, particle/energy densities and adiabatic index in the post–shock fluid with an index 2. The shock Lorentz factor and velocity will be Γ and U respectively, while post–shock fluid Lorentz factor and velocity relative to the unshocked fluid will be γ and u respectively. Adiabatic indices will be named $\hat{\gamma}$.

As shown in appendix A, if the shock is ultra relativistic, i.e. $\Gamma \gg 1$ we have

$$\gamma = \frac{\Gamma}{\sqrt{2}} \tag{3.7}$$

$$n_2 = 2\sqrt{2} n_1 \Gamma \tag{3.8}$$

$$e_2 = 2\Gamma^2 n_1 m_p c^2 \tag{3.9}$$

$$p_2 = \frac{2}{3}\Gamma^2 n_1 m_p c^2 \tag{3.10}$$

$$\hat{\gamma}_1 = \frac{4}{3} \tag{3.11}$$

Remind that here e_2 represents the *internal* energy density of the post–shock fluid, but in the ultra relativistic case the internal energy is the dominant component of the post–shock fluid total energy and can be assumed equal to it.

From appendix C we can derive the corresponding relations for a non relativistic shock, i.e. $\frac{U}{c} \ll 1$

$$u = \frac{2}{\hat{\gamma}_2 + 1} U \tag{3.12}$$

$$n_2 = n_1 \frac{\hat{\gamma}_2 + 1}{\hat{\gamma}_2 - 1} \tag{3.13}$$

$$e_2 = (\hat{\gamma}_2 - 1) p_2 \tag{3.14}$$

$$p_2 = \frac{2}{\hat{\gamma}_2 + 1} n_1 m_p U^2 \tag{3.15}$$

$$\hat{\gamma}_2 = \frac{5}{3} \tag{3.16}$$

These two sets of relations must be limits in the ultra relativistic and non relativistic case of "more general" laws. Since in our calculation we are going to deal with shocks

decelerating from ultra relativistic velocities to non relativistic ones, we need to use generalized jump conditions having as ultra relativistic and non relativistic limits the expressions above.

These generalized jump conditions have been calculated by Blandford &McKee in [Blandford & McKee 1976] and are the following

$$\Gamma = \sqrt{\frac{(\gamma+1)\left(\hat{\gamma}_2(\gamma-1)+1\right)^2}{\hat{\gamma}_2(2-\hat{\gamma}_2)(\gamma-1)+2}} \tag{3.17}$$

$$n_2 = n_1 \frac{(\hat{\gamma}_2\gamma+1)}{(\hat{\gamma}_2-1)} \tag{3.18}$$

$$e_2 = n_1 \frac{(\hat{\gamma}_2\gamma+1)}{(\hat{\gamma}_2-1)} m_p c^2(\gamma-1) \tag{3.19}$$

$$p_2 = \frac{e_2}{(\hat{\gamma}_2-1)} \tag{3.20}$$

For $\Gamma \gg 1$ and $\hat{\gamma}_2 = \frac{4}{3}$ these equations tend to (3.7), (3.8), (3.9) and (3.10) while for $\frac{U}{c} \ll 1$ and $\hat{\gamma}_2 = \frac{5}{3}$ they reduce to (3.12), (3.13), (3.14) and (3.15).

3.4 Energy conservation

The adiabatic expansion of the spherical blast wave produced by a strong explosion in a cold homogeneous medium is expected to approach the Sedov self–similar solution in case of non relativistic shock expansion velocity or the Blandford & McKee self–similar solution in case of ultra relativistic shock expansion velocity. The two solutions are presented in appendices C and B. Since both solutions are adiabatic, in both cases the total energy of the explosion E_T, once converted into internal and bulk kinetic energy of the flow, must conserve. In both cases, the conserved energy E_T can be expressed as a function of the shock radius $R(t)$ and velocity $U(t)$ (or the shock Lorentz factor $\Gamma(t)$).

For the Sedov solution we have calculated (see equation (C.33))

$$E_T = 3K(\hat{\gamma})\frac{4}{3}\pi m_p n_i R^3(t)U(t)^2 \tag{3.21}$$

where n_i is the unshocked particle density and $\hat{\gamma}$ is the shocked fluid adiabatic index. For $\hat{\gamma} = \frac{5}{3}$ the constant $K(\hat{\gamma})$ is equal to ~ 0.245.

For the Blandford & McKee solution we have calculated (see equation (B.29))

$$E_T = \frac{8}{17}\pi n_i m_p c^2 R(t)^3 \Gamma(t)^2 \tag{3.22}$$

Since the only quantity we can measure is the post–shock fluid velocity $u(t)$ (or the post–shock fluid Lorentz factor $\gamma(t)$), we'd better rewrite (3.21) and (3.22) in terms of $u(t)$ and $\gamma(t)$ respectively using (3.12) and (3.7). We have

$$E_T = 3K(5/3)\frac{16}{9}\frac{4}{3}\pi m_p n_i R^3(t)u(t)^2 \tag{3.23}$$

$$E_T = \frac{16}{17}\pi n_i m_p c^2 R(t)^3 \gamma(t)^2 \tag{3.24}$$

Note that the right hand side in (3.24) is the total energy of the flow (rest mass of the shocked matter included), while in principle the conserved energy E_T has been converted into internal and kinetic energy only. In the ultra relativistic limit (3.24) represents a very good approximation, but in order to have a slightly more general conservation law we should write

$$E_T = \frac{16}{17}\pi n_i m_p c^2 R(t)^3 \gamma(t)^2 - \frac{4}{3}\pi n_i m_p c^2 R(t)^3 \sim \frac{16}{17}\pi n_i m_p c^2 R^3 \left(\gamma(t)^2 - 1\right) \tag{3.25}$$

Then, note that when $\frac{u(t)}{c} \ll 1$ we can write

$$u(t)^2 = c^2\left(1 - \frac{1}{\gamma(t)^2}\right) = \frac{c^2}{\gamma(t)^2}\left(\gamma(t)^2 - 1\right) \sim c^2\left(\gamma(t)^2 - 1\right)$$

so also the energy conservation for the Sedov expansion can be generalized as

$$E_T = 3K(5/3)\frac{16}{9}\frac{4}{3}\pi m_p n_i c^2 R^3(t)\left(\gamma(t)^2 - 1\right) \tag{3.26}$$

The two energy conservation laws (3.25) and (3.26) can be thought as the limiting cases for $\gamma(t) \gg 1$ and $\gamma(t) \sim 1$ respectively of the general law

$$E_T = \Omega(t)\pi m_p n_i c^2 R^3(t)\left(\gamma(t)^2 - 1\right) \tag{3.27}$$

if the factor $\Omega(t)$ tends to the constant $\Omega_{BM} = \frac{16}{17}$ when $\gamma(t) \gg 1$ and tends to the constant $\Omega_{SED} = \frac{64}{9}K(5/3)$ when $\gamma(t) \sim 1$.

An expanding spherical blast wave that decelerates adiabatically from very high Lorentz factors to Newtonian velocities should smoothly change its evolution laws from the Blandford & McKee self–similar solution to the Sedov self–similar solution. Since (3.24) should hold at the beginning of the evolution and (3.23) should hold at the end of the evolution, once the complete evolution is known, it is always possible to define a function $\Omega(t)$ such that equation (3.27) holds at any time. But we don't know the complete shock radius and post–shock Lorentz factor evolution laws for a spherical blast wave that decelerates from very high to very low velocities, so we cannot calculate the exact function $\Omega(t)$. We will prefer approximating the functions $R(t)$ and $\gamma(t)$ for our spherical expanding blast wave during the transition form the Blandford & McKee stage to the Sedov stage in such a way that (3.27) holds with a reasonable choice for the function $\Omega(t)$, like for example a linear change with time from the value Ω_{BM} to the value Ω_{SED}.

3.5 Detailed evolution of a Spherical Fireball

In this section I present the detailed analytic treatment of the impulsive fireball evolution previously illustrated in section 3.2.

For each stage the forward shock radius and Lorentz factor evolution laws are explicitly written down together with matter distributions behind the shock. The transition times and radii are calculated.

3.5.1 Free expansion stage

The free expansion stage is the initial accelerated expansion of the fireball. During this stage the fireball is double shell shaped. We start at $t = 0$ from a sphere of radius r_i containing a total mass M_T in cold baryons and a total energy E_T. At $t > 0$ we have an inner homogeneous shell of ejecta of total mass M_T, radius $R(t)$ and lab frame thickness $\Delta_{ej} = r_i$, and an outer shell of shocked matter, homogeneous as well, having a lab frame thickness $\Delta(t)$ such that the forward shock radius is

$$R_s(t) = R(t) + \Delta(t)$$

the total mass in the shell is

$$M_s(t) = \frac{4}{3}\pi n_i \left(R_s(t)^3 - r_i^3\right)$$

and the comoving particle density is equal to the expected post–shock density

$$n'_s(t) = n_i \frac{(\hat{\gamma}\gamma_s(t) + 1)}{(\hat{\gamma} - 1)}$$

where $\gamma_s(t)$ is the post–shock fluid Lorentz factor and $\hat{\gamma}$ is the post–shock fluid adiabatic index, set equal to $\frac{4}{3}$ during the whole stage.

The two shells expand at the same Lorentz factor $\gamma_s(t) = \frac{R(t)}{r_i}$ and the forward shock expands at a slightly higher Lorentz factor $\Gamma_s(t)$ given by

$$\Gamma_s(t) = \sqrt{\frac{(\gamma_s(t) + 1)\left(\hat{\gamma}(\gamma_s(t) - 1) + 1\right)^2}{\hat{\gamma}(2 - \hat{\gamma})(\gamma_s(t) - 1) + 2}}$$

This system of equations can be solved completely giving us the following solution

$$\gamma_s(t) = \sqrt{1 + \left(\frac{ct}{r_i}\right)^2} \tag{3.28}$$

$$R(t) = r_i \gamma_s(t) \tag{3.29}$$

$$R_s(t) = R(t) + \Delta(t) \tag{3.30}$$

with $\Delta(t)$ solution of the equation

$$n_i \frac{(\hat{\gamma}\gamma_s(t) + 1)}{(\hat{\gamma} - 1)} = \frac{\frac{4}{3}\pi n_i \left(R_s(t)^3 - r_i^3\right)}{\frac{4}{3}\pi R_s(t)^3 - \frac{4}{3}\pi \left(R_s(t) - \gamma_s(t)\Delta(t)\right)^3} \tag{3.31}$$

The right hand side term of this equation is simply the comoving particle density in the shell of shocked matter given as the ratio of the swept up mass and the comoving volume calculated as the difference between the volume of the sphere of radius $R_s(t)$ and the volume of the sphere of radius $R_s(t) - \gamma_s(t)\Delta(t)$, being $\gamma_s(t)\Delta(t)$ the comoving thickness of the shell. Equation (3.31) is a cubic equation in $\Delta(t)$ with a unique real solution that can be easily found using the general solution for cubic equations in [Abramowitz & Stegun 1970].

Note that when $R_s(t) \gg r_i$, i.e. when $t \gg r_i/c$, equation (3.31) reduces to

$$n_i \frac{(\hat{\gamma}\gamma_s(t) + 1)}{(\hat{\gamma} - 1)} = \frac{\frac{4}{3}\pi n_i R_s(t)^3}{\frac{4}{3}\pi R_s(t)^3 - \frac{4}{3}\pi \left(R_s(t) - \gamma_s(t)\Delta(t)\right)^3} \tag{3.32}$$

So, at $t \gg r_i/c$ we can approximate $\Delta(t)$ with the solution of equation (3.32), i.e. we expect

$$\Delta(t) \sim R(t) \frac{1 - \left(\frac{\hat{\gamma}(\gamma_s(t)-1)+2}{\hat{\gamma}\gamma_s(t)+1}\right)^{1/3}}{\gamma(t) - \left(1 - \left(\frac{\hat{\gamma}(\gamma_s(t)-1)+2}{\hat{\gamma}\gamma_s(t)+1}\right)^{1/3}\right)} \tag{3.33}$$

This approximation is expected to be valid at the end of the free expansion stage, unless the baryon loading parameter is too small ($\eta < 10$), that is the initial amount of baryons is too large. Since we want to use η values as low as 3, we will not use (3.33) in the general case. We will prefer solving exactly equation (3.31).

The free expansion ends when the expansion Lorentz factor reaches the value η, i.e. at the time

$$t_c = \frac{r_i}{c}\sqrt{\eta^2 - 1} \tag{3.34}$$

and we have $t_c \gg r_i/c$ if only if $\eta \gg 1$.

At the time t_c the ejecta shell has reached a radius $r_c = \eta\, r_i$ and the forward shock has reached a radius $R_c = r_c + \Delta_c$ with Δ_c solution of the equation (3.31) at the time t_c.

If $\eta \gg 1$ we can use approximation (3.33) and write

$$R_c = \frac{r_i \eta^2}{\eta - 1 + \left(\frac{\hat{\gamma}(\eta-1)+2}{\hat{\gamma}\eta+1}\right)^{1/3}} \tag{3.35}$$

As far as the shocked matter distributions are concerned, since we have just said that during the free expansion the shocked matter is confined within an homogeneous shell, we will define the comoving particle density, the internal energy density and the fluid Lorentz factor distributions as constant functions in the radial position behind the shock as follows:

$$n'(t,x) = \begin{cases} n_i \frac{(\hat{\gamma}\gamma_s(t)+1)}{(\hat{\gamma}-1)} & x_{min}(t) \leq x \leq 1 \\ 0 & 0 \leq x < x_{min}(t) \end{cases} \tag{3.36}$$

$$e'(t,x) = \begin{cases} n_i \frac{(\hat{\gamma}\gamma_s(t)+1)}{(\hat{\gamma}-1)} m_p c^2 (\gamma_s(t) - 1) & x_{min}(t) \leq x \leq 1 \\ 0 & 0 \leq x < x_{min}(t) \end{cases} \tag{3.37}$$

$$\gamma(t,x) = \begin{cases} \gamma_s(t) & x_{min}(t) \leq x \leq 1 \\ 1 & 0 \leq x < x_{min}(t) \end{cases} \tag{3.38}$$

with

$$x_{min}(t) = \frac{R(t)}{R_s(t)} = 1 - \frac{\Delta(t)}{R_s(t)} \tag{3.39}$$

Remember that during this stage the post–shock Lorentz factor is $\gamma_s(t) = \sqrt{1 + \left(\frac{ct}{r_i}\right)^2}$, the forward shock radius is $R_s(t) = r_i \gamma_s(t)$, the shocked shell thickness is $\Delta(t)$ satisfying (3.31), the time t varies between 0 and t_c and the radial coordinate relative to the forward shock, x, is defined as $x = \frac{r}{R_s}$ where r is the distance from the centre of explosion of a generic point inside the sphere of radius $R_s(t)$.

3.5.2 Coasting stage

The coasting stage is the second stage of expansion during which the fireball is composed by two homogeneous shells expanding at the same speed, but the expansion Lorentz factor is now constant and equal to $\gamma_c = \eta$.

In this case we have

$$\gamma_s(t) = \eta \tag{3.40}$$

$$\Gamma_s(t) = \sqrt{\frac{(\eta+1)\left(\hat{\gamma}(\eta-1)+1\right)^2}{\hat{\gamma}(2-\hat{\gamma})(\eta-1)+2}} = \Gamma_c \tag{3.41}$$

$$R(t) = r_c + c\left(1 - \frac{1}{\eta^2}\right)^{1/2}(t - t_c) \tag{3.42}$$

$$R_s(t) = R(t) + \Delta(t) \tag{3.43}$$

with $\Delta(t)$ solution of the equation (3.31).

In this case, being Γ_s constant too and equal to Γ_c, we should better use

$$R_s(t) = R_c + c\left(1 - \frac{1}{\Gamma_c^2}\right)^{1/2}(t - t_c) \tag{3.44}$$

and redefine $R(t)$ in such a way that $R(t) = R_s(t) - \Delta(t)$ with $\Delta(t)$ solution of (3.31).

The coasting stage will last until the total swept up mass is equal to M_T/γ_c, i.e. until the forward shock has expanded out to a radius R_d such that

$$\frac{4}{3}\pi n_i m_p \left(R_d^3 - r_i^3\right) = \frac{M_T}{\gamma_c}$$

Thus, the end of the coasting stage corresponds to a shock radius

$$R_d = \left(\frac{E_T}{\frac{4}{3}\pi n_i m_p c^2 \eta \gamma_c} + r_i^3\right)^{1/3} \tag{3.45}$$

or equivalently a time

$$t_d = t_c + \frac{(R_d - R_c)}{c\left(1 - \frac{1}{\Gamma_c^2}\right)^{1/2}} \tag{3.46}$$

During the coasting stage the inner shell of ejecta becomes optically thin. We have already calculated in section 3.2.1 that this happens when the ejecta shell reaches a radius r_{th} such that

$$r_{th} = \left(\frac{\sigma_T}{4\pi}\frac{E_T}{\eta\ m_p c^2}\right)^{1/2} \tag{3.47}$$

The corresponding time of thinning t_{th} will be about

$$t_{th} = t_c + \frac{(r_{th} - r_c)}{c\left(1 - \frac{1}{\gamma_c^2}\right)^{1/2}} \tag{3.48}$$

Another happening of the coasting stage is the broadening of the ejecta shell that start when it reaches the radius $r_b = r_i\eta^2$, or equivalently at the time

$$t_b = t_c + \frac{(r_b - r_c)}{c\left(1 - \frac{1}{\gamma_c^2}\right)^{1/2}} \tag{3.49}$$

Before this time we had $\Delta_{ej}(t) = r_i$. After this time we will have $\Delta_{ej}(t) = \frac{R(t)}{\gamma_s(t)^2}$.

The shocked matter comoving particle density, internal energy density and Lorentz factor distributions during the coasting stage are defined exactly as during the free expansion stage provided that now the post–shock fluid Lorentz factor is $\gamma_s(t) = \eta$ and the forward shock radius is $R_s(t) = R_c + c\left(1 - \frac{1}{\Gamma_c^2}\right)^{1/2}(t - t_c)$.

3.5.3 First transition stage

This is the stage lasting from the end of the coasting stage to the beginning of the Blandford & McKee stage.

We do not know exactly how the shock radius should evolve during this stage, we simply know from numerical simulations that the Blandford & McKee stage should start when the post–shock Lorentz factor γ_s has reduced more or less to $\gamma_0 = \frac{2}{3}\gamma_c = \frac{2}{3}\eta$.

Note that the knowledge of the initial post–shock Lorentz factor γ_0 allows to constrain also the initial radius R_0 of the shock front. Since the fireball expansion is assumed adiabatic from the beginning and the fireball total energy E_T during the Blandford & McKee stage can be simply expressed in terms of the shock radius and the post–shock Lorentz factor as explained in section 3.4, we can derive the value R_0 of the shock radius corresponding to the post–shock Lorentz factor γ_0 by solving the Blandford & McKee energy conservation equation

$$E_T = \Omega_{BM}\pi n_i m_p c^2 R_0^3\left(\gamma_0^2 - 1\right) \tag{3.50}$$

with $\Omega_{BM} = \frac{8}{3}\sigma_{BM}$ and $\sigma_{BM} = \frac{6}{17}$. We get

$$R_0 = \left(R_d^3 - r_i^3\right)^{1/3}\left(\frac{1}{\frac{8}{3}\sigma_{BM}\frac{3}{4}}\frac{\eta^2}{\gamma_0^2 - 1}\right)^{1/3} \sim R_d\left(\frac{1}{\frac{8}{3}\sigma_{BM}\frac{3}{4}}\frac{\eta^2}{\gamma_0^2 - 1}\right)^{1/3} \tag{3.51}$$

We do not know yet at what time t_0 the Blandford & McKee stage starts and we will not know until we fix a particular radius evolution law $R_s(t)$.

The easiest choice for $R_s(t)$ we can do is

$$R_s(t) = At^2 + Bt + C \tag{3.52}$$

with the coefficients $A < 0$, B, C and the time t_0 to be determined through the continuity conditions

$$R_s(t_d) = R_d \tag{3.53}$$

$$R_s(t_0) = R_0 \tag{3.54}$$

$$\Gamma_s(t_d) = \Gamma_d = \Gamma_c \tag{3.55}$$

$$\Gamma_s(t_0) = \Gamma_0 = \sqrt{\frac{(\gamma_0 + 1)\left(\hat{\gamma}(\gamma_0 - 1) + 1\right)^2}{\hat{\gamma}(2 - \hat{\gamma})(\gamma_0 - 1) + 2}} \tag{3.56}$$

the adiabatic index being $\hat{\gamma} = \frac{4}{3}$ and

$$\Gamma_s(t) = \frac{1}{\sqrt{1 - \left(\frac{2At+B}{c}\right)^2}} \tag{3.57}$$

The solution can be easily calculated and is the following

$$A = \frac{1}{4}\frac{V_0^2 - V_d^2}{R_0 - R_d} \tag{3.58}$$

$$B = -2At_d + V_d \tag{3.59}$$

$$C = R_d - t_d V_d + A t_d^2 \tag{3.60}$$

and

$$t_0 = t_d + 2\frac{R_0 - R_d}{V_0 + V_d} \tag{3.61}$$

where

$$V_d = c\sqrt{1 - \frac{1}{\Gamma_d^2}} \tag{3.62}$$

$$V_0 = c\sqrt{1 - \frac{1}{\Gamma_0^2}} \tag{3.63}$$

Once the shock front radius and Lorentz factor evolution laws $R_s(t)$ and $\Gamma_s(t)$ are known we can calculate the post–shock Lorentz factor evolution law $\gamma_s(t)$ too solving at each t the cubic equation

$$\Gamma_s(t)^2 = \frac{(\gamma_s(t) + 1)\left(\hat{\gamma}(\gamma_s(t) - 1) + 1\right)^2}{\hat{\gamma}(2 - \hat{\gamma})(\gamma_s(t) - 1) + 2} \tag{3.64}$$

with $\hat{\gamma} = \frac{4}{3}$.

Now we must specify the post–shock matter distributions $n'(t, x)$, $e'(t, x)$ and $\gamma(t, x)$. They should be functions that connect continuously the corresponding uniform shell distributions and Blandford & McKee distributions. A simple way to define them is a time weighted linear combination as the following

$$n'(t, x) = \frac{1}{t_0 - t_d}\left[n'_{shell}(t, x)(t_0 - t) + n'_{BM}(t, x)(t - t_d)\right] \tag{3.65}$$

$$e'(t,x) = \frac{1}{t_0 - t_d}\left[e'_{shell}(t,x)(t_0 - t) + e'_{BM}(t,x)(t - t_d)\right] \tag{3.66}$$

$$\gamma'(t,x) = \frac{1}{t_0 - t_d}\left[\gamma'_{shell}(t,x)(t_0 - t) + \gamma'_{BM}(t,x)(t - t_d)\right] \tag{3.67}$$

where $n'_{shell}(t,x)$, $e'_{shell}(t,x)$ and $\gamma'_{shell}(t,x)$ are defined as in (3.36), (3.37) and (3.38); $n'_{BM}(t,x)$, $e'_{BM}(t,x)$ and $\gamma'_{BM}(t,x)$ are defined as in (3.69), (3.70) and (3.71).

3.5.4 Blandford & McKee stage

This is the self–similar relativistic stage of adiabatic decelerated expansion that sets in at the time

$$t_0 = t_d + 2\frac{R_0 - R_d}{V_0 + V_d}$$

when the forward shock has reached a radius

$$R_0 = \left(R_d^3 - r_i^3\right)^{1/3}\left(\frac{1}{\frac{8}{3}\sigma_{BM}\frac{3}{4}}\frac{\eta^2}{\gamma_0^2 - 1}\right)^{1/3}$$

and the post–shock Lorentz factor has decreased to

$$\gamma_0 = \frac{2}{3}\gamma_c$$

Since we want to model the fireball expansion also at late times and marginally relativistic expansion speed, we prefer to use a slightly modified version of the classical Blandford & McKee solution for a spherical adiabatic flow presented in appendix B, which is strictly valid only for shock Lorentz factors $\gg 1$.

First of all remember that we have always used the generalized jump conditions at the shock introduced in section 3.3 because they are more appropriate for fireballs with rather law baryon loading parameter ($\eta \gtrsim 3$) i.e. fireballs with rather high initial baryon contamination. We should go on using these jump conditions also during the Blandford & McKee stage and after. This can be simply done by rewriting (B.20) in terms of γ_s instead of Γ_s via the relation $\gamma_s = \Gamma_s/\sqrt{2}$ that holds when $\Gamma_s \gg 1$, and then defining

$$\chi(t,x) = 1 + 16\gamma_s(t)^2(1 - x) \tag{3.68}$$

$$n'(t,x) = n_i\frac{(\hat{\gamma}\gamma_s(t) + 1)}{(\hat{\gamma} - 1)}\chi(t,x)^{-5/4} \tag{3.69}$$

$$e'(t,x) = n_i\frac{(\hat{\gamma}\gamma_s(t) + 1)}{(\hat{\gamma} - 1)}m_p c^2(\gamma_s(t) - 1)\chi(t,x)^{-17/12} \tag{3.70}$$

$$\gamma(t,x) = \gamma_s(t)\chi(t,x)^{-1/2} \tag{3.71}$$

These functions reduce to (B.20), (B.19), (B.21) and (B.17) in the limit $\gamma_s(t) \gg 1$ with $\hat{\gamma} = 4/3$, but can be used also for lower values of $\gamma_s(t)$. Note that e' is the internal energy density of the shock fluid, while the corresponding energy density e_2 used in appendixes A and B is the total energy density in the shocked fluid. In the ultra relativistic limit the post–shock rest mass energy density is negligible with respect to the internal energy density, and total and internal energy density are comparable. This is why the asymptotic expression of (3.70) for $\gamma_s(t) \gg 1$ can be compared to (B.21).

As far as the functions $\gamma_s(t)$ and $R_s(t)$ are concerned, since we want the generalized energy conservation law (3.25) to be valid from now on, we expect

$$\gamma_s(t) = \sqrt{1 + \frac{E_T}{\frac{8}{3}\sigma_{BM}\pi n_i m_p c^2 R_s(t)^3}} = \sqrt{1 + \frac{(\gamma_0^2 - 1)R_0^3}{R_s(t)^3}} \tag{3.72}$$

Note that the law (3.72) reduces to the familiar Blandford & McKee law $\gamma_s(t) = \gamma_0 \left(\frac{R_s(t)}{R_0}\right)^{-3/2}$ in the limit $\gamma_0 \gg 1$.

The function $R_s(t)$ should be found as the solution of the Cauchy problem

$$\begin{cases} \frac{dR_s}{dt} & = c\left(1 - \frac{1}{\Gamma_s(t)^2}\right)^{1/2} \\ R_s(t_0) & = R_0 \end{cases} \tag{3.73}$$

where

$$\Gamma_s(t) = \sqrt{\frac{(\gamma_s(t)+1)(\hat{\gamma}(\gamma_s(t)-1)+1)^2}{\hat{\gamma}(2-\hat{\gamma})(\gamma_s(t)-1)+2}}, \quad \hat{\gamma} = \tfrac{4}{3} \tag{3.74}$$

but we will prefer using a different function $R_s(t)$, whose numerical calculation is less time consuming, provided that it approximates reasonably well the exact solution of (3.73). Now we are going to introduce it.

We will explain in section 3.6.1 that the time interval T a far observer measures from the explosion is different from the coordinate time t of the lab frame we are using. Moreover, simultaneously emitted photons do not arrive simultaneously to the observer and in principle there is no unique relation between a time of emission (i.e. radius R_s) and a time of observation of photons emitted by the fireball as a whole.

Let us concentrate on photons emitted by the post–shock fluid on the line of sight (the volume element just behind the forward shock along the line of sight). If the shock radius at the time t after the explosion is $R_s(t)$, the observer will be reached by photons emitted at the time t by the selected volume element after T seconds from the time he has been reached by photons emitted at time $t = 0$, with

$$T = t - \frac{R_s(t)}{c} + \frac{r_i}{c} \tag{3.75}$$

The differential time interval between arrival of photons emitted at time t and arrival of photons emitted at time $t + dt$ will be

$$dT = dt - \frac{V_s(t)}{c}dt = dt - \left(1 - \frac{1}{\Gamma_s(t)^2}\right)^{1/2} dt \tag{3.76}$$

If $\Gamma_s(t) \gg 1$ we have

$$\left(1 - \frac{1}{\Gamma_s(t)^2}\right)^{1/2} \sim 1 - \frac{1}{2\Gamma_s(t)^2}$$

and

$$V_s(t) \sim c \quad \Rightarrow \quad dR \sim cdt$$

so that

$$dT \sim \frac{dR}{2c\Gamma_s(t)^2} \tag{3.77}$$

If the fireball expansion follows the Blandford & McKee law $\Gamma_s(t) = \Gamma_0 \left(\frac{R_s(t)}{R_0}\right)^{-3/2}$ for $t > t_0$, the observer sees photons emitted at a time t arriving $T - T_0$ seconds after photons emitted at t_0 with

$$T - T_0 = \int_{R_0}^{R_s(t)} dT \sim \int_{R_0}^{R_s(t)} \frac{dR}{2c\Gamma(R)^2} = \frac{R_s(t)}{8c\Gamma_s(t)^2} - \frac{R_0}{8c\Gamma_0^2} \tag{3.78}$$

provided that approximation (3.77) is valid up to time t. On the other hand, using (3.75) we can write

$$T_0 = t_0 - \frac{R_0}{c} + \frac{r_i}{c} \tag{3.79}$$

and

$$T = t - \frac{R_s(t)}{c} + \frac{r_i}{c} \tag{3.80}$$

Thus, for $t > t_0$ we have

$$t - t_0 + \frac{R_s(t) - R_0}{c} = \frac{R_s(t)}{8c\Gamma_s(t)^2} - \frac{R_0}{8c\Gamma_0^2} \tag{3.81}$$

The Blandford & McKee shock radius evolution law $R_s(t)$ should be well approximated by the solution of equation (3.81) until $\Gamma_s(t) = \Gamma_0 \left(\frac{R_s(t)}{R_0}\right)^{-3/2} \gg 1$.

We expect that with a relativistic shock evolution law $R_s(t)$ slightly different from the classical Blandford & McKee one, the arrival times of photons emitted by the post–shock fluid on the line of sight, T, would be slightly different from those predicted by (3.78), but well approximated by a law similar to (3.78) like the following:

$$T - T_0 = \frac{R_s(t)}{8\lambda c\Gamma_s(t)^2} - \frac{R_0}{8\lambda c\Gamma_0^2} \sim \frac{R_s(t)}{16\lambda c\gamma_s(t)^2} - \frac{R_0}{16\lambda c\gamma_0^2} \tag{3.82}$$

with the constant $\lambda \neq 1$ depending on the particular shock radius evolution law we are using. A constant speed shock radius evolution law would need, for instance, $\lambda = 0.25$.

We choose to approximate our $R_s(t)$ for $t > t_0$ (the solution of the Cauchy problem (3.73,3.74)) as the solution of the system of equations

$$\begin{cases} T - T_0 &= \frac{R_s(t)}{16\lambda_{BM} c \gamma_s(t)^2} - \frac{R_0}{16\lambda_{BM} c \gamma_0^2} \\ T &= t - \frac{R_s(t)}{c} + \frac{r_i}{c} \\ T_0 &= t_0 - \frac{R_0}{c} + \frac{r_i}{c} \\ \gamma_s(t) &= \sqrt{1 + (\gamma_0^2 - 1)\frac{R_0^3}{R_s(t)^3}} \end{cases} \tag{3.83}$$

with λ_{BM} such that $T_0 = \frac{R_0}{16\lambda_{BM} c \gamma_0^2}$, i.e.

$$\lambda_{BM} = \frac{ct_0 - R_0 + r_i}{R_0}\ 16\ c\ \gamma_0^2 \tag{3.84}$$

Thus, we will use $R_s(t)$ such that for each $t > t_0$

$$\begin{cases} R_s(t)\left(1 + \frac{1}{16\lambda_{BM}\gamma_s(t)^2}\right) = ct + r_i \\ \gamma_s(t) = \sqrt{1 + (\gamma_0^2 - 1)\frac{R_0^3}{R_s(t)^3}} \end{cases} \tag{3.85}$$

or equivalently

$$R_s(t)\left(1 + \frac{1}{16\lambda_{BM}\left[1 + (\gamma_0^2 - 1)\frac{R_0^3}{R_s(t)^3}\right]}\right) = ct + r_i \tag{3.86}$$

with λ_{BM} given by (3.84).

The values of λ_{BM} with η varying from 3 to 300 are always around 0.3 (from ~ 0.27 for $\eta \sim 3$ to ~ 0.34 for $\eta \sim 300$).

The relativistic expansion stage we have just defined can last until the post–shock velocity is high enough that the internal energy density dominates the total post–shock energy density. When the rest mass energy density becomes important as a component of the post–shock energy density, the adiabatic index in the shocked fluid cannot be assumed equal to 4/3 any longer. A transition to the Newtonian adiabatic index value 5/3 starts.

We will set the end of the Blandford & McKee stage when $\gamma_s(t) = \gamma_{crit} \sim 2$, i.e. when a radius

$$R_{crit} = R_0\left(\frac{\gamma_0^2 - 1}{\gamma_{crit}^2 - 1}\right)^{1/3} \tag{3.87}$$

is reached, and consequently at a time

$$t_{crit} = \frac{R_{crit}}{c}\left(1 + \frac{1}{16\lambda_{BM}\gamma_{crit}^2}\right) - \frac{r_i}{c} \tag{3.88}$$

3.5.5 Second transition stage

The second transient stage in the fireball evolution is the one connecting the self–similar relativistic stage of expansion to the self–similar non relativistic stage of expansion known as the Sedov stage.

The only things we ask to this second transient stage are *(i)* that it is accompanied by a smooth change in the adiabatic index from the value $\frac{4}{3}$ to the value $\frac{5}{3}$, *(ii)* that it is adiabatic as the rest of the evolution and *(iii)* that the constant total energy of the fireball E_T smoothly changes its expression as a function of the shock radius and the post–shock velocity from (3.24) to (3.23).

As we have explained in section 3.4 we can assume for simplicity a linear change with time of the value of the adiabatic index $\hat{\gamma}$ from $\hat{\gamma}_{BM} = \frac{4}{3}$ to $\hat{\gamma}_{SED} = \frac{5}{3}$ and a linear change with time of the factor $\Omega(t)$ in the conservation of energy law (3.25) from the value $\Omega_{BM} = \frac{8}{3}\sigma_{BM} = \frac{8}{3}\frac{6}{17}$ to the value $\Omega_{SED} = \frac{64}{9}K(5/3)$.

The start time for the change will be t_{crit}, and the end time for the change will be the time t_{sed} corresponding to the beginning of the Sedov stage that we are going to calculate later.

The exact functions $\hat{\gamma}(t)$ and $\Omega(t)$ we have used are

$$\hat{\gamma}(t) = \begin{cases} \hat{\gamma}_{BM} & t \leq t_{crit} \\ \frac{1}{t_{sed}-t_{crit}}\left[\hat{\gamma}_{BM}(t_{sed}-t) + \hat{\gamma}_{SED}(t-t_{crit})\right] & t_{crit} < t < t_{sed} \\ \hat{\gamma}_{SED} & t \geq t_{sed} \end{cases} \tag{3.89}$$

$$\Omega(t) = \begin{cases} \Omega_{BM} & t \leq t_{crit} \\ \frac{1}{t_{sed}-t_{crit}}\left[\Omega_{BM}(t_{sed}-t) + \Omega_{SED}(t-t_{crit})\right] & t_{crit} < t < t_{sed} \\ \Omega_{SED} & t \geq t_{sed} \end{cases} \tag{3.90}$$

The shock radius evolution law $R_s(t)$, post–shock Lorentz factor $\gamma_s(t)$ have been defined as during the Blandford & McKee stage:

$$R_s(t)\left(1 + \frac{1}{16\lambda_{BM}\left[1 + (\gamma_0^2 - 1)\frac{\Omega_{BM}R_0^3}{\Omega(t)R_s(t)^3}\right]}\right) = ct + r_i \tag{3.91}$$

$$\gamma_s(t) = \sqrt{1 + (\gamma_0^2 - 1)\frac{\Omega_{BM} R_0^3}{\Omega(t) R_s(t)^3}} \tag{3.92}$$

with λ_{BM} still given by (3.84).

The post–shock fluid distributions $n'(t,x)$, $e'(t,x)$ and $\gamma(t,x)$ have been defined as during the first transition stage as a time weighted linear combination of the distributions expected during the Blandford & McKee stage and those expected during the Sedov stage. An alternative way to define the distributions $n'(t,x)$, $e'(t,x)$ and $\gamma(t,x)$ would be the weighted linear combination that follows

$$n'(t,x) = \frac{(\Gamma_s(t)^2 - 1) n'_{BM}(t,x) + n'_{SED}(t,x)\frac{1}{(\Gamma_s(t)^2-1)}}{(\Gamma_s(t)^2 - 1) + \frac{1}{(\Gamma_s(t)^2-1)}} \tag{3.93}$$

$$e'(t,x) = \frac{(\Gamma_s(t)^2 - 1) e'_{BM}(t,x) + e'_{SED}(t,x)\frac{1}{(\Gamma_s(t)^2-1)}}{(\Gamma_s(t)^2 - 1) + \frac{1}{(\Gamma_s(t)^2-1)}} \tag{3.94}$$

$$\gamma(t,x) = \frac{(\Gamma_s(t)^2 - 1) \gamma_{BM}(t,x) + \gamma_{SED}(t,x)\frac{1}{(\Gamma_s(t)^2-1)}}{(\Gamma_s(t)^2 - 1) + \frac{1}{(\Gamma_s(t)^2-1)}} \tag{3.95}$$

$$\tag{3.96}$$

where $n'_{BM}(t,x)$, $e'_{BM}(t,x)$ and $\gamma_{BM}(t,x)$ are given by (3.69), (3.70) and (3.71), and $n'_{SED}(t,x)$, $e'_{SED}(t,x)$ and $\gamma_{SED}(t,x)$ are given by (3.109), (3.110) and (3.111). The definitions (3.93), (3.94) and (3.95) do not connect smoothly to the corresponding distributions in the Blandford & McKee and the Sedov stages, but it is clear that they can be extended also to these stages without introducing large errors: the Sedov distribution would not contribute substantially during the relativistic stages and the Blandford & McKee one would not contribute substantially during the non relativistic stage. Thus, if we want to use (3.93), (3.94) and (3.95) we must similar definitions for all the fireball evolution.

We have tried both the alternatives and checked that we cannot appreciate the difference in the final light curves.

The Sedov stage should start more or less when a total mass of external matter equivalent to the total energy E_T has been swept up. This will happen at a radius R_{trans} such that

$$\frac{4}{3}\pi n_i m_p R_{trans}^3 c^2 = E_T \tag{3.97}$$

$$R_{trans} = \left(\frac{E_T}{\frac{4}{3}\pi n_i m_p c^2}\right)^{1/3} \tag{3.98}$$

Substitution of R_{trans} in (3.91) would give us a tentative start time for the Sedov stage t_{trans}. The Sedov expansion start time and radius, t_{sed} and R_{sed}, should satisfy the relation $R_{sed} = S\ t_{sed}^{2/5}$ with S given by

$$S = \left(\frac{75}{16\pi} \frac{1}{3K(5/3)} \frac{E_T}{n_i m_p} \right)^{1/5} \tag{3.99}$$

and $K(5/3) \sim 0.245$ (see appendix C).

Since $S t_{trans}^{2/5} \neq R_{trans}$, we cannot use t_{trans} and R_{trans} as Sedov expansion start time and radius. We need to define

$$R_{sed} = \alpha\ R_{trans} \tag{3.100}$$

with α such that the Sedov start time

$$t_{sed} = \left(\frac{R_{sed}}{S} \right)^{5/2} = \alpha^{5/2} \left(\frac{R_{trans}}{S} \right)^{5/2} \tag{3.101}$$

satisfies equation (3.91). The value of the constant α will slightly depend on η and E_T, but it always has a value very close to 2.6. (the exact value goes from ~ 2.33 for $\eta \sim 3$ to ~ 2.268 for $\eta \sim 300$). The last important quantity to calculate is the post–shock Lorentz factor at the Sedov stage starting, γ_{sed}. We can solve equation (3.92) at $t = t_{sed}$ and get

$$\gamma_{sed} = \sqrt{1 + (\gamma_0^2 - 1) \frac{\Omega_{BM} R_0^3}{\Omega_{SED} R_{sed}^3}} \tag{3.102}$$

Finally, the forward shock Lorentz factor at the time t_{sed}, Γ_{sed}, will be related to the post–shock fluid Lorentz factor γ_{sed} as usual by equation (3.17) with adiabatic index $\frac{5}{3}$. From such a Γ_{sed} we get the forward shock velocity $V_{sed} = c \left(1 - \frac{1}{\Gamma_{sed}^2} \right)$ that in principle should be equal to the velocity $V'_{sed} = \frac{2}{5} \frac{R_{sed}}{t_{sed}}$ (see appendix C). This last equality is not satisfied, but the two velocities are comparable, and our Γ_{sed} is in any case a very good approximation of $\Gamma'_{sed} = \left(1 - \left(\frac{V'_{sed}}{c} \right)^2 \right)^{-1/2}$.

3.5.6 Sedov stage

When entering the non relativistic stage of expansion the fireball is expected to approach the self-similar Sedov solution.

We are going to assume that during this stage the shock radius expansion law is exactly the Sedov one

$$R_s(t) = S\ t^{2/5} \tag{3.103}$$

with S given by (3.99).

The start time, radius and post–shock Lorentz factor for the non relativistic expansion stage previously calculated can be expressed in terms of the constants S, $K(5/3)$ and α as follows:

$$\begin{aligned} R_{sed} &= \alpha \left(\tfrac{12}{25}\tfrac{K(5/3)}{c^2}\right)^{1/3} S^{5/3} \\ t_{sed} &= \alpha^{5/2} \left(\tfrac{12}{25}\tfrac{K(5/3)}{c^2}\right)^{5/6} S^{5/3} \\ \gamma_{sed} &= \sqrt{1 + \tfrac{1}{\frac{4}{3}\alpha^3 4 K(5/3)}} \end{aligned} \tag{3.104}$$

The post–shock Lorentz factor evolution law will be defined as in section (3.5.4) and (3.5.5) through the energy conservation law. For any $t > t_{sed}$ we can write

$$\begin{aligned} E_T = \Omega_{BM}\pi n_i m_p R_{crit}^3(\gamma_{crit}^2 - 1) &= \Omega_{SED}\pi n_i m_p R_{sed}^3(\gamma_{sed}^2 - 1) = \\ &= \Omega_{SED}\pi n_i m_p \left(St^{2/5}\right)^3 (\gamma_s(t)^2 - 1) \end{aligned} \tag{3.105}$$

The function $\gamma_s(t)$ that satisfies (3.105) can be rewritten as

$$\gamma_s(t) = \sqrt{1 + \frac{9}{25}\frac{1}{4}\frac{S^2}{c^2} t^{-6/5}} \tag{3.106}$$

The forward shock Lorentz factor will be

$$\Gamma_s(t) = \sqrt{\tfrac{(\gamma_s(t)+1)(\hat{\gamma}_{SED}(\gamma_s(t)-1)+1)^2}{\hat{\gamma}_{SED}(2-\hat{\gamma}_{SED})(\gamma_s(t)-1)+2}}, \quad \hat{\gamma}_{SED} = \tfrac{5}{3} \tag{3.107}$$

Note that for $t \to +\infty$ the forward shock velocity

$$V_s(t) = c\left(1 - \frac{1}{\Gamma_s(t)^2}\right)^{1/2} \quad \to \quad \frac{2}{5}St^{-3/5} = \frac{2}{5}\frac{R_s(t)}{t} = \frac{dR_s(t)}{dt} \tag{3.108}$$

Thus definition (3.107) gives a good approximation to the Sedov forward shock velocity, and guarantees the expansion laws we are using to approach asymptotically to the exact Sedov laws.

Finally the post-shock distributions we will use during this last evolution stage are

$$n'(t,x) = n_i \frac{(\hat{\gamma}\gamma_s(t)+1)}{(\hat{\gamma}-1)} F_\rho(x) \tag{3.109}$$

$$e'(t,x) = n_i \frac{(\hat{\gamma}\gamma_s(t)+1)}{(\hat{\gamma}-1)} m_p c^2 (\gamma_s(t)-1) F_p(x) \tag{3.110}$$

$$\gamma(t,x) = \left[1 - \left(\frac{v(t,x)}{c}\right)^2\right]^{-1/2} \tag{3.111}$$

$$v(t,x) = c\left(1 - \frac{1}{\gamma_s(t)^2}\right)^{1/2} F_v(x) \tag{3.112}$$

The functions $F_\rho(x)$, $F_p(x)$ and $F_v(x)$ are those presented in appendix C.

Note that to define the internal energy density $e'(t,x)$ we have used the relation $e'(t,x) = \frac{p'(t,x)}{\hat{\gamma}_{SED}-1}$.

3.6 The observer view

3.6.1 Time of the observer

The natural reference frame for describing the fireball evolution is the frame in quiescence with respect to the fireball centre of mass, usually named lab frame. The lab frame coordinate time t (i.e. the time measured by a clock located at the centre of mass of the fireball, which is also the centre of the explosion and the origin of the coordinate system) is the natural time to use to describe the evolution of the fireball. The zero for the time t has been set coincident with the explosion. However, a terrestrial observer at a distance D from the centre of explosion will set his zero reference time at the GRB detection, i.e. after about D/c seconds from the explosion. Moreover, the observer will assign a time T to any subsequent event measuring how many seconds after the GRB the photons produced in that event are received. The relativistic motion of the fireball will cause the time intervals between events as measured by the observer to be different from (shorter than) the coordinate time intervals between them. A far observer will see a relativistically expanding fireball evolving on a timescale shorter than the true one by a factor $\sim 1/\Gamma^2$.

To illustrate this, suppose that a spherically symmetric fireball expands at constant relativistic speed V corresponding to a constant Lorentz factor $\Gamma \gg 1$. The coordinate time interval that passes while the shock front expands from a radius R_1 to a radius R_2 is

$$\Delta t = \frac{R_2 - R_1}{V} \sim \frac{\Delta R}{c}\left(1 + \frac{1}{2\Gamma^2}\right) \sim \frac{\Delta R}{c}$$

On the other hand, the time interval between the arrival of photons emitted just behind the shock on the line of sight at the two radii R_1 and R_2 is

$$\Delta T = \frac{R_2}{V} + \frac{D - R_2}{c} - \left[\frac{R_1}{V} + \frac{D - R_1}{c}\right] = \frac{R_2 - R_1}{V} - \frac{R_2 - R_1}{c} \sim \frac{\Delta R}{2c\Gamma^2} \sim \frac{\Delta t}{2\Gamma^2}$$

This is the time required for the shock to travel a distance ΔR in the observer's opinion, and it is shorter by a factor $\sim 1/\Gamma^2$ than the true time it takes the shock to expand. If the fireball were not expanding at constant speed but according to the law $\Gamma \propto R^{-3/2}$ (with $\Gamma \gg 1$ during all the time of interest), the observer would estimate the time required to travel the distance ΔR as

$$\begin{aligned}\Delta T = & \int_{R_0}^{R_2} \frac{dR}{V} + \frac{D-R_2}{c} - \left[\int_{R_0}^{R_1} \frac{dR}{V} + \frac{D-R_1}{c}\right] = \int_{R_1}^{R_2} \frac{dR}{V} - \frac{(R_2-R_1)}{c} \sim \\ & \sim \int_{R_1}^{R_2} \left(1 + \frac{1}{2\Gamma^2}\right) \frac{dR}{c} - \frac{(R_2-r_1)}{c} \sim \frac{\Delta R}{8c\Gamma^2} \sim \frac{\Delta t}{8\Gamma^2}\end{aligned}$$

The expansion timescale is again contracted by a factor $\sim 1/\Gamma^2$.

Since we want to calculate observed afterglow light curves and spectra, we must use the time of the terrestrial observer T instead of the lab frame coordinate time t.

Unfortunately it is not possible to find a unique conversion function $T(t)$ because photons simultaneously emitted by different portions of the fireball do not arrive simultaneously to the observer. The only thing we can do to properly calculate the observed radiation at a given observer time T is taking in account all contributions from different emission times.

First of all we need a definition of the zero for the time of the observer T. As we said, the zero for T should be the GRB detection time as no other reference time makes sense in real observations, but for our purposes this is not a well defined zero time.

In the following we are going to call time of the observer T the time measured from a terrestrial observer starting from the arrival of photons emitted at $t = 0$ by matter just behind the shock on the line of sight. According to this definition the time T at which photons emitted at the lab time t_{em} by the point with coordinates $(r_{em}, \vartheta, \varphi)$ are seen by the observer is

$$T = t_{em} + \frac{D - r_{em}\cos\vartheta}{c} - \frac{D - r_i\cos\vartheta}{c} = t_{em} - \frac{r_{em}\cos\vartheta}{c} + \frac{r_i}{c} \tag{3.113}$$

If the internal/external shock scenario is correct and GRB photons start to be produced after optical thinning of the ejecta the GRB detection will not be at time $T = 0$ but at time $T_{GRB} > t_{th} - \frac{R_{th}}{c} + \frac{r_i}{c}$.

Since the definition of T depends also on the angle ϑ formed with the line of sight by the line connecting the emitting point and the centre of explosion, the observer will see the fireball entering the different evolution stages at different times in different directions. The shock portion on the line of sight expanding towards the observer will appear to be the first entering a new stage, while the opposite portion of the fireball will appear to be the last.

We will define the direction dependent observer times of transition from one stage to another as follows:

- Coasting stage beginning

$$T_c(\vartheta) = t_c - \frac{R_c}{c}\cos\vartheta + \frac{r_i}{c} \tag{3.114}$$

- Thinning of the ejecta

$$T_{th}(\vartheta) = t_{th} - \frac{R_{th}}{c}\cos\vartheta + \frac{r_i}{c} \tag{3.115}$$

- Deceleration stage beginning

$$T_d(\vartheta) = t_d - \frac{R_d}{c}\cos\vartheta + \frac{r_i}{c} \tag{3.116}$$

- Blandford & McKee stage beginning

$$T_0(\vartheta) = t_0 - \frac{R_0}{c}\cos\vartheta + \frac{r_i}{c} \tag{3.117}$$

- Transition to non relativistic expansion beginning

$$T_{crit}(\vartheta) = t_{crit} - \frac{R_{crit}}{c}\cos\vartheta + \frac{r_i}{c} \tag{3.118}$$

- Sedov stage beginning

$$T_{sed}(\vartheta) = t_{sed} - \frac{R_{sed}}{c}\cos\vartheta + \frac{r_i}{c} \tag{3.119}$$

All the lab frame transition times and radii have been defined and calculated in the previous sections.

3.6.2 The Equal–T Surface

As we have explained in section 3.6.1, photons simultaneously emitted by a spherical expanding shock do not arrive simultaneously to the observer because of relativistic light travel delays, and to calculate the radiation observed at a given observer time one needs to know the region from which simultaneously detected photons come. The surface limiting such a region will be named Equal-T surface.

The observed radiation at the time T will be the volume integral on the region surrounded by the equal-T surface of the radiation emitted, properly boosted and Doppler shifted.

The Equal–T Surface is the surface from which photons emitted by the shock front arrive to the observer at the same time T. The volume inside it will be the region from which photons emitted by the fireball interior arrive to the observer at T too.

The Equal–T surface will be represented by a function $ReqT(\vartheta, \varphi, T)$ giving the radius of the region from which photons arrive to the observer at the time T as a

function of the direction ϑ, φ. If the fireball is spherical the Equal-T surface is axially symmetric, i.e. the function $ReqT$ does not explicitly depend on φ.

Now we explain how to calculate the function $ReqT$.

If $ReqT$ is the radius of the Equal–T Surface in the direction ϑ, φ, photons emitted by the shock in that position (and seen by the observer at the time T) must be emitted at the time $t_{em} = T + \frac{ReqT}{c}\cos\vartheta - \frac{r_i}{c}$. At that time the shock radius in the direction $\vartheta\varphi$, should have been exactly $ReqT$. Thus, the function $ReqT$ must be such that

$$R_s(T + \frac{ReqT}{c}\cos\vartheta - \frac{r_i}{c}) = ReqT \tag{3.120}$$

This equation in the variable $ReqT$ can be solved once the analytic expression of $R_s(t)$ is known.

The shock radius evolution law $R_s(t)$ we have defined in the previous sections is composed by different analytic expressions at different times, so we expect the function $ReqT(\vartheta, T)$ to be composed by different expressions too.

The general definition of $ReqT(\vartheta, T)$ will be

$$ReqT(\vartheta,T) = \begin{cases} ReqT_{FREE}(\vartheta,T) & T < T_c(\vartheta) \\ ReqT_{COAST}(\vartheta,T) & T_c(\vartheta) \leq T < T_d(\vartheta) \\ ReqT_{DEC}(\vartheta,T) & T_d(\vartheta) \leq T < T_0(\vartheta) \\ ReqT_{BM}(\vartheta,T) & T_0(\vartheta) \leq T < T_{crit}(\vartheta) \\ ReqT_{TRANS}(\vartheta,T) & T_{crit}(\vartheta) \leq T < T_{tran}(\vartheta) \\ ReqT_{SED}(\vartheta,T) & T \geq T_{tran}(\vartheta) \end{cases} \tag{3.121}$$

where the times $T_c(\vartheta)$, $T_d(\vartheta)$, $T_0(\vartheta)$, $T_{crit}(\vartheta)$ and $T_{sed}(\vartheta)$ have been defined in section 3.6.1 and the functions $ReqT_{FREE}(\vartheta,T)$, $ReqT_{COAST}(\vartheta,T)$, $ReqT_{DEC}(\vartheta,T)$, $ReqT_{BM}(\vartheta,T)$, $ReqT_{TRANS}(\vartheta,T)$ and $ReqT_{SED}(\vartheta,T)$ are the functions solving the equation (3.120) with the different analytic expressions of $R_s(t)$ corresponding to the different stages.

During the coasting stage, for instance, we have

$$R_s(t) = R_{COAST}(t) = R_c + c\left(1 - \frac{1}{\Gamma_c^2}\right)^{1/2}(t - t_c)$$

and the Equal-T surface will be the solution of the equation

$$R_{COAST}(T + \frac{ReqT}{c}\cos\vartheta - \frac{r_i}{c}) = ReqT$$

$$R_c + c\left(1 - \frac{1}{\Gamma_c^2}\right)^{1/2}(T + \frac{ReqT}{c}\cos\vartheta - \frac{r_i}{c} - t_c) = ReqT$$

so

$$ReqT_{COAST}(\vartheta, T) = \frac{R_c + V_c\left(T - t_c - \frac{r_i}{c}\right)}{1 - \frac{V_c}{c}\cos\vartheta} \tag{3.122}$$

with $V_c = c\left(1 - \frac{1}{\Gamma_c^2}\right)^{1/2}$.

During the first deceleration stage

$$R_s(t) = R_{DEC}(t) = At^2 + Bt + C$$

and the Equal-T surface will be the solution of the equation

$$R_{DEC}(T + \frac{ReqT}{c}\cos\vartheta - \frac{r_i}{c}) = ReqT$$

so

$$ReqT_{DEC}(\vartheta, T) = \begin{cases} -\left\{2A(cT - r_i)\cos\vartheta + c\left[B\cos\vartheta - c + \right.\right. & \\ \left.\left.\sqrt{(B\cos\vartheta - c)^2 - 4A\cos\vartheta(cT - r_i + C\cos\vartheta)}\right]\right\}\frac{1}{2A\cos\vartheta^2} & \vartheta \neq \frac{\pi}{2} \\ \frac{1}{c^2}\left[r_i^2 A - r_i c(2TA + B) + c^2\left(T(TA + B) + C\right)\right] & \vartheta = \frac{\pi}{2} \end{cases}$$

During the remaining stages the solution of equation (3.120) must be found numerically.

The Blandford & McKee stage, for instance, has a shock radius evolution law $R_{BM}(t)$ such that

$$R_{BM}(t)\left(1 + \frac{R_{BM}^3(t)}{16\lambda_{BM}\left[R_{BM}^3(t) + (\gamma_0^2 - 1)R_0^3\right]}\right) = ct + r_i$$

The Equal-T surface must be $ReqT_{BM}$ such that

$$T = t_{eqt} - \frac{ReqT_{BM}}{c}\cos\vartheta + \frac{r_i}{c}$$

with t_{eqt} satisfying

$$ReqT_{BM}\left(1 + \frac{ReqT_{BM}^3}{16\lambda_{BM}\left[ReqT_{BM}^3 + (\gamma_0^2 - 1)R_0^3\right]}\right) = ct_{eqt} + r_i$$

Thus the equation to solve for $ReqT_{BM}$ will be

$$T = \frac{ReqT_{BM}}{c}\left(1 - \cos\vartheta + \frac{ReqT_{BM}^3}{16\lambda_{BM}\left[ReqT_{BM}^3 + (\gamma_0^2 - 1)R_0^3\right]}\right) \tag{3.123}$$

and, similarly, the equation to solve to calculate $ReqT_{TRANS}$ will be

$$T = \frac{ReqT_{TRANS}}{c}\left(1 - \cos\vartheta + \frac{ReqT^3_{TRANS}}{16\lambda_{BM}\left[ReqT^3_{TRANS} + \frac{\Omega_{BM}(\gamma_0^2-1)R_0^3}{\Omega(T+\frac{ReqT_{TRANS}}{c}-\frac{r_i}{c})}\right]}\right) \tag{3.124}$$

Finally, the Equal-T surface $ReqT_{SED}$ during the Sedov stage will be the solution of the equation

$$S^5\left(T + \frac{ReqT_{SED}}{c}\cos\vartheta - \frac{r_i}{c}\right)^2 = ReqT^5_{SED} \tag{3.125}$$

The Equal-T surface gives the fireball shape the observer actually sees. The observed fireball shape is very different from the intrinsic one even in the spherical case. Figure (3.5) shows that for a spherical fireball the Equal-T surface is egg shaped for almost all the fireball evolution. It can also be seen how the egg curvature evolves with time.

3.6.3 Detailed calculation of afterglow light curve/spectrum

If we assume that the shocked plasma emits radiation via a specific radiation mechanism, knowing the complete hydrodynamics of the fireball we can calculate the comoving emissivity $j'(\nu')$ of each fireball fluid element at any time[†]. Once the instantaneous comoving emissivity of a fireball fluid element is known, the calculation of the instantaneous observed spectrum contributed by the given element is straightforward. Now I am going to illustrate it.

First of all, suppose that a fireball fluid element emits radiation at the lab frame coordinate time t_{em} from the position $(r_{em}, \vartheta, \varphi)$[‡] such that $x_{em} = \frac{r_{tem}}{R_s(tem)} < 1$. The lab frame volume of the fluid element will be $dV = r^2_{em}dr_{em}\sin\vartheta d\vartheta d\varphi = R_s(t_{em})^3 x^2_{em}dx_{em}\sin\vartheta d\vartheta d\varphi$. The comoving particle and internal energy densities will be $n'(t_{em}, x_{em})$ and $e'(t_{em}, x_{em})$. The fluid element Lorentz factor relative to the lab frame will be $\gamma(t_{em}, x_{em})$, and the fluid element will expand radially. The comoving particle density $n'(t, x)$, the internal energy density $e'(t, x)$, and the shocked fluid velocity field $\gamma(t, x)$ can in principle depend also on the angle ϑ and on the second coordinate angle φ of the spherical coordinate system having the line of sight as z axis.

[†]Remember that if emission in the comoving frame is isotropic, the quantity $dP'_{\nu'} = 4\pi j'(\nu')dV$ will be the instantaneous comoving spectrum emitted by the element

[‡]Remember that because of the spherical coordinate system choice in the lab frame the line of sight forms an angle ϑ with the radial direction connecting the fluid element to the centre of the explosion.

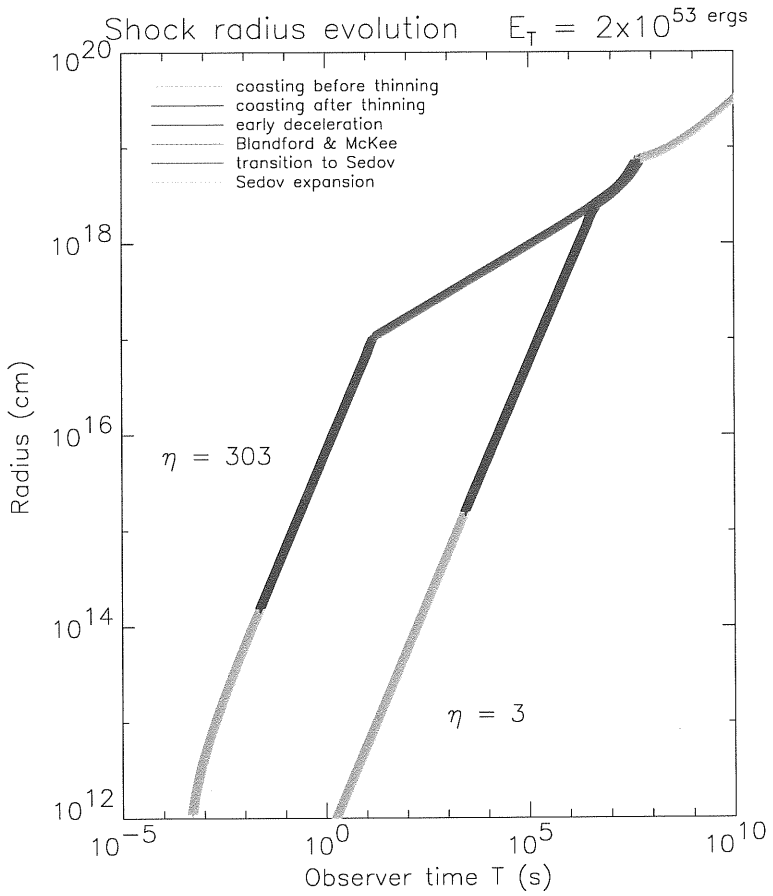

Figure 3.4: *The shock radius evolution with the time of the observer is shown. Segments of different colors represent different evolutionary stages as in the legend. The upper line refers to a spherical fireball with a baryon loading parameter* $\eta = 300$ *and a total energy* $E_T = 2 \times 10^{53}$ *ergs, and the lower line refers to a fireball with a baryon loading parameter* $\eta = 3$ *and a total energy* $E_T = 2 \times 10^{51}$ *ergs. Since the total energy is the same in both cases the two curves meet during the Sedov stage. The non relativistic self–similar expansion looses completely memory about initial conditions with the only exception of the total energy of the explosion.*

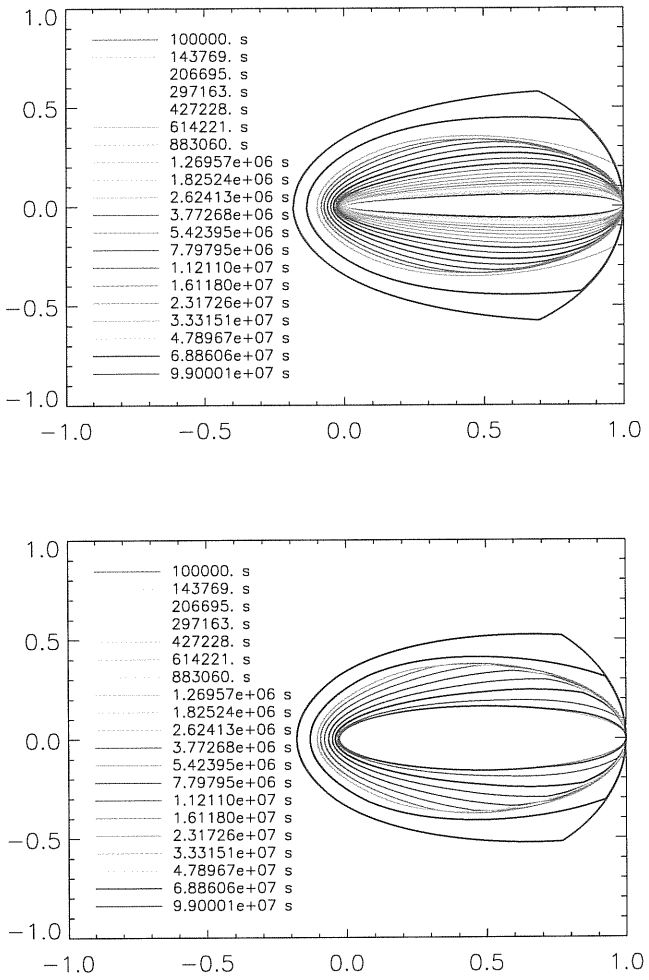

Figure 3.5: *In this figure we can see how the Equal-T surface evolves with the time of the observer in the two extreme cases* $\eta = 303$ *(upper panel) and* $\eta = 3$ *(lower panel) with the same total energy* $E_T = 2 \times 10^{53}$ *ergs. We plot the function* $ReqT(\vartheta, T)/ReqT(0, T)$ *for* T *growing from about* 10^5 *s to about* 10^8 *s. The line of sight is the horizontal direction, with the observer far on the right side of the figures and the centre of the explosion corresponding to the origin. You can see the front of equal–T surface gradually becoming spherical after the time* $T_{sed}(0)$ *at which the fireball front starts non relativistic Sedov expansion.*

This happens for instance for non spherical fireballs. Nothing changes in what follows provided that angular dependencies are properly added everywhere.

If the line connecting the fluid element position to the observer forms an angle Ξ with the radial direction, then the emitted frequency ν' will be observed as the frequency ν such that

$$\nu' = \nu\gamma(t_{em}, x_{em})(1 - \beta(t_{em}, x_{em}) \cos \Xi) \tag{3.126}$$

Note that the comoving emissivity $j'(\nu')$ should depend on the local comoving particle density, on the local internal energy density and also on the comoving time elapsed since the shock passage t'. The times t_{em} and t' are related as follows:

$$t' = \int_{t_s}^{t_{em}} \frac{dt}{\gamma(t, x_f(t))} \tag{3.127}$$

where t_s is the lab frame coordinate time at which the volume element has been shocked and $x_f(t)$ is defined as $x_f(t) = \frac{r_f(t)}{R_s(t)}$ with $r_f(t)$ being the solution of the Cauchy problem $\frac{dr_f}{dt} = \left(1 - \frac{1}{\gamma^2(t, x_f(t))}\right)^{1/2} c$, $r_f(t_s) = R_s(t_s)$. Both t_s and t' are expected to be known functions of r_{em} and t_{em} (see section 3.8).

After expanding all possible dependencies, we can write the comoving emissivity as a function of the same variables used for the hydrodynamical quantities and the frequency: $j'(\nu', t_{em}, x_{em})$.

Then, remember that $\frac{j'(\nu')}{\nu'^2}$ is a Lorentz invariant, so that the lab frame emissivity $j(\nu)$ is related to the comoving emissivity $j'(\nu')$ by the expression

$$j(\nu) = j'(\nu') \left(\frac{\nu}{\nu'}\right)^2 \tag{3.128}$$

Using (3.126) we van conclude that

$$j(\nu, t_{em}, x_{em}, \Xi) = \frac{j'(\nu\gamma(t_{em}, x_{em}) \left[1 - \beta(t_{em}, x_{em}) \cos \Xi\right], t_{em}, x_{em})}{\gamma^2(t_{em}, x_{em}) \left[1 - \beta(t_{em}, x_{em}) \cos \Xi\right]^2} \tag{3.129}$$

from which we see that the lab frame emissivity depends on the observation angle Ξ, i.e. the emission in the lab frame is no longer isotropic as expected by the relativistic beaming effect.

Now that we know the lab frame emissivity $j(\nu, t_{em}, x_{em}, \Xi)$ we can say that the contribution of the fluid element to the observed flux is

$$dF_\nu = j(\nu, t_{em}, x_{em}, \Xi) \frac{dr_{em}}{\cos \Xi} \frac{\cos \Xi \, r_{em}^2 \sin \vartheta d\vartheta d\varphi}{d^2} = \frac{j(\nu, t_{em}, x_{em}, \Xi) dV}{d^2} \tag{3.130}$$

where d is the distance of the fluid element from the observer, that depends on r_{em}, and Ξ is the angle formed with the radial direction by the line connecting the observer and the fluid element at the time t_{em}. The angle Ξ depends on the volume element position too.

In the case of a very distant observer we can approximate d with the distance of the center of the explosion from the observer D, which is constant, and the angle Ξ with ϑ because all the directions to the observer can be considered parallel directions.

The final result is

$$dF_\nu(t_{em}, x_{em}, \vartheta) = \frac{j'[\nu\gamma(t_{em},x_{em})(1-\beta(t_{em},x_{em})\cos\vartheta),t_{em},x_{em}]}{\gamma^2(t_{em},x_{em})[1-\beta(t_{em},x_{em})\cos\vartheta]^2} \times \frac{R_s(t_{em})^3 x_{em}^2 dx_{em}\sin\vartheta\ d\vartheta d\varphi}{D^2} \tag{3.131}$$

If the fireball is not spherical, then we expect the functions γ and β to depend also on the angles ϑ and φ, and the elementary observed flux will depend also on φ.

The elementary flux (3.131) will be observed at the time

$$T = t_{em} - \frac{r_{em}}{c}\cos\vartheta + \frac{r_i}{c} \tag{3.132}$$

We already know that if we fix the lab frame time of emission t_{em}, different fluid elements of the fireball will contribute to the observed flux at frequency ν with elementary fluxes dF_ν that will reach the observer at different times T depending on their different positions (r_{em}, ϑ). In order to calculate the observed flux at a fixed observer time T, we must take in account elementary fluxes emitted by different portions of the fireball at different lab frame times t_{em}. The volume from which the observer gets radiation at the time T is the region inside the Equal-T surface, i.e. the place of all the shock front positions from which the emitted radiation reaches the observer at the same time T. The Equal-T Surface is a closed surface around the centre of the explosion, described through a function $ReqT(\vartheta, T)$ that gives the radius corresponding to the direction (ϑ, φ)[§].

In conclusion, the observed flux at T will be obtained by integration of the elementary observed fluxes (3.131) over the whole volume enclosed by the Equal–T surface. In this way we can in principle calculate both the total observed flux at the time T, $F(T)$, and the monochromatic observed flux at the time T, $F_\nu(T)$, i.e. the observed instantaneous spectrum.

Since the generic fluid element centered on the point $(r_{em}, \vartheta, \varphi)$ internal to the Equal–T Surface (i.e. such that $0 < r_{em} < ReqT(\vartheta, T)$), contributes to the radiation

[§]Only in case of anisotropic fireballs the function $ReqT$ depends explicitly also on the angle φ.

observed at the time T by emitting at the time $t_{em} = T - \frac{r_{em}}{c}\cos\vartheta + \frac{r_i}{c}$ an elementary flux $dF_\nu(t_{em}, x_{em}, \vartheta)$ where $x_{em} = \frac{r_{em}}{R_s(t_{em})}$, the observed spectrum at T will be

$$F_\nu(T) = \int dF_\nu(t,x,\vartheta) = \int \frac{j'\left[\nu\gamma(t,x)\left[1-\beta(t,x)\cos\vartheta\right],t,x\right]}{\gamma^2(t,x)\left[1-\beta(t,x)\cos\vartheta\right]^2}\,\frac{dV}{D^2} \tag{3.133}$$

more precisely

$$F_\nu(T) = \frac{1}{D^2}\int_0^{2\pi} d\varphi \int_0^{\pi} \sin\vartheta\, d\vartheta \int_0^{ReqT(\vartheta,T)} \frac{j'\left[\nu\gamma(t,x)\left[1-\beta(t,x)\cos\vartheta\right],t,x\right]}{\gamma^2(t,x)\left[1-\beta(t,x)\cos\vartheta\right]^2}\, r^2 dr \tag{3.134}$$

where

$$t \equiv t\left(r,\vartheta,T\right) = T + \frac{r}{c}\cos\vartheta - \frac{r_i}{c}$$

$$x \equiv x\left(r,\vartheta,T\right) = \frac{r}{R_s(T + \frac{r}{c}\cos\vartheta - \frac{r_i}{c})}$$

and the observed bolometric light curve will be

$$F(T) = \int d\nu F_\nu(T) \tag{3.135}$$

Anyway, what is usually observed is not an instantaneous broad band spectrum nor a bolometric light curve, but a narrow band frequency integrated light curve, which is expected to be well approximated by (3.134) at fixed ν once normalized at the mean frequency of the observation band.

In order to simplify the numerical calculation we can do the following change of variables

$$X = \frac{r}{ReqT(\vartheta,T)} \tag{3.136}$$

and rewrite (3.134) as

$$F_\nu(T) = \frac{1}{D^2}\int_0^{2\pi} d\varphi \int_0^{\pi} \sin\vartheta\; ReqT(\vartheta,T)^3\, d\vartheta \int_0^1 I(X,\vartheta,T,\nu)X^2 dX \tag{3.137}$$

where

$$I(X,\vartheta,T,\nu) = \frac{j'\left[\nu h(X,\vartheta,T), t(X,\vartheta,T), \xi(X,\vartheta,T)\right]}{h(X,\vartheta,T)^2} \tag{3.138}$$

with

$$\begin{aligned} h(X,\vartheta,T) &= \gamma\left(t(X,\vartheta,T),\xi(X,\vartheta,T)\right) \\ &\quad \left[1-\beta\left(t(X,\vartheta,T),\xi(X,\vartheta,T)\right)\cos\vartheta\right] \end{aligned} \tag{3.139}$$

$$\xi(X,\vartheta,T) = \frac{X\,ReqT(\vartheta,T)}{R_s(t(X,\vartheta,T))} \tag{3.140}$$

and

$$t(X,\vartheta,T) = T + \frac{X\,ReqT(\vartheta,T)}{c}\cos\vartheta - \frac{r_i}{c} \tag{3.141}$$

Finally

$$F_\nu(T) = \frac{1}{D^2}\int_0^{2\pi} d\varphi \int_0^{\pi} d\vartheta\ \sin\vartheta \int_0^{1} dX\ X^2\ ReqT(\vartheta,T)^3\ I(X,\vartheta,T,\nu) \tag{3.142}$$

In the case of anisotropic fireball the functions $ReqT$, I, h, ξ and t explicitly depend on φ too. For spherical fireballs, on the contrary, we can simply write

$$F_\nu(T) = \frac{2\pi}{D^2}\int_0^{\pi} d\vartheta\ \sin\vartheta \int_0^{1} dX\ X^2\ ReqT(\vartheta,T)^3\ I(X,\vartheta,T,\nu) \tag{3.143}$$

Results of the calculation of (3.143) for different values of the fireball parameters and a different observation frequencies will be shown in sections 5.3.1 and 5.3.2.

3.6.4 The integration volume

The change of variables (3.136) apparently makes the integration volume a sphere of radius 1. But the situation is more complex.

At any given time T and for each fixed direction (ϑ, φ), any value of the variable X corresponds to a value of the position relative to the shock radius at the emission, $x = \frac{XReqT(\vartheta,T)}{R_s(t(X,\vartheta,T))}$. We know that if the time of emission $t(X, \vartheta, T)$ is such that the fireball is in the coasting stage (or even before it), the fireball is shell shaped and only values of x greater than $x_{min} = 1 - \frac{\Delta}{R_s}$ are allowed. So the (low) X values corresponding to times of emission lower than t_d and x lower than x_{min} must be excluded by the integration region.

If $0 < \vartheta < \frac{\pi}{2}$, when X grows then $t(X, \vartheta, T)$ grows but x grows all the same. If $\frac{\pi}{2} < \vartheta < \pi$, when X grows then $t(X, \vartheta, T)$ decreases and x grows even faster. So, the integration in X must be limited to the interval from $X_{min}(T, \vartheta)$ to 1, with $X_{min}(T, \vartheta)$ such that for any $X \geq X_{min}(T, \vartheta)$ the corresponding x is greater than x_{min}, that is

$$\frac{XReqT(\vartheta, T)}{R_s(t(X, \vartheta, T))} \geq 1 - \frac{\Delta(t(X, \vartheta, T))}{R_s(t(X, \vartheta, T))}$$

or equivalently

$$XReqT(\vartheta, T) \geq R_s(t(X, \vartheta, T)) - \Delta(t(X, \vartheta, T)) = R(t(X, \vartheta, T))$$

You can easily see that $X_{min}(T, \vartheta)$ approaches 0 as T grows, and there is a time T_{fill} after which $X_{min}(T, \vartheta) = 0$ in every direction. In the spherical case we are now considering $T_{fill} = t_d + \frac{R_d}{c} + \frac{r_i}{c}$. See fig. 3.6.

The final formula to use for the calculation of the observed monochromatic light curve is

$$F_\nu(T) = \frac{1}{D^2} \int_0^{2\pi} d\varphi \int_0^{\pi} d\vartheta \, \sin\vartheta \int_{X_{min}(T,\vartheta)}^{1} dX \, X^2 \, ReqT(\vartheta, T)^3 \, I(X, \vartheta, T, \nu) \quad (3.144)$$

In the spherical case the integration in φ simply gives a factor 2π but (3.144) is valid also in the general anisotropic case, when X_{min}, $ReqT$ and I are actually φ dependent.

3.6.5 Effects of the volume integration

Following [Granot, Piran & Sari 1999c] I have tried to single out the angular integration and the radial integration in the afterglow light curve calculation from a spherical

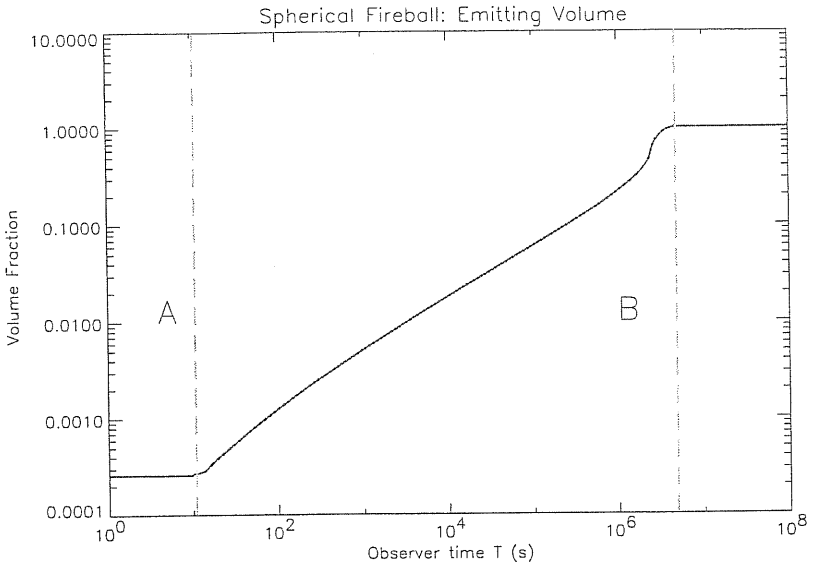

Figure 3.6: *The growth of the integration volume for the observed flux calculation as a function of the observer time T is shown. We illustrate the case of a spherical fireball. The solid line in the plot is the fraction V_{int}/V_{tot}, where $V_{int} = \int_0^{2\pi} d\varphi \int_0^{\pi} d\vartheta \sin\vartheta \int_{X_{min}(T,\vartheta)}^1 dX\ X^2 ReqT(\vartheta,T)^3$ is the volume of the integration domain to use in (3.144) and $V_{tot} = \int_0^{2\pi} d\varphi \int_0^{\pi} d\vartheta \sin\vartheta \int_0^1 dX\ X^2 ReqT(\vartheta,T)^3$ is the whole volume delimited by the Equal-T surface. The vertical line A represents the beginning of the deceleration stage on the front of the fireball and the vertical line B represents the beginning of the deceleration on the back of the fireball, i.e. the time T_{fill} after which we expect to be reached by radiation from the whole volume V_{tot}. Actually the solid line becomes constant and equal to 1 after the vertical line B representing T_{fill}.*

fireball, in order to find out the different effects each integration has on the observed flux.

The importance of radial integration can be investigated calculating the observed flux due to photons emitted along the line of sight only. To do this we assume that at each point photons are emitted only radially in the fluid element comoving frame. This would correspond to a comoving emissivity

$$j'_{rad}(\nu') = j'(\nu')\delta\left(\Omega' - \Omega'(\hat{r})\right)$$

where $j'(\nu')$ is the isotropic comoving emissivity defined in the previous section, Ω' the solid angle in comoving frame and $\hat{r}$ the unit vector parallel to the radial direction in the comoving frame. Since passing from the comoving to the lab frame the solid angle

transforms as $d\Omega = \gamma^2(1-\beta\cos\vartheta)^2 d\Omega'$ [Rybicki & Lightman 1979] we obtain

$$\delta\left(\Omega' - \Omega'(\hat{r})\right) = \gamma^2(1-\beta\cos\vartheta)^2\,\delta\left(\Omega - \Omega(\hat{r})\right)$$

and the calculation of the observed flux in this case leads to

$$F_\nu^{rad}(T) = \frac{4\pi}{D^2}\int_0^{ReqT(0,T)} j'\left[\nu'(\nu,T,r), T + \frac{r-r_i}{c}, \frac{r}{R_s(T+\frac{r-r_i}{c})}\right] r^2 dr \qquad (3.145)$$

with

$$\nu'(\nu,T,r) = \nu\gamma(T + \frac{r-r_i}{c}, \frac{r}{R_s(T+\frac{r-r_i}{c})})\left[1 - \beta(T + \frac{r-r_i}{c}, \frac{r}{R_s(T+\frac{r-r_i}{c})})\right] \qquad (3.146)$$

On the other hand, in order to single out the effect of angular integration, I should calculate the observed radiation as if it were coming from a thin shell of lab frame thickness Δ just behind the shock, and take the limit for $\Delta \to 0$. Since I do not use the same change of variables used by [Granot, Piran & Sari 1999c] for volume integration, because it is optimized for the Blandford & McKee solution and easy to be used only during that evolutionary stage, I do not follow Granot's exact calculation of the afterglow light curve from a infinitely thin shell. I simply calculate

$$F_\nu^{ang}(T) = \frac{1}{D^2}\int_0^{2\pi} d\varphi \int_0^{\pi} d\vartheta\ \sin\vartheta\ ReqT(\vartheta,T)^3\ I(1,\vartheta,T,\nu) \qquad (3.147)$$

where the function I is defined by (3.138).

It will be shown in section 5.3.1 (fig.5.7) that in the spherical case both radial and angular integration become important in a light curve calculation when the fireball front decelerates to Lorentz factors below ~ 2 (i.e. the transition to non relativistic expansion starts; see the definition of γ_{crit} in section 3.5.4). At earlier times the light curve is reasonably well approximated (with the exception of the time interval around the peak) by the emission of electrons just behind the shock front along the line of sight. The volume integration is important to establish the light curve peak or break shape and the shape of spectral breaks.

3.6.6 Normalization of afterglow light curve/spectrum

If we believe that afterglow radiation is produced by synchrotron emission from relativistic electrons accelerated at the forward shock, then we can estimate the observed monochromatic light curve and spectra in a very rough way assuming that at any time T all emitting electrons are mono energetic with a Lorentz factor $\gamma_m(T)$ equal to the

minimum Lorentz factor of just shocked electrons along the line of sight, i.e. (see section 3.7.2)

$$\gamma_m(T) \equiv \gamma_{e,min}(T) = \sqrt{1 + \left[\frac{(p-2)}{(p-1)}\frac{\epsilon_e}{m_e c^2}\left(\frac{e'_{los}(T)}{n'_{los}(T)}\right)\right]^2} \tag{3.148}$$

where

$$R_{los}(T) = ReqT(T, 0) \tag{3.149}$$

$$\gamma_{los}(T) = \gamma\left(T + \frac{R_{los}(T)}{c} - \frac{r_i}{c}, 1\right) \tag{3.150}$$

$$n'_{los}(T) = n'\left(T + \frac{R_{los}(T)}{c} - \frac{r_i}{c}, 1\right) \tag{3.151}$$

$$e'_{los}(T) = e'\left(T + \frac{R_{los}(T)}{c} - \frac{r_i}{c}, 1\right) \tag{3.152}$$

$$B_{los}(T) = \sqrt{8\pi\epsilon_B e'_{los}(T)} \tag{3.153}$$

are respectively the shock radius and the post-shock Lorentz factor, particle density, internal energy density and magnetic field strength at the time T along the line of sight.

The total number of emitting electrons can be assumed to be the total number of external electrons the forward shock has swept up, i.e.

$$N(T) = \frac{4}{3}\pi R_{los}(T)^3 n_i \tag{3.154}$$

Each emitting electron will emit an instantaneous spectrum peaked at a comoving frequency (see appendix D)

$$\nu'_m(T) = \nu'_{sync}(\gamma_m(T)) = \frac{3}{16}\frac{eB_{los}(T)}{m_e c}\gamma_m(T)^2 \tag{3.155}$$

The observed peak frequency will be

$$\nu_m(T) = \frac{\nu'_m(T)}{\gamma_{los}(T)(1 - \beta_{los}(T))} \tag{3.156}$$

Moreover, since the total power emitted by the single emitting electron in the comoving frame can be estimated as

$$P'_{tot}(T) = \frac{4}{3}\sigma_T c \beta_m(T)^2 \gamma_m(T)^2 \frac{B_{los}(T)^2}{8\pi} \tag{3.157}$$

and, consequently, the observed total power from a single electron is

$$P_{tot}(T) = \frac{P'_{tot}(T)}{\gamma_{los}(T)^4(1-\beta_{los}(T))^3} \tag{3.158}$$

we can conclude that the radiation observed at the time T, peaking at the frequency $\nu_m(T)$, should produce a total flux per unit frequency

$$F_{tot}(T) = \frac{1}{4\pi D^2}N(T)\frac{P_{tot}(T)}{\nu_m(T)} = \frac{1}{4\pi D^2}N(T)\frac{P'_{tot}(T)}{\nu'_m(T)}\frac{1}{\gamma_{los}(T)^3(1-\beta_{los}(T))^2} \tag{3.159}$$

Note that in the limit $\gamma_{los}(T) \gg 1$ we have $1-\beta_{los}(T) \sim \frac{1}{2\gamma_{los}(T)^2}$ and consequently

$$\nu_m(T) \sim 2\nu'_m(T)\gamma_{los}(T) \tag{3.160}$$

$$P_{tot}(T) \sim 8P'_{tot}(T)\gamma_{los}(T)^2 \tag{3.161}$$

$$F_{tot}(T) = \frac{1}{4\pi D^2}N(T)\frac{P'_{tot}(T)}{\nu'_m(T)}4\gamma_{los}(T) \tag{3.162}$$

A better approximation might be obtained assuming the emitting electrons are power law distributed, with an average Lorentz factor equal to $\gamma_m(T)$. In this case the total flux per unit frequency at frequency $\nu_m(T)$ of the observed radiation would be (see appendix D.1.3)

$$F_{tot}(T) = 0.88\frac{4(p-1)}{3p-1}\frac{1}{4\pi D^2}N(T)\frac{P_{tot}(T)}{\nu_m(T)} =$$
$$= 0.88\frac{4(p-1)}{3p-1}\frac{1}{4\pi D^2}N(T)\frac{P'_{tot}(T)}{\nu'_m(T)}\frac{1}{\gamma_{los}(T)^3(1-\beta_{los}(T))^2} \tag{3.163}$$

where the factor $0.88\frac{4(p-1)}{3p-1}$ has been added to fit the synchrotron peak of the approximated spectrum produced by a power law distributed electron population without any high energy cut off due to cooling.

After substitution of (3.154), (3.155) and (3.157) we get

$$F_{tot}(T) = 0.88\frac{4(p-1)}{3p-1}\frac{n_i}{3D^2}\frac{4}{3}\sigma_T c\frac{16m_e c}{3e}\sqrt{\frac{\epsilon_B}{8\pi}}\frac{\beta_m(T)^2 R_{los}(T)^3\sqrt{e'_{los}(T)}}{\gamma_{los}(T)^3(1-\beta_{los}(T))^2} \tag{3.164}$$

In the ultra relativistic limit

$$F_{tot}(T) \sim 0.88\frac{4(p-1)}{3p-1}\frac{n_i}{3D^2}\frac{4}{3}\sigma_T c\frac{16m_e c}{3e}\sqrt{\frac{\epsilon_B}{8\pi}}R_{los}(T)^3\sqrt{e'_{los}(T)}4\gamma_{los}(T) \tag{3.165}$$

The estimated total flux per unit frequency (3.164) is now independent on the average Lorentz factor of the emitting electrons. If the hydrodynamical evolution of the

fireball follows the Blandford & McKee law we can write $\gamma_{los}(T) \propto R_{los}(T)^{-3/2}$ and since $e'_{los}(T) \sim 4\gamma_{los}(T)^2 m_p n_i c^2$ we conclude that $F_{tot}(T) \propto R_{los}(T)^3 \sqrt{e'_{los}(T)}\gamma_{los}(T) \propto R_{los}(T)^3 \gamma_{los}(T)^2 \propto E_T \propto constant$. Thus, the quantity (3.164) is expected to be constant during the Blandford & McKee stage, and for this reason can be used as a normalization constant for the function $F_\nu(T)$ calculated with the (3.144). It is of course a total energy (or baryon loading parameter) depending constant.

In our case, since the approximation $\beta_m(T) \sim 1$ might not be verified during all the Blandford & McKee stage for low baryon loading parameter values and since we are not using the original Blandford & McKee law $\gamma_{los}(T) \propto R_{los}(T)^{-3/2}$ but a slightly modified one, we will not have a perfectly constant $F_{tot}(T)$ during the Blandford & McKee stage. Calculation shows a very slow growth of about the 5%. We will then choose as normalization constant F_{max} the value of $F_{tot}(T)$ at the beginning of the Blandford & McKee stage, i.e. at $T = T_0(0) = t_0 - \frac{R_0}{c} + \frac{r_i}{c}$. In this way we have again an unambiguously determined baryon loading parameter dependent constant.

In conclusion, we are going to use as normalization constant for light curves and spectra the quantity

$$F_{max} = \frac{1}{8} F_{tot}(T_d(0)) \tag{3.166}$$

that is

$$F_{max} = 0.88 \frac{4(p-1)}{3p-1} \frac{64}{27} \frac{n_i \sigma_T}{D^2} \frac{m_e c^2}{e} \sqrt{\frac{\epsilon_B}{8\pi}} \frac{\beta_m(T_d(0))^2 R_{los}(T_d(0))^3 \sqrt{e'_{los}(T_d(0))}}{\gamma_{los}(T_d(0))^3 (1-\beta_{los}(T_d(0)))^2} \frac{1}{8} \tag{3.167}$$

where the factor $\frac{1}{8}$ has been added to improve the fit with the true peak heights of numerically calculated monochromatic afterglow light curves that actually peak during the Blandford & McKee stage.

For η decreasing from 300 to 3 our F_{max} decreases of about 4% and we can write

$$F_{max}(\eta) = 372.6 \times \left(\frac{E_T}{10^{52}}\right) \epsilon_B^{1/2} n_i^{1/2} \left(\frac{D}{10^{28}}\right)^{-2} f(\eta) \text{ mJy} \tag{3.168}$$

where the total energy E_T is measured in ergs, the distance D is measured in cm and the adimensional function $f(\eta)$ is plotted in fig. 3.7. Our flux normalization is about 5 times greater than the one used in [Granot, Piran & Sari 1999c]. This difference is due to the modified hydrodynamical evolution we adopt during the Blandford & McKee stage.

Recall that for comparison with observed afterglows as distance D the luminosity distance value should be used and a redshift factor $(1+z)$ should be added to (3.168).

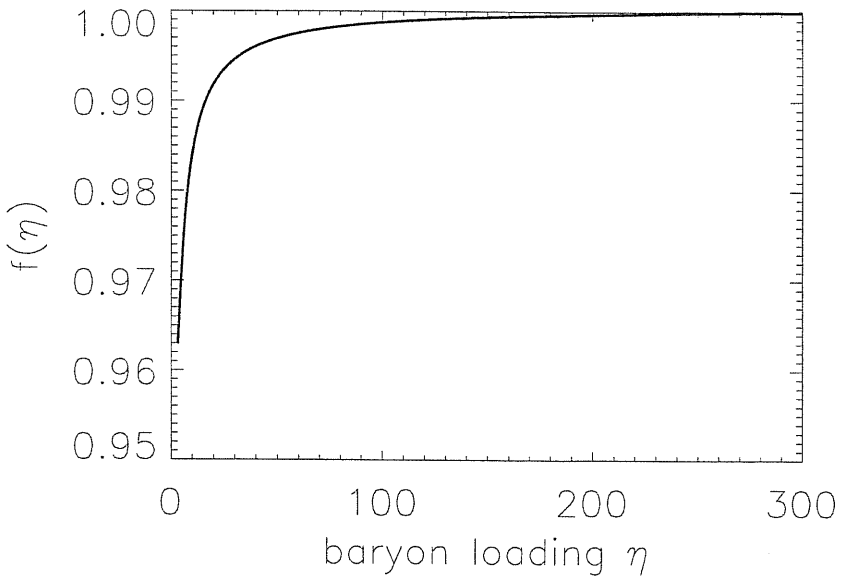

Figure 3.7: Plot of the function used in (3.168)

3.6.7 Self–similarity of afterglow light curve/spectrum

Before ending the chapter note that if the afterglow spectrum at the time T peaks at a frequency strictly proportional to $\nu_m(T)$ given by (3.156), then the monochromatic light curve at the generic frequency ν is expected to peak at a time $T_{peak}(\nu)$ such that $\nu/\nu_m(T_{peak}) = constant$ (i.e. independent on ν). Moreover, for a peak occurring during the Blandford & McKee stage we expect that also the quantity $F_\nu(T_{peak})/F_{max}$ does not depend on ν.

As have been noted by Granot, when electron cooling is completely neglected, during the Blandford & McKee stage it is possible to define a self–similar variable

$$\phi(\nu, T) = \frac{\nu}{\nu_m(T)} \tag{3.169}$$

and a universal function $f(\phi)$ with a peak at $\phi_{peak} \sim 2$ such that $f\left(\phi(\nu, T)\right) = \frac{F_\nu(T)}{F_{max}}$. The function $f(\phi)$ will represent both an afterglow spectrum at a fixed time and an afterglow monochromatic light curve at a fixed frequency.

The function ϕ that Granot defines will be called hereafter ϕ_{granot} and is strictly proportional to $\nu\ T^{-3/2}$. Actually the definition (3.169) gives exactly this result in the ultra relativistic limit (corresponding to high baryon loading parameter values)

with a perfect Blandford & McKee evolution. We prefer to adopt (3.169) instead of Granot definition to be consistent with the deviations introduced by our generalization of the evolution laws. The function $f(\phi)$ required to describe afterglow light curves and spectra will be such that $f(\phi) \propto \phi^{1/3}$ for $\phi \ll \phi_{peak}$ and that $f(\phi) \propto \phi^{-(p-1)/2}$ for $\phi \gg \phi_{peak}$ also for us (see section 5.2, and in particular function $F_\nu^{app}(T)$ defined by (5.17)). However, the self–similarity property of afterglow light curve/spectrum is expected to hold only during the Blandford & McKee stage. In particular, the peak time $T_{peak}(\nu)$ is expected to satisfy the condition $\phi(\nu, T_{peak}(\nu)) = constant = 2$ only if belonging to the Blandford & McKee stage. Light curves peaking before or after such a stage may have "unusual" peak times or profiles, and it would be interesting to investigate how evident are such effects and if they could be observed.

Finally, when we stop neglecting electron cooling, we have two characteristic frequencies to deal with (see section 5.2) and the study of Blandford & McKee afterglows self–similar properties is no longer useful.

3.7 Radiation emitted by the shocked matter

We have already said that the most likely radiation process in GRB afterglows is synchrotron emission from relativistic electrons accelerated at the shocks.

The parameters that determine synchrotron emission from a shocked plasma are the emitting electrons energy distribution and the magnetic field strength.

For all known astrophysical sources that are believed to emit synchrotron radiation, a power law distribution for the emitting electrons energy provides a good fit to the observed spectra, and this is true for afterglow spectra as well. Also theoretical studies suggest that the most reasonable energy distribution expected for charged particles accelerated at shocks is a power law [Draine & McKee 1993]. The range, slope and normalization of this power law should in principle be extracted by the microscopic physical processes that take place at the shock and compared to the corresponding observed values to test the acceleration process theory, but astrophysicists usually prefer to assume them as free parameters and constrain them through observations because, unfortunately, the acceleration process theory itself is somewhat incomplete.

Another parameter that is usually left free in modeling a shocked plasma is the degree of amplification of the ambient magnetic field at the shock, likely due to turbulence in the plasma.

Now I am going to describe the current view on the microscopic strûcture and composition of a shocked astrophysical plasma.

Then I will introduce the mathematical formalism required for detailed calculation of the synchrotron total power and spectrum emitted by an element of shocked plasma.

3.7.1 Particle acceleration at shocks

Many astrophysical plasmas are so rarefied that the particle mean free path is too large to allow energy dissipation through collisions at a shock. The free path for a proton in the solar wind, for example, is larger than the distance of the earth from the sun [Longair 1981, Draine & McKee 1993]. For this reason, shocks that are relevant in an astrophysical context are collisionless shocks, i.e. shocks where the plasma is heated and compressed in a very thin transition layer via the interaction with electromagnetic fields due to collective motions of the charged particles. Actually collisionless shocks are expected to compress and amplify seed magnetic fields too.

Collisionless shocks are observed in nature. The best known example is the bow

shock between the solar wind and the earth magnetosphere, that is a stationary shock. It is so close to us that we can even send instruments and perform direct measures on it. Moreover, many planets and satellites in the solar system show similar bow shocks. Other widely accepted examples of collisionless shocks are the forward and reverse shocks in galactic Supernova remnants, that are non relativistically expanding shocks. Such shocks are clearly visible in many shell remnant images at different wavelengths. On the contrary, relativistic shocks (collisionless or not) have not been directly observed yet. We have only indirect evidences of their existence in nature.

In what follows I will outline the physical principles underlying our theoretical understanding of collisionless shocks.

At a collisionless shock, the particle heating process being electromagnetic, incoming protons and electrons feel the same forces, so electrons, that are significantly lighter than protons, are accelerated to a larger extent. Since accelerated charged particles radiate proportionally to the fourth power of their acceleration, electrons immediately loose almost all the energy that the shock gives them, unlike protons. After escaping the shock, the still cold shocked electrons actually heat a bit more in collisions with the hot shocked protons, but equipartition is not reached because of the very low rate of encounters due to the plasma low density.

Then, electrons and protons in the shocked plasma are expected to be thermal but at substantially different temperatures.

Anyway, because of their low mass, electrons are faster than protons, and in particular a small fraction of them, the fraction living in the high energy tail of the Maxwell–Boltzmann energy distribution, has a thermal velocity greatly higher than the average one. Since the cross section for scattering is inversely proportional to the squared velocity of the particle, those highest velocity electrons in the shocked plasma that are occasionally scattered back toward the shock can travel freely such a long distance that can eventually cross the shock before being scattered back again. These fast electrons that go up and down the stream many times gain energy at each shock re-crossing via the Fermi acceleration process [Protheroe 1998, Gallant, Achterberg & Kirk 1999a]. They quickly form a second population of **non–thermal high energy electrons** with a power low energy distribution, which is expected to emit radiation mainly via synchrotron cooling because of the presence of the magnetic field in the plasma. The thermal electron population is expected to emit radiation but mainly via thermal bremsstrahlung process.

The total internal energy density of the shocked plasma e' can be expressed as the

sum of the protons thermal energy density e'_p and the electrons energy density e'_e. The latter can be further split up into the sum of the thermal electrons energy density $e'_{e,th}$ and the non thermal electrons energy density $e'_{e,non-th}$. All these quantities are measured in the shocked fluid comoving frame. Another component of the comoving internal energy density of the plasma to be accounted for is the the magnetic energy density e'_B, but for the moment we will neglect it basing on the fact that it is expected to be a smaller component.

Despite of the Fermi acceleration process, that helps enhancing the electrons energy, equipartition between electrons and protons is hardly reached and the electrons energy density e'_e is expected to be a fraction $\epsilon_e < 0.5$ of e'. So we will always write

$$e'_e = \epsilon_e e' \tag{3.170}$$

with

$$e'_e = e'_{e,non-th} + e'_{e,th} \tag{3.171}$$

Behind a **non relativistic collisionless shock** non–thermal electrons, i.e. Fermi accelerated electrons, are actually not the bulk of the electron population. In this case thermal electrons are much more numerous than the non–thermal ones and

$$e'_{e,th} \sim e'_e = \epsilon_e e'$$

Measures of particle temperatures behind terrestrial bow shocks and observations of the other bow shocks in the solar system tell us that for non relativistic shocks $\epsilon_e \lesssim 0.1$ [Schwartz, Thomsen, Bame & Stansberry 1988] and the ϵ_e value is lower for stronger shocks. Observations of the X–ray emission of some Supernova remnants tell us that behind a non relativistic strong shock the non–thermal electrons take with them an energy density $e'_{e,non-th}$ that is only a fraction $\zeta \lesssim 0.1$ of the thermal electrons energy density $e'_{e,th}$.

Then, the plasma shocked by a non relativistic collisionless shock is thought to be composed of a population of thermal protons, an extended population of thermal electrons at a temperature lower than the protons such that $e'_{e,th} \sim e'_e = \epsilon_e e'$ with $\epsilon_e \sim 0.1$, and a restricted population of non–thermal electrons generated via Fermi acceleration processes (that is the one we are interested in) such that $e'_{e,non-th} = \zeta e'_{e,th} \sim \zeta \epsilon_e e'$ with $\zeta \sim 0.1$.

As far as **ultra–relativistic collisionless shocks** are concerned, no direct measures of post–shock temperatures and densities have been possible yet and only rough

theoretical predictions are at disposal. What is known is that the average electron energy increase $< \Delta E >$ at each shock crossing from downstream to upstream, is greater in the case of a relativistic shock than in the case of a non relativistic shock. The Fermi process theory states that for an electron of energy E, $\frac{<\Delta E>}{E} \sim \frac{v_s}{c}$ if $v_s \ll c$ [Protheroe 1998] while $\frac{<\Delta E>}{E} \sim 2$ if $\gamma_s \gg 1$ [Gallant, Achterberg & Kirk 1999a]. Then, non relativistic shocks accelerate electrons through many small kicks (the process is slow and continuous, and only the electrons that do many crossing/re-crossing of the shock front definitely leave the thermal population) while relativistic shocks accelerate electrons through few big kicks (the process is fast and more efficient and a greater number of thermal electrons enter the non thermal population as a few crossing/re-crossing are enough to have an energy substantially greater than the average). When the shock is ultra–relativistic we expect the number of non thermal electrons to enhance at the expense of the number of thermal electrons and the Fermi accelerated electrons to become the bulk population. We expect $e'_{e,non-th}$ to be much greater than $e'_{e,th}$ and almost equal to the total electron energy density e'_e, which is supposed to be approximately the same fraction of the total internal energy density of the shocked fluid e' as in the non relativistic shock case (i. e. about 10%).

The plasma shocked by an ultra–relativistic shock can then be roughly described as a two component fluid, made of a population of thermal protons and a population of non thermal electrons whose energy density is given by

$$e'_{e,non-th} \sim e'_e = \epsilon_e e'$$

with $\epsilon_e \sim 0.1$.

In the case of non relativistic collisionless shock as well as in the case of ultra–relativistic collisionless shocks, we expect the non–thermal electrons to have a power law energy distribution and we prefer to assume the power law range, slope and normalization as free parameters to be constrained through observations rather than deducing their values by the microscopic physical process acting at the shock with aim at comparing them with the observations to test the physical acceleration process theory.

In our fireball evolution the forward shock gradually slows down from ultra relativistic velocities to non relativistic ones. We should take in account that at the shock derelativization the post-shock energy density of accelerated electrons is expected to become a lower fraction of the fluid internal energy density, passing from $e'_{e,non-th} \sim \epsilon_e e'$ with $\epsilon_e \sim 0.1$ when $\gamma_s \gg 1$ to $e'_{e,non-th} \sim \zeta \epsilon_e e'$ with $\zeta \sim \epsilon_e \sim 0.1$ when $\gamma_s \sim 1$ but we prefer to neglect this effect because it would complicate too much the calculation.

Thus, we will assume that just behind the shock

$$e'_{e,non-th} \sim e'_e = \epsilon_e e'$$

with a constant $\epsilon_e \sim 0.1$ during all the fireball evolution.

Before ending the section remember that the protons temperature just behind the shock can be estimated as (see section 3.3)

$$kT_p \sim (\hat{\gamma} - 1)\frac{e'_p}{n'} \sim (\hat{\gamma} - 1)\frac{e'}{n'} \sim (\hat{\gamma} - 1)m_p c^2(\gamma_s - 1) \tag{3.172}$$

that is

$$T_p \sim 10^{13}(\gamma_s - 1) \text{ K} \tag{3.173}$$

3.7.2 The post–shock electron distribution

As astrophysicists usually do, we will assume that electrons accelerated via Fermi acceleration processes just behind a planar shock traveling in a uniform medium have the following power law distribution:

$$dN = N(\gamma_e)d\gamma_e = N_e\gamma_e^{-p}d\gamma_e \tag{3.174}$$

Here dN represents the number of shock accelerated electrons per unit volume with Lorentz factor between γ_e and$\gamma_e + d\gamma_e$, $p > 0$ is the slope of the distribution and γ_e varies between $\gamma_{e,min}$ and $\gamma_{e,max}$.

The existence of an upper limit for the velocity that accelerated electrons can reach is quite reasonable. The maximum energy electrons can acquire via shock acceleration is limited by synchrotron losses occurring during the acceleration process itself [Piran 1999]. Other limits on the maximum energy are placed by the dimensions of the acceleration region and the time available for acceleration. In realistic cases $\gamma_{e,max}$ is so high as compared to $\gamma_{e,min}$ that in first approximation we can use $\gamma_{e,max} = +\infty$ in all calculations. This is what has been assumed in all previous works and we will assume it as well. In addition, we anticipate that a realistic standard value for p is about 2.5.

The normalization factor N_e in (3.7.2) is to be determined in such a way that the integral of $N(\gamma_e)$ over the range $[\gamma_{e,min}, +\infty]$ gives exactly the total number of shock accelerated electrons per unit volume in the shocked plasma, n'_e. Then we have the relation

$$n'_e = \int_{\gamma_{e,min}}^{+\infty} N_e\gamma_e^{-p}d\gamma_e = \frac{N_e}{(p-1)}\gamma_{e,min}^{1-p} \tag{3.175}$$

Note that we must assume $p > 1$ if we want the right hand side in (3.175) to be finite.

As we stated in section 3.7.1, in the case of an **ultra–relativistic collisionless shock** the shock accelerated electrons are the bulk of the electron population in the shocked plasma, and the total number of electrons per unit volume is always expected to be equal to the total number of protons per unit volume in the shocked plasma n' because of plasma charge neutrality, so $n'_e \sim n'$.

In the case of a **non relativistic collisionless shock** the bulk electron population is made of thermal electrons, and we do not know exactly the number per unit volume of shock accelerated electrons. It will be only a fraction of n'. This would lead to the introduction of a new free parameter representing this fraction. We might infer it from the observations of Supernova remnants shocks, but we prefer not to introduce it and to assume $n'_e \sim n'$ also for marginally relativistic and non relativistic shocks.

Another important relation to be satisfied is the following: the total energy per unit volume of shock accelerated electrons, e'_e, must be equal to the integral of $N(\gamma_e)\gamma_e$ over the range $[\gamma_{e,min}, +\infty]$. Thus we must have

$$e'_e = \int_{\gamma_{e,min}}^{+\infty} N_e \gamma_e^{1-p} m_e c^2 d\gamma_e = \frac{N_e}{(p-2)} m_e c^2 \gamma_{e,min}^{2-p} \tag{3.176}$$

We see again that in order to have a finite value of the right hand side we have to use only p values greater that 2.

We have already said in section 3.7.1 that e'_e is expected to be a fraction of the total internal energy per unit volume of the shocked plasma e', i.e. $e'_e = \epsilon_e e'$. The coefficient ϵ_e, like the slope of the electron energy distribution, cannot be reliably predicted by the microscopic processes and is left as a constant free parameter neglecting the fact that it would be lower for the non relativistic shocks than for the ultra relativistic ones (by up to a factor 10). A realistic value for ϵ_e in the ultra–relativistic case is about 0.1.

At this point note that the average Lorentz factor of shocked electrons $< \gamma_e >$ can be calculated as follows

$$< \gamma_e >= \frac{\int_{\gamma_{e,min}}^{+\infty} N_e \gamma_e^{-p} \gamma_e d\gamma_e}{\int_{\gamma_{e,min}}^{+\infty} N_e \gamma_e^{-p} d\gamma_e} = \frac{1}{m_e c^2} \epsilon_e \left(\frac{e'}{n'}\right) \tag{3.177}$$

Thus, combining (3.177) with the ration of (3.175) and (3.176)

$$< \gamma_e >= \gamma_{e,min} \frac{(p-1)}{(p-2)} \tag{3.178}$$

This means that in all cases the bulk of the electron population has a Lorentz factor roughly equal to the minimum one. The acceleration process produces an almost mono

energetic population of shocked electrons. The high energy electrons are very few and whatever approximation we make about the upper limit to the energy range is surely not important. A very rough approximation could be treating all shocked electrons as having the same Lorentz factor $\gamma_{e,min}$ but randomly distributed directions of motion.

Finally, we know that the comoving proton number density and energy density of the shocked matter, n' and e', are completely determined by the comoving properties of the unshocked matter and by the shock Lorentz factor Γ_s through the jump conditions (3.17), (3.18) and (3.19). Thus we can conclude that, once p and ϵ_e are fixed, $\gamma_{e,min}$, N_e and $< \gamma_e >$ are completely determined by the shock Lorentz factor Γ_s, the unshocked particle density n_i and the shocked matter adiabatic index $\hat{\gamma}$. We get

$$\gamma_{e,min} = \frac{(p-2)}{(p-1)} \epsilon_e \frac{m_p}{m_e}(\gamma_s - 1) \tag{3.179}$$

$$< \gamma_e >= \epsilon_e \frac{m_p}{m_e}(\gamma_s - 1) \tag{3.180}$$

$$N_e = (p-1) n' \gamma_{e,min}^{p-1} \tag{3.181}$$

where

$$n' = n_i \frac{(\hat{\gamma}\gamma_s + 1)}{(\hat{\gamma} - 1)} \tag{3.182}$$

and the post shock Lorentz factor γ_s satisfies

$$\Gamma_s = \sqrt{\frac{(\gamma_s + 1)\left(\hat{\gamma}(\gamma_s - 1) + 1\right)^2}{\hat{\gamma}(2 - \hat{\gamma})(\gamma_s - 1) + 2}} \tag{3.183}$$

In the particular case of a strong relativistic shock with $\Gamma_s \gg 1$ the above formulae must reduce to the standard ones used for example by [Granot, Piran & Sari 1999a]. First of all we have

$$n' \sim 2\sqrt{2}\Gamma_s n_i, \qquad e' \sim 2\Gamma_s^2 m_p c^2 n_i, \qquad \Gamma_s = \sqrt{2}\gamma_s$$

(see appendix A). Then we get

$$\gamma_{e,min} = \epsilon_e \frac{(p-2)}{(p-1)} \frac{m_p}{m_e} \gamma_s \tag{3.184}$$

$$< \gamma_e >= \epsilon_e \frac{m_p}{m_e} \gamma_s \tag{3.185}$$

Note that if $\Gamma_s \sim 100$, $p = 2.5$ and $\epsilon_e = 0.1$ then $\gamma_{e,min} \sim 4 \times 10^3$.

The definitions (3.179) and (3.180) have a serious problem when the value of γ_s decreases too much: $\gamma_{e,min}$ and $< \gamma_e >$ become lower than 1, and this is not acceptable

for a Lorentz factor! To solve the problem we must find a generalized definition for $\gamma_{e,min}$ and $< \gamma_e >$ that reduce respectively to (3.179) and (3.180) when $\gamma_s \gg 1$ but never give unphysical values for $\gamma_{e,min}$ and $< \gamma_e >$ when $\gamma_s \to 1$.

A way to generalize (3.179) and (3.180) is recalling that, to be precise, particle shock acceleration produces a non thermal electron population with power law distributed *momentum*. In case of ultra relativistic shock, all the accelerated electrons are ultra relativistic as well, their momentum p_e is almost directly proportional to their energy because the relation $p_e c \sim \gamma_e m_e c^2$ holds, and a power law in momentum roughly corresponds to a power law in energy and/or Lorentz factor. The approximation that the newly shocked electrons follow a power law energy distribution is very good for ultra relativistic shocks, and is not that bad even for non relativistic shocks, but the use of the true electron distribution (i.e. that corresponding to a power law for the momentum) in the ultra relativistic limit leads to slightly different estimates of $\gamma_{e,min}$, $< \gamma_e >$ and N_e more convenient for a generalization to the non relativistic case.

Let us assume the shock accelerated electron distribution to be

$$N_{p_e}(p_e) = K_p p_e^{-\delta}, \qquad p_e > p_{e,min} \tag{3.186}$$

The electron momentum p_e is related to the electron energy by the relation

$$\gamma_e m_e c^2 = \sqrt{p_e^2 c^2 + m_e^2 c^4} = m_e c^2 \sqrt{1 + \frac{p_e^2}{m_e^2 c^2}} \tag{3.187}$$

and the fluid element electron number density and energy density are given by

$$n'_e = \int_{p_{e,min}}^{+\infty} N_{p_e}(p_e) 4\pi p_e^2 dp_e = 4\pi K_p \int_{p_{e,min}}^{+\infty} p_e^{2-\delta} dp_e = 4\pi K_p \frac{p_{e,min}^{3-\delta}}{\delta - 3} \tag{3.188}$$

$$\begin{aligned} e'_e &= \int_{p_{e,min}}^{+\infty} N_{p_e}(p_e) m_e c^2 \sqrt{1 + \frac{p_e^2}{m_e^2 c^2}} 4\pi p_e^2 dp_e = \\ &= 4\pi K_p m_e c^2 \int_{p_{e,min}}^{+\infty} p_e^{2-\delta} \sqrt{1 + \frac{p_e^2}{m_e^2 c^2}}\, dp_e \end{aligned} \tag{3.189}$$

In writing (3.189) we are making the approximation that the electrons are always so relativistic that their internal energy e'_e is almost equal to the total energy.

The energy distribution corresponding to (3.186) will be $N(\gamma_e)$ such that

$$N(\gamma_e) d\gamma_e = N_{p_e}(p_e) 4\pi p_e^2 dp_e \tag{3.190}$$

Using (3.186) and (3.187) we can conclude that

$$N(\gamma_e) = 4\pi K_p (m_e c)^{3-\delta} \gamma_e \left(\gamma_e^2 - 1\right)^{\frac{1-\delta}{2}}, \qquad \gamma_e > \gamma_{e,min} = \sqrt{1 + \frac{p_{e,min}}{m_e c}} \tag{3.191}$$

The true energy distribution (3.191) reduces to $N(\gamma_e) = N_e \gamma_e^{-p}$ in the ultra relativistic limit if we define

$$K_p = \frac{N_e}{4\pi} (m_e c)^{\delta-3}, \qquad \delta = p + 2 \tag{3.192}$$

In the ultra relativistic limit we can also assume $\frac{p_e}{m_e c} \gg 1$ and approximate (3.189) as follows

$$e'_e = 4\pi K_p c \int_{p_{e,min}}^{+\infty} p_e^{3-\delta} dp_e = 4\pi K_p \, c \, \frac{p_{e,min}^{4-\delta}}{\delta - 4} \tag{3.193}$$

Note that being $p > 2$ we are guaranteed that $\delta > 4$.

At this point the ratio of (3.193) and (3.188) gives us

$$p_{e,min} = \frac{\delta - 4}{\delta - 3} \frac{e'_e}{n'_e} \frac{1}{c} = \frac{p-2}{p-1} \frac{e'}{n'} \frac{\epsilon_e}{c} \tag{3.194}$$

and consequently

$$\gamma_{e,min} = \sqrt{1 + \left[\frac{p-2}{p-1} \left(\frac{e'}{n'}\right) \frac{\epsilon_e}{m_e c^2}\right]^2} \tag{3.195}$$

$$N_e = 4\pi K_p (m_e c)^{3-\delta} = (\delta - 3) n' p_{e,min}^{\delta-3} (m_e c)^{3-\delta} = (p-1) n' \left(\gamma_{e,min}^2 - 1\right)^{\frac{p-1}{2}} \tag{3.196}$$

Moreover we can calculate

$$< p_e >= \frac{\int_{p_{e,min}}^{+\infty} N_{p_e}(p_e) p_e 4\pi p_e^2 dp_e}{n'_e} = 4\pi K_p \frac{p_{e,min}^{4-\delta}}{\delta - 4} \frac{\delta - 3}{p_{e,min}^{3-\delta}} \frac{1}{4\pi K_p} \tag{3.197}$$

so

$$< p_e >= \frac{p-1}{p-2} p_{e,min} = \left(\frac{e'}{n'}\right) \frac{\epsilon_e}{c} \tag{3.198}$$

and then

$$< \gamma_e >= \sqrt{1 + \left[\left(\frac{e'}{n'}\right) \frac{\epsilon_e}{m_e c^2}\right]^2} \tag{3.199}$$

Finally we can use the definitions of n' and e' in terms of the post–shock Lorentz factor and conclude

$$\gamma_{e,min} = \sqrt{1 + \left[\frac{p-2}{p-1} \epsilon_e \frac{m_p}{m_e} (\gamma_s - 1)\right]^2} \tag{3.200}$$

$$< \gamma_e >= \sqrt{1 + \left[\epsilon_e \frac{m_p}{m_e} (\gamma_s - 1)\right]^2} \tag{3.201}$$

$$N_e = (p-1) n' (\gamma_{e,min}^2 - 1)^{\frac{p-1}{2}} \tag{3.202}$$

As we have anticipated, the definitions (3.200), (3.201) and (3.202) are generalizations of (3.179), (3.180) and (3.181) respectively having the same ultra relativistic limit, but never leading to unphysical values in the non relativistic regime. So we will prefer to use the power law electron energy distribution $N(\gamma_e) = N_e \gamma_e^{-p}$ for $\gamma_e > \gamma_{e,min}$ with N_e, $\gamma_{e,min}$ and $< \gamma_e >$ defined through (3.202), (3.200) and (3.201).

3.7.3 Magnetic field strength and orientation in a shocked plasma

Another important topic is equipartition of energy between magnetic field and particles in the shocked plasma.

If we assume that the cold and uniform unshocked medium is slightly magnetized, then we expect a shock to compress and amplify it. We expect that turbulent processes in the hot shocked plasma may further amplify the seed magnetic field after the shock compression, and randomize its orientation. Then, the magnetic energy density in the shocked plasma might be substantially higher than what expected as a result of pure compression of the frozen in field lines. The magnetic energy density enhancing should of course happen at the expense of the particle thermal energy because any turbulent process is expected to lead to equipartition of energy. Since relevant timescales for these turbulent processes might be too long as compared to the hydrodynamical timescale to guarantee perfect equipartition among the various forms of energy involved (particle thermal energy and magnetic energy), we expect the magnetic energy density behind the shock to be only a fraction of the internal energy density of the shocked plasma. This fraction could in principle be estimated theoretically, but we prefer, as usual, to leave it as a constant free parameter to be constrained by the observations. We will introduce the parameter ϵ_B and write

$$e'_B = \frac{B^2}{8\pi} = \epsilon_B e' \tag{3.203}$$

or equivalently

$$B = \sqrt{8\pi \epsilon_B e'} \tag{3.204}$$

A typical value for ϵ_B could be ~ 0.01.

Relation (3.204) can be used as a definition of the magnetic field strength in the newly shocked plasma. The hypothesis about the magnetic field orientation underlining (3.204) is that the magnetic field in the shocked plasma is completely tangled.

In order to give an idea of the order of magnitude of the post–shock magnetic field amplitude recall that if we assume, for instance, $e' = 2m_p c^2 \Gamma_s^2 n_i$ as it is in the case of a relativistic shock, then we can say that

$$B^2 = 16\pi \epsilon_B m_p c^2 \Gamma_s^2 n_i \tag{3.205}$$

and if $\Gamma_s \sim 100$, $\epsilon_B \sim 0.01$ and $n_i \sim 1$ cm^{-3} then $B \sim 3$ Gauss.

Note that the turbulent magnetic field amplification process is expected to act everywhere in the shocked plasma, not only just behind the shock. It requires only the existence of a seed magnetic field to amplify. So, we can in principle use the relation (3.204) to define the magnetic field everywhere within the fireball, regardless of what the external magnetic field were. The parameter ϵ_B is assumed to be a universal one, though it might depend in principle on the shock Lorentz factor and the time elapsed from the shock passage. Anyway we want to explore also the alternative case in which turbulent processes are no longer efficient far from the shock and the magnetic field generated at the shock with the strength (3.204) subsequently evolves as a frozen in magnetic field conserving the magnetic flux. In this alternative case we will use (3.204) only for the magnetic field B_s just behind the shock and then assume

$$B = B_s \left(\frac{n'}{n'_s} \right)^{2/3} \tag{3.206}$$

elsewhere. Here quantities with the subscript s regard the fluid element just behind the shock and the corresponding quantities without the subscript s are the ones characterizing the fluid element at later times or a fluid element far from the shock.

So we can conclude that strictly speaking the equipartition relations (3.170) and (3.204) can be applied only to matter immediately behind the shock. In the case of an expanding fireball whose internal density, pressure and energy density profiles are given by the fireball hydrodynamic evolution, it is not known whether equations (3.170) and (3.204) are valid throughout the fireball volume and whether ϵ_e and ϵ_B are universal constants.

We are going to test two different assumptions about the magnetic field strength: *(i)* the definition (3.204) is valid at any time throughout the fireball volume with a universal ϵ_B and *(ii)* the definition (3.204) is valid only for newly shocked matter and after the shock passage the magnetic field evolves conserving the magnetic flux, i.e. according to (3.206).

On the contrary, in the general case the relation (3.170) will always be used only for newly shocked matter, but with a universal value of ϵ_e. The electron energy density

long after the shock passage will be determined according to the evolution of the initial electron energy distribution due to synchrotron radiation losses and volume expansion. Doing this we are neglecting any other possible electron heating process but the acceleration at the shock.

We will use the relation (3.170) at any time throughout the fireball volume with a universal ϵ_e, together with the hypothesis that the electron energy distribution is always a power law up to arbitrarily high γ at any time throughout the fireball volume only to reproduce Granot's results.

3.7.4 The evolution of the shocked electrons energy distribution

For the reasons we have explained in section 3.7.1 the electron energy distribution in a fluid element of shocked matter immediately after the shock passage (i.e. at the time $t' = 0$ of a comoving observer) is expected to be the power law (3.174). The range and normalization of (3.174) are $(\gamma_{e,min}(0), +\infty)$ and $N_e(0)$ such that

$$\gamma_{e,min}(0) = \sqrt{1 + \left[\frac{(p-2)}{(p-1)}\frac{1}{m_e c^2}\left(\frac{e'_e}{n'_e}\right)\right]^2} \tag{3.207}$$

$$N_e(0) = (p-1)n'_e(0)(\gamma_{e,min}(0)^2 - 1)^{\frac{p-1}{2}} \tag{3.208}$$

where we assume $n'_e(0) = n'(0)$ and $e'_e(0) = \epsilon_e e'(0)$ regardless of the shock velocity. The exact expressions for $n'(0)$ and $e'(0)$ depend on the shock velocity and on the external particle density as prescribed by the generalized jump conditions at a shock presented in section 3.3. In principle the parameter ϵ_e ought to be different for relativistic and non relativistic shocks (much lower in the latter case, see discussion in section 3.7.1), but we will neglect this effect and use always the same value for ϵ_e. The same problem would exist for the relation $n'_e(0) = n'(0)$, which ought not to be used in the case of non relativistic shocks, since the non–thermal electrons are only a fraction of the total in that case, but we will assume it all the same.

Since the electron acceleration timescale is short compared to the hydrodynamical timescale, it is reasonable to think that the power law of electrons (3.174) with the range and normalization (3.207) and (3.208) is instantaneously injected in the fluid element at the shock passage and left there to radiate and cool afterwards.

If the comoving observer looks at the electron energy distribution a given time interval t' after the shock passage, he will see only those electrons whose cooling time was longer than t'. Moreover he will see even the "survived" electrons having an energy slightly different than the initial one because of radiation losses. If the fluid element is also expanding adiabatically, the adiabatic cooling of the shocked matter will affect the electron energy distribution too.

The right formalism to calculate the evolution of an injected electron energy distribution by taking in account the most important energy loss processes, adiabatic cooling included, is discussed in appendix E. Over there we show also that the dominating radiation process in our case is synchrotron radiation and diffusion of shocked accelerated electrons to adjacent fluid elements can be neglected.

Now I only stress that the energy distribution per unit volume $N(\gamma_e, t')$ of the electron population in the shocked matter must always be a function such that the comoving number density of electrons at the comoving time t' is given by

$$n'_e(t') = \int_{\gamma_{e,min}(t')}^{\gamma_{e,max}(t')} N(\gamma_e, t') d\gamma_e \tag{3.209}$$

and the comoving energy density of electrons at the comoving time t' is given by

$$e'_e(t') = \int_{\gamma_{e,min}(t')}^{\gamma_{e,max}(t')} \gamma_e N(\gamma_e, t') d\gamma_e \tag{3.210}$$

where we must have $n'_e(t') = n'(t')$ at any time after the shock passage in order to guarantee charge neutrality but we do not expect any longer $e'_e(t') = \epsilon_e e'(t')$ after the shock passage.

The electron energy distribution $N(\gamma_e, t')$ is simply related to the corresponding distribution $N_E(E, t')$ introduced in appendix E by the relation

$$N(\gamma_e, t') = N_E(\gamma_e m_e c^2, t') m_e c^2 \tag{3.211}$$

The time of the shock passage in the comoving frame will be $t' = 0$. So, the assumption that a power law distributed electron population is injected instantaneously at the shock passage corresponds to the following initial condition for the electron energy distribution

$$N(\gamma_e, 0) = N_e(0) \gamma_e^{-p} \quad \text{for} \quad \gamma_e > \gamma_{e,min}(0) \tag{3.212}$$

with $N_e(0)$ and $\gamma_{e,min}(0)$ given by (3.208) and (3.207), or equivalently

$$N_E(E, 0) = K(0) E^{-p} \quad \text{for} \quad E > E_{min}(0) \tag{3.213}$$

with $K(0) = N_e(0)(m_e c^2)^{p-1}$ and $E_{min}(0) = \gamma_{e,min}(0) m_e c^2$.

If we assume that the injected power law of electrons radiates mainly via synchrotron radiation and is affected by adiabatic energy losses, we find (see again appendix E) that at the generic time t' the distribution of the emitting electrons is

$$N(\gamma_e, t') = \begin{cases} \frac{N_e(t')\gamma_e^{-p} G(t')}{[G(t') - a m_e c^2 H^2(t')]^{2-p}} & \gamma_{e,min}(t') < \gamma_e < \gamma_{e,max}(t') \\ 0 & \gamma_e < \gamma_{e,min}(t') \text{ or } \gamma_e > \gamma_{e,max}(t') \end{cases} \tag{3.214}$$

with

$$\gamma_{e,min}(t') = \frac{\gamma_{e,min}(0) G(t')}{1 + a m_e c^2 \gamma_{e,min}(0) H^2(t')} \tag{3.215}$$

$$\gamma_{e,max}(t') = \frac{G(t')}{a m_e c^2 H^2(t')} \tag{3.216}$$

and

$$N_e(t') = (p-1) n'_f(t') (\gamma_{e,min}(0)^2 - 1)^{\frac{p-1}{2}} \tag{3.217}$$

and where

$$a = \frac{4}{3} \frac{\sigma_T c}{(m_e c^2)^2} \frac{1}{8\pi} \tag{3.218}$$

$$G(t') = e^{-\int_0^{t'} g(x) dx} \tag{3.219}$$

$$H^2(t') = \int_0^{t'} G(s) B^2(s) ds \tag{3.220}$$

$$B(t')^2 = 8\pi \epsilon_B e'_f(t') \quad or \quad B(t')^2 = 8\pi \epsilon_B e'(0) \left(\frac{n'_f(t')}{n'(0)} \right)^{\frac{4}{3}} \tag{3.221}$$

$$g(t') = \frac{1}{3} (\nabla \cdot \mathbf{v}_f)(t') \tag{3.222}$$

The functions $e'_f(t')$, $n'_f(t')$ and $\mathbf{v}_f(t')$ are the comoving energy density, the comoving particle density and velocity of the fluid element we are considering, and they actually vary with the comoving time.

In order to say what exactly $e'_f(t')$, $n'_f(t')$ and $\mathbf{v}_f(t')$ are, we recall that the distribution of matter behind the shock is known through the functions $e'(t,x)$, $n'(t,x)$, and $\gamma(t,x)$ where t is the coordinate time of the lab frame (not the comoving observer time) and x is the radial coordinate, spanning from 0 to 1, that gives the position of the fluid element behind the shock relative to the shock radius, i.e. $x = \frac{r}{R_s(t)}$ with r radial coordinate of the polar coordinate system in the lab frame. Any fluid element

of shocked matter will "move" through the space according to an $r_f(t)$ law, such that the shock passage occurs at the time t_s, i.e. $r_f(t_s) = R_s(t_s)$ and, at any t after t_s,

$$\frac{dr_f}{dt} = \left(1 - \frac{1}{\gamma^2(t, r_f(t)/R_s(t))}\right)^{1/2} c \tag{3.223}$$

Thus, the comoving time elapsed from the shock passage at the lab time t after t_s will be

$$t' = \int_{t_s}^{t} \frac{dz}{\gamma(z, r_f(z)/R_s(z))} \tag{3.224}$$

Finally we can say that

$$e'_f(t') = e'(t, r_f(t)/R_s(t)) \tag{3.225}$$

$$n'_f(t') = n'(t, r_f(t)/R_s(t)) \tag{3.226}$$

and

$$v_f(t') = \left(1 - \frac{1}{\gamma_f^2(t')}\right)^{1/2} c \tag{3.227}$$

with

$$\gamma_f(t') = \gamma(t, r_f(t)/R_s(t)) \tag{3.228}$$

where t is the coordinate time corresponding to the comoving time t' through the equation (3.224).

Before ending the section remember that the fluid velocity field in our shocked plasma is purely radial, so

$$g(t') = \frac{1}{3}\left(\nabla \cdot \mathbf{v}_f\right)(t') \sim \frac{v_f(t')}{r_f(t')}\gamma_f(t') \tag{3.229}$$

3.7.5 Synchrotron radiation from the shocked matter

We have seen in section 3.6.3 that in order to calculate the radiation seen by a distant observer at a given time T we must know the comoving monochromatic emissivity of the fluid, i.e. the function $j'(\nu', t, x)$ giving the power per unit volume, per unit solid angle and unit frequency emitted in the comoving frame by a fluid element located at $x = r/R_s(t)$ behind the shock front at the lab frame time t. Once we know this function, we can simply calculate the Equal-T surface at the time T and perform the numerical integration over the volume it surrounds using the formula (3.142).

If we assume that the shocked fluid emits only via synchrotron radiation, we can calculate the comoving monochromatic emissivity of a fluid element emitting from the

position r_{em} at the lab frame time t_{em}[¶] as

$$j'\left(\nu', t_{em}, \frac{r_{em}}{R_s(t_{em})}\right) = \int_{\gamma_{e,min}(t')}^{\gamma_{e,max}(t')} d\gamma_e N(\gamma_e, t') < P'_{\gamma_e}(\nu') > \tag{3.230}$$

where t' is the comoving time elapsed since the fluid element was shocked, $< P'_{\gamma_e}(\nu') >$ is the average single particle spectrum of synchrotron emission (see the exact definition (D.14) in appendix D) and $N(\gamma_e, t')$ is the evolved electron distribution (3.214) whose range $(\gamma_{e,min}(t'), \gamma_{e,max}(t'))$ is given by (3.215) and (3.216).

We have already explained that in order to find the right value of t' for our emitting element we must calculate the lab frame time t_s at which the fluid element was shocked and the evolution law of its position $r_f(t)$ during the time interval from t_s to t_{em}. After that we can define

$$t' = \int_{t_s}^{t_{em}} \frac{dt}{\gamma(t, x_f(t))} \tag{3.231}$$

where $x_f(t) = \frac{r_f(t)}{R_s(t)}$.

If we knew the time of shock passage t_s we might simply calculate the function $r_f(t)$ as the solution of the Cauchy problem

$$\frac{dr_f}{dt} = \left(1 - \frac{1}{\gamma^2(t, x_f(t))}\right)^{1/2} c, \qquad r_f(t_s) = R_s(t_s) \tag{3.232}$$

but unfortunately we do not know t_s. A way to calculate both t_s and $r_f(t)$ is solving analytically the Cauchy problem (3.232) leaving t_s as a free parameter and then find t_s as the solution of the equation

$$r_f(t_{em}) = r_{em} \tag{3.233}$$

This is actually what I have done, but the detailed calculation has been seriously complicated by the fact that the function $\gamma(t, x)$ has different analytical expressions in the different evolution stages. The way to deal with the actual function $\gamma(t, x)$ defined in section 3.5 will be illustrated below in section 3.8.1.

Now I only want to point out that the parameter $G(t')$ that characterize the electron distribution in the fluid element at the time of emission t_{em} can be calculated using the following relation

$$\ln G(t') = -\int_0^{t'} g'(s)ds = -\int_{t_s}^{t_{em}} \frac{v(t, x_f(t))}{r_f(t)} \gamma(t, x_f(t)) \frac{dt}{\gamma(t, x_f(t))} = \\ = -\int_{t_s}^{t_{em}} \frac{v(t, x_f(t))}{r_f(t)}\, dt \tag{3.234}$$

[¶]If the emitted radiation is to be observed at the time T then t_{em} and r_{em} must be related by the equation $t_{em} = T + \frac{r_{em}}{c}\cos\vartheta - \frac{r_i}{c}$. See section 3.6.1.

and the same change of variable can be used to calculate $H^2(t')$. Anyway in real calculation the value of $H^2(t')$ has been approximated as

$$H^2(t') \sim \frac{1}{2}(G(t')B^2(t') + B^2(0))t' \tag{3.235}$$

because precision on the value of H is less important than on the value of G.

3.8 The comoving time

In this section I am going to show the result of the calculation of the lab frame coordinate time t_s at which the fluid element emitting at the lab frame time t_{em} from the position r_{em} was shocked. I am also going to calculate the comoving time t' elapsed between shock passage and emission, given by

$$t' = \int_{t_s}^{t_{em}} \frac{dt}{\gamma(t, x_f(t))} \tag{3.236}$$

where $x_f(t)$ is defined as $x_f(t) = \frac{r_f(t)}{R_s(t)}$ with $r_f(t)$ solution of the Cauchy problem

$$\begin{cases} \frac{dr_f}{dt} = \left(1 - \frac{1}{\gamma^2(t, x_f(t))}\right)^{1/2} c \\ r_f(t_s) = R_s(t_s) \end{cases}$$

The detailed calculation of t_s and t' depends on the value of the time of emission.

3.8.1 Calculation of the time of shock passage

Emission during the Free expansion stage

If the time t_{em} is such that $0 < t_{em} < t_c$, then the shock passage must have occurred during the free expansion stage too.

Looking at the evolution laws defined in section 3.5.1 we can say that the evolution of the fluid element position $r_f(t)$ from $R_s(t_s)$ at the time t_s to r_{em} at the time t_{em} must have been such that

$$\frac{dr_f}{dt} = \frac{ct}{r_i}\left[1 + \left(\frac{ct}{r_i}\right)^2\right]^{-1/2} \tag{3.237}$$

The general solution of such a differential equation passing from the position $\bar{r}$ at the time $\bar{t}$ is

$$r_{0f}(t, \bar{t}, \bar{r}) = r_i\sqrt{1 + \left(\frac{ct}{r_i}\right)^2} - r_i\sqrt{1 + \left(\frac{c\bar{t}}{r_i}\right)^2} + \bar{r} = R(t) - R(\bar{t}) + \bar{r} \tag{3.238}$$

with

$$R(t) = r_i\sqrt{1 + \left(\frac{ct}{r_i}\right)^2} \tag{3.239}$$

So, the time of shock passage t_s must be the solution of the equation

$$r_{0f}(t_s, t_{em}, r_{em}) = R_s(t_s) = R(t_s) + \Delta(t_s) \tag{3.240}$$

or equivalently

$$\Delta(t_s) = r_{em} - R(t_{em}) \tag{3.241}$$

with

$$\frac{(\hat{\gamma}\gamma_s(t_s)+1)}{(\hat{\gamma}-1)} = \frac{(R(t_s)+\Delta(t_s))^3 - r_i^3}{(R(t_s)+\Delta(t_s))^3 - (R(t_s)+\Delta(t_s)-\gamma_s(t_s)\Delta(t_s))^3} \tag{3.242}$$

provided that

$$\gamma_s(t_s) = \frac{R(t_s)}{r_i}, \qquad \hat{\gamma} = \frac{4}{3} \tag{3.243}$$

In conclusion, to find t_s we must solve the equation in z

$$2(2z+1)\left(r_i z + y\right)^3 = (4z+3)\left(r_i z - y(z-1)\right)^3 - r_i^3 \tag{3.244}$$

with

$$y = r_{em} - R(t_{em}) \tag{3.245}$$

and once the solution of (3.244) has been found numerically we can say that

$$t_s = \frac{r_i}{c}\sqrt{z^2-1} \tag{3.246}$$

Finally, we can calculate the comoving time elapsed between shock passage and emission and conclude that

$$t' = \tau_{free}(t_s, R_s(t_s), t_{em}, r_{em}) \tag{3.247}$$

with

$$\tau_{free}(t_1, r_1, t_2, r_2) = \frac{r_i}{c}\log\left[\frac{ct_2 + R(t_2)}{ct_1 + R(t_1)}\right] \tag{3.248}$$

Emission during the Coasting stage

If the time t_{em} is such that $t_c \leq t_{em} < t_d$ the shock passage can have occurred during the coasting stage or during the free expansion stage.

- Let's start assuming $t_s > t_c$ (shock passage in the coasting stage, like the emission time).

  Looking at the evolution laws defined in section 3.5.2 we can say that the evolution of the fluid element position $r_f(t)$ from $R_s(t_s)$ at the time t_s to r_{em} at the time t_{em} must have been such that

$$\frac{dr_f}{dt} = c\sqrt{1 - \frac{1}{\eta^2}} \tag{3.249}$$

The general solution of such a differential equation passing from the position $\bar{r}$ at the time $\bar{t}$ is

$$r_{1f}(t,\bar{t},\bar{r}) = ct\sqrt{1-\frac{1}{\eta^2}} - c\bar{t}\sqrt{1-\frac{1}{\eta^2}} + \bar{r} = R(t) - R(\bar{t}) + \bar{r} \tag{3.250}$$

with

$$R(t) = ct\sqrt{1-\frac{1}{\eta^2}} + \frac{r_i}{\eta} \tag{3.251}$$

So, the time of shock passage t_s must be the solution of the equation

$$r_{1f}(t_s, t_{em}, r_{em}) = R_s(t_s) = R(t_s) + \Delta(t_s) \tag{3.252}$$

or equivalently

$$\Delta(t_s) = r_{em} - R(t_{em}) \tag{3.253}$$

with

$$\frac{(\hat{\gamma}\gamma_s(t_s)+1)}{(\hat{\gamma}-1)} = \frac{(R(t_s)+\Delta(t_s))^3 - r_i^3}{(R(t_s)+\Delta(t_s))^3 - (R(t_s)+\Delta(t_s)-\gamma_s(t_s)\Delta(t_s))^3} \tag{3.254}$$

provided that

$$\gamma_s(t_s) = \eta \qquad \hat{\gamma} = \frac{4}{3} \tag{3.255}$$

In conclusion, to find t_s we must solve the cubic equation in z

$$z^3 + a_2 z^2 + a_1 z + a_0 = 0 \tag{3.256}$$

with

$$a_0 = -y^3\left[(3+4\eta)\left(1-(1-\eta)^3\right)-1\right] - r_i^3 \tag{3.257}$$

$$a_1 = -3y^2\left[(3+4\eta)\left(1-(1-\eta)^2\right)-1\right] \tag{3.258}$$

$$a_2 = -3y\left[(3+4\eta)\eta - 1\right] \tag{3.259}$$

and

$$y = r_{em} - R(t_{em}) \tag{3.260}$$

and once the solution of (3.256) has been found we can say that

$$t_s = \left(z - \frac{r_i}{\eta}\right)\frac{1}{c\sqrt{1-\frac{1}{\eta^2}}} \tag{3.261}$$

Finally, we can calculate the comoving time elapsed between shock passage and emission and conclude that

$$t' = \tau_{coast}(t_s, R_s(t_s), t_{em}, r_{em}) \tag{3.262}$$

with

$$\tau_{coast}(t_1, r_1, t_2, r_2) = \frac{t_2}{\eta} - \frac{t_1}{\eta} \tag{3.263}$$

- If the value given by (3.261) is less than t_c, we must assume the fluid element has been shocked during the free expansion stage rather than during the coasting stage. In this case the evolution of the fluid element position from $R_s(t_s)$ at the time t_s to r_{em} at the time t_{em} must have been $r_f(t)$ satisfying (3.237) from t_s to t_c and (3.249) from t_c to t_{em}. So we will need to use r_{0f} from t_s to t_c and r_{1f} from t_c to t_{em}. Then the time of shock passage t_s will be the solution of the equation

$$r_{0f}(t_c, t_s, R_s(t_s)) = r_{1f}(t_c, t_{em}, r_{em}) \tag{3.264}$$

or equivalently

$$R(t_c) - R(t_s) + R_s(t_s) = R(t_c) - R(t_{em}) + r_{em} \tag{3.265}$$

which can be rewritten as

$$\Delta(t_s) = r_{em} - R(t_{em}) \tag{3.266}$$

with $R(t_{em}) = ct_{em}\sqrt{1 - \frac{1}{\eta^2}} + \frac{r_i}{\eta}$ and $\Delta(t_s)$ satisfying (3.242) associated to the laws (3.239) and (3.243).

In conclusion, to find t_s we must solve the equation in z (3.244) with

$$y = r_{em} - c\, t_{em}\sqrt{1 - \frac{1}{\eta^2}} + \frac{r_i}{\eta} \tag{3.267}$$

and once the solution of (3.244) has been found numerically we can say that

$$t_s = \frac{r_i}{c}\sqrt{z^2 - 1} \tag{3.268}$$

Then, we conclude that the comoving time elapsed between shock passage and emission is

$$t' = \tau_{free}(t_s, R_s(t_s), t_c, r_{1f}(t_c, t_{em}, r_{em})) + \tau_{coast}(t_c, r_{1f}(t_c, t_{em}, r_{em}), t_{em}, r_{em}) \tag{3.269}$$

or simply

$$t' = \frac{r_i}{c}\log\left[\frac{ct_c + \sqrt{r_i^2 + c^2t_c^2}}{ct_s + \sqrt{r_i^2 + c^2t_s^2}}\right] + \left(\frac{t_{em}}{\eta} - \frac{t_c}{\eta}\right) \tag{3.270}$$

Emission during the Relativistic deceleration

Let's assume the emission time t_{em} has a value between t_d and t_{sed}. In this ways we are going to treat as a single evolutionary stage all the three stages that we had previously distinguished in: transition from the coasting stage to the Blandford & McKee stage, Blandford & McKee stage and transition from the Blandford & McKee stage to the Sedov stage. In all of these stages we can use the same approximation for the Lorentz factor distribution of shocked matter:

$$\gamma(t,r) \sim \gamma_s(t)\chi(t,r)^{-1/2} \tag{3.271}$$

with

$$\chi(t,r) = 1 + 16\gamma_s(t)^2\left(1 - \frac{1}{R_s(t)}\right) \sim 16\gamma_s(t)^2\left(1 - \frac{r}{c\,t}\right) \tag{3.272}$$

so

$$\gamma(t,r) \sim \frac{1}{4\sqrt{1-\frac{r}{c\,t}}} \tag{3.273}$$

This approximation is surely good for $\gamma_s \gg 1$ and must be verified a posteriori at decreasing values of γ_s.

Anyway, if we use (3.273), in the case the time of shock passage t_s is greater than t_d like the emission time we expect that the evolution of the fluid element position $r_f(t)$ from $R_s(t_s)$ at t_s to r_{em} at t_{em} is such that

$$\frac{dr_f}{dt} = c - 8c\left(1 - \frac{r_f(t)}{c\,t}\right) \tag{3.274}$$

The general solution of such a differential equation passing from the position $\bar{r}$ at the time $\bar{t}$ will be

$$r_{2f}(t,\bar{t},\bar{r}) = c\,t - t^8\,\frac{c\,\bar{t} - \bar{r}}{\bar{t}^8} \tag{3.275}$$

So, the time of shock passage t_s must be the solution of the equation

$$R_s(t_s) = c\,t_s - t_s^8\,\frac{c\,t_{em} - r_{em}}{t_{em}^8} \tag{3.276}$$

that can be rewritten as

$$t_s^8 - \frac{c}{y}t_s + \frac{1}{y}R_s(t_s) = 0 \tag{3.277}$$

with

$$y = \frac{c\,t_{em} - r_{em}}{t_{em}^8} \tag{3.278}$$

The solution of (3.277) can be found numerically. Then, we can calculate the comoving time elapsed between shock passage and emission and get

$$t' = \tau_{dec}(t_s, R_s(t_s), t_{em}, r_{em}) \tag{3.279}$$

with

$$\tau_{dec}(t_1, r_1, t_2, r_2) = \frac{8}{9} t_2 \sqrt{1 - \frac{r_2}{c\ t_2}} - \frac{8}{9} t_1 \sqrt{1 - \frac{r_1}{c\ t_1}} \tag{3.280}$$

If the solution of (3.277) is $< t_d$, then we expect the fluid element has been shocked during the coasting stage, or even before. We must distinguish the two cases.

- If the fluid element has been shocked during the coasting stage the evolution of its position from $R_s(t_s)$ at the time t_s to r_{em} at the time t_{em} must be $r_f(t)$ satisfying (3.249) from t_s to t_d and (3.274) from t_d to t_{em}. So we will need to use r_{1f} from t_s to t_d and r_{2f} from t_d to t_{em}. Then, the time of shock passage t_s will be the solution of the equation

$$r_{1f}(t_d, t_s, R_s(t_s)) = r_{2f}(t_d, t_{em}, r_{em}) \tag{3.281}$$

or equivalently

$$R(t_d) - R(t_s) + R_s(t_s) = r_{2f}(t_d, t_{em}, r_{em}) \tag{3.282}$$

that can be rewritten as

$$\Delta(t_s) = r_{2f}(t_d, t_{em}, r_{em}) - R(t_d) \tag{3.283}$$

with $r_{2f}(t_d, t_{em}, r_{em}) = c\ t_d - t_d^8 \frac{c\ t_{em} - r_{em}}{t_{em}^8}$, $R(t_d) = ct_d\sqrt{1 - \frac{1}{\eta^2}} + \frac{r_i}{\eta}$ and $\Delta(t_s)$ satisfying (3.254) associated to (3.251) and (3.255).

Thus, the time of shock passage t_s during the coasting stage will be

$$t_s = \left(z - \frac{r_i}{\eta}\right) \frac{1}{c\sqrt{1 - \frac{1}{\eta^2}}} \tag{3.284}$$

with z solution of the cubic equation (3.256) in the case

$$y = r_{2f}(t_d, t_{em}, r_{em}) - R(t_d) \tag{3.285}$$

and finally the comoving time elapsed between shock passage and emission will be

$$t' = \tau_{coast}(t_s, R_s(t_s), t_d, r_{2f}(t_d, t_{em}, r_{em})) + \tau_{dec}(t_d, r_{2f}(t_d, t_{em}, r_{em}), t_{em}, r_{em}) \tag{3.286}$$

or simply

$$t' = \left(\frac{t_d}{\eta} - \frac{t_s}{\eta}\right) + \frac{8}{9}\left[t_{em}\sqrt{1 - \frac{r_{em}}{c\ t_{em}}} - t_d\sqrt{1 - \frac{r_{2f}(t_d, t_{em}, r_{em})}{c\ t_d}}\right] \tag{3.287}$$

- If the fluid element has been shocked during the free expansion stage the evolution of its position from $R_s(t_s)$ at the time t_s to r_{em} at the time t_{em} will be $r_f(t)$ satisfying (3.237) from t_s to t_c, (3.249) from t_c to t_d and (3.274) from t_d to t_{em}. So we will need to use r_{0f} from t_s to t_c, r_{1f} from t_c to t_d and r_{2f} from t_d to t_{em}. Then the time of shock passage t_s will be the solution of the equation

$$r_{0f}(t_c, t_s, R_s(t_s)) = r_{1f}(t_c, t_d, r_{2f}(t_d, t_{em}, r_{em})) \tag{3.288}$$

or equivalently

$$R(t_c) - R(t_s) + R_s(t_s) = r_{1f}(t_c, t_d, r_{2f}(t_d, t_{em}, r_{em})) \tag{3.289}$$

that can be rewritten as

$$\Delta(t_s) = r_{1f}(t_c, t_d, r_{2f}(t_d, t_{em}, r_{em})) - R(t_c) \tag{3.290}$$

with $R(t_c) = r_i\sqrt{1 + \left(\frac{c\ t_c}{r_i}\right)^2}$ and $\Delta(t_s)$ satisfying (3.242) associated to (3.243) and (3.239).

Thus, a time of shock passage t_s during the free expansion stage will be

$$t_s = \frac{r_i}{c}\sqrt{z^2 - 1} \tag{3.291}$$

with z solution of the equation (3.244) in the case

$$y = r_{1f}(t_c, t_d, r_{2f}(t_d, t_{em}, r_{em})) - R(t_c) \tag{3.292}$$

and finally the comoving time elapsed between shock passage and emission will be

$$\begin{aligned} t' = {} & \tau_{free}(t_s, R_s(t_s), t_c, r_{1f}(t_c, t_d, r_{2f}(t_d, t_{em}, r_{em}))) + \\ & \tau_{coast}(t_c, r_{1f}(t_c, t_d, r_{2f}(t_d, t_{em}, r_{em})), t_d, r_{2f}(t_d, t_{em}, r_{em})) + \\ & \tau_{dec}(t_d, r_{2f}(t_d, t_{em}, r_{em}), t_{em}, r_{em}) \end{aligned} \tag{3.293}$$

or simply

$$\begin{aligned} t' = {} & \frac{r_i}{c}\log\left[\frac{ct_c + \sqrt{r_i^2 + c^2t_c^2}}{ct_s + \sqrt{r_i^2 + c^2t_s^2}}\right] + \left(\frac{t_d}{\eta} - \frac{t_c}{\eta}\right) + \\ & \frac{8}{9}\left[t_{em}\sqrt{1 - \frac{r_{em}}{c\ t_{em}}} - t_d\sqrt{1 - \frac{r_{2f}(t_d, t_{em}, r_{em})}{c\ t_d}}\right] \end{aligned} \tag{3.294}$$

Emission during the non relativistic expansion

If the emission time t_{em} is such that $t_{em} > t_{sed}$, then the shock passage can have occurred during the non relativistic expansion stage or before. Looking at the evolution laws defined in section 3.5.6 and in appendix C we can say that during the non relativistic expansion stage

$$v(t,r) = c\left(1 - \frac{1}{\gamma_s(t)^2}\right)^{1/2} F_v\left(\frac{r}{R_s(t)}\right) \sim c\left(1 - \frac{1}{\gamma_s(t)^2}\right)^{1/2} \frac{4}{3}\frac{r}{R_s(t)} \tag{3.295}$$

that can be rewritten as

$$v(t,r) = \frac{2}{5}\,\frac{r}{t}\,\frac{1}{\sqrt{1 + \left(\frac{3}{10}\,\frac{S}{c\,t^{3/5}}\right)^2}} \tag{3.296}$$

Let's assume $t_s > t_{sed}$ too. In this case the evolution of the fluid element position from $R_s(t_s)$ at the time t_s to r_{em} at the time t_{em} must have been $r_f(t)$ such that

$$\frac{dr_f}{dt} = v(t, r_f(t)) \tag{3.297}$$

with $v(t,r)$ given by (3.296). The general solution of such a differential equation passing from the position $\bar{r}$ at the time $\bar{t}$ is

$$r_{3f}(t,\bar{t},\bar{r}) = \bar{r}\,\frac{t^{2/5}\left[1 + \sqrt{1 + \left(\frac{3}{10}\,\frac{S}{c\,t^{3/5}}\right)^2}\right]^{2/3}}{\bar{t}^{2/5}\left[1 + \sqrt{1 + \left(\frac{3}{10}\,\frac{S}{c\,\bar{t}^{3/5}}\right)^2}\right]^{2/3}} \tag{3.298}$$

Then the time of shock passage will be the analytic solution of the equation

$$R_s(t_s) = r_{3f}(t_s, t_{em}, r_{em}) \tag{3.299}$$

that can be rewritten as

$$S t_s^{2/5} = r_{em}\,\frac{t_s^{2/5}\left[1 + \sqrt{1 + \left(\frac{3}{10}\,\frac{S}{c\,t_s^{3/5}}\right)^2}\right]^{2/3}}{t_{em}^{2/5}\left[1 + \sqrt{1 + \left(\frac{3}{10}\,\frac{S}{c\,t_{em}^{3/5}}\right)^2}\right]^{2/3}} \tag{3.300}$$

or equivalently

$$S\,t_{em}^{2/5}\left[1 + \sqrt{1 + \left(\frac{3}{10}\,\frac{S}{c\,t_{em}^{3/5}}\right)^2}\right]^{2/3} = r_{em}\left[1 + \sqrt{1 + \left(\frac{3}{10}\,\frac{S}{c\,t_s^{3/5}}\right)^2}\right]^{2/3} \tag{3.301}$$

The comoving time elapsed between shock passage and emission will be

$$t' = \tau_{sed}(t_s, R_s(t_s), t_{em}, r_{em}) \tag{3.302}$$

with τ_{sed} approximated as

$$\tau_{free}(t_1, r_1, t_2, r_2) = t_2 - t_1 \tag{3.303}$$

If the solution of (3.301) is $< t_{sed}$, then the fluid element has been shocked before the non relativistic expansion beginning.

- Let's start assuming $t_d < t_s < t_{sed}$. In this case the evolution of the fluid element position from $R_s(t_s)$ at the time t_s to r_{em} at the time t_{em} will be $r_f(t)$ satisfying (3.274) from t_s to t_{sed} and (3.297) from t_{sed} to t_{em}. So we will need to use r_{2f} from t_s to t_{sed} and r_{3f} from t_{sed} to t_{em}. Then the time of shock passage t_s will be the solution of the equation

$$r_{2f}(t_{sed}, t_s, R_s(t_s)) = r_{3f}(t_{sed}, t_{em}, r_{em}) \tag{3.304}$$

or equivalently the solution of equation (3.277) with

$$y = \frac{c\, t_{sed} - r_{3f}(t_{sed}, t_{em}, r_{em})}{t_{sed}^8} \tag{3.305}$$

and the comoving time elapsed between shock passage and emission will be

$$t' = \tau_{dec}(t_s, R_s(t_s), t_{sed}, r_{3f}(t_{sed}, t_{em}, r_{em}))) + \tau_{sed}(t_{sed}, r_{3f}(t_{sed}, t_{em}, r_{em}), t_{em}, r_{em}) \tag{3.306}$$

or simply

$$t' = \frac{8}{9}\left[t_{sed}\sqrt{1 - \frac{r_{3f}(t_{sed}, t_{em}, r_{em})}{c\, t_{sed}}} - t_s\sqrt{1 - \frac{R_s(t_s)}{c\, t_s}}\right] + (t_{em} - t_{sed}) \tag{3.307}$$

- If the solution of (3.277) as calculated above is $< t_d$ then we must expect the fluid element has been shocked during the coasting stage. In this case the evolution of its position from $R_s(t_s)$ at the time t_s to r_{em} at the time t_{em} would be $r_f(t)$ satisfying (3.249) from t_s to t_d, (3.274) from t_d to t_{sed} and (3.297) from t_{sed} to t_{em}. So we will need to use r_{1f} from t_s to t_d, r_{2f} from t_d to t_{sed} and r_{3f} from t_{sed} to t_{em}. Then, the time of shock passage t_s will be the solution of the equation

$$r_{1f}(t_d, t_s, R_s(t_s)) = r_{2f}(t_d, t_{sed}, r_{3f}(t_{sed}, t_{em}, r_{em})) \tag{3.308}$$

or equivalently

$$R(t_d) - R(t_s) + R_s(t_s) = r_{2f}(t_d, t_{sed}, r_{3f}(t_{sed}, t_{em}, r_{em})) \tag{3.309}$$

that can be rewritten as

$$\Delta(t_s) = r_{2f}(t_d, t_{sed}, r_{3f}(t_{sed}, t_{em}, r_{em})) - R(t_d) \tag{3.310}$$

with $R(t_d) = ct_d\sqrt{1-\frac{1}{\eta^2}} + \frac{r_i}{\eta}$ and $\Delta(t_s)$ satisfying (3.254) associated to (3.255) and (3.251).

Thus, the time of shock passage t_s during the coasting stage will be

$$t_s = \left(z - \frac{r_i}{\eta}\right) \frac{1}{c\sqrt{1-\frac{1}{\eta^2}}} \tag{3.311}$$

with z solution of the cubic equation (3.256) in the case

$$y = r_{2f}(t_d, t_{sed}, r_{3f}(t_{sed}, t_{em}, r_{em})) - R(t_d) \tag{3.312}$$

and finally the comoving time elapsed between shock passage and emission will be

$$\begin{aligned} t' = \tau_{coast}(t_s, R_s(t_s), t_d, r_{2f}(t_d, t_{sed}, r_{3f}(t_{sed}, t_{em}, r_{em}))) + \\ \tau_{dec}(t_d, r_{2f}(t_d, t_{sed}, r_{3f}(t_{sed}, t_{em}, r_{em})), t_{sed}, r_{3f}(t_{sed}, t_{em}, r_{em})) + \\ \tau_{sed}(t_{sed}, r_{3f}(t_{sed}, t_{em}, r_{em}), t_{em}, r_{em}) \end{aligned} \tag{3.313}$$

- If the fluid element had been shocked during the free expansion stage the evolution of its position from $R_s(t_s)$ at the time t_s to r_{em} at the time t_{em} would be $r_f(t)$ satisfying (3.237) from t_s to t_c, (3.249) from t_c to t_d, (3.274) from t_d to t_{sed} and (3.297) from t_{sed} to t_{em}. So we will need to use r_{0f} from t_s to t_c, r_{1f} from t_c to t_d, r_{2f} from t_d to t_{sed} and r_{3f} from t_{sed} to t_{em}. Then the time of shock passage t_s will be the solution of the equation

$$r_{0f}(t_c, t_s, R_s(t_s)) = r_{1f}(t_c, t_d, r_{2f}(t_d, t_{sed}, r_{3f}(t_{sed}, t_{em}, r_{em}))) \tag{3.314}$$

or equivalently

$$R(t_c) - R(t_s) + R_s(t_s) = r_{1f}(t_c, t_d, r_{2f}(t_d, t_{sed}, r_{3f}(t_{sed}, t_{em}, r_{em}))) \tag{3.315}$$

that can be rewritten as

$$\Delta(t_s) = r_{1f}(t_c, t_d, r_{2f}(t_d, t_{sed}, r_{3f}(t_{sed}, t_{em}, r_{em}))) - R(t_c) \tag{3.316}$$

with $R(t)$ given by (3.239) and $\Delta(t_s)$ satisfying (3.242) associated to (3.243) and (3.239).

Thus, a time of shock passage t_s during the free expansion stage would be

$$t_s = \frac{r_i}{c}\sqrt{z^2 - 1} \tag{3.317}$$

with z solution of the equation (3.244) in the case

$$y = r_{1f}(t_c, t_d, r_{2f}(t_d, t_{sed}, r_{3f}(t_{sed}, t_{em}, r_{em}))) - R(t_c) \tag{3.318}$$

and finally the comoving time elapsed between shock passage and emission would be

$$t' = \tau_{free}(t_s, R_s(t_s), t_c, r_{1f}(t_c, t_d, r_{2f}(t_d, t_{sed}, r_{3f}(t_{sed}, t_{em}, r_{em})))) +$$
$$\tau_{coast}(t_c, r_{1f}(t_c, t_d, r_{2f}(t_d, t_{sed}, r_{3f}(t_{sed}, t_{em}, r_{em}))), t_d, r_{2f}(t_d, t_{sed}, r_{3f}(t_{sed}, t_{em}, r_{em}))) +$$
$$\tau_{dec}(t_d, r_{2f}(t_d, t_{sed}, r_{3f}(t_{sed}, t_{em}, r_{em})), t_{sed}, r_{3f}(t_{sed}, t_{em}, r_{em})) +$$
$$\tau_{sed}(t_{sed}, r_{3f}(t_{sed}, t_{em}, r_{em}), t_{em}, r_{em})$$

Chapter 4

Anisotropic fireballs

In this thesis we have worked entirely within the framework of the fireball model. In other words, we believe that the event at the origin of a GRB is a sort of explosion, that is a prompt release of a large amount of energy entraining a small amount of baryons (the ejecta) in a rather small region surrounded by a very tenuous medium. Such an initial event quickly produces an expanding cloud of optically thick hot plasma (a *fireball*) driving an ultra relativistic blast wave into the surrounding medium, and along with the fireball subsequent evolution the observed radiation is produced. According to the internal/external shock scenario, the GRB radiation might be produced at shocks arising in collisions between different shells of ejecta traveling at different speeds, while afterglow radiation might be synchrotron radiation from relativistic electrons accelerated at the forward shock sweeping the external matter.

The ultimate goal of this work is intended to be the detailed calculation of the observed afterglow when the expanding fireball is not isotropic from the very beginning of its evolution and the observer looks at it by an arbitrary direction. I want to investigate effects of "smooth" anisotropy on afterglow light curves and spectra. For simplicity I have always assumed that the fireball expansion takes place in a cold and uniform interstellar medium (ISM).

In this chapter I want to illustrate how the spherical fireball model illustrated in chapter 3.5 can be easily modified adding appropriate angular dependencies to the physical quantities, in order to be transformed into an anisotropic fireball model, and which difficulties are introduced by these modifications in the afterglow light curve and spectra calculation described in section 3.6.3.

The situation which we are interested in corresponds to the existence of a preferen-

tial direction for the energy ejection mechanism which is not aligned with the observer line of sight. Then, we will characterize the fireball intrinsic anisotropy by assuming that the *baryon loading parameter* η, i.e. the initial ratio of internal energy to baryon rest mass energy of the ejecta, is direction dependent and peaks along a given axis, but not negligible ejection occurs also normally to the preferred axis. The particular direction dependent *baryon loading parameter* law we use will be described in section 4.2.

Finally, in sections 4.3 and 4.4 we will show that the fireball anisotropic model we are building evolves radially as if it were a portion of a spherical fireball in every direction, i.e. it can be calculated varying the spherical model with varying direction. For this reason, a unique code has been written for the numerical calculation of afterglows and spectra from spherical and anisotropic fireballs, that can be run for different viewing angles relative to the axis of symmetry of the anisotropic model. By default the program calculates the afterglow from the spherical fireball corresponding to the radial evolution of the anisotropic model along the line of sight, eventually allowing for an artificial change of the total energy, and the baryon loading parameter value of the spherical model can be changed changing the viewing angle. Thus, the range of allowed values of η corresponds to the range of the function (4.29), and by default the total energy of each spherical fireball model is proportional to the baryon loading parameter (see section 4.2.3). An appropriate flag makes the program run for calculating the afterglows from the anisotropic fireball viewed from the chosen direction. Other flags control the use of different magnetic field evolution laws, the inclusion of electron cooling effects and so on. The code is flexible enough to allow an easy change of the baryon loading parameter angular distribution function, and test other anisotropic models.

To date the code has been tested on all the spherical models needed for the full anisotropic calculation, which is very time consuming and is still ongoing. Results of the spherical afterglow calculation have been presented in chapter 4. Results for the full anisotropic calculation are expected in a few months.

4.1 Afterglows in an Anisotropic Fireball Model

If the fireball is not isotropic because of a direction dependent baryon loading parameter, then the spherical symmetry of the external shocks breaks down.

As a first approximation we can neglect internal friction and transversal pressure gradients. Under this approximation we can assume that the fireball evolution along

any fixed direction is not affected by the adjacent directions and resembles that of a spherical fireball having the same baryon loading parameter that the anisotropic fireball has in that direction and a total energy $\sim 4\pi$ times the energy ejected in that direction.

We expect the directions with less baryon contamination (i.e. higher values of the baryon loading parameter η) to develop faster forward shocks (remembering that the coasting Lorentz factor equals η) and to start deceleration at smaller distances from the centre of explosion (remember that the required amount of swept up ISM matter for starting deceleration is inversely proportional to the coasting Lorentz factor, that is η). In this situation the forward shock cannot be spherical around the centre of explosion. It must be axially symmetric and elongated in the direction of the greatest energy output.

The delays in the arrival times of simultaneously emitted photons lead to a further distortion of the fireball shape in the observer's view (i.e. the equal-T surface), especially when the line of sight is not aligned with the preferred direction for energy ejection.

Moreover, the faster traveling regions of the blast wave are going to accelerate electrons at higher average Lorentz factors and give rise to harder synchrotron radiation, but also to more beamed emission. Remember that the opening angle of the emission beam of a radially expanding fluid element is $\sim 1/\gamma$ centered on the radial direction and the that emission beam widens as emitting matter slows down.

As usual, at any given time the observer will see only that part of the shock front (and fireball interior) whose radiation beam includes a direction parallel to the line of sight. Thus we expect that at the beginning only matter confined within a narrow cone around the line of sight is really important for afterglow emission, so that the observer would think to be looking at a spherical fireball with baryon loading parameter corresponding to the direction pointing to him (and total energy according to it). But if the fireball were anisotropic and if the line of sight were not perfectly aligned with the fireball axis it might happen that the fastest part of the forward shock, always emitting radiation harder than the radiation coming from line of sight, even if it was not visible at the beginning because of beaming, becomes visible after a while when the beaming angles widen enough and provides a re-burst at a frequency higher than the typical emission frequency of matter along the line of sight. This effect may substantially modify afterglow light curves and spectra. Slopes, peak times and peak heights will be affected and the deviations from spherical fireball afterglows will depend on the

viewing angle and on the baryon loading parameter angular variation law.

The whole volume integration of emission from the fireball interior will be carefully taken in account in our afterglow light curve and spectra calculation. However, we have already seen that in the spherical case the approximated calculations based on post–shock conditions along the line of sight only is good enough up to the end of the Blandford & McKee stage, and we could use it for rough approximation in the anisotropic case too. Finally, the effect of electron cooling will be fully considered.

4.2 Mathematical Description of the Model

Now I am going to introduce the formalism required for the calculation of the light curve of a GRB afterglow produced by an anisotropic expanding fireball. We shall assume an axially symmetric distribution of the ejected energy to ejecta rest mass ratio. We shall use a distribution peaked along the fireball axis of symmetry, forming an angle ε with respect to the line of sight. The sharpness of this distribution will be established in section 4.2.4 in order to satisfy the pure radial expansion approximation.

4.2.1 Coordinate Systems for the Lab Frame

First of all we will call z_a the fireball axis of symmetry. Then, given the observer line of sight, already named z, intersecting the z_a axis in the centre of the explosion O at an angle ε with the z_a axis itself, we can define two different Cartesian coordinate systems $\mathrm{x}_a\mathrm{y}_a\mathrm{z}_a$ and xyz for the lab frame in the following way: choose as x_a axis the perpendicular in O to the plane $\mathrm{z}_a\mathrm{z}$, set the x axis coincident with x_a and place the y_a and y axis accordingly. In this way the system xyz is obtained from the system $\mathrm{x}_a\mathrm{y}_a\mathrm{z}_a$ through a clockwise rotation by an angle ε around the $\mathrm{x}_a \equiv \mathrm{x}$ axis. The coordinate transformations are the following:

$$\begin{cases} \mathrm{x}_a = \mathrm{x} \\ \mathrm{y}_a = \mathrm{y}\cos\varepsilon + \mathrm{z}\sin\varepsilon \\ \mathrm{z}_a = -\mathrm{y}\sin\varepsilon + \mathrm{z}\cos\varepsilon \end{cases} \qquad \begin{cases} \mathrm{x} = \mathrm{x}_a \\ \mathrm{y} = \mathrm{y}_a\cos\varepsilon - \mathrm{z}_a\sin\varepsilon \\ \mathrm{z} = \mathrm{y}_a\sin\varepsilon + \mathrm{z}_a\cos\varepsilon \end{cases} \tag{4.1}$$

We can also introduce the two polar coordinate systems $r\vartheta_a\varphi_a$ and $r\vartheta\varphi$ respectively

associated to the Cartesian systems $x_a y_a z_a$ and xyz in the standard way:

$$\begin{cases} x_a = r \sin\vartheta_a \cos\varphi_a \\ y_a = r \sin\vartheta_a \sin\varphi_a \\ z_a = r \cos\vartheta_a \end{cases} \qquad \begin{cases} x = r \sin\vartheta \cos\varphi \\ y = r \sin\vartheta \sin\varphi \\ z = r \cos\vartheta \end{cases} \tag{4.2}$$

Note that the radial coordinate r is the same for both the polar systems. We will use mainly the $x_a y_a z_a$ and the $r\vartheta_a\varphi_a$ coordinate systems for the mathematical description of fireball intrinsic properties and the remaining two coordinate systems for the calculation of fireball observed properties.

4.2.2 The Observed Time

We are still going to use both the lab frame coordinate time t and the time T measured from the terrestrial observer starting from the GRB photons arrival.

The zero reference time for T will correspond to the hypothetical arrival of photons emitted at the time $t = 0$ form the point at distance r_i from the lab frame origin on the line of sight. So, the time T at which photons emitted by a generic point at the lab time t are seen by the observer is

$$T = t - \frac{r\cos\vartheta}{c} + \frac{r_i}{c} \tag{4.3}$$

where (r, ϑ, φ) are the polar coordinates of the emitting point with respect to the xyz reference frame.

Remember that the zero reference time we have chosen for T corresponds to a moment slightly preceding the GRB detection itself, so that our light curves, usually calculated from time $T = 0$ on, must be considered "observable" only after a time equal to the average observed duration of long GRBs, i.e. for $T \gtrsim 100$.

4.2.3 Initial Conditions

In the spherically symmetric fireball model [Mészáros, Laguna & Rees 1993] the expanding fireball arises from the evolution of an initial compact sphere of radius r_i containing a photon–pair plasma of total energy E_T uniformly polluted with baryons of total mass M_T. In the simplest version of the model, the external medium too is assumed uniform with particle density n_i, cold (i.e. $e'_i \sim n_i m_p c^2$) and quite rarefied as compared to the initial baryon density inside the sphere of radius r_i (i.e. $n_i m_p \ll \frac{3M_T}{4\pi r_i^3}$),

so that its presence does not affect the fireball evolution during the very early stages. The initial conditions for spherical fireball expansion are then completely summarized through the following three parameters: initial fireball radius r_i, initial total energy of the fireball E_T and baryon loading parameter $\eta = \frac{E_T}{M_T c^2}$.

An anisotropic fireball too may arise from an initial compact sphere of radius r_i containing a photon–pair plasma polluted with baryons and surrounded by a uniform rarefied cold medium, but in this case we must assume the plasma and baryon distributions within the sphere of radius r_i are not uniform and there are, for instance, directions where the internal energy to baryon rest mass energy ratio (i.e. the local baryon loading parameter) is lower/higher.

Thus, the initial conditions for an anisotropic fireball can be given through the parameters r_i (initial fireball radius), E_T (initial total energy of the fireball), M_T (total mass of the baryons polluting the photon-pair plasma) plus a function specifying the internal energy to baryon rest mass energy ratio in each direction within the sphere of radius r_i, i.e. a **direction dependent baryon loading parameter** law.

The definition of a **direction dependent baryon loading parameter** law should be the following: given an infinitesimal solid angle element $d\Omega = \sin\vartheta_a d\vartheta_a d\varphi_a$ centered on the direction (ϑ_a, φ_a) let dE and dM be respectively the fireball initial internal energy and the fireball initial baryon mass within $d\Omega$. Then, the baryon loading parameter in the fixed direction is

$$\eta(\vartheta_a, \varphi_a) \equiv \frac{1}{c^2}\frac{dE}{dM} \tag{4.4}$$

If we define $\tilde{E}(\vartheta_a, \varphi_a) \equiv \frac{dE}{d\Omega}$ and $\tilde{M}(\vartheta_a, \varphi_a) \equiv \frac{dM}{d\Omega}$, then we have

$$\eta(\vartheta_a, \varphi_a) = \frac{1}{c^2}\frac{\tilde{E}(\vartheta_a, \varphi_a)}{\tilde{M}(\vartheta_a, \varphi_a)} \tag{4.5}$$

The total initial internal energy and mass of the fireball can be expressed in terms of the just defined quantities as

$$E_T \equiv \int_0^{2\pi} d\varphi_a \int_0^{\pi} \tilde{E}(\vartheta_a, \varphi_a)\sin\vartheta_a d\vartheta_a = \int_0^{2\pi} d\varphi_a \int_0^{\pi} \eta(\vartheta_a, \varphi_a)\tilde{M}(\vartheta_a, \varphi_a)c^2 \sin\vartheta_a d\vartheta_a \tag{4.6}$$

and

$$M_T \equiv \int_0^{2\pi} d\varphi_a \int_0^{\pi} \tilde{M}(\vartheta_a, \varphi_a)\sin\vartheta_a d\vartheta_a \tag{4.7}$$

Then we will define *total baryon loading parameter* of the fireball the quantity

$$\eta_T = \frac{E_T}{M_T c^2} \tag{4.8}$$

and *average baryon loading parameter* of the fireball the quantity

$$< \eta >= \frac{1}{4\pi} \int_0^{2\pi} d\varphi_a \int_0^{\pi} \eta(\vartheta_a, \varphi_a) \sin \vartheta_a d\vartheta_a \tag{4.9}$$

Note that, in the most general case

$$\eta_T \neq < \eta > \tag{4.10}$$

Actually

$$\eta_T = < \eta > \quad \Leftrightarrow \quad \tilde{M}(\vartheta_a, \varphi_a) = \frac{M_T}{4\pi} \tag{4.11}$$

We will work under the simplifying assumption of **uniform initial baryon pollution**, i.e.

$$\tilde{M}(\vartheta_a, \varphi_a) = constant \quad \Rightarrow \quad \tilde{M}(\vartheta_a, \varphi_a) = \frac{M_T}{4\pi} \tag{4.12}$$

This will make every property of the baryon loading parameter function directly related to a corresponding property of the energy ejection mechanism.

In case of an **axially symmetric fireball** we expect the initial conditions are axially symmetric too, so we expect the functions $\tilde{E}$ and η do not depend on φ_a , i.e.

$$\tilde{E}(\vartheta_a, \varphi_a) \equiv \tilde{E}(\vartheta_a), \quad \text{and} \quad \eta(\vartheta_a, \varphi_a) \equiv \eta(\vartheta_a)$$

In this case we can rewrite, for instance,

$$E_T = 2\pi \int_0^{\pi} \tilde{E}(\vartheta_a) \sin \vartheta_a d\vartheta_a = \int_0^{\pi} E'(\vartheta_a) d\vartheta_a = \int_0^{\pi} \eta(\vartheta_a) M'(\vartheta_a) c^2 d\vartheta_a \tag{4.13}$$

by defining

$$E'(\vartheta_a) \equiv 2\pi \tilde{E}(\vartheta_a) \sin \vartheta_a \tag{4.14}$$

and

$$M'(\vartheta_a) \equiv 2\pi \tilde{M}(\vartheta_a) \sin \vartheta_a = \frac{1}{2} M_T \sin \vartheta_a \tag{4.15}$$

Finally remember that we want to study the axially symmetric case corresponding to the **existence of a strongly preferred direction for the energy ejected by the GRB progenitor** (the fireball axis of symmetry z_a), with a **smooth transition in the energy output going from the preferred direction to the normal ones.** Then we expect a further reflection symmetry of the initial conditions (as of the resulting fireball) with respect to the plane normal to the z_a axis through the centre of the explosion (the plane $x_a y_a$). In such a case the fireball baryon loading parameter analytic expression must have the further following property:

$$\eta(\pi - \vartheta_a) = \eta(\vartheta_a) \tag{4.16}$$

We will refer to such a property as to a front–back symmetry.

Before ending this section recall the definition of the solid angle covered by the double–sided cone of half opening $\vartheta_a \leq \frac{\pi}{2}$:

$$\Omega(\vartheta_a) = 2 \times 2\pi \int_0^{\vartheta_a} \sin x dx = 4\pi(1 - \cos\vartheta_a) \tag{4.17}$$

and of the corresponding solid angle fraction:

$$\varepsilon(\vartheta_a) = \frac{\Omega(\vartheta_a)}{4\pi} = (1 - \cos\vartheta_a) \tag{4.18}$$

The total energy emitted within such a cone if the initial internal energy distribution is axially symmetric, front–back symmetric and uniformly baryon polluted as we have supposed, will be:

$$E(\vartheta_a) = 2 \times \int_0^{\vartheta_a} E'(x)dx = M_T c^2 \int_0^{\vartheta_a} \eta(x) \sin x dx \tag{4.19}$$

4.2.4 Physical Constraints to the Initial Conditions

As a further constraint, we want to choose our fireball baryon loading parameter $\eta(\vartheta_a)$ in such a way that

$$E(\vartheta_{a,2}) - E(\vartheta_{a,1}) = constant \tag{4.20}$$

whenever

$$\Omega(\vartheta_{a,2}) = constant \times \Omega(\vartheta_{a,1}) \tag{4.21}$$

We might be interested, for instance, in a situation such that every time the solid angle of the cone centered on the z_a axis is increased by a factor ten, the fireball energy output within it increases by a fixed amount ΔE. So, if in a fraction 10^{-n} of the solid angle (n positive integer) a total energy E_{core} is emitted, then, in a fraction 10^{-n+1} the energy output will be $E_{core} + \Delta E$, in a fraction 10^{-n+2} the energy output will be $E_{core}+2\Delta E$ and so on. The total energy output of the fireball will be $E_T = E_{core}+n\Delta E$.

This condition is to be considered reasonable because if an almost linear relation existed between the energy output per unit solid angle in a given direction and the GRB luminosity observed from that direction, then a random distribution of viewing angles would naturally correspond to a few decades broad distribution in estimated isotropic energy γ–rays of the GRBs, with the property that GRBs presenting isotropic energy 10 times larger than the average are 10 times less numerous, which is roughly what is observed. Unfortunately, theoretical studies are not yet able to tell precisely the

relation connecting the fireball energy output and the observed energy in γ–rays, and this is usually assumed to be a power law with a free parameter slope to be constrained by observations.

A function $\eta(\vartheta_a)$ satisfying (4.16) and satisfying also (4.20) whenever (4.21) occurs can be, for example, the following:

$$\eta(\vartheta_a) \propto \frac{1}{1 - |\cos\vartheta_a| + \varepsilon_0} \tag{4.22}$$

The small parameter ε_0 in (4.22) allows us to avoid a divergence for $\vartheta_a \to 0$ and $\vartheta_a \to \pi$ and leads to a finite E_T (see below). It can be chosen very small in order to very slightly perturb the $(1 - |\cos\vartheta_a|)^{-1}$ dependence of η out of a narrow cone centered on the z_a axis. However, we will show later (in section 4.4) that ε_0 cannot be too small if we want the fireball evolution to resemble the spherical one in all directions. We will also show that typical values for a realistic fireball will be $\varepsilon_0 \sim 10^{-2}$. According to our previous definitions, the parameter ε_0 can be regarded as the solid angle fraction covered by a narrow double–sided cone centered on the z_a axis within which all fireball properties are roughly uniform. The fireball properties start to change significantly with ϑ_a outside this central cone. The central cone half–opening will be $\vartheta_{a,0} = \arccos(1 - \varepsilon_0)$.

We can easily check that the analytic expression (4.22) has the required properties by noting that

$$\cos(\pi - \vartheta_a) = -\cos\vartheta_a \tag{4.23}$$

and that for

$$\varepsilon_0 \ll \varepsilon(\vartheta_{a,1}) = \frac{\varepsilon(\vartheta_{a,2})}{K}, \qquad K > 1 \ \textit{and} \ \vartheta_{a,2} < \frac{\pi}{2} \tag{4.24}$$

we find

$$E(\vartheta_{a,2}) - E(\vartheta_{a,1}) \propto M_T c^2 \int_{\vartheta_{a,1}}^{\vartheta_{a,2}} \frac{\sin\vartheta_a}{1 - \cos\vartheta_a + \varepsilon_0} d\vartheta_a \propto \int_{\vartheta_{a,1}}^{\vartheta_{a,2}} \frac{d(\varepsilon(\vartheta_a) + \varepsilon_0)}{\varepsilon(\vartheta_a) + \varepsilon_0} =$$

$$\int_{\varepsilon(\vartheta_{a,1})+\varepsilon_0}^{\varepsilon(\vartheta_{a,2})+\varepsilon_0} \frac{dz}{z} = \ln\left(\frac{\varepsilon(\vartheta_{a,2}) + \varepsilon_0}{\varepsilon(\vartheta_{a,1}) + \varepsilon_0}\right) \sim \ln K = \textit{constant} \tag{4.25}$$

The required normalization factor N_1 in equation (4.22) can be calculated by using equations (4.13), (4.15) and (4.12):

$$E_T = 2 \times \frac{M_T c^2}{4\pi} 2\pi \int_0^{\pi} \eta(\vartheta_a) \sin\vartheta_a d\vartheta_a = M_T c^2 N_1 \int_0^{\pi/2} \frac{\sin\vartheta_a d\vartheta_a}{1 - \cos\vartheta_a + \varepsilon_0} =$$

$$= M_T c^2 N_1 \int_0^{\pi/2} \frac{d(\varepsilon(\vartheta_a) + \varepsilon_0)}{\varepsilon(\vartheta_a) + \varepsilon_0} = M_T c^2 N_1 \int_{\varepsilon_0}^{1+\varepsilon_0} \frac{dz}{z} = M_T c^2 N_1 \ln\left(1 + \frac{1}{\varepsilon_0}\right) \tag{4.26}$$

then, we can say that

$$N_1 = \frac{E_T}{M_T c^2} \times \frac{1}{\ln\left(1+\frac{1}{\varepsilon_0}\right)} = \frac{\eta_T}{\ln\left(1+\frac{1}{\varepsilon_0}\right)} \tag{4.27}$$

and consequently

$$\eta(\vartheta_a) = \frac{N_1}{1-|\cos\vartheta_a|+\varepsilon_0} = \frac{\eta_T}{\ln\left(1+\frac{1}{\varepsilon_0}\right)} \frac{1}{(1-|\cos\vartheta_a|+\varepsilon_0)} \tag{4.28}$$

The function (4.28) is our final choice for the direction dependent baryon loading parameter of an homogeneous sphere of radius r_i containing a total mass M_T in baryons and a total internal energy E_T in photons-pairs plasma that represent our initial condition for the expanding fireball.

Summary

We approximate the anisotropic fireball generation process through the prompt emission of a total energy E_T within a spherical region of radius r_i uniformly polluted with a mass M_T of baryons. We assume that the rarefied medium outside the sphere of radius r_i is uniform and cold. We further assume that the energy is emitted anisotropically, that a preferential direction z_a for the energy ejection exists, and that the corresponding direction dependent baryon loading parameter is given by

$$\eta(\vartheta_a) \equiv \eta_{\varepsilon_0}(\vartheta_a) = \frac{\eta_T}{\ln\left(1+\frac{1}{\varepsilon_0}\right)} \times \frac{1}{1-|\cos\vartheta_a|+\varepsilon_0} \tag{4.29}$$

where ϑ_a is the angle with respect to the preferred direction z_a.

This model has the free parameter, $0 < \varepsilon_0 < 1$, that determines the half–opening $\vartheta_{a,0}$ ($\vartheta_{a,0} = \arccos(1-\varepsilon_0)$) of a central cone where the energy output is roughly uniform.

The constant η_T that appears in equation (4.29) is not a free parameter, since it is related to the total energy and ejecta mass by the formula

$$\eta_T = \frac{E_T}{M_T c^2} \tag{4.30}$$

It represents the average baryon loading parameter of the fireball.

Note that a constant $\eta(\vartheta_a)$ (i.e. a spherical fireball) cannot be obtained for any value of ε_0, so the spherical fireball model cannot be considered as a particular case of our anisotropic fireball model.

Reasonable choice for E_T , M_T and ε_0

Let us call *dynamical range* of our anisotropic fireball the parameter

$$D \equiv \frac{\eta(0)}{\eta\left(\frac{\pi}{2}\right)} = \frac{1+\varepsilon_0}{\varepsilon_0} = 1 + \frac{1}{\varepsilon_0}$$

A reasonable assumption is $\eta(0) \sim 300$ (about the maximum baryon loading parameter value expected in real GRBs) and $D \sim 100$.

This assumption corresponds to

$$\varepsilon_0 \sim 10^{-2}$$

(which is marginally compatible with the condition for no lateral expansion discussed in section 4.4) and leads to

$$\eta_T = \eta(0)\varepsilon_0 \ln\left(1 + \frac{1}{\varepsilon_0}\right) \sim 14$$

Furthermore, we can assume $E_T \sim 10^{52}$ ergs and consequently

$$M_T = \frac{E_T}{\eta_T c^2} \sim 4 \times 10^{-4}\ \mathrm{M}_\odot$$

These are the physical parameters that we are going to use.

4.3 The anisotropic fireball evolution

We shall assume that within the solid angle $d\Omega$ centered on the direction (ϑ_a, φ_a), the evolution of our anisotropic fireball resembles that of an adiabatically expanding spherical fireball with baryon loading parameter $\eta(\vartheta_a)$ and total energy $E_{spherical}(\vartheta_a) = \eta(\vartheta_a) M_T c^2$. This will be a good approximation when interactions with the fluid evolving in the adjacent directions can be neglected. We will discuss the validity of this approximation in section 4.4. The standard adiabatic evolution of a spherical fireball has already been discussed in chapter 3.5. Thus, the shock radius, shock Lorentz factor and internal structure of our anisotropic fireball can be simply deduced adding a ϑ_a dependence on the baryon loading parameter and on the total energy in all laws introduced in chapter 3.5, and remembering that the angle ϑ_a represents the angle between the generic radial direction and the fireball axis z_a, which forms an angle ε with the

line of sight z. For the complete description of the anisotropic fireball evolution from the observer point of view we can simply recall that

$$\cos\vartheta_a = \cos\varepsilon\cos\vartheta_a - \sin\varepsilon\sin\vartheta_a\sin\varphi_a \tag{4.31}$$

We expect that all transition radii and transition times are now direction dependent. The fireball intrinsic shape will not be spherical any longer; it will be slightly elongated along the axis z_a, and consequently the equal-T surface will not be axially symmetric around line of sight any longer. This will introduce a true φ dependence in the analytic expression of $ReqT$, and the φ integration in (3.142) will be unavoidable.

Finally, the normalization of the light curve will be done using the normalization factor F_{max} defined by (3.167) relative to the line of sight. The normalization will be viewing angle dependent.

4.4 Sideways expansion

Now we discuss the approximation of spherical–like radial evolution. Such an approximation is strictly related to the so called problem of sideways expansion expected at late times for any narrow uniform jet expanding in vacuum. We can think of our anisotropic fireball as being composed of many adjacent narrow jets evolving independently from each other (and thus evolving as if they were a portion of a sphere) until sideways expansion takes place. We will show that for large enough values ($\gtrsim 10^{-2}$) of the core solid angle ε_0, we can avoid sideways expansion and assume spherical–like evolution along every direction at any time.

4.4.1 General Criterion

From the point of view of a comoving observer comoving with the shock front in the position ϑ_a at the lab time t, the local causally connected region has a radius

$$l(\vartheta_a, t) = \int_0^t c_s(\vartheta_a, t')\frac{dt'}{\Gamma_s(\vartheta_a, t')} \tag{4.32}$$

where $c_s(\vartheta_a, t)$ is the velocity of sound for shocked matter just behind the shock in the position ϑ_a at the time t, and $d\tau = \frac{dt}{\Gamma_s(\vartheta_a,t)}$ is the comoving time interval corresponding to the lab time interval dt. We can define $\tau(\vartheta_a, t)$, the time elapsed from the explosion in the comoving observer's opinion in the following way

$$\tau(\vartheta_a, t) = \int_0^t \frac{dt'}{\Gamma_s(\vartheta_a, t')} \tag{4.33}$$

Remember that a locally comoving observer just behind the shock sees the shocked matter around him as homogeneous and at rest, so $l(\vartheta_a, t)$ represents the maximum distance from which elements of such an homogeneous fluid can have sent signals to him up to the time $\tau(t)$, i.e. $l(\vartheta_a, t)$ defines the causally connected region for the observer.

The causally connected region around our comoving observer subtends an angle $\Delta\vartheta_a$ to the center of the explosion that is roughly

$$\Delta\vartheta_a(\vartheta_a, t) \sim \frac{l(\vartheta_a, t)}{R_s(\vartheta_a, t)} \tag{4.34}$$

Our comoving observer will not be able to realize that he is sitting on the expanding front of an anisotropic fireball, if the variations of the Lorentz factor $\Gamma_s(\vartheta_a, t)$ within an angle $\Delta\vartheta_a$ from the observer's position are negligible, i.e. if

$$\left| \frac{\Gamma_s(\vartheta_a - \Delta\vartheta_a, t) - \Gamma_s(\vartheta_a + \Delta\vartheta_a, t)}{\Gamma_s(\vartheta_a, t)} \right| \ll 1 \tag{4.35}$$

or equivalently

$$\left| \Delta\vartheta_a \times \frac{\partial\Gamma_s}{\partial\vartheta_a}(\vartheta_a, t) \right| \times \frac{1}{\Gamma_s(\vartheta_a, t)} \ll 1 \tag{4.36}$$

in the case $\Delta\vartheta_a \ll 1$.

If the comoving observer cannot realize that the fireball is not isotropic, locally he will see the evolution going on as if the fireball were spherical. The evolution along a given direction will resemble the evolution of a spherical fireball having the same baryon loading parameter (and the same energy output per unit solid angle) that our comoving observer measures. No local sideways expansion will take place.

We have calculated numerically the left hand side of (4.35) versus the angle ϑ_a through the whole fireball evolution and found out that it is always definitely less than 1 for $\varepsilon_0 \gtrsim 10^{-2}$ (see fig.4.1). The "critical" time, i.e. the moment at which the left hand side of (4.35) reaches its maximum, is before the end of the Blandford & McKee stage. At that time, the observer at an angle $\sim \vartheta_{a,0}$ with the fireball axis might realize to be living on an anisotropic fireball if the central cone of half–opening $\vartheta_{a,0}$ were too narrow, and we might expect this central cone to expand laterally as if it were in vacuum. In order to avoid this complication that we are not able to treat consistently we calculate our models only for $\varepsilon_0 \gtrsim 10^{-2}$.

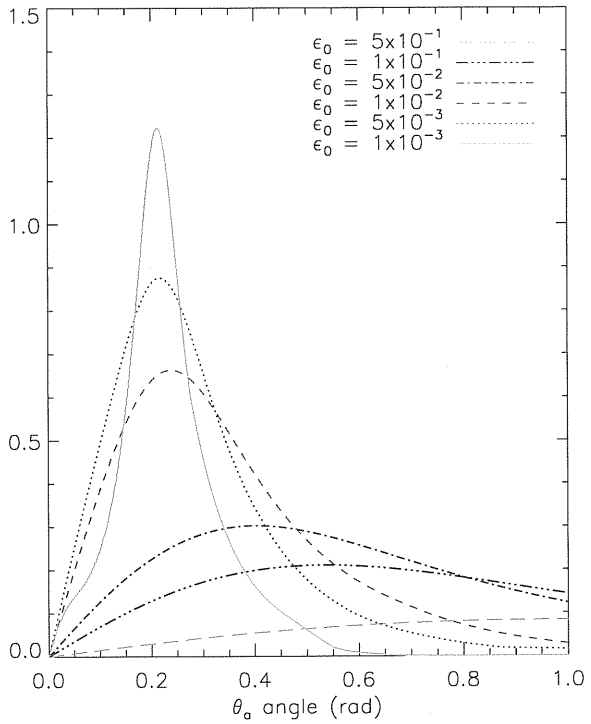

Figure 4.1: *Plots of the left hand side of (4.35) versus the angle ϑ_a at the time t_{crit} for different values of ε_0 (as indicated in the legend) at constant maximum baryon loading parameter value $\eta(0) = 300$. The peak drops below 1 for $\varepsilon_0 \gtrsim 10^{-2}$. The peak angle is $\sim \vartheta_{a,0} = \arccos(1 - \varepsilon_0)$.*

Chapter 5

Results

5.1 Introduction

We have restricted our attention to spherical fireballs only. As explained in chapter 4, an essential ingredient for an anisotropic fireball model with smooth anisotropy is the knowledge of spherical evolution, so we start studying those spherical fireballs that are needed for the anisotropic calculation. From this study we can, nevertheless, extract some general predictions about afterglows from spherical fireballs and devise behaviours that have not been considered before.

First of all, in section 5.3.1, we show that the afterglow light curves and spectra we obtain under the assumption of pure slow cooling and magnetic field equipartition agree with the results obtained by [Granot, Piran & Sari 1999c] for high baryon loading parameter values ($\eta \gtrsim 100$) on the observer time interval corresponding to the Blandford & McKee stage, i.e. more or less the time interval between $T_0(0)$ and $T_{crit}(0)$ (see definitions in section 3.6.1). Actually the standard choice of $\eta \gtrsim 100$ is the one for which the time interval between $T_0(0)$ and $T_{crit}(0)$ corresponds to the typical timescale of afterglow search and detection unless extreme values for the other fireball parameters are invoked. We show that for baryon loading parameter values $\eta < 100$, corresponding to "non standard" GRBs, the Blandford & McKee stage beginning $T_0(0)$ shifts to times so late that afterglow emission produced during an earlier stage of evolution might be accessible to observations. Afterglow peaks might occur before $T_0(0)$ and, in such a case, the peak shape and behaviour would be different and emission over the time interval between $T_0(0)$ and $T_{crit}(0)$ would result dimmer than expected as if the energy conversion efficiency were lower.

Then, in section 5.3.2, we show the results of the calculation when we take into account electron cooling by synchrotron radiation and adiabatic energy losses. In this case, the combination of the effect of cooling on the fluid comoving emissivity and detailed volume integration of emitted radiation seems to cancel any definite power law raise or decay far from peaks and/or breaks either in spectra and light curves. As already noted by [Granot & Sari 2002], in this case broadband spectral fitting with analytic models different from a simple broken power law is required for the complete determination of the burst parameters. The break shape too becomes a signature of cooling.

The radiation process model could be further complicated (including for example synchrotron self–absorption, inverse Compton radiation etc.) but we have restricted our attention to the very basic model illustrated in section 3.7.5, provided that the choice of fireball parameters is such that neglected effects are really negligible, in order to disentangle more easily geometrical and radiation effects in the calculation of afterglows light curves and spectra from anisotropic fireballs.

We do not aim at including all possible radiation and electron cooling mechanisms in our afterglow calculation Actually this has been done by [Granot & Sari 2002] and [Sari & Esin 2001] and we will refer to them (or to previous classical works) for a check of our results whenever comparison is possible. We focus our attention to effects of generalized hydrodynamics including early and late expansion stages that these authors do not take in account, both for the new perspectives they give in the spherical case (see discussion in section 5.3.3) and for the more consistent treatment of the anisotropic case that will come later.

We have explored mainly spherical fireball models needed for building up an anisotropic fireball model as explained in chapter 4. Baryon loading parameter values between $\eta \sim 3$ and $\eta \sim 300$ have been used, because the anisotropic fireball model presented in chapter 4 has a maximum η value compatible with the "standard" expected one for spherical fireballs ($\gtrsim 100$) and a dynamical range of two decades in η at most in order to satisfy the condition of no lateral expansion (see section 4.2.4). A total energy E_T between 2×10^{51} and 2×10^{53} ergs is then required for building up the anisotropic fireball model with η varying from 3 to 300 of chapter 4. Since we have assumed a constant ejecta mass per unit solid angle and have chosen a maximum value of E_T consistent with the maximum GRB isotropic energy ever observed, $\sim 10^{54}$ ergs, the values of E_T to explore must span at least as many decades as the values of η. In any case we have used also values of the fireball total energy E_T as low as 2×10^{49} ergs.

Observation frequencies between 10^{10} and 10^{19} Hz have been explored, roughly corresponding to the whole range of afterglow detection from radio to hard X–rays. We can more or less consider a light curve at 10^{19} Hz (or 40 keV) as a typical afterglow in the soft γ–ray band, a light curve at 10^{18} Hz (or 4 keV) as a typical X–ray afterglow, a light curve at 10^{17} Hz (or 0.4 keV) as a typical afterglow in the soft X–ray band, a light curve at 10^{16} Hz (or 40 eV) as a typical ultraviolet afterglow, a light curve at 10^{15} Hz (or 3000 Å) as a typical optical afterglow, a light curve at 10^{14} Hz (or 30 μ) as a typical afterglow in the Near Infrared, a light curve at 10^{13} Hz (or 300 μ) as a typical afterglow in the Far Infrared, a light curve at 10^{11} Hz (or 3 mm) as a typical afterglow in the microwave band.

The external particle density n_i has been always fixed to the value of 1 cm^{-3} typical of Interstellar Medium.

Equipartition parameters ϵ_e and ϵ_B have been fixed to values such that "relevant frequencies" (peak and cooling frequency) actually fall in the frequency range above in most cases and we can consistently neglect synchrotron self–absorption and inverse Compton radiation (see section 5.2).

The electron power law slope p has been fixed to an average value among the "measured" ones. In particular, the value $p = 2.6$ we use is the same used by [Granot, Piran & Sari 1999c].

Note that radio afterglow detections actually are at frequencies of a few GHz, but we do not show any calculation at $\nu = 10^9$ Hz because for a right description of afterglow emission at this frequency over the whole range of fireball parameters we use we should have taken into account synchrotron self–absorption. However qualitative behaviour at 10^9 Hz neglecting synchrotron self–absorption can be inferred from results at 10^{10} Hz according to the scaling properties that will be discussed in the following sections.

5.2 Rough estimate of the expected light curves

We can calculate in a very rough way the expected monochromatic afterglow light curves assuming that the emitting electrons at the time T are a single population with a power law energy distribution having a minimum Lorentz factor $\gamma_m(T)$ equal to the minimum Lorentz factor of electrons shocked along the line of sight at the time T, $\gamma_{e,min}(T)$, and a cut off Lorentz factor $\gamma_c(T)$ such that only electrons with a Lorentz factor lower than it have not cooled down during the comoving time interval corresponding to the observer time T.

Relevant frequencies

First of all we define the shock radius along the line of sight at the time T, $R_{los}(T)$, and all the quantities regarding matter just shocked along the line of sight, $\gamma_{los}(T)$, $n'_{los}(T)$, $e'_{los}(T)$ and $B_{los}(T)$ as we have done in section 3.6.6.

Then we can define the minimum Lorentz factor of the emitting electrons as

$$\gamma_m(T) \equiv \gamma_{e,min}(T) = \sqrt{1 + \left[\frac{p-2}{p-1}\frac{\epsilon_e}{m_e c^2}\frac{e'_{los}(T)}{n'_{los}(T)}\right]^2} \tag{5.1}$$

and the observed synchrotron frequency of electrons with Lorentz factor $\gamma_m(T)$ as

$$\nu_m(T) = \frac{3}{16}\frac{eB_{los}(T)}{m_e c}\frac{\gamma_m(T)^2}{\gamma_{los}(T)(1-\beta_{los}(T))} \tag{5.2}$$

Then, we estimate the comoving time corresponding to the observer time T as

$$\Delta t' = \int_0^T \left(\frac{dt'}{dt}\right) / \left(\frac{dT}{dt}\right) dT = \int_0^T \frac{ds}{\gamma_{los}(s)(1-\beta_{los}(s))} \tag{5.3}$$

The cut off Lorentz factor for our power law will be $\gamma_c(T)$ such that

$$\Delta t' = t_{cool}\left(\gamma_{e,c}(T)\right) \sim \frac{3}{4}\frac{8\pi m_e c}{\sigma_T B_{los}(T)^2}\frac{1}{\gamma_c(T)} \tag{5.4}$$

thus

$$\gamma_c(T) = \frac{3}{4}\frac{8\pi m_e c}{\sigma_T B_{los}(T)^2}\frac{1}{\Delta t'} \tag{5.5}$$

and the observed synchrotron frequency of electrons with Lorentz factor $\gamma_c(T)$, known as the cooling frequency, will be

$$\nu_c(T) = \frac{3}{16}\frac{eB_{los}(T)}{m_e c}\frac{\gamma_c(T)^2}{\gamma_{los}(T)(1-\beta_{los}(T))} \tag{5.6}$$

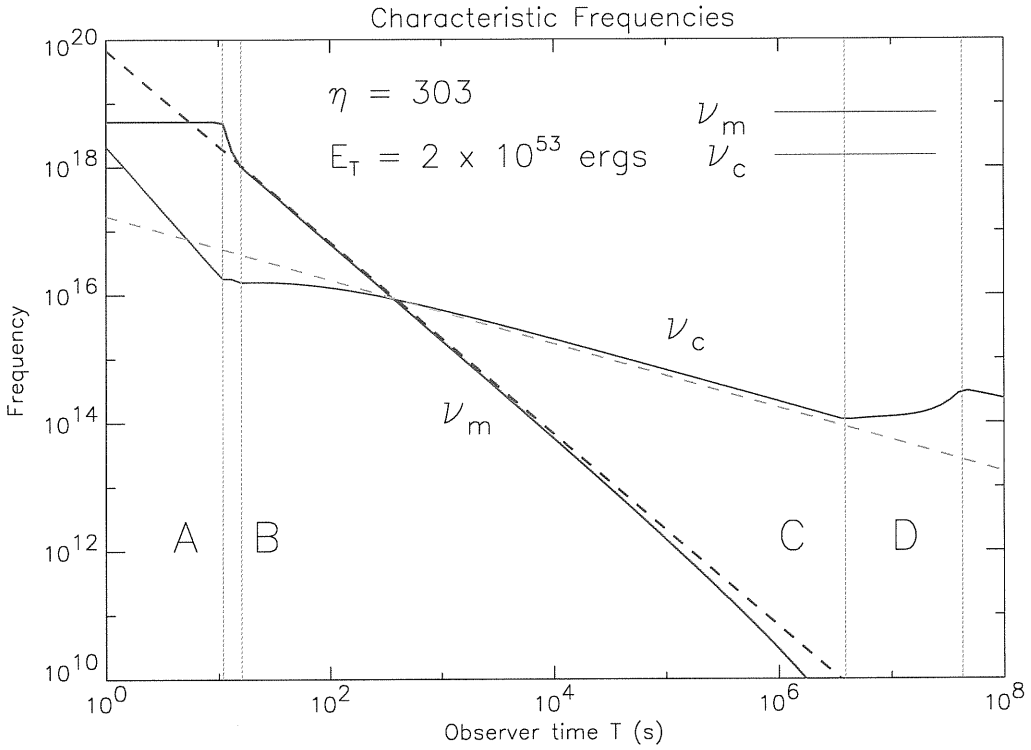

Figure 5.1: *Temporal evolution of the peak and cooling frequencies ν_m and ν_c for a spherical fireball with total energy $E_T \sim 2 \times 10^{53}$ ergs, baryon loading parameter $\eta = 303$, and equipartition parameters $\epsilon_e = 0.1$ and $\epsilon_B = 0.01$. The dashed lines represent corresponding estimation by [Sari, Piran & Narayan 1998], i.e. laws (5.9) and (5.10), expected to be in agreement with (5.2) and (5.6) only during the Blandford & McKee stage, i.e. in the time interval between the vertical line B and the vertical line C, after multiplication by 1.5 and 0.77 respectively (see text). The cross point corresponds to the time T_{fs} at which occurs the transition from fast-cooling regime (all emitting electrons cool on a timescale shorter than the hydrodynamical timescale) and slow-cooling regime (only electrons with a Lorentz factor greater than γ_c cool on a timescale shorter than the hydrodynamical timescale). The slopes of the solid curves during the other stages of expansion (coasting stage up to the vertical line A, first deceleration stage in between the vertical line A and the vertical line B, transition to Sedov in between C and D and Sedov after D) agree with the predictions in section 5.2.1.*

Note that the peak and cooling frequencies ν_m and ν_c we calculate through (5.2) and (5.6) respectively are in good agreement with the peak and cooling frequencies calculated by [Sari, Piran & Narayan 1998] in case of adiabatic expansion (see equation (11) therein) during the time interval corresponding to the Blandford & McKee stage (see fig.5.1, region between the vertical lines B and C).

The Blandford & McKee stage can be roughly assumed to last from the time $T_0(0)$ to the time $T_{crit}(0)$. These times are roughly given by

$$T_0(0) \sim 1.1 \times 10^2 \left(\frac{E_T}{10^{52}}\right)^{1/3} \left(\frac{\eta}{100}\right)^{-8/3} \text{ s} \tag{5.7}$$

$$T_{crit}(0) \sim 1.4 \times 10^6 \left(\frac{E_T}{10^{52}}\right)^{1/3} \text{ s} \tag{5.8}$$

A further slight dependence on η would lead to a 40% greater value of $T_0(0)$ and a 30% greater value of $T_{crit}(0)$ at $\eta = 3$, but as a first approximation we can neglect this effect and use (5.7) and (5.8).

We can rewrite [Sari, Piran & Narayan 1998] expressions for ν_m and ν_c as

$$\nu_m \sim 1.77 \times 10^{19} \left(\frac{\epsilon_B}{0.01}\right)^{1/2} \left(\frac{\epsilon_e}{0.1}\right)^{2} \left(\frac{E_T}{10^{52}}\right)^{1/2} T^{-3/2} \text{ Hz} \tag{5.9}$$

$$\nu_c \sim 7.9 \times 10^{17} \left(\frac{\epsilon_B}{0.01}\right)^{-3/2} \left(\frac{E_T}{10^{52}}\right)^{-1/2} n_i^{-1} T^{-1/2} \text{ Hz} \tag{5.10}$$

In principle the peak frequency $\nu_m(T)$ weakly depends on the electron power law slope p and [Sari, Piran & Narayan 1998] use the value $p = 2.5$, which represents the average of the best fit values obtained in case of observed afterglows, while we use $p = 2.6$ as done by [Granot, Piran & Sari 1999c] for a better comparison with their results. In (5.9) we have reported the value of $\nu_m(T)$ corrected to $p = 2.6$*. Nevertheless we find that in order to have the laws (5.9) and (5.10) tangent to ours within the time interval corresponding to the Blandford & McKee stage in the case $p = 2.6$ (the value we always use) we must multiply (5.9) by 1.2 and (5.10) by 0.77. This discrepancy must be ascribed to the approximated Blandford & McKee hydrodynamics we adopt. Following [Sari, Piran & Narayan 1998] we can define the time T_{fs} at which $\nu_m(T) = \nu_c(T)$. This will be the time at which the fireball passes from fast–cooling regime to slow–cooling regime and will depend on the fireball total energy E_T, on the baryon loading parameter η, on the external particle density n_i and on the equipartition parameters ϵ_e and ϵ_B.

*The correction factor is simply $\frac{f(2.6)}{f(2.5)} \sim 1.26$ with $f(p) = \frac{(p-2)^2}{(p-1)^2}$.

The approximated expression given by [Sari, Piran & Narayan 1998], or the expression obtained equating the "corrected" (5.9) and (5.10),

$$T_{fs} \sim 22 \left(\frac{\epsilon_B}{0.01}\right)^2 \left(\frac{\epsilon_e}{0.1}\right)^2 \left(\frac{E_T}{10^{52}}\right) n_i \quad \text{s} \tag{5.11}$$

approximates reasonably well our exact value of T_{fs} when it happens during the Blandford & McKee stage. A correction factor of 1.56 accounts for our approximated Blandford & McKee hydrodynamics and provides a better match between the value given by (5.11) and T_{fs}.

Actually, for the typical values we use for the equipartition parameters $\epsilon_e = 0.1$ and $\epsilon_B = 0.01$, the time T_{fs} given by (5.11) is expected to be a time of the Blandford & McKee stage, i.e. a time in between $T_0(0)$ and $T_{crit}(0)$, for $\eta \gtrsim 155 \left(\frac{E_T}{10^{52}}\right)^{-1/4}$, that is for high baryon loading parameter values. This case corresponds to the one usually studied in literature by authors that use pure Blandford & McKee evolution [Granot & Sari 2002]. Thus, in the following sections we will discuss first of all predictions and results for this typical case. In the case $\eta \lesssim 155 \left(\frac{E_T}{10^{52}}\right)^{-1/4}$ the transition time from fast cooling to slow cooling fixes at about $T_0(0)$ and eventually disappears at very low values of the baryon loading parameter. In fig.5.2 it can be seen, for instance, what happens to the transition from fast to slow cooling in the case already presented in fig.5.1 at decreasing η. First of all it can be seen the fast cooling stage reducing to a short episode at the beginning of the deceleration preceded by a slow cooling stage, then, for baryon loading parameter values < 20 we have no fast cooling episode at all.

Then, to conlude the discussion about the relevant frequencies in our afterglow spectrum, we recall Granot's estimation of the synchrotron self–absorption frequency ν_{sa}, i.e. the observer frequency below which the Blandford & McKee expanding fireball of shocked ISM would be optically thick to its synchrotron radiation [Granot , Piran & Sari 2000, Granot & Sari 2002]

$$\nu_{sa} \sim 4.9 \times 10^9 \frac{(p-1)^{3/5}}{(3p+2)^{3/5}} \frac{(p-1)}{(p-2)} \left(\frac{\epsilon_e}{0.1}\right)^{-1} \left(\frac{\epsilon_B}{0.01}\right)^{1/5} \left(\frac{E_T}{10^{52}}\right)^{1/5} n_i^{3/5} \quad \text{Hz} \tag{5.12}$$

The range of values we use for the total energy E_T makes us sure that this frequency is usually below the interval of observed frequencies 10^{10}–10^{19} Hz we are exploring, provided that the equipartition parameters ϵ_e and ϵ_B and the electron power law slope p are not too far from the standard values indicated. Thus we are self consistent in neglecting synchrotron self–absorption.

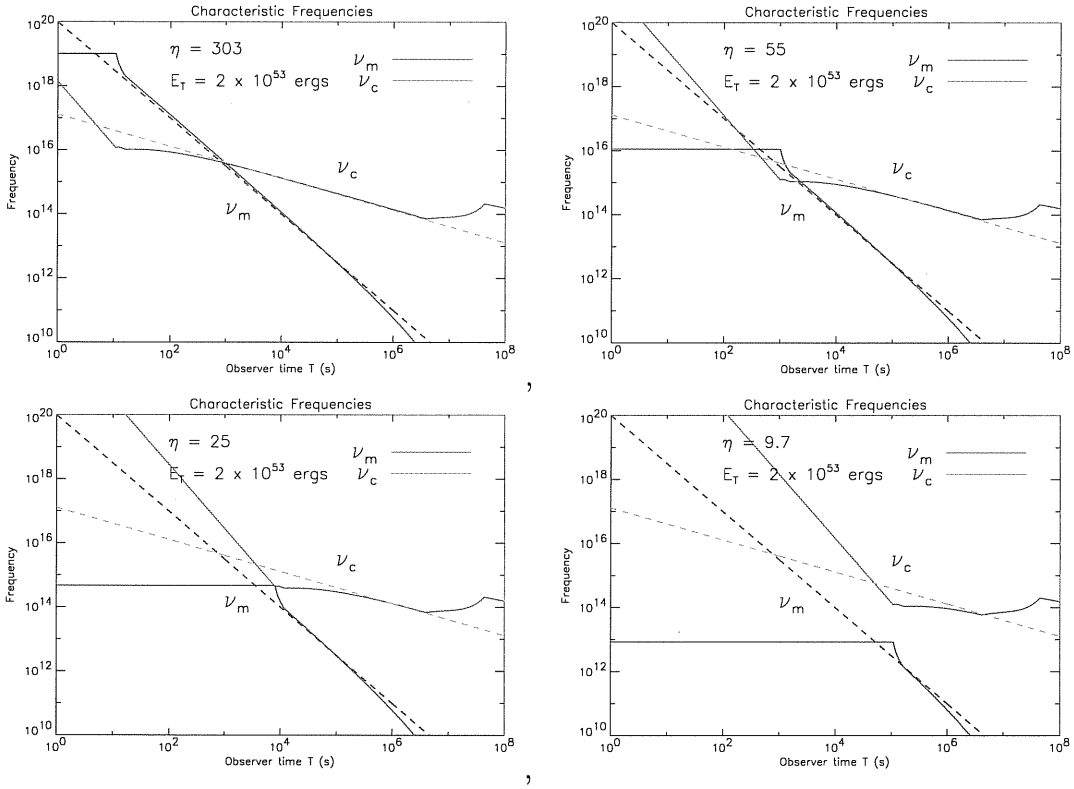

Figure 5.2: *Temporal evolution of the peak and cooling frequencies ν_m and ν_c for spherical fireballs with total energy $E_T \sim 2 \times 10^{53}$ ergs, different baryon loading parameter values and equipartition parameters $\epsilon_e = 0.1$ and $\epsilon_B = 0.01$. The dashed lines represent corresponding estimation by [Sari, Piran & Narayan 1998] just renormalized as explained in the text, i.e. laws (5.9) and (5.10) corrected by factors 1.2 and 0.77 respectively.*

Total Flux per unit frequency

The total number of emitting electrons will be

$$N(T) = \frac{4}{3}\pi R_{los}(T)^3 n_i \tag{5.13}$$

like in section 3.6.6, and the observed total flux per unit frequency (at peak frequency) is expected to be

$$F_{tot}(T) = \frac{1}{8}0.88\frac{4(p-1)}{3p-1}\frac{n_i}{3D^2}\frac{4}{3}\sigma_T c\frac{16m_e c}{3e}\sqrt{\frac{\epsilon_B}{8\pi}}\frac{\beta_m(T)^2 R_{los}(T)^3\sqrt{e'_{los}(T)}}{\gamma_{los}(T)^3(1-\beta_{los}(T))^2} \tag{5.14}$$

exactly as calculated in section 3.6.6, but the factor $\frac{1}{8}$, which have been added to improve the fit to numerical results.

Monochromatic Light curves and Spectra

Then, if we remember that the spectrum emitted by a cooled electron power law is expected to be a broken power law as explained in [Sari, Piran & Narayan 1998] (see fig.2.6) we can conclude that a reasonable approximation to the afterglow light curve might be following:

$$F_\nu^{app}(T) = \begin{cases} F_{tot}(T)\left(\frac{\nu}{\nu_c(T)}\right)^{1/3} & \nu < \nu_c(T) \\ F_{tot}(T)\left(\frac{\nu}{\nu_c(T)}\right)^{-1/2} & \nu_c(T) \le \nu \le \nu_m(T) \\ F_{tot}(T)\left(\frac{\nu_m(T)}{\nu_c(T)}\right)^{-1/2}\left(\frac{\nu}{\nu_m(T)}\right)^{-p/2} & \nu > \nu_m(T) \end{cases} \tag{5.15}$$

in the case $\nu_c(T) < \nu_m(T)$ (fast–cooling regime, equivalent to $T < T_{fs}$), or

$$F_\nu^{app}(T) = \begin{cases} F_{tot}(T)\left(\frac{\nu}{\nu_m(T)}\right)^{1/3} & \nu < \nu_m(T) \\ F_{tot}(T)\left(\frac{\nu}{\nu_m(T)}\right)^{-(p-1)/2} & \nu_m(T) \le \nu \le \nu_c(T) \\ F_{tot}(T)\left(\frac{\nu_c(T)}{\nu_m(T)}\right)^{-(p-1)/2}\left(\frac{\nu}{\nu_c(T)}\right)^{-p/2} & \nu > \nu_c(T) \end{cases} \tag{5.16}$$

in the case $\nu_c(T) > \nu_m(T)$ (slow–cooling regime, equivalent to $T > T_{fs}$).

If we wanted to neglect completely synchrotron cooling as done by [Granot, Piran & Sari 1999c] we would obtain a light curve approximated by

$$F_\nu^{app}(T) = \begin{cases} F_{tot}(T)\left(\frac{\nu}{\nu_m(T)}\right)^{1/3} & \nu < \nu_m(T) \\ F_{tot}(T)\left(\frac{\nu}{\nu_m(T)}\right)^{-(p-1)/2} & \nu \ge \nu_m(T) \end{cases} \tag{5.17}$$

5.2.1 Slopes prediction

Starting from (5.15), (5.16) and (5.17) and using the definitions (5.2), (5.6) and (5.14) together with the hydrodynamical evolution laws, we can easily predict the expected slopes of light curves and spectra in all possible cases. In order to illustrate the procedure, now we are going to discuss in detail predictions in the "standard" case presented in fig.5.1, i.e. a case with high baryon loading parameter (low initial baryon contamination), high total energy, and transition from fast to slow cooling during the Blandford & McKee stage.

- During the **coasting stage** (for $T_c(0) < T < T_d(0)$), for instance, we have approximately $\gamma_{los} \sim constant$, $R_{los} \propto t$, $T \propto t$, $e'_{los} \propto \gamma^2_{los} \sim constant$, $n'_{los} \propto \gamma_{los} \sim constant$, $B_{los} \propto \gamma_{los} \sim constant$ thus we expect $\nu_m \sim constant$, $\nu_c \propto T^{-2}$ and $F_{tot} \propto T^3$. The frequency range we investigate (from 10^{10} to 10^{19} Hz) is completely below ν_m. As a consequence, we expect that when we neglect the cooling of electrons

$$F_\nu^{app}(T) \propto T^3 \nu^{1/3} \tag{5.18}$$

  If we allow for electron cooling, since for the choice of fireball parameters made we should be in the fast cooling regime, then we expect

$$F_\nu^{app}(T) \propto \begin{cases} T^{11/3}\nu^{1/3} & \nu < \nu_c(T) \\ T^2\nu^{-1/2} & \nu_c(T) \leq \nu \leq \nu_m(T) \\ T^2\nu^{-p/2} & \nu > \nu_m(T) \end{cases} \tag{5.19}$$

- During the **Blandford & McKee stage** (for $T_0(0) < T < T_{crit}(0)$) we have approximately $\gamma_{los} \propto T^{-3/8}$, $R_{los} \propto T^{1/4}$, $e'_{los} \propto \gamma^2_{los}$, $n'_{los} \propto \gamma_{los}$, $B_{los} \propto \gamma_{los}$ thus we expect $\nu_m \propto T^{-3/2}$, $\nu_c \propto T^{-1/2}$ and $F_{tot} \sim constant$. As a consequence, we expect that when we neglect the cooling of electrons

$$F_\nu^{app}(T) \propto \begin{cases} T^{1/2}\nu^{1/3} & \nu < \nu_m(T) \\ T^{-\frac{3}{4}(p-1)}\nu^{-\frac{(p-1)}{2}} & \nu > \nu_m(T) \end{cases} \tag{5.20}$$

  If we allow for electron cooling, since the transition from fast cooling to slow cooling occurs during this stage, we expect

$$F_\nu^{app}(T) \propto \begin{cases} T^{1/6}\nu^{1/3} & \nu < \nu_c(T) \\ T^{-1/4}\nu^{-1/2} & \nu_c(T) \leq \nu \leq \nu_m(T) \\ T^{-\frac{(3p-2)}{4}}\nu^{-p/2} & \nu > \nu_m(T) \end{cases} \tag{5.21}$$

for $T < T_{fs}$ (or $\nu_c(T) < \nu_m(T)$) and

$$F_\nu^{app}(T) \propto \begin{cases} T^{1/2}\nu^{1/3} & \nu < \nu_m(T) \\ T^{-\frac{3}{4}(p-1)}\nu^{-\frac{(p-1)}{2}} & \nu_m(T) \leq \nu \leq \nu_c(T) \\ T^{-\frac{(3p-2)}{4}}\nu^{-p/2} & \nu > \nu_c(T) \end{cases} \tag{5.22}$$

for $T > T_{fs}$ (or $\nu_m(T) < \nu_c(T)$).

- During the **Sedov stage** (for $T > T_{sed}(0)$), we have approximately $\gamma_{los} \sim 1$, $\beta_{los} \propto T^{-3/5}$, $R_{los} \propto T^{2/5}$, $e'_{los} \propto \beta_{los}^2$, $n'_{los} \sim constant$, $B_{los} \propto \beta_{los}$ thus we expect $\nu_m \propto T^{-3}$, $\nu_c \propto T^{-1/5}$ and $F_{tot} \sim T^{3/5}$. Now the frequency range we investigate is completely above ν_m. As a consequence, we expect that when we neglect the cooling of electrons

$$F_\nu^{app}(T) \propto \ T^{-3\frac{(5p-7)}{10}}\nu^{-\frac{(p-1)}{2}} \tag{5.23}$$

If we allow for electron cooling, since we should be in the slow cooling regime and above ν_m, we expect

$$F_\nu^{app}(T) \propto \begin{cases} T^{-3\frac{(5p-7)}{10}}\nu^{-\frac{(p-1)}{2}} & \nu_m(T) \leq \nu \leq \nu_c(T) \\ T^{-\frac{(3p-4)}{2}}\nu^{-p/2} & \nu > \nu_c(T) \end{cases} \tag{5.24}$$

Discussion of the expected slopes of light curves and spectra during the transition stages is not as simple because gross time dependencies of ν_m, ν_c and F_{tot} are not pure power laws. So, we will not give explicit predictions for expected slopes during these stages.

5.3 Reproducing results in literature.... and beyond

5.3.1 Results neglecting the cooling of the electrons

This is the case that has been already calculated in [Granot, Piran & Sari 1999c]. However Granot's results should be used only for the description of afterglows produced during the Blandford & McKee stage, i.e. over the time interval between $T_0(0)$ and $T_{crit}(0)$, and are especially devoted to explore and characterize the light curve peak shape.

We have described the fireball hydrodynamics in a self–consistent way also before and after the Blandford & McKee stage, so we can follow the afterglow light curve on a more extended temporal range, including early evolutionary stages and transition to the non relativistic expansion stage. We will show when and how the light curve behaviour should differ from Granot's predictions and discuss if such deviations might be observed.

In what follows we will often plot light curves down to very low (and likely undetectable) flux levels, or late observer times, just to check the consistency of the results of our numerical calculations.

In this section, first we will discuss the general behaviour of a set of afterglow light curves in different bands form a single fireball, i.e. with a fixed value of the baryon loading parameter and a fixed value of the total energy. We will present the set of light curves referring to $\eta = 303$ (high value) and $E_T = 2 \times 10^{53}$ ergs in fig.5.3 and then we will show that our results match very well Granot's results on the time interval corresponding to the Blandford & McKee stage and also agree with the approximated light curve estimation calculated as described in section 5.2 on the same time interval, though the properly calculated light curve peaks are smoother and broader. At this regard fig.5.4 will illustrate the matching of light curve peak times with Granot's predictions, fig.5.5 will illustrate the agreement of light curve slopes with predictions of section 5.2.1 and fig.5.6 will show the comparison of calculated light curves with their rough approximations $F_\nu^{app}(T)$ given by (5.17). As far as the reliability of the shape of the light curves set of fig.5.3 is concerned, figs.5.7 and 5.9, always referring to $\eta = 303$ and $E_T = 2 \times 10^{53}$ ergs will show respectively that pure radial and pure

angular integration equally contribute to the observed flux, though becoming important only by the end of the Blandford & McKee stage, and that the effect of exact synchrotron emissivity calculation is making light curve peaks even broader than what obtained with the broken power law approximation. Finally fig.5.8 shows that the light curve segments in the time interval corresponding to the Blandford & McKee stage are scarcely contributed by radiation emitted before the Blandford & McKee stage.

Then, fig.5.17 referring to $\eta = 25$ (moderately low value) and $E_T = 1.8 \times 10^{51}$ ergs, gives a second set of afterglow light curves at fixed baryon loading parameter and total energy. In this case it is apparent that the agreement with Granot's results over the time interval corresponding to the Blandford & McKee stage is not universal any longer because there is a sub set of light curves having a different shape and peak time evolution with the observed frequency.

At this point we will study the effect of varying the total energy at fixed baryon loading parameter (fig.5.10 for $\eta = 303$ and fig.5.16 for $\eta = 25$) on the light curves peak time, just to conclude the comparison with Granot's results and start introducing the new ones.

After that, since we have seen comparing figs.5.3 and 5.17 that decreasing the η and E_T values a new family of light curves appears, we will discuss the general behaviour of a set of light curves in a fixed band produced by a sample of spherical fireballs having the same total mass of ejecta M_T and different total energy E_T, i.e. different baryon loading parameter η. We will show the set of light curves in fig.5.12, we will illustrate the considerations about peak times in figs.5.13 and 5.14 and the considerations about the slopes in fig.5.15. All these figures refer to the observed frequency 10^{16} Hz). The sample of spherical fireballs with fixed ejecta mass we use covers the whole range of spherical models required to build up an anisotropic fireball as described in chapter 4. Just before of fig.5.12, we will present also the effect on the afterglow light curve of varying the mass of ejecta at fixed total energy, i.e. varying the value of η at fixed E_T instead that at fixed M_T (see fig.5.11, always referring to the single observed frequency 10^{16} Hz). The aim of plotting and analysing all these light curves is the identification of the ranges of fireball parameters and observed frequency for which the light curves do not match Granot's ones, and the characterization of the properties of the just identified second family of light curves. Thus, a global discussion on the afterglow peaks will be presented and looking again at figs.5.4, 5.13, 5.14 and 5.17 will help in summarizing the properties of the two families of light curves. Finally, fig.5.18 is shown as a tool to establish peaks detectability.

Now I will discuss in details all the figures I have just quoted.

In **fig.5.3** we see a set of afterglow light curves calculated under the same physical assumptions of [Granot, Piran & Sari 1999c]: no electron cooling, magnetic field equipartition at a constant level ϵ_B, power law distributed shocked electrons energy, total electron energy equal to a constant fraction ϵ_e of the fluid internal energy, local comoving emissivity approximated as a broken power law as shown in appendix D.1.3.

In this figure, as in all figures that follow, the equipartition parameters ϵ_e and ϵ_B have been fixed to the values 0.1 and 0.01 respectively, and the electron power law slope p has been fixed to the value 2.6.

The parameter p affects mainly light curve slopes[†] and we have chosen the same value used in [Granot, Piran & Sari 1999c] for a better comparison with their results. As it comes out from the discussion in section 5.2 the parameters ϵ_e and ϵ_B, instead, sensibly affect the peak and cooling frequencies $\nu_m(T)$ and $\nu_c(T)$ and the "transition time" T_{fs}. Their values have been chosen in such a way that, for total energies and baryon loading parameter values varying respectively in the ranges 10^{50}–10^{53} ergs and 3–300, at least one of the relevant frequencies ν_m or ν_c is always in the "observable" frequency range going from 10^{10} Hz (radio) to 10^{19} Hz (soft γ–rays), while ν_{sa} is always below it and synchrotron self–absorption never affects our considerations. Remember the parameter ϵ_B also influences the light curve normalization, though less than the fireball total energy, being $F_{max} \propto \epsilon_B^{1/2} E_T$.

For the light curves shown in fig.5.3, the shape between the vertical lines B and C that mark the beginning and the end of the Blandford & McKee stage should be, and actually is, the same found by [Granot, Piran & Sari 1999c]. According to section 3.6.7, the peak times T_{peak} falling between B and C are well approximated by the solutions of the equation $\phi(\nu, T) = \frac{\nu}{\nu_m(T)} = \phi_{peak}$ with $\phi_{peak} = 2$[‡]. A change of variable from T to ϕ actually makes all the curves a single one, at least in the part near the peak occurring at $\phi \sim \phi_{peak}$ (remember that we do not expect self–similarity in the variable ϕ out of the Blandford & McKee stage) with the exception of the highest and lowest frequency light curves. Such curves peak outside the time interval delimited by B and C and have respectively a slightly less broad and a slightly broader peak. The

[†]From definitions (5.2) and (5.14) it is apparent that also the peak frequency $\nu_m(T)$ and the total flux per unit frequency at $\nu_m(T)$, $F_{tot}(T)$, slightly depend on p, but this dependency is weaker than anyone else.

[‡]Remember that in [Granot, Piran & Sari 1999c] the light curve peak time T_{peak} was found as the solution of the equation $\phi_{granot}(\nu, T) = \phi_{peak}$ with $\phi_{peak} = 1.88$

estimated peak time values found as solutions of the equation $\phi(\nu, T) = \phi_{peak}$ with $\phi_{peak} = 2$ start to disagree slightly from the "true" peak times when the observation frequency ν decreases (see **fig.5.4**) and/or when η decreases (see **fig.5.13**). In the general case, in our model, light curve peaks occurring during the Blandford & McKee stage correspond to values of ϕ equal to $\phi_{peak}(\eta, \nu) = 2g(\eta, \nu)$ where the function g is equal to 1 within about 20% over the range of frequencies and baryon loading parameter values we explore. This varying behaviour of ϕ_{peak}, interpreted as a small violation of self–similarity of afterglows, is related to the modified evolution laws we use for the Blandford & McKee stage, which are slightly violating self–similarity themselves.

Remembering that during the Blandford & McKee stage the peak frequency $\nu_m(T)$ can be approximated with the law (5.9) times the factor 1.2, that the start time of the Blandford & McKee stage can be approximated with the law (5.7), and using the approximation $\phi_{peak}(\eta, \nu) \sim 2$, we can rewrite the condition that the peak time $T_{peak}(\nu)$ satisfying the equation $\phi(\nu, T_{peak}(\nu)) = \frac{\nu}{\nu_m(T_{peak}(\nu))} = \phi_{peak}(\eta, \nu)$ actually falls between the lines B and C (i.e. $T_{peak}(\nu) > T_0(0)$) as

$$\eta > 80 \left(\frac{\nu}{10^{16}}\right)^{1/4} \left(\frac{\epsilon_B}{0.01}\right)^{-1/8} \left(\frac{\epsilon_e}{0.1}\right)^{-1/2} \left(\frac{E_T}{10^{52}}\right)^{1/24} \tag{5.25}$$

The relation (5.25) can be interpreted as a law saying which minimum baryon loading parameter a fireball must have in order to see the afterglow peak during the Blandford & McKee stage (or after) at a given frequency ν, or below which frequency the afterglow would be seen peaking in the Blandford & McKee stage (or after) given a certain fireball with its fixed baryon loading parameter. A further relation telling the maximum baryon loading parameter for which the afterglow at a given frequency peaks in the Blandford & McKee stage (or before), or the minimum frequency at which the afterglow from a given fireball peaks in the Blandford & McKee stage (or before) can be found from the condition $T_{peak}(\nu) < T_{crit}(0)$, but for our choice of fireball parameters and observation frequencies it is less constraining than the previous one, and for simplicity we will not use it.

The relation (5.25) is telling us the range of parameters for which we expect to be consistent with Granot's results, and the light curve is expected to have the self–similar shape discussed in [Granot, Piran & Sari 1999c].

Actually it can be calculated that for $\eta = 303$ and $E_T = 2 \times 10^{52}$ ergs (the values used for fig.5.3), the light curve at 10^{19} Hz should peak before the Blandford & McKee stage, while for $\eta = 25$ and $E_T = 1.8 \times 10^{52}$ ergs (the values used for fig.5.17), all the light curves at $\nu > 10^{14}$ Hz should peak before the Blandford & McKee stage. In both

cases only the lowest frequency light curve at 10^{10} Hz is expected to peak just at the end of the Blandford & McKee stage.

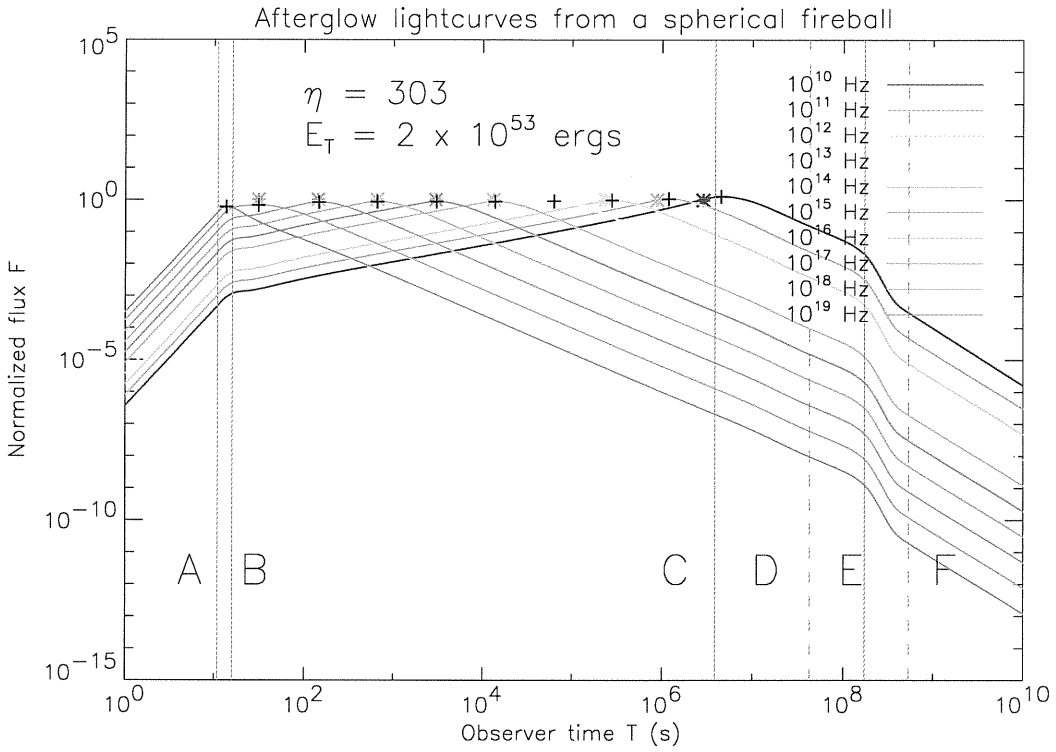

Figure 5.3: *Monochromatic afterglow light curves from a fireball with total energy* $E_T = 2 \times 10^{53}$ *ergs and baryon loading parameter* $\eta = 303$ *in the case* $\epsilon_e = 0.1$ *and* $\epsilon_B = 0.01$ *and for an electron power law slope* $p = 2.6$. *The vertical lines A,B,C and D represent the times at which the fireball front enters respectively the deceleration stage, the Blandford & McKee stage, the transition to the Sedov stage and the Sedov stage. The vertical lines E and F represent the times at which the fireball back enters the transition to Sedov stage and the Sedov stage respectively. The black crosses mark the peak positions and the coloured crosses indicate estimated peak positions according to the requirement* $\phi(\nu, T) = \frac{\nu}{\nu_m(T)} = constant = 2$. *These light curves have been calculated approximating the fluid element emissivity with the same broken power law used by [Granot, Piran & Sari 1999c] (see section D.1.3, equations (D.25) and (D.34)) for a better comparison with their results.*

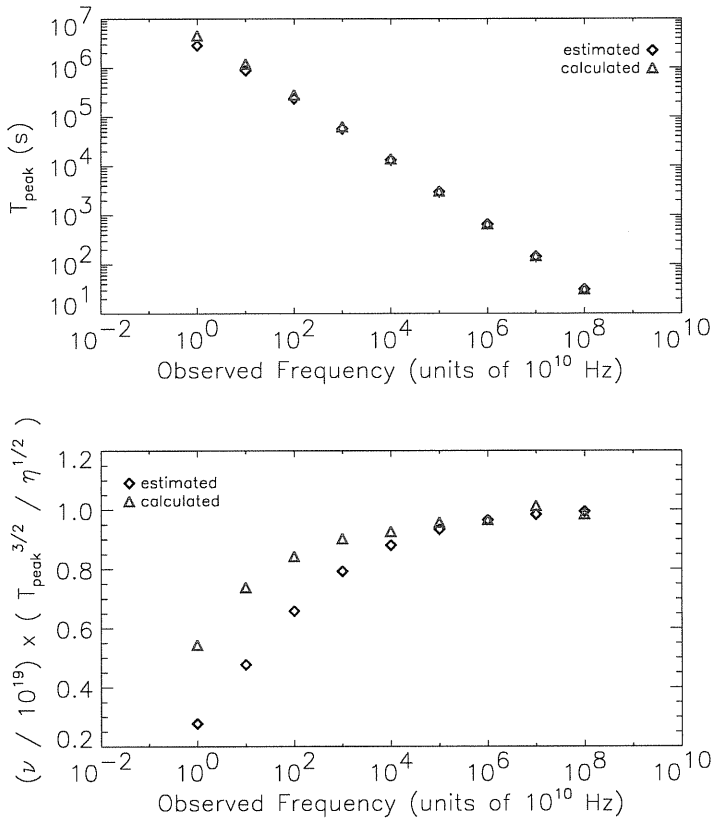

Figure 5.4: *In the upper panel peak times T_{peak} of the light curves in fig.5.3 are plotted versus the observed frequency. Only the frequencies for which the peak is expected during the Blandford & McKee stage are shown. The agreement between estimated values (coloured crosses in fig.5.3) and "true" values (black crosses in fig.5.3) is quite good. In the lower panel I plot versus the observed frequency a quantity proportional to $\phi_{granot}(\nu, T_{peak}) \propto \nu\, T_{peak}^{3/2} \eta^{-1/2}$, expected to be constant for peaks occurring during the Blandford & McKee stage if the hydrodynamics were exactly that used by [Granot, Piran & Sari 1999c] (see section 3.6.7). It can be seen that neither the estimated values of T_{peak} nor the "true" ones give rise to an horizontal line. This was expected in the case of estimated peak times because they have been calculated solving $\phi(\nu, T) = \frac{\nu}{\nu_m(T)} = \phi_{peak} = 2$ with $\nu_m(T)$ given by (5.2) instead of solving $\phi_{granot}(\nu, T) = \phi_{peak} = 2$. However, the small discrepancy between the two curves in the lower panel, corresponding to estimated and "true" T_{peak} values respectively, tells us that the self–similarity property of afterglows during the Blandford & McKee stage is slightly violated, clearly because of our generalizations of evolution laws. To be precise the "true" values of the peak time T_{peak} do not satisfy the relation $\phi(\nu, T_{peak}(\nu)) = \phi_{peak} = 2$ but the relation $\phi(\nu, T_{peak}(\nu)) = \phi_{peak}\; g(\nu)$ where $g(\nu)$ is a function dependent on the modifications we have done to the pure Blandford & McKee evolution laws that must be calculated numerically. We find that $g(\nu) \sim 1$ within 17% for ν varying from 10^{10} to 10^{19} Hz, and $g\,(10^{16}) = 1$.*

It is interesting to note that for all light curves in fig.5.3 the same decay slope observed while the front of the fireball goes through the Blandford & McKee stage (i.e. between B and C) stays approximately constant until the back of the fireball too definitely exits such evolutionary stage (vertical line E). Then a steepening occurs that seems to end just before the whole fireball (back included) has started Sedov expansion. After that, the decay slope starts again to agree with predictions (see **fig.5.5**). The transient steepening between the times E and F should be further investigated because it might be related to the hydrodynamics of the transition from Blandford & McKee to Sedov, which has been modeled just to join smoothly the two known self–similar stages. Since light curve slopes during these stages are reliable, it is not so important that the detailed behaviour of the light curves on the short time interval between the lines E and F is transition dependent. In any case, form an observational point of view, at times as late as the beginning of Sedov stage, the predicted afterglow flux at frequencies higher than radio is so low that it is unlikely to be detectable.

Before changing the fireball parameters and see what happens, we stop and analyze all the other properties of the light curves of fig.5.3. First of all the agreement with the analytic approximation (5.17). In **fig.5.6** some light curves of fig.5.3 are compared to corresponding light curves due to radiation from newly shocked electrons along the line of sight only, i.e. light curves given by (5.17). Emission from the whole volume behind the shock and emission from matter just behind the shock along the line of sight start to disagree during the transition to the Sedov stage, i.e. when the effect of volume integration starts to be significant. Remember that when the fireball expansion velocity is highly relativistic, emission is highly beamed, and the observer is actually reached only by radiation emitted from a small portion of the fireball around the line of sight. As the fireball slows down, the visible portion of the fireball increases and observed radiation has significant contributions also from directions different from the line of sight and/or matter far behind the the shock (see also fig. 5.7).

Another question to be addressed is about the importance of the whole integration in the resulting afterglow light curve shape. This can be studied calculating separately contributions from the radial integration and the angular integration, and from the different volume regions corresponding to different evolutionary stages in time of emission.

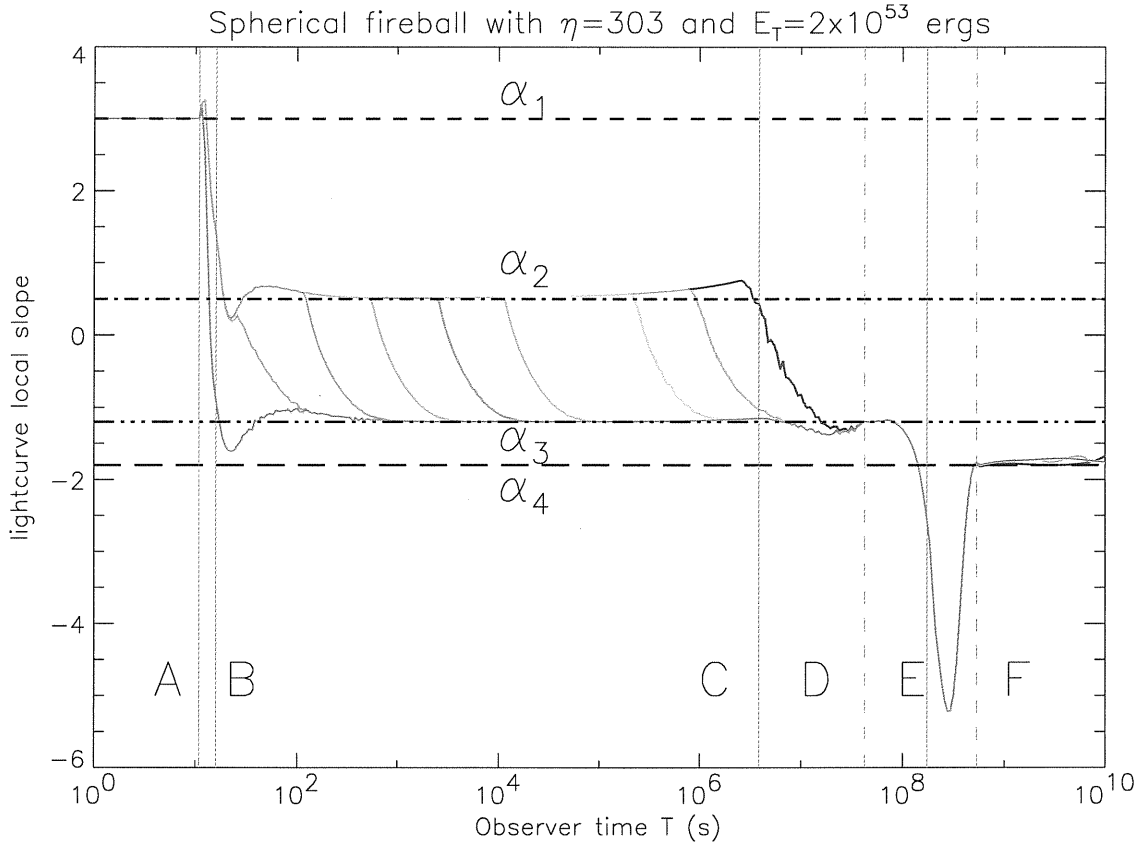

Figure 5.5: *Plot of the local slopes of afterglow light curves in fig.5.3 versus the observer time. The vertical lines A,B,C,D,E and F have the same meaning as in fig.5.3. Same colors as in fig.5.3 have been used to indicate different frequencies. The horizontal lines* $\alpha_1 = 3$, $\alpha_2 = \frac{1}{2}$, $\alpha_3 = -\frac{3}{4}(p-1)$ *and* $\alpha_4 = -\frac{3}{10}(5p-7)$ *represent the slopes expected respectively during the coasting stage, during the Blandford & McKee stage before the peak, during the Blandford & McKee stage after the peak and during the Sedov stage (see section 5.2.1). It can be seen each light curve has segments following the right power law decay according to predictions.*

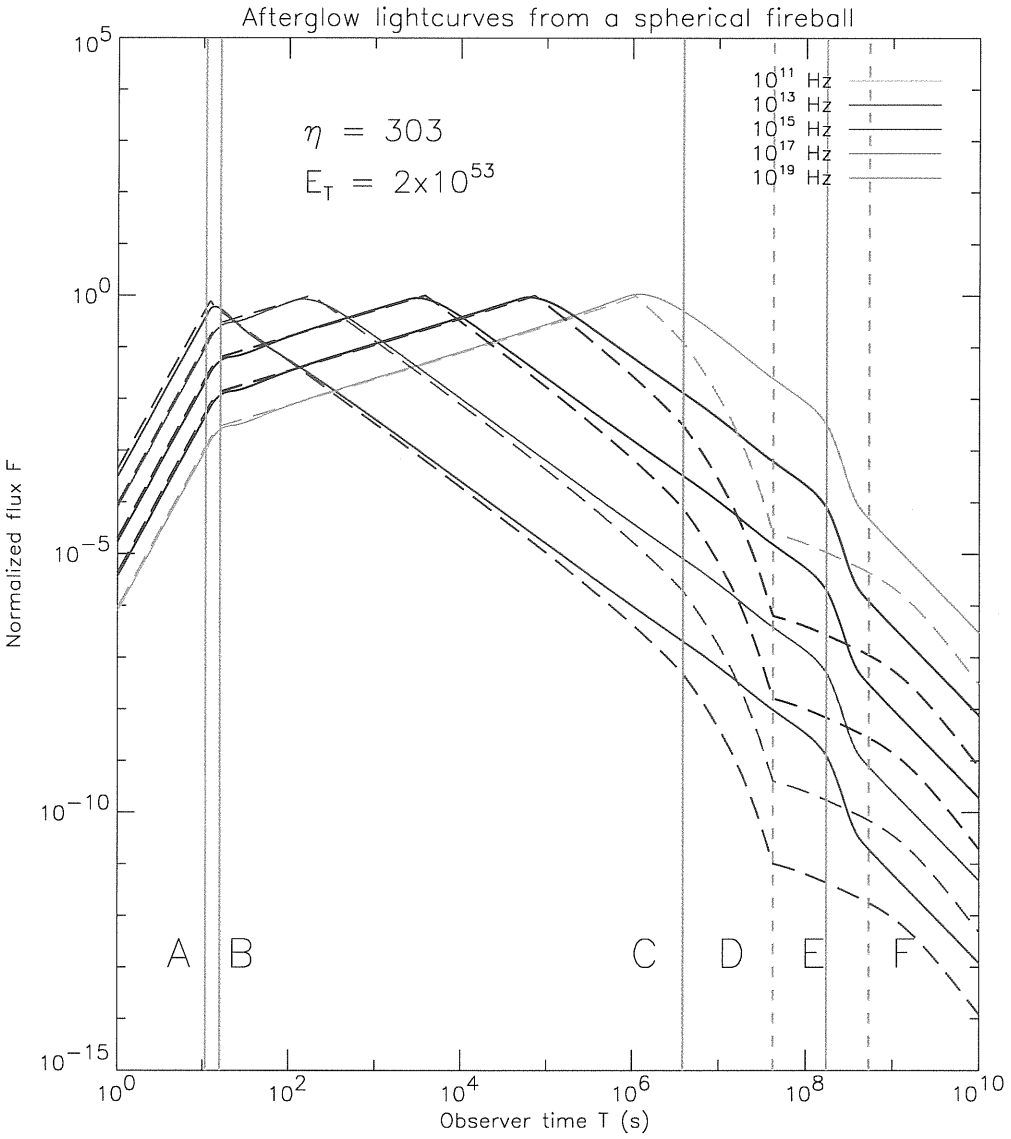

Figure 5.6: *In this figure, some of the light curves already plotted in fig.5.3 are compared to the corresponding approximated light curves calculated using $F_\nu^{app}(T)$ given by (5.17). Since for a time T of the Blandford & McKee stage the volume integrated observed spectrum $F_\nu(T)$ peaks at a frequency $\nu_{peak} \sim 2\ \nu_m(T)$, while $F_\nu^{app}(T)$ peaks at $\nu_m(T)$, we have calculated $F_\nu^{app}(T)$ using a peak frequency value $2\ \nu_m(T)$ in order to make peaks coincident and help the visual comparison.*

In **fig.5.7** is it shown how pure radial and pure angular integration contribute in the calculation of one of the afterglow light curves of fig.5.3. It is apparent that both radial and angular integration start to give substantial contribution to the light curve (i.e. whole volume integration becomes important) just before the vertical line C, that is at the end of the Blandford & McKee stage, when the integration volume has filled the whole equal–T surface (see section 3.6.4, and fig.3.6 in particular) and expansion velocity of the fireball front has decreased enough that the beaming cone of lateral fluid elements intersects the line of sight and radiation from off axis matter can reach the observer.

In **fig.5.8** it can be seen that the effect of emission during the early stages of evolution becomes negligible on the portion of afterglow light curve corresponding to the Blandford & McKee stage and following stages. However, taking in account the early stages of fireball evolution is important when formulating predictions about afterglow light curves from spherical fireballs having low baryon loading parameter and/or total energy.

Now we must address how much is relevant for the final afterglow light curve shape the broken power law approximation we have used for the synchrotron comoving emissivity. In **fig.5.9** it can be seen that using the exact synchrotron spectrum for radiation emitted by a single volume element instead of the broken power law approximation discussed in appendix D only makes the afterglow light curve more rounded near the peak.

Finally, we check that the peak time dependence of light curves of fig.5.3 on the fireball total energy and frequency is as expected. In **fig.5.10** it can be seen that for peaks occurring during the Blandford & McKee stage, the peak time T_{peak} roughly scales as $E_T^{1/3}\nu^{-2/3}$. All the light curves in this figure are due to fireballs having the same value of η. Different panels correspond to different observation frequencies ν and different line styles within each panel correspond to different values of E_T. Peak times are earlier at higher frequency and lower energy. On the other hand, it can be seen in **fig.5.11**, that lowering η at constant total energy E_T has no effect on the peak time for peaks occurring during the Blandford & McKee stage (light curves with $\eta \gtrsim 90$ in this case). From the same figure it is also apparent that light curves from fireballs with low η (i.e. light curves that peak before the Blandford & McKee stage beginning according to the relation (5.25)) have a different peaking behaviour. We start recognizing the existence of two class of peaks (or light curves). We will discuss it below.

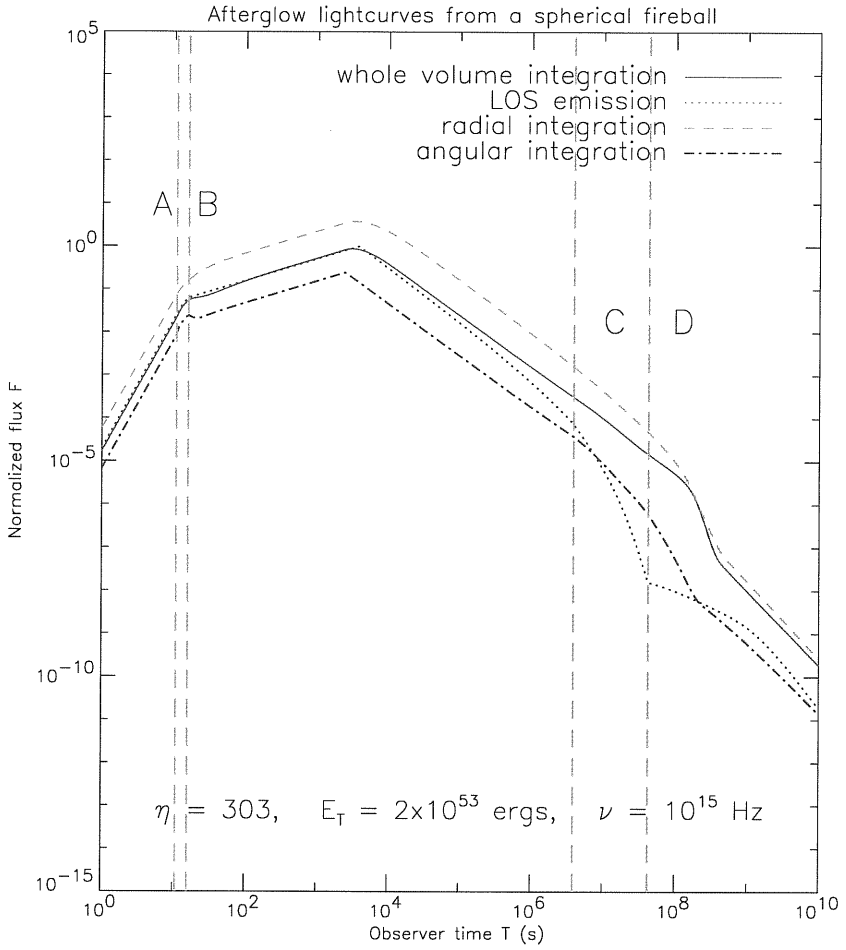

Figure 5.7: *The afterglow light curve at* 10^{15} *Hz already shown in fig.5.3 (solid line) is plotted together with the corresponding approximated light curve* $F_\nu^{app}(T)$ *given by (5.17) as in fig.5.6 (dotted line). The other two curves represent respectively the result of pure radial (dashed line) and pure angular integration (dot dashed line) discussed in section 3.6.5. The normalization constants have been artificially changed in order to make the comparison easier. The dashed and dot dashed curves follow the solid line better than the dotted line. They simply peak a slightly different times. It is then apparent that whole volume integration becomes important by the of the Blandford & McKee stage (vertical line C) and after and that both radial and angular integration are relevant. On the other hand, the small bump at the end of the transient deceleration (vertical line B) seems to be entirely an effect of the angular integration.*

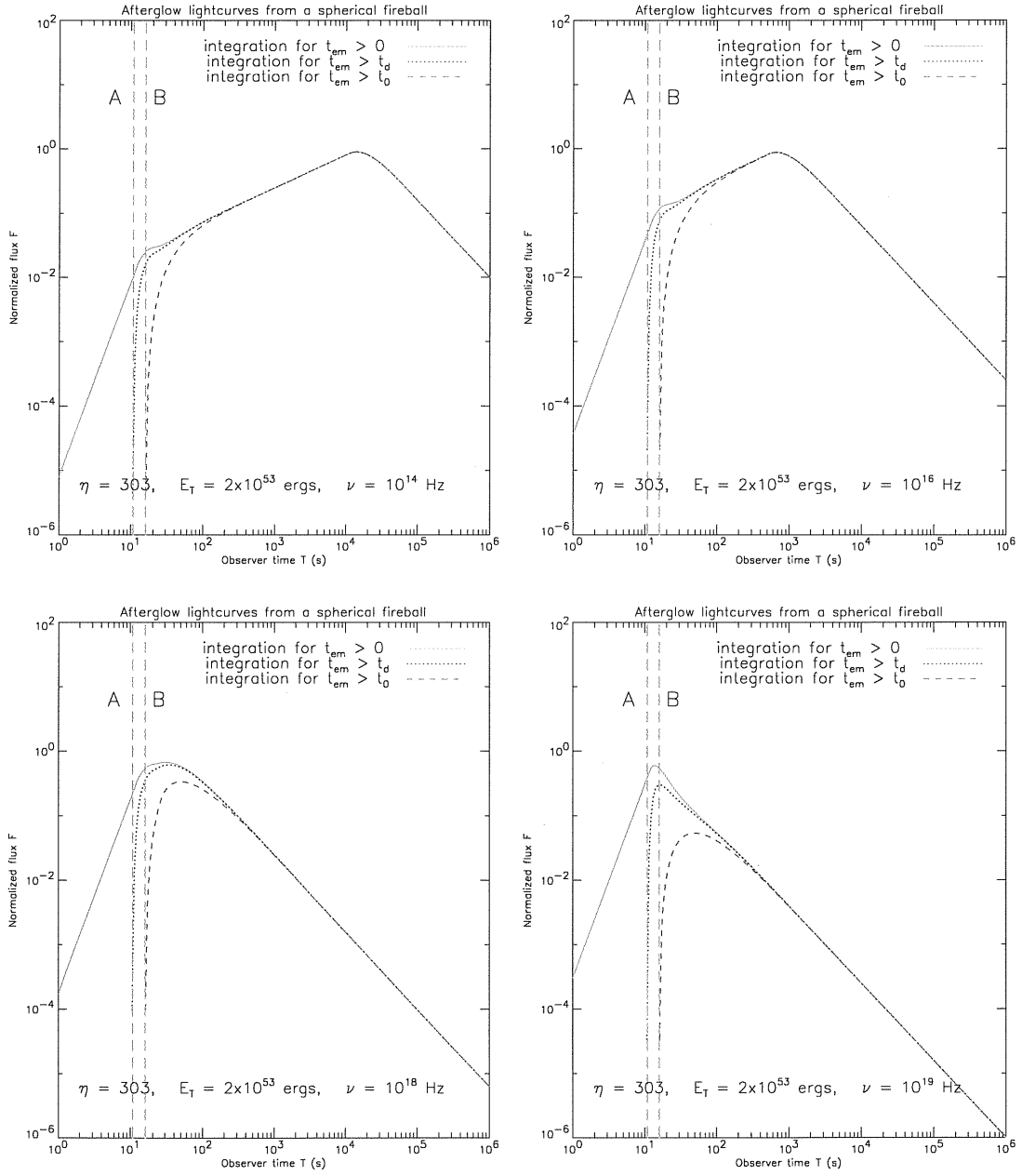

Figure 5.8: *Solid lines in these four panels are four afterglow light curves extracted from the set presented in fig.5.3. The dotted lines are the corresponding light curves calculated by taking in account only fireball fluid elements emitting at a time greater than t_d, i.e. neglecting emission from the fireball portion in the coasting or free expansion stage. The dashed lines are what we obtain by taking in account only fireball fluid elements emitting at a time greater than t_0, i.e. neglecting emission from stages before the Blandford & McKee.*

It is clear that the contribution of radiation emitted during the coasting stage, or even before, is not relevant on the portion of the afterglow light curve corresponding to the Blandford & McKee stage. Contribution of radiation emitted during the transient early deceleration stage quickly becomes not relevant too.

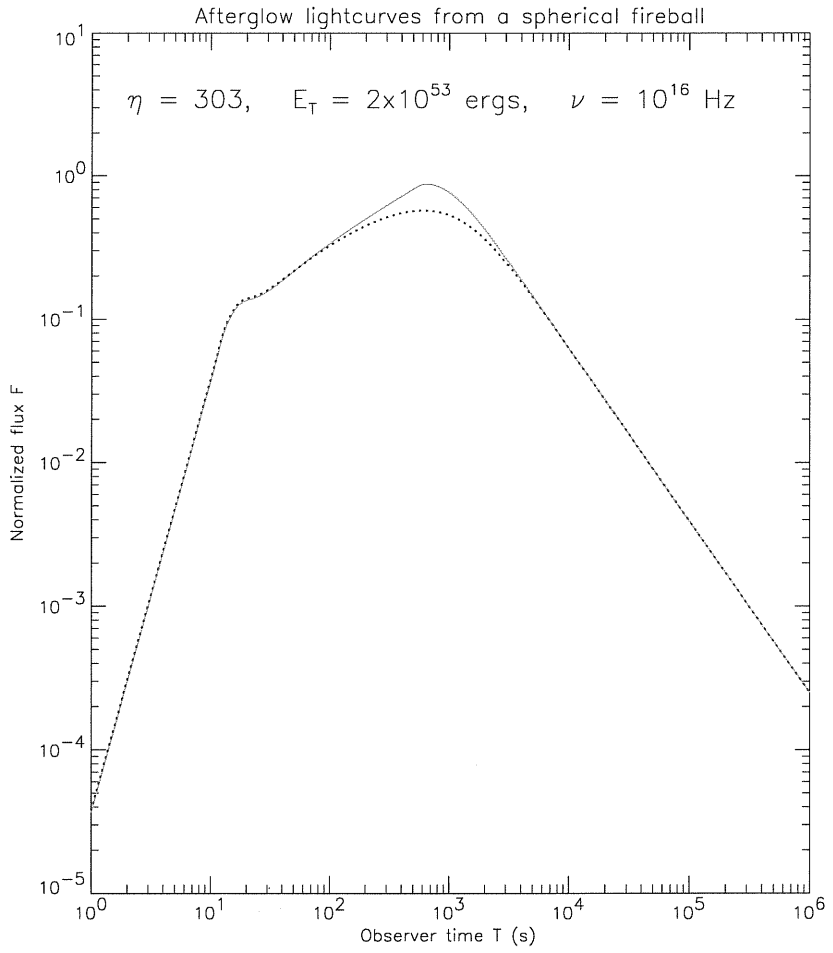

Figure 5.9: *The solid line is the* 10^{16} *Hz afterglow light curve already plotted in fig.5.3. The dotted line is the corresponding light curve obtained without approximating the fluid element comoving emissivity with the same broken power law used by [Granot, Piran & Sari 1999c]. The true comoving emissivity has been calculated through numerical integration as* $j'(\nu') = \int_{\gamma_{e,min}}^{+\infty} d\gamma_e N(\gamma_e) < P'_{\gamma_e}(\nu') >$ *with the single particle spectrum* $< P'_{\gamma_e}(\nu') >$ *defined by (D.14) in appendix D and the electron distribution* $N(\gamma_e)$ *defined as an infinite power–law with slope* p *and low energy cut off* $\gamma_{e,min}$ *given by (3.195) with the local particle and energy density evaluated at the time of emission.*

It can be seen that the only difference between the solid and the dotted curve is a more rounded peak surely due to the more rounded peak in the true single particle spectrum as compared to the broken power–law approximation.

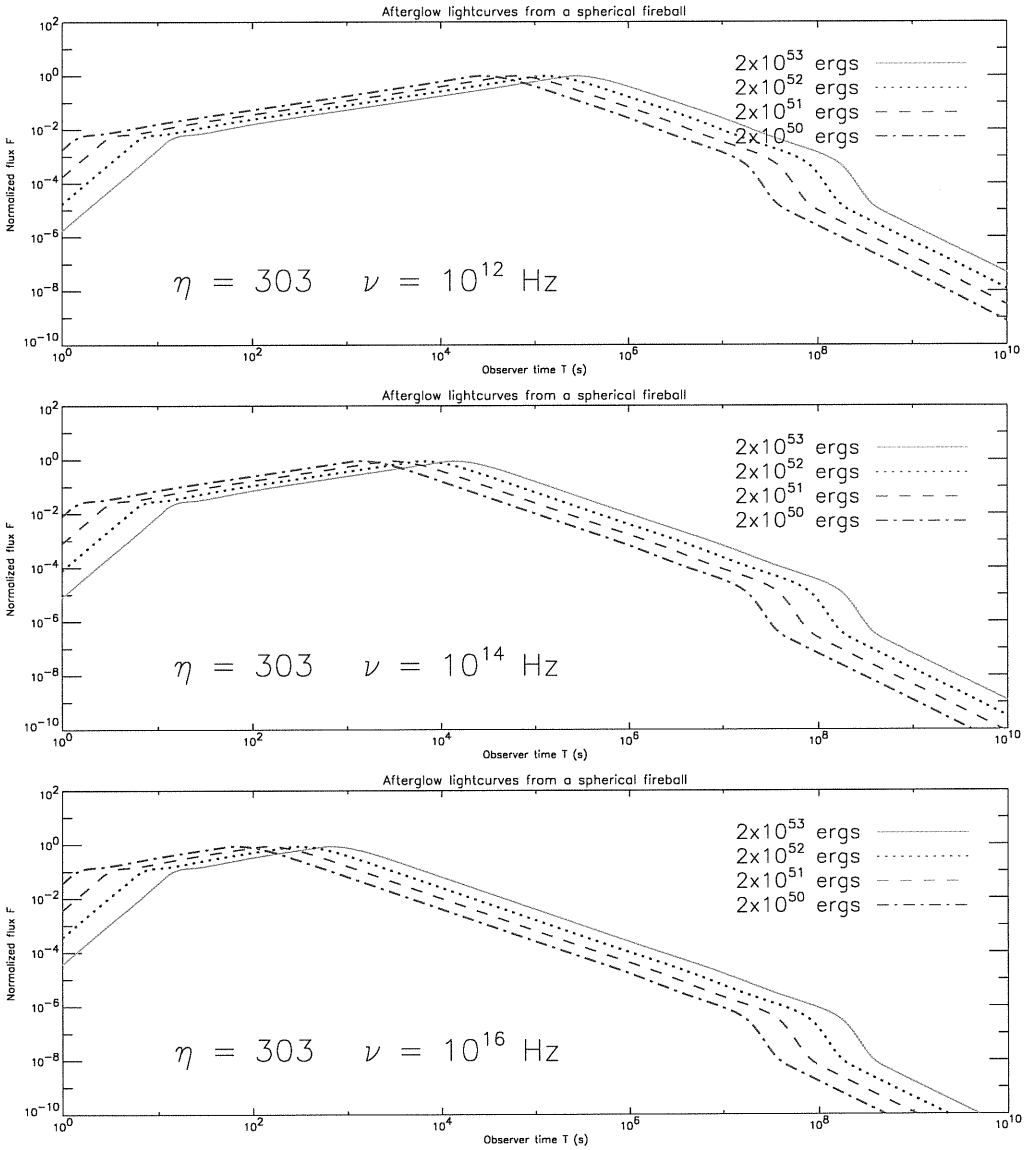

Figure 5.10: *Afterglow light curves for spherical fireballs at constant baryon loading parameter* $\eta = 303$ *and different total energies. Equipartition parameters and electron power law slope are as in fig.5.3,* $\epsilon_e = 0.1$, $\epsilon_B = 0.01$ *and* $p = 2.6$, *and electron cooling is neglected as in [Granot, Piran & Sari 1999c]. In all these cases the peak time* T_{peak} *is always a time of the Blandford & McKee stage and moves to lower values at decreasing total energy and increasing frequency as expected from the discussion in the caption of fig.5.4. The normalized peak heights are unaffected by baryon loading parameter/total energy and frequency.*

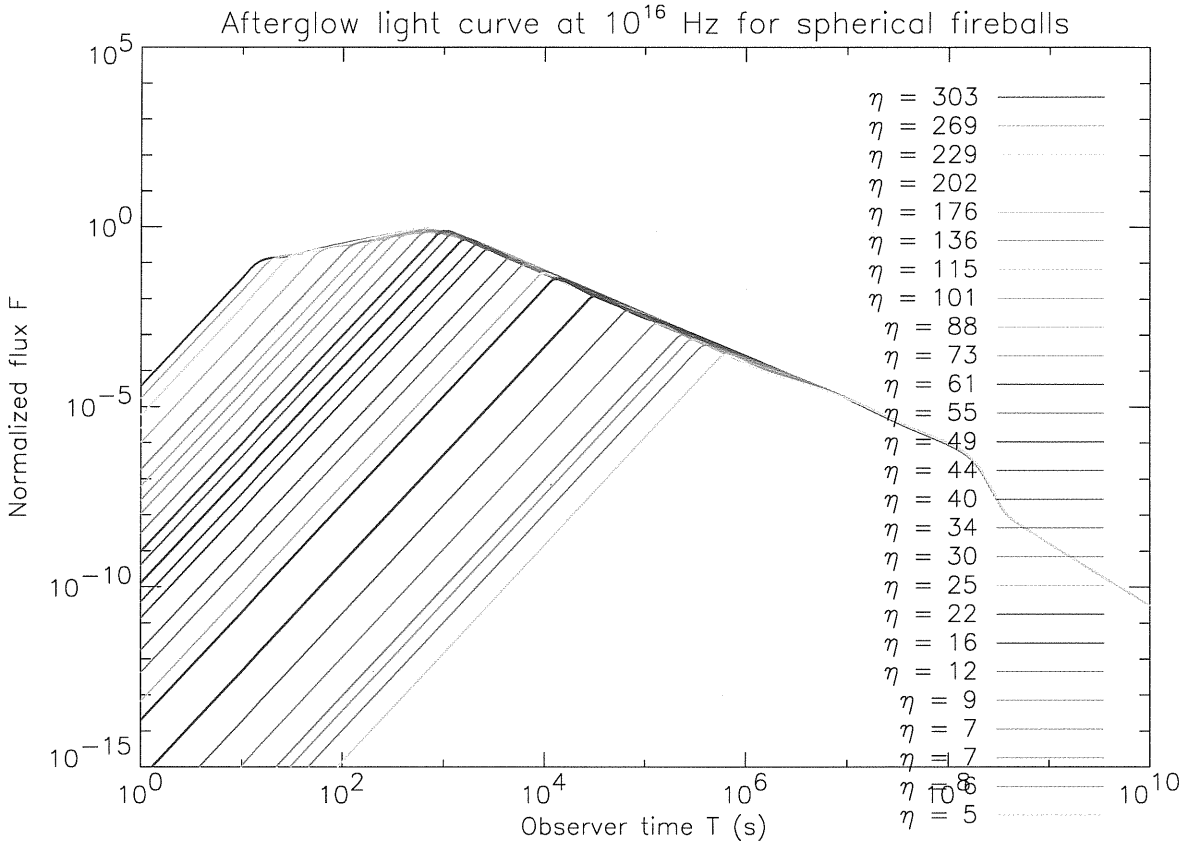

Figure 5.11: *Afterglow light curves at* 10^{16} *Hz for spherical fireballs with fixed energy* $E_T \sim 2\times10^{53}$ *ergs and different values of the baryon loading parameter* η. *Electron cooling has been neglected as in [Granot, Piran & Sari 1999c] and equipartition parameters and electron slope are, as usual,* $\epsilon_e = 0.1$, $\epsilon_B = 0.01$ *and* $p = 2.6$, *in all cases. The baryon loading parameter sampling is the same as in fig.5.12. The high sampling in baryon loading parameter that makes the figure crowded is required for the study of the peak properties illustrated in figs.5.13, 5.14 and 5.18. The normalized peak heights are always identical to normalized peak heights of corresponding light curves in fig.5.12 having the same baryon loading parameter but different total energy. According to the discussion in the text about the relation (5.25), light curves with* $\eta \gtrsim 90$ *are those peaking during the Blandford & McKee stage, the remaining ones are those peaking before the Blandford & McKee stage beginning. For light curves peaking during the Blandford & McKee stage, the peak time is roughly constant, according to the fact that we expect* $T_{peak} \propto E_T^{1/3}$ *and* E_T *is constant. For the other light curves, the peak time scales as* $\eta^{-8/3}$.

In order to study simultaneously the peak properties of the two classes of light curves just noticed, we cannot have constant peak times for the light curves of one of the two classes, as we have in fig.5.11. Thus it is useful to deal with a set of monochromatic light curves at decreasing η but also decreasing energy. **Fig.5.12** shows the afterglow light curves at 10^{16} Hz from spherical fireballs with varying value of η but constant mass of ejecta M_T, i.e. total energy E_T varying too, according to the relation $\frac{E_T}{\eta} = M_T c^2$. These are the spherical models required to build an anisotropic fireball as described in chapter 4.

In fig.5.12, as in fig.5.11 two families of light curves can be distinguished: a first family of light curves having $\eta \gtrsim 90$ peaking during the Blandford & McKee stage (i.e. always on the right of the dotted vertical line of the same color of the light curve) whose peak times T_{peak} roughly scale as $E_T^{1/3} \propto \eta^{1/3}$ and whose normalized peak heights are ~ 1, and a second family of light curves having $\eta \lesssim 90$ peaking during the transient deceleration stage (i.e. always in between the dashed and the dotted vertical line of the same color of the light curve) whose peak times T_{peak} roughly scale as $\eta^{-8/3}$ in fig.5.11 and as $\eta^{-7/3}$ in fig.5.12 and whose normalized peak heights roughly scale as $\eta^{2(p-1)}$.

Now we analyze the peak time properties of the two families of light curves.

Fig.5.13 gives a study of the peak times for light curves of fig.5.12 peaking during the Blandford & McKee stage analogous to the one of fig.5.4, confirming that a peak in the Blandford & McKee stage roughly corresponds to $\phi(\nu, T) = \phi_{peak} = 2$.

Fig.5.14, instead, is devoted to the peak times of the second family of light curves of fig.5.12. We show that the relative position of the peak with respect to the vertical lines representing the beginning and the end of the transient deceleration stage is fixed and is just in the middle of the quoted time interval: we find $T_{peak} \sim \frac{5}{4} T_d(0) \sim \frac{5}{6} T_0(0)$. Since we know that $T_d(0) \sim \frac{2}{3} T_0(0)$,[§] we can easily calculate that $T_{peak} - T_d(0) \sim T_0(0) - T_{peak} \sim \frac{1}{6} T_0(0)$ and since we know also that $T_0(0) \propto \left(\frac{E_T}{\eta^2}\right)^{1/3} \eta^{-2}$, we can conclude that this should be the scaling law for T_{peak} as well. Actually this prediction agrees with what already observed in figs.5.11 and 5.12.

[§]To be precise $T_0(0) = \frac{R_0}{16 \lambda_{BM} c \gamma_0^2}$, where $R_0 \sim 2R_d \propto \left(\frac{E_T}{\eta^2}\right)^{1/3}$, $\lambda_{BM} \sim 0.3$ and $\gamma_0 = \frac{2}{3}\eta$. Moreover, it can be easily verified that $T_d(0) \sim \frac{R_d}{2c\eta^2}$, thus we can estimate that $T_d(0) \sim \frac{2}{3} T_0(0)$ and $T_0(0) \propto \left(\frac{E_T}{\eta^2}\right)^{1/3} \eta^{-2}$.

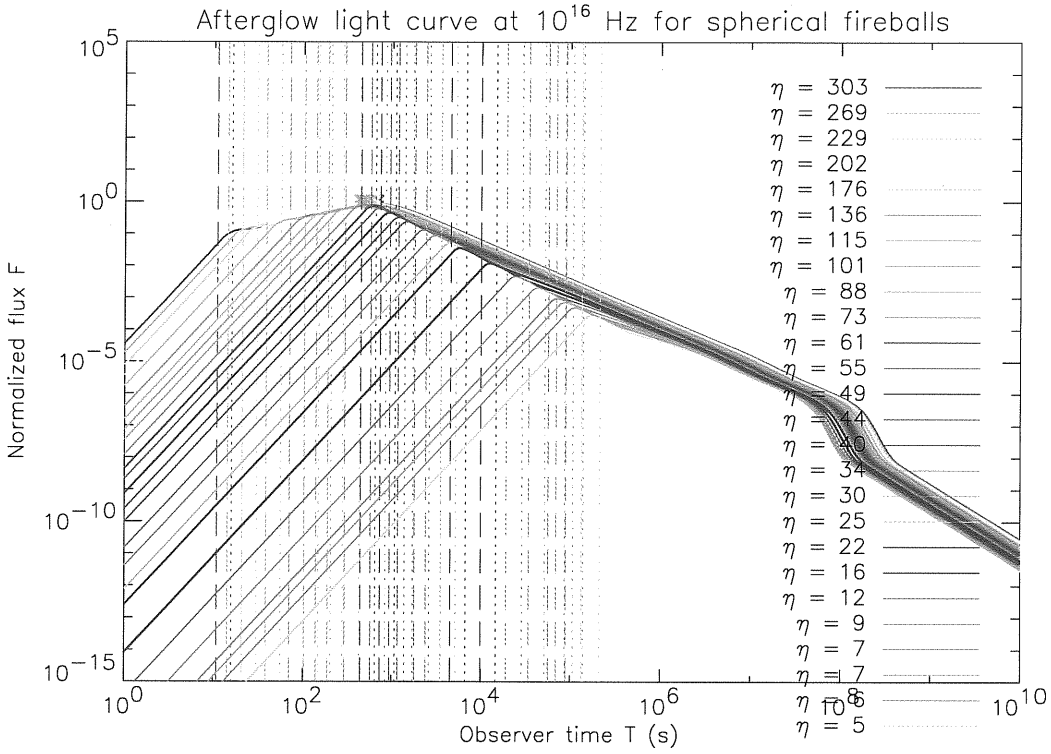

Figure 5.12: *Afterglow light curves at* 10^{16} *Hz for spherical fireballs with decreasing baryon loading parameter* η *and decreasing total energy* E_T *according to the relation* $E_T/\eta = M_T c^2 =$ *constant* $\sim 4 \times 10^{-4} M_\odot c^2$. *In calculating all these light curves electron cooling has been neglected as in [Granot, Piran & Sari 1999c] and equipartition parameters and electron power law slope have been fixed as in fig.5.3:* $\epsilon_e = 0.1$, $\epsilon_B = 0.01$ *and* $p = 2.6$. *Coloured vertical lines mark deceleration starting time* $T_d(0)$ *(dashed) and Blandford & McKee starting time* $T_0(0)$ *(dotted) for each fireball. For high values of the baryon loading parameter (*$\eta \gtrsim 86$ *according to the relation (5.25)) the afterglow peak occurs during the Blandford & McKee stage and progressively moves towards the deceleration beginning as* η *decreases, with the peak height staying roughly constant and equal to 1. For low values of the baryon loading parameter, the peak always occurs during the early deceleration stage and the peak height decreases with* η. *I have calculated that peak heights of peaks occurring during the early deceleration scale* $\propto \eta^{3.3} \sim \eta^{2(p-1)}$. *Remember that all light curves are normalized to the expected total flux per unit frequency at the beginning of the Blandford & McKee stage* F_{max} *defined by (3.167), which is roughly proportional to* E_T *(see equation (3.168) and fig.3.7), or equivalently to* η. *So "true" peak heights in physical units will be* $\propto \eta$ *for peaks occurring during the Blandford & McKee stage and* $\propto \eta^{4.3} \sim \eta^{2p-1}$ *for peaks occurring during the early deceleration stage. See also fig.5.18.*

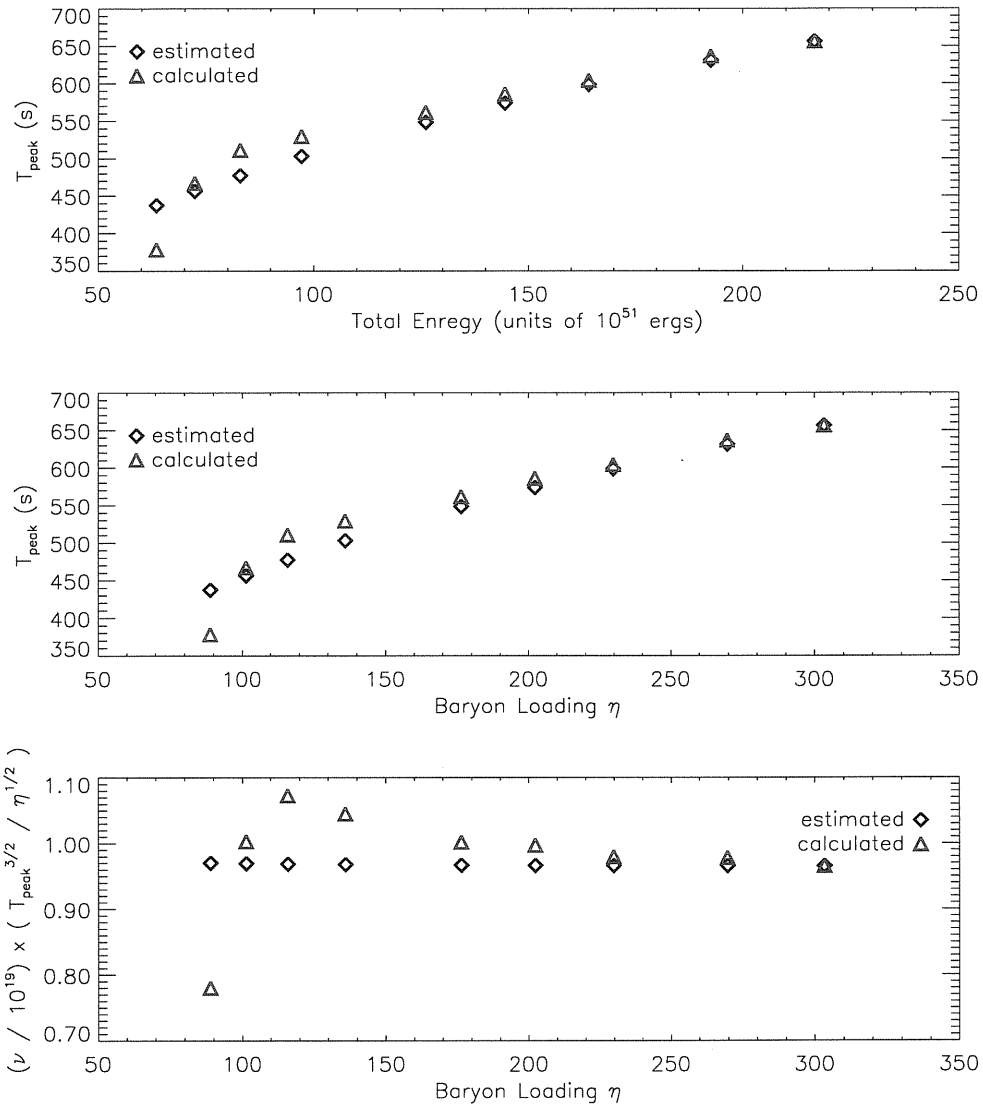

Figure 5.13: *For the light curves of fig.5.12 peaking during the Blandford & McKee stage, T_{peak} is plotted versus the fireball total energy (upper panel) or the baryon loading parameter (central panel). As in fig.5.4 "true" and estimated peak times are shown on the same plot. In the lower panel we plot versus the baryon loading parameter a quantity proportional to $\phi_{granot}(\nu, T_{peak}) \propto \nu\, T_{peak}^{3/2} \eta^{-1/2}$ expected to be constant for peaks occurring during the Blandford & McKee stage if the hydrodynamics were exactly that used by [Granot, Piran & Sari 1999c]. It is apparent that at least estimated peak times lie on an horizontal line (i.e. ϕ_{granot} and ϕ have more or less the same η dependence), while "true" peak times deviate from it. Recalling the discussion of results of fig.5.4 we conclude that "true" peak time prediction during our version of the Blandford & McKee stage should be done solving an equation $\phi(\nu, T_{peak}(\nu, \eta)) = \phi_{peak}\, g(\nu, \eta)$ with an appositely calculated function g which is approximately equal to 1 within the 20% such that $g\,(10^{16}, 303) = 1$, and $\phi_{peak} = 2$.*

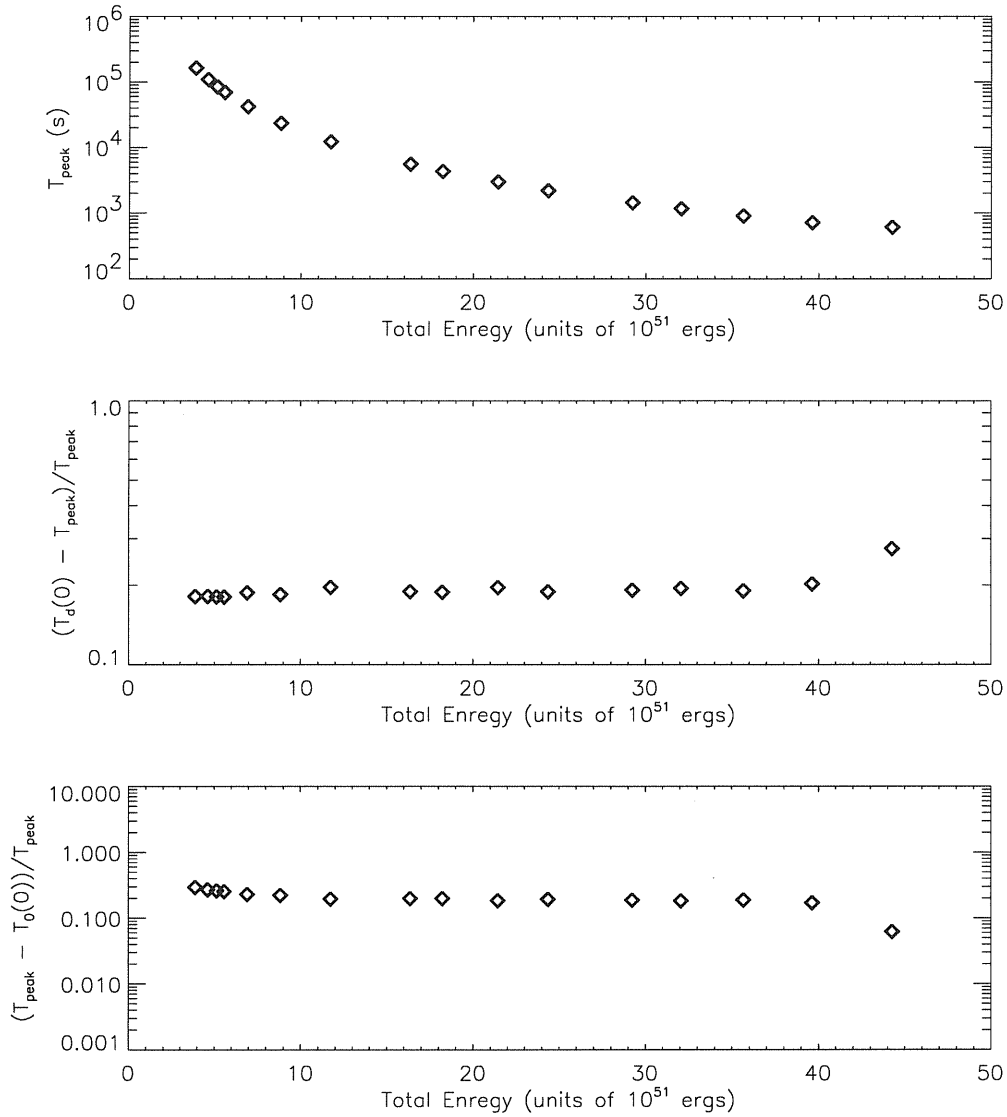

Figure 5.14: *For the light curves of fig.5.12 peaking out of the Blandford & McKee stage, T_{peak} is plotted versus the fireball total energy (upper panel). Remember that for the set of models we are dealing with, baryon loading parameter has been chosen proportional to the total energy. As we have already noted in the caption of fig.5.12, for low baryon loading parameter values the afterglow light curve peak always occurs during the transient early deceleration. From the plots in the central and lower panel we can guess that peak position relative to the beginning and the end of this stage is roughly constant. We find $T_{peak} \sim \frac{5}{4}T_d(0) \sim \frac{5}{6}T_0(0)$. This might depend on the way we have modeled the transition itself and should be further investigated.*

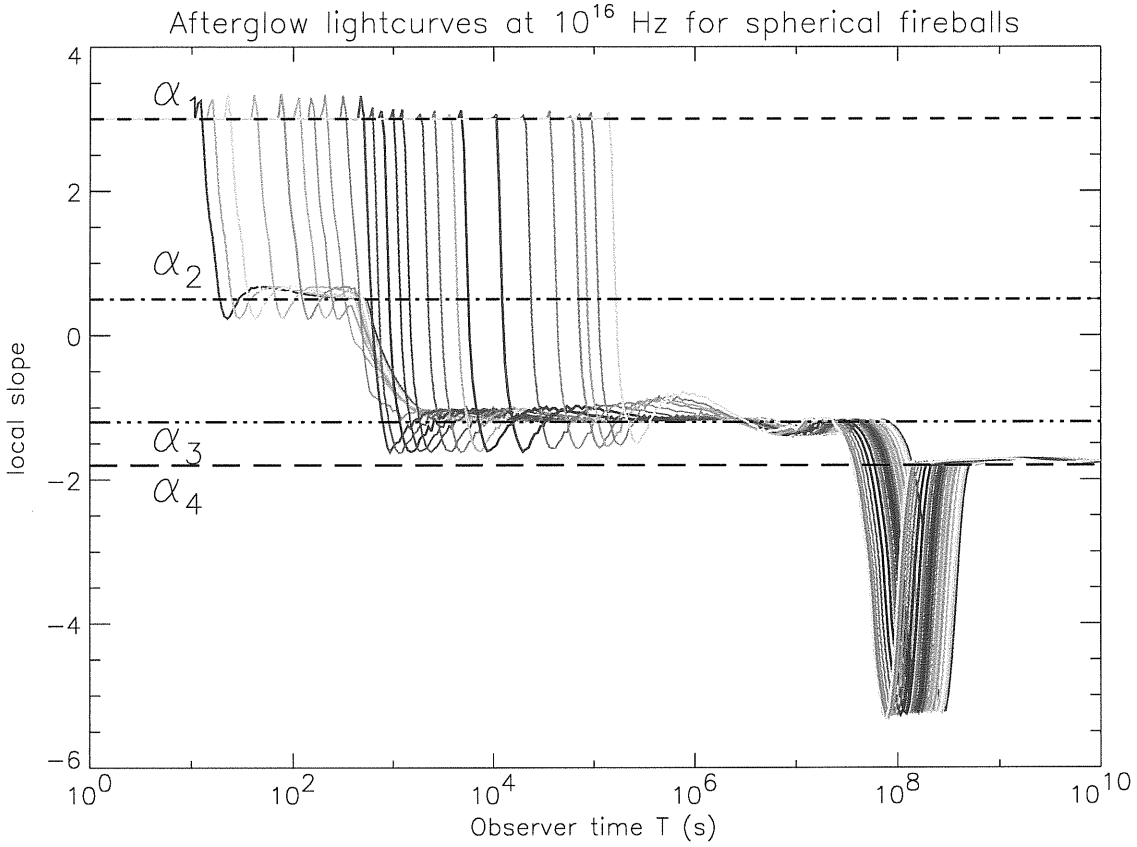

Figure 5.15: *Local slopes of the light curves of fig.5.12 plotted versus the observer time. The meaning and the values of α_1, α_2, α_3 and α_4 are as in fig.5.5. In this case I do not show vertical lines marking the starting times of different stages because they are different from one curve to another.*

For a further investigation, in **fig.5.16** we have plotted two sets of light curves peaking in the transient deceleration stage, corresponding to $\eta = 25$ and different total energies. It is shown that peak times in the transient deceleration stage are affected by total energy variation at constant η just as expected but are not affected by the observation frequency. Another example of this can be found in the set of light curves of fig.**fig.5.17**. In that fig. it can be seen that, once the total energy and the baryon loading parameter of the fireball are fixed, light curves at frequencies greater than the critical value set by (5.25) actually peak during the transient deceleration stage and the peak time is constant.

Then, the local slopes plot of **Fig.5.15** show that also light curves of fig.5.12 have slopes in agreement with predictions. Light curves peaking during the transient deceleration stage are those that do not show a plateau on the horizontal line α_2.

The final evidence to discuss is about light curve peak heights.

Figs.5.11 and 5.12 clearly show that the two families of light curve peaks just identified, differ also in the peak heights behaviour: peaks occurring during the Blandford & McKee stage have a constant and ~ 1 normalized height, while peaks occurring during the transient deceleration have not. Actually, from fig.5.12 we can infer that peaks occurring during the transient deceleration stage have normalized peak heights scaling $\propto \eta^{2(p-1)}$; from fig.5.16 we can infer that normalized peak heights of peaks occurring during the transient deceleration stage are not affected by E_T and from fig.5.17 we can see they scale $\propto \nu^{-\frac{(p-1)}{2}}$.

The plot in **Fig.5.18**, at the end, gives an idea of the expected value in physical units of the light curve peak flux at 10^{16} Hz as a function of η. This plot has been simply obtained multiplying the normalized peak heights of light curves in fig.5.12 by the corresponding normalization constants as given by equation (3.168). The change of slope form $2p-1$ to 1 marks the separation between the two families of light curves: the ones peaking during the transient deceleration stage (lower η values) and the ones peaking during the Blandford & McKee stage (higher η values).

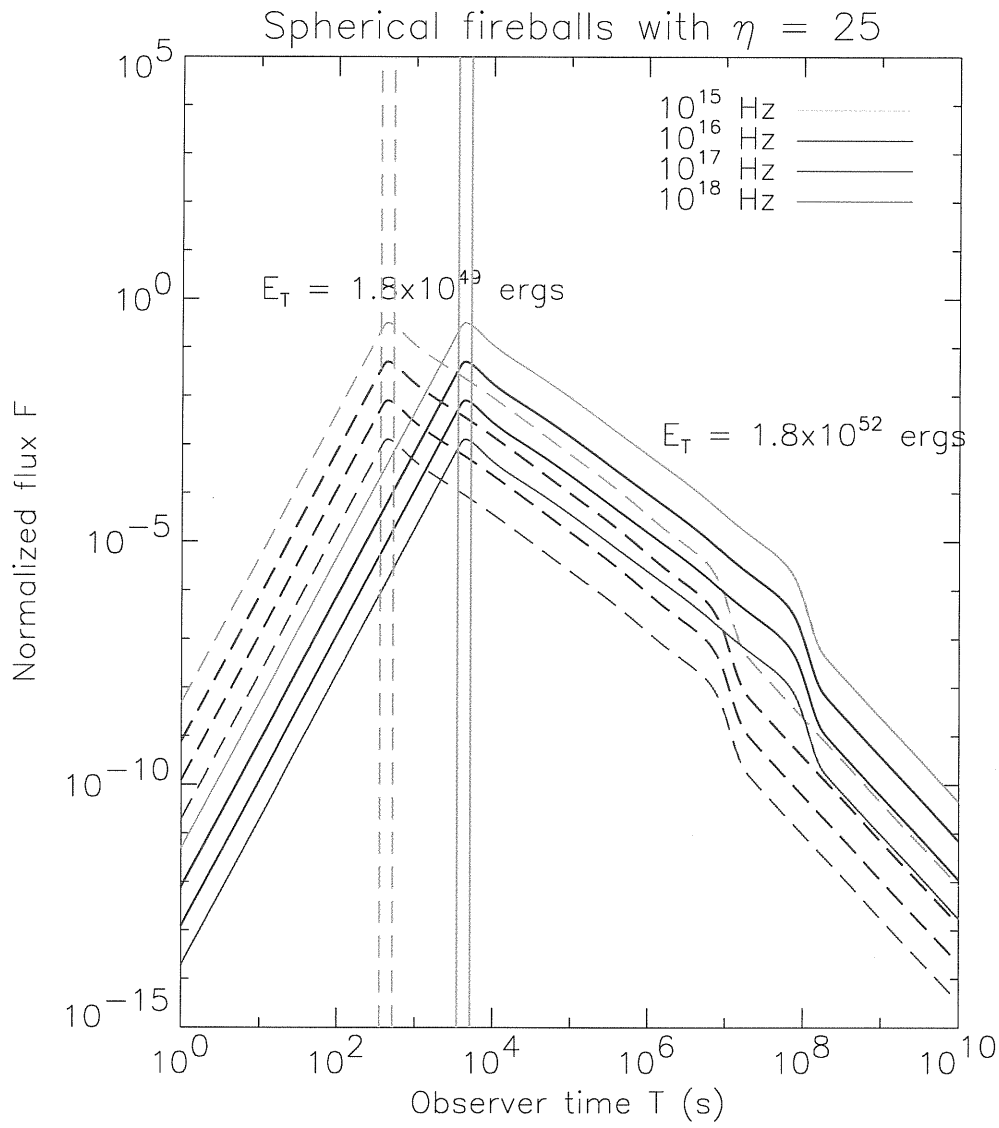

Figure 5.16: *Afterglow light curves for spherical fireballs with fixed baryon loading parameter* $\eta = 25$ *and different total energy (*1.8×10^{49} *ergs for the dashed light curves on the left and* 1.8×10^{52} *ergs for the solid light curves on the right). Electron cooling has been neglected and equipartition parameters and electron slope are, as usual,* $\epsilon_e = 0.1$, $\epsilon_B = 0.01$ *and* $p = 2.6$, *in all cases. Vertical lines mark the times at which the fireball front starts the deceleration and the Blandford & McKee evolution respectively in the two cases. The fireball total energy does not affect the normalized peak height also when the peak occurs during the early deceleration stage. It only affects the peak time because of the dependence on* $\left(\frac{E_T}{\eta^2}\right)^{1/3} \eta^{-2}$ *of* $T_0(0)$ *(see section 3.5.4).*

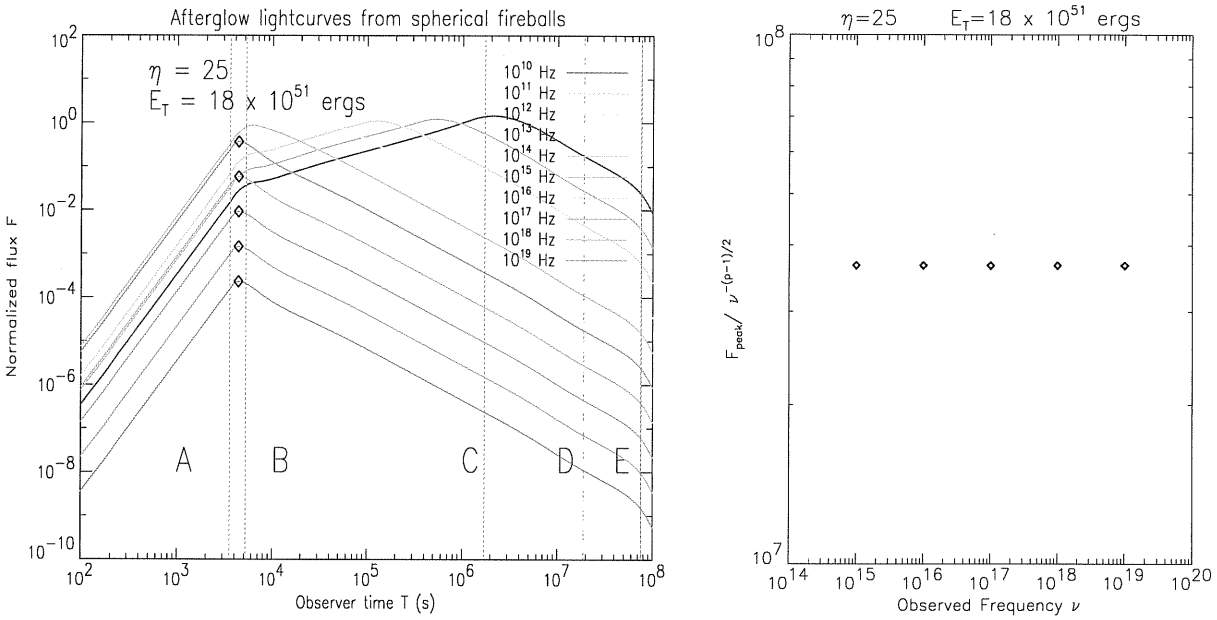

Figure 5.17: *In the left panel we plot afterglow light curves from a spherical fireball with baryon loading parameter* $\eta = 25$ *and total energy* $E_T \sim 2 \times 10^{52}$ *ergs, with electron cooling neglected. Equipartition parameters and electron power law slope are as in fig.5.3, i.e.* $\epsilon_e = 0.1$, $\epsilon_B = 0.01$ *and* $p = 2.6$. *Higher frequency light curves peak before the Blandford & McKee stage start (vertical line B), and the peak time is frequency independent.*
In the right panel it is shown that the peak height of peaks occurring during the transient deceleration stage scale as $\nu^{-\frac{(p-1)}{2}}$ *according to the fact that for all of these peaks* $\nu > \nu_m(T_{peak})$.

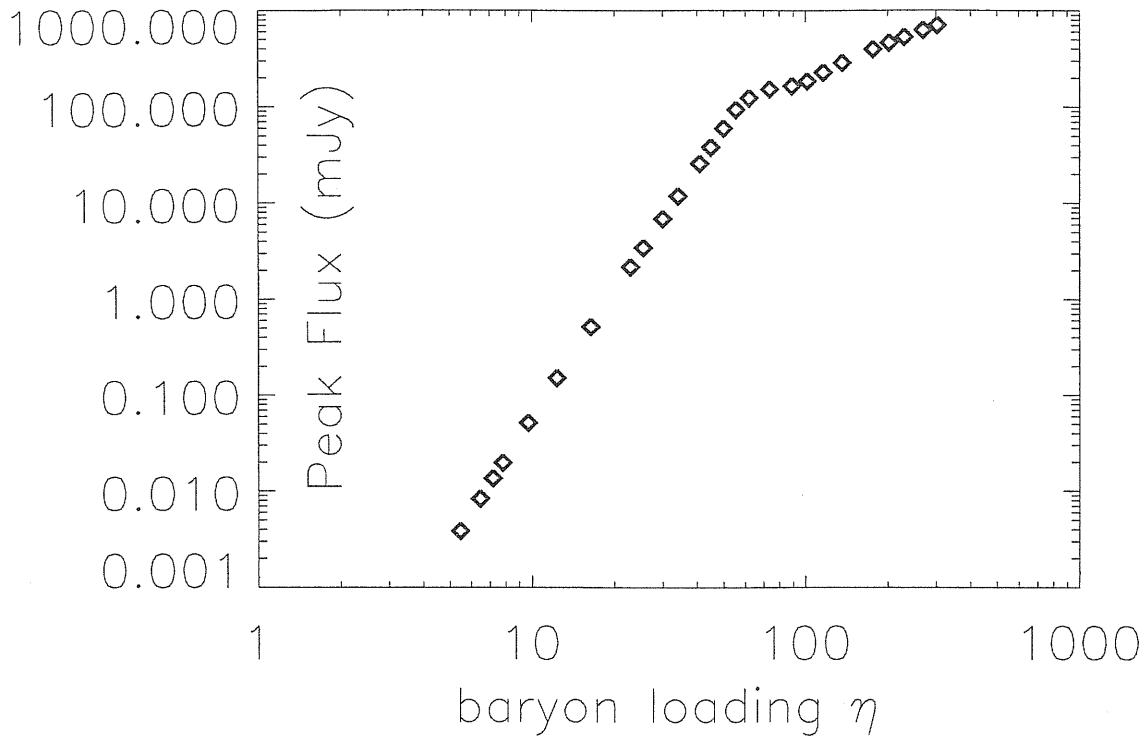

Figure 5.18: *Value of the peak flux in physical units versus the baryon loading parameter for light curves at* $1.e16Hz$ *plotted in in fig.5.12, that have total energy* $E_T \sim 4 \times 10^{-4} M_\odot\ c^2 \eta$. *Each point has been obtained multiplying the normalized peak height of the a light curve taken from fig.5.12 and the normalization constant (3.168) corresponding to the baryon loading parameter/total energy used for calculating the same light curve. We have always used* $\epsilon_B = 0.01$ *(as in fig.5.12) and* $D = 10^{28}$ *cm. An additional factor* $1+z$ *should be added to account for the redshift. It can be clearly seen the slope changing as explained in the caption of fig.5.12 when we pass from the low baryon loading parameter/total energy values at which the peak occurs during the early deceleration stage to the high baryon loading parameter/total energy values at which the peak occurs during the Blandford & McKee stage.*

Discussion

The existence of two families of light curve peaks, with different peak time and peak height dependence on the fireball parameters and observation frequency can be generally explained recalling predictions illustrated in section 5.2.1 in the case electron cooling is neglected: during the coasting stage (i.e. before $T_d(0)$) the afterglow light curve slope can only be positive and equal to 3. On the other hand, during the Blandford & McKee stage (i.e. after $T_0(0)$) the afterglow light curve might be still growing (with slope 1/3) or already decreasing (with slope $-(p-1)/2$), depending on the relative values of the frequency of observation ν and the "critical" frequency $\nu_{crit} = \phi_{peak}\, \nu_m(T_0(0))$ (see below). In the former case the peak will occur during the Blandford & McKee stage and all considerations about self–similarity of the light curve will apply. In the latter case, the peak can only occur during the stage in between $T_d(0)$ and $T_0(0)$, i.e. the transient early deceleration stage. Thus, all peaks at times before the beginning of the Blandford & McKee stage will be peaks in the transient deceleration stage. The roughly constant position of these peaks in the middle of the time interval from $T_d(0)$ to $T_0(0)$, likely related to the way we have modeled the transition, leads to the observed dependence of the peak time from the fireball parameters we have already illustrated. Due to the shortness of the transient deceleration stage, a different modeling of the stage itself cannot change the value of T_{peak} more than 20% (we expect $T_{peak} = \left(\frac{5}{6} \pm \frac{1}{6}\right) T_0(0)$). The normalized peak heights too are to be considered "model dependent". We can estimate $F_{peak} = F_{peak}(\frac{5}{6}T_0(0))(1 \pm 0.18)$ when the peak time T_{peak} spans from $T_d(0)$ to $T_0(0)$.

Once we adopt the value $T_{peak} \sim \frac{5}{6}T_0(0)$ for light curves peaking in the transient deceleration stage, and $T_{peak} \propto E_T^{1/3}\nu^{-2/3}$ for light curves peaking in the Blandford & McKee stage we can also explain the normalized peak heights scaling. The normalized peak height F_{peak}/F_{max} of a monochromatic afterglow light curve at the time T_{peak} is expected to be $\propto F_\nu^{app}(T_{peak})/F_{max}$, with F_ν^{app} given by (5.16) and F_{max} given by (3.167). Since during the Blandford & McKee stage $F^{tot}(T)$ is roughly equal to F_{max} (see section 3.6.6), and for a peak in the Blandford & McKee stage T_{peak} is such that $\left(\frac{\nu}{\nu_m(T_{peak})}\right)$ is roughly a universal constant (see section 3.6.7 and figure captions 5.3, 5.4 and 5.13) we can conclude that in this case the normalized peak height is constant. If the peak is in the transient deceleration stage, instead, we can estimate $R_{los}(T_{peak}) \propto R_{los}(T_0(0)) = R_0 \propto \left(\frac{E_T}{\eta^2}\right)^{1/3}$, (see fig.3.4), $\gamma_{los}(T_{peak}) \propto \gamma_{los}(T_0(0)) = \gamma_0 \propto \eta$, $e'_{los}(T_{peak}) \propto \gamma^2_{los}(T_{peak}) \propto \eta^2$, $\beta_m(T_{peak}) \sim 1$ and consequently $F_{tot}(T_{peak}) \propto E_T$,

$\nu_m(T_{peak}) \propto E_T^{1/2} \left(E_T^{1/3}\eta^{-8/3}\right)^{-3/2} \propto \eta^4$ so that $F_{peak} \propto F_\nu^{app}(T_{peak}) \propto E_T\, \eta^{2(p-1)}\, \nu^{-\frac{(p-1)}{2}}$ and $\frac{F_{peak}}{F_{max}} \propto \eta^{2(p-1)}\, \nu^{-\frac{(p-1)}{2}}$.

To summarize the light curve peaks properties in a few analytic expressions we must recall once more that peaks occurring during the Blandford & McKee stage have peak times $T_{peak}(\nu)$ such that $T_0(0) < T_{peak}(\nu) < T_{crit}(0)$ and

$$\phi(\nu, T_{peak}) = \frac{\nu}{\nu_m\left(T_{peak}\right)} = \phi_{peak} \sim 2 \tag{5.26}$$

Since we know that the function $\nu_m(T)$ is decreasing with T (see fig.5.1), it is clear that if $\nu > \nu_{crit} = \phi_{peak}\ \nu_m(T_0(0))$ the equation (5.26) cannot be satisfied by any time of the Blandford & McKee stage, and the light curve peak cannot be in the Blandford & McKee stage. In this case the afterglow light curve must be decreasing with slope $-(p-1)/2$ during all the Blandford & McKee stage because the condition $\nu > \nu_m(T)$ always holds, so the peak must have been reached before the Blandford & McKee stage, i.e. in the transient deceleration stage.

If $\nu < \nu_{crit}$, the afterglow light curve peaks during the Blandford & McKee stage, unless the frequency of observation is as low as $\nu < \nu_{min} = \phi_{peak}\ \nu_m(T_{crit}(0))$. In this last case the peak time is expected after the end of the Blandford & McKee stage. For the range of fireball parameters we explore, just the lowest observed frequency in the range 10^{10}–10^{19} Hz is slightly below ν_{min}, and we actually do not have a third class of peaks to study.

Once we adopt the value $T_{peak} \sim \frac{5}{6}T_0(0)$ for light curves peaking in the transient deceleration stage, and, as a first approximation, $T_{peak} \propto \eta^{1/3}\nu^{-2/3}$ for light curves peaking in the Blandford & McKee stage, we expect that the peak time of a monochromatic afterglow light curve T_{peak} scale as follows

$$T_{peak}(\nu, E_T, \eta) \propto \begin{cases} \left(\frac{E_T}{\eta^2}\right)^{1/3} \eta^{-2} & \nu > \nu_{crit} \\ \eta^{1/3}\nu^{-2/3} & \nu < \nu_{crit} \end{cases} \tag{5.27}$$

Then, summarizing the results illustrated and discussed in the captions of the figures 5.11, 5.12, 5.16 and 5.17 we can say that, as a first approximation, the peak flux per unit frequency of a monochromatic afterglow light curve F_{peak} scales as follows

$$F_{peak}(\nu, E_T, \eta) \propto \begin{cases} E_T\ \eta^{2(p-1)}\nu^{-\frac{(p-1)}{2}} & \nu > \nu_{crit} \\ E_T & \nu < \nu_{crit} \end{cases} \tag{5.28}$$

Finally, we point out that the critical frequency $\nu_{crit} = \phi_{peak}\ \nu_m(T_0(0))$ can be roughly approximated as

$$\nu_{crit} \sim 3.068 \times 10^{16} \left(\frac{\epsilon_B}{0.01}\right)^{1/2} \left(\frac{\epsilon_e}{0.1}\right)^2 \left(\frac{\eta}{100}\right)^4 \quad \text{Hz} \tag{5.29}$$

Now it is important to understand if all the features of afterglow light curves we have discussed are observable.

First of all remember that the zero reference time we have chosen for the observer time T is virtually a time preceding the GRB detection, and the afterglow light curves we calculate are to be considered undetectable in their initial part because of superposition of brighter emission due to the GRB (at high frequencies) and brighter emission possibly due to reverse shock burning the ejecta shell (in the visual band) and because it is simply unconceivable to point a GRB source before its explosion. We could only hope it happens by chance. Since we have not built a consistent model including internal shocks, we cannot exactly tell when we expect the GRB to start and end in our model, but we can estimate the GRB will not start before optical thinning of the ejecta (i.e. before $T_{th}(0) \sim 10^{-4}$ s) and assume it will not be much longer than the average duration of observed (long) GRBs $\sim$ 50–100 s. Thus, we should simply look at our plots assuming the part at $T < 100$ s has a very low probability to be observed.

Then remember that the beginning of fireball deceleration $T_d(0)$ and the starting time of the Blandford & McKee stage $T_0(0)$, usually represented by the vertical lines A and B respectively in all our figures, roughly scale with the fireball baryon loading parameter and total energy $\propto \left(\frac{E_T}{\eta^2}\right)^{1/3} \eta^{-2}$. For relatively low total energy and baryon loading parameter values, the coasting stage can last far beyond the first 100 s: we might expect to see afterglows from fireballs that are still in an early stage of evolution, and consequently afterglow peaks of the second family. Actually in figs.5.11 and 5.12 it can be seen that for relatively low η values, the Blandford & McKee stage beginning can be quite late and GRB emission is very likely to have ended before it. Moreover, the critical frequency $\nu_{crit} = \phi_{peak}\ \nu_m(T_0(0))$ can be as low as 10^{15}–10^{16} Hz, and afterglow peaking during the transient early deceleration might be observed in the optical and at higher frequencies if the peak flux were not too dim. To have an idea of the expected peak height values in physical units look at fig.5.18 and remember the scaling law (5.28).

5.3.2 Results including electron cooling

Now we show the results of calculation of afterglows from spherical fireballs including the detailed treatment of the radiation mechanism described in the previous chapter (sections 3.7 and 3.8). This case has also been calculated by [Granot & Sari 2002], but, as usual, restricted to the pure Blandford & McKee evolution.

As far as the light curves are concerned, we will present sets of light curves at constant fireball parameters, compare them with the corresponding sets of light curves obtained without taking into account the cooling of the electrons and with approximated light curves. Then we will discuss effects on the light curve shape of the whole integration, and after that we will present time resolved afterglow spectra and discuss them.

Light curves shown in **fig.5.19** are an example of results obtained with full accounting of electron cooling (by synchrotron radiation and adiabatic expansion) and assuming the magnetic field to be in equipartition with the shocked fluid internal energy just behind the shock and subsequently frozen in (see the second magnetic field evolution law in (3.221)). If we use the first magnetic field evolution law in (3.221), corresponding to constant equipartition (as in [Granot & Sari 2002]), we obtain curves indistinguishable within the thickness of the line from those plotted in fig.5.19. If we neglect adiabatic expansion contribution to the electron cooling (i.e. calculate the light curve with the artificial setting $G(t') = 1$ for all t' in (3.214), (3.215) and (3.216)) we also obtain light curves indistinguishable from those shown in fig.5.19. Thus, both the magnetic field strength distribution and the adiabatic cooling contribution do not leave a clear signature in the light curve shape.

The comparison between light curves of fig.5.19 and the ones obtained with the simpler radiative model that neglects electron cooling and uses a broken power law approximation for the fluid comoving emissivity (i.e. the case discussed in the previous section and calculated in [Granot, Piran & Sari 1999c]) is presented in **fig.5.20**.

Note that, looking at $\nu_m(T)$ and $\nu_c(T)$ plots in fig.5.1, which have been build using the same fireball parameters used for light curves in fig.5.19, we expect to see a cooling break in the light curve (with the slope passing from $-\frac{3}{4}(p-1) = -1.2$ to $-\frac{(3p-2)}{4} = -1.45$) only at 10^{15} Hz ($T_{break} \sim 7 \times 10^4$ s). The lower frequency light curves should have the same decay slope they had neglecting the electron cooling: $-\frac{3}{4}(p-1) = -1.2$. The 10^{16} Hz light curve, roughly corresponding to the case $\nu_m = \nu_c$, should have a broad peak after about 600 s and a decay slope $-\frac{(3p-2)}{4} = -1.45$. The

10^{17} Hz light curve should have a break at $\sim$ 100 s passing form the decay slope $-1/4 = -0.25$ to the decay slope $-\frac{(3p-2)}{4} = -1.45$. The 10^{18} Hz light curve should have the decay slope $-\frac{(3p-2)}{4} = -1.45$ during all the Blandford & McKee stage. An analogous discussion can be done for the rising slopes during the coasting stage: all the light curves at frequencies $\leq 10^{16}$ Hz are expected to grow as $T^{11/3}$, while the light curves at 10^{17} Hz and 10^{18} Hz should have a flattening of the growing law from $T^{11/3}$ to T^2 before the end of the coasting stage. All these predicted behaviours are quite difficult to be recognized by eye on the shown curves because they are considerably smoother than all previously calculated light curves. They cannot be fitted by simple broken power law models. Anyway there is a general trend of steepening of the decay at higher frequencies (as compared to corresponding light curves in fig.5.3) that could fit the predictions, and also the initial rising slopes seem to be slightly steeper than 3.

The last relevant feature of light curves in fig.5.19 is a sharp peak occurring during the early deceleration stage. The origin of this peak must be further investigated. The calculation of the effect of pure radial and pure angular integration in this case shows that the "secondary" peak in the transient early deceleration stage is probably due to a radial enhancing in the emissivity in the internal regions of the integration volume. Nevertheless, the emitting volume contributing to this peak is clearly the region in which the emitting fluid elements have been shocked at a time t_s before the beginning of the deceleration. This can be seen from **fig.5.21** where we show the result of light curve calculation with electron cooling, truncating the integration volume to regions shocked after the beginning of the deceleration and to regions shocked after the beginning of Blandford & McKee evolution. In cases at lower baryon loading parameter values the "secondary" peak in the transient deceleration stage disappears (see fig.5.22), and this suggests the existence of numerical problems related to approximations in calculating the time of shock passage and/or the average magnetic field for volume elements shocked during the coasting stage. In any case, for the light curves in fig.5.19, any peak in the transient deceleration stage would probably be not visible because occurring before the end of the GRB, and, as shown in fig.**5.23**, on the time scale of observations the agreement of the detailed calculation with the rough approximation (5.15) is as expected.

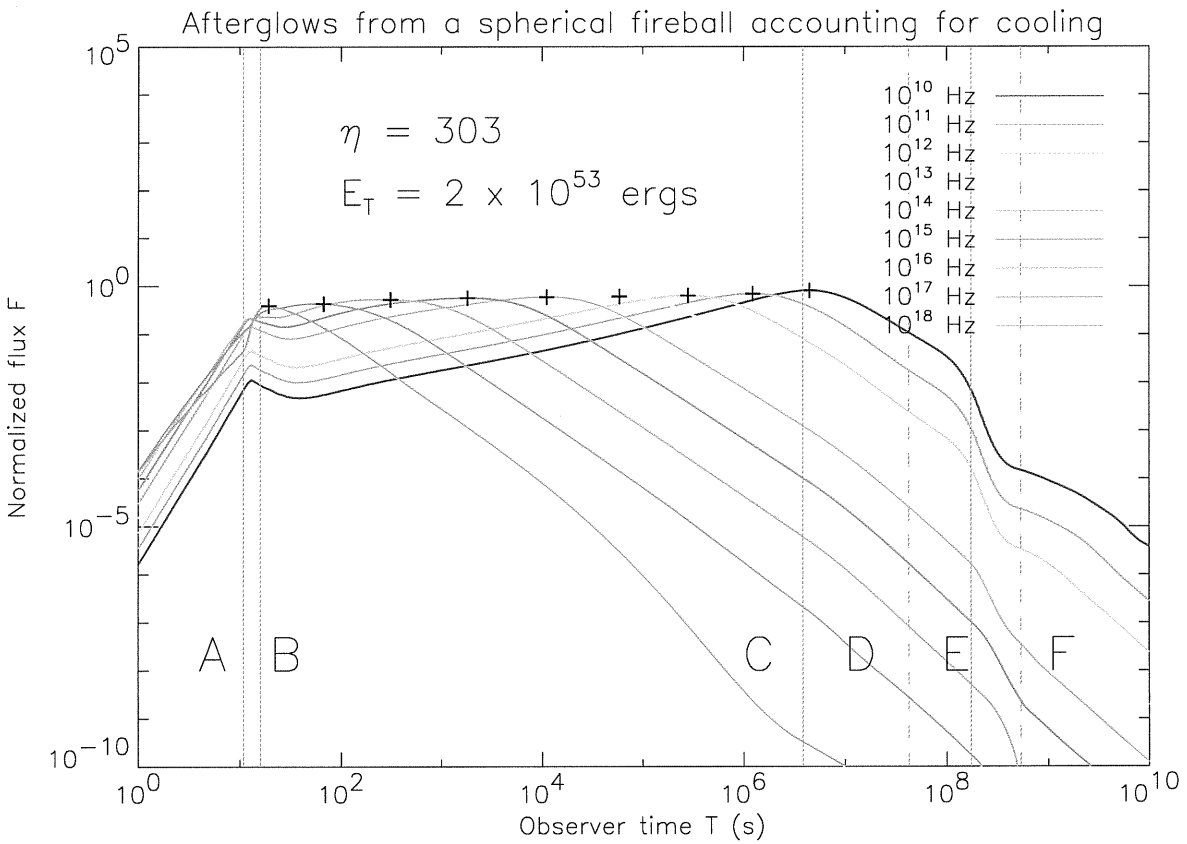

Figure 5.19: *Light curves from a spherical fireball with baryon loading parameter* $\eta = 303$ *and total energy* $E_T = 2 \times 10^{53}$ *ergs calculated accounting for cooling of shocked electrons via synchrotron radiation and adiabatic expansion as explained in section 3.7. The equipartition parameters and the electron energy distribution slope have been fixed, as usual, to the values* $\epsilon_e = 0.1$, $\epsilon_B = 0.01$ *and* $p = 2.6$. *In the present calculation we have used the magnetic field evolution law (3.206), assuming the magnetic field to be in equipartition with the shocked fluid internal energy only just behind the shock and subsequently frozen in. The alternative model of constant magnetic field equipartition gives indistinguishable results. Another alternative calculation has been done neglecting the adiabatic cooling of electrons (i.e. artificially setting* $G \equiv 1$ *in the expressions of the cooled electron distribution (3.214), and its range (3.215) and (3.216)). The resulting light curves are again indistinguishable from those presented here, meaning that adiabatic cooling is likely a negligible cooling effect on emitting electrons as compared to synchrotron radiation.*

The vertical lines A,B,C,D,E and F have the usual meaning (see fig.5.3).

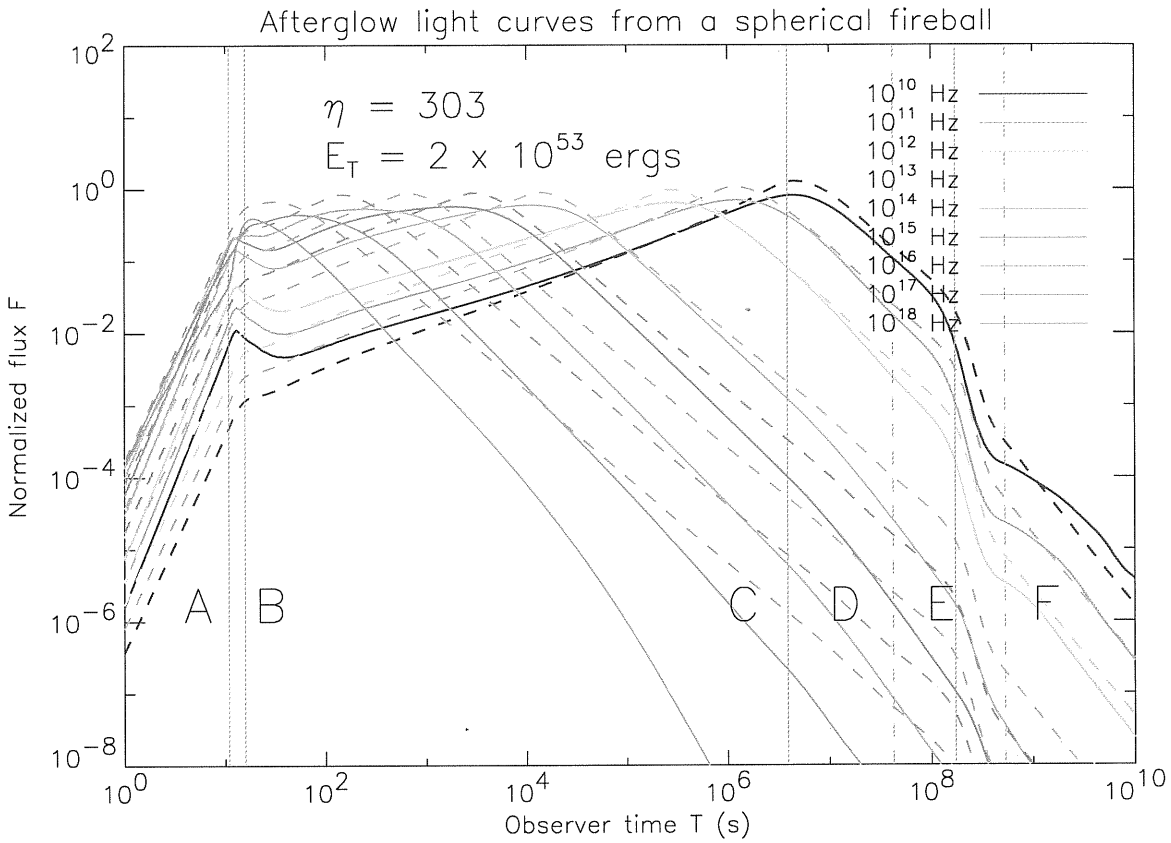

Figure 5.20: *The same light curves presented in fig.5.19 (solid lines) compared to the corresponding light curves extracted from fig.5.3 obtained with same fireball parameters but neglecting electron cooling (dashed lines). Peak times corresponds very well. Peaks of the solid curves seem broader and lower because in this case no broken power law approximation of the comoving emissivity have been used. We have already seen in fig.5.9 that the effect of exact synchrotron emission calculation on the afterglow light curve is a peak broadening.*

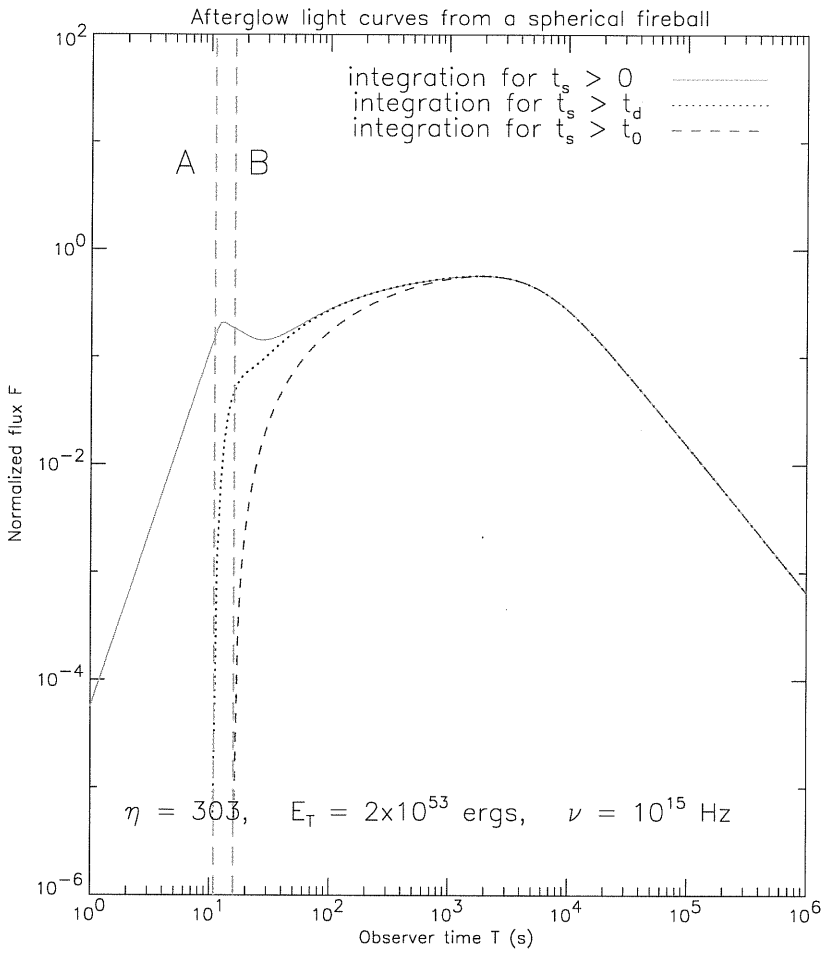

Figure 5.21: *The light curve at* 10^{15} *Hz already shown in fig.5.19 (solid line) has been calculated again neglecting radiation emitted by the fireball portion that was shocked before the beginning of the deceleration (dotted curve) and radiation emitted by the fireball portion that was shocked before the beginning of the Blandford & McKee stage (dashed curve). As in the case of neglected electron cooling, radiation emitted during the early evolutionary stages does not affect significantly the part of the light curve after Blandford & McKee stage beginning,* $T_0(0)$.

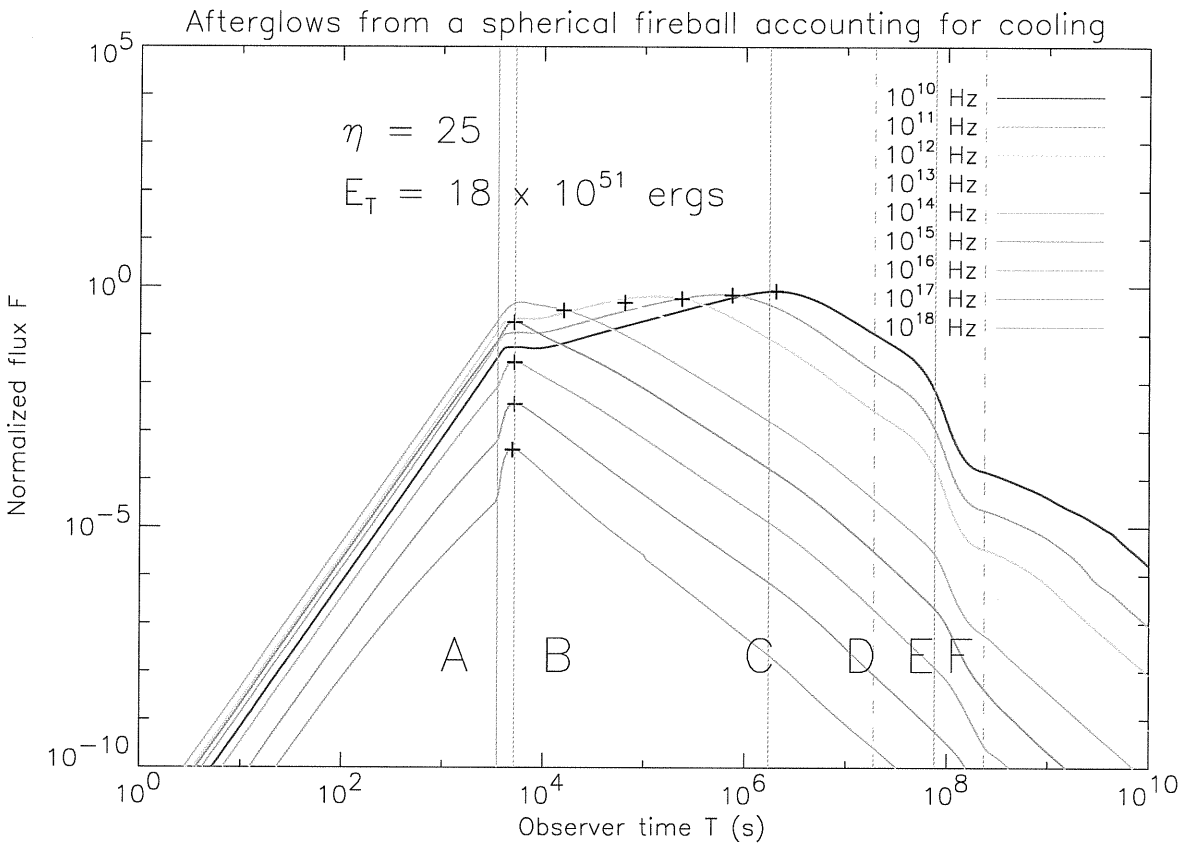

Figure 5.22: *Another example of afterglow light curves obtained taking in account electron cooling. Now the fireball has a lower baryon loading parameter and total energy and we find the same behaviour of the peaks we have discussed in the corresponding case of fig.5.17 and all related figures. The only main difference is that peak times in the early deceleration stage are now closer to* $T_0(0)$ *and slightly frequency dependent. Light curves peaking during the Blandford & McKee stage do not present a preliminary sharper peak in the early deceleration stage as happened for higher baryon loading parameter values.*

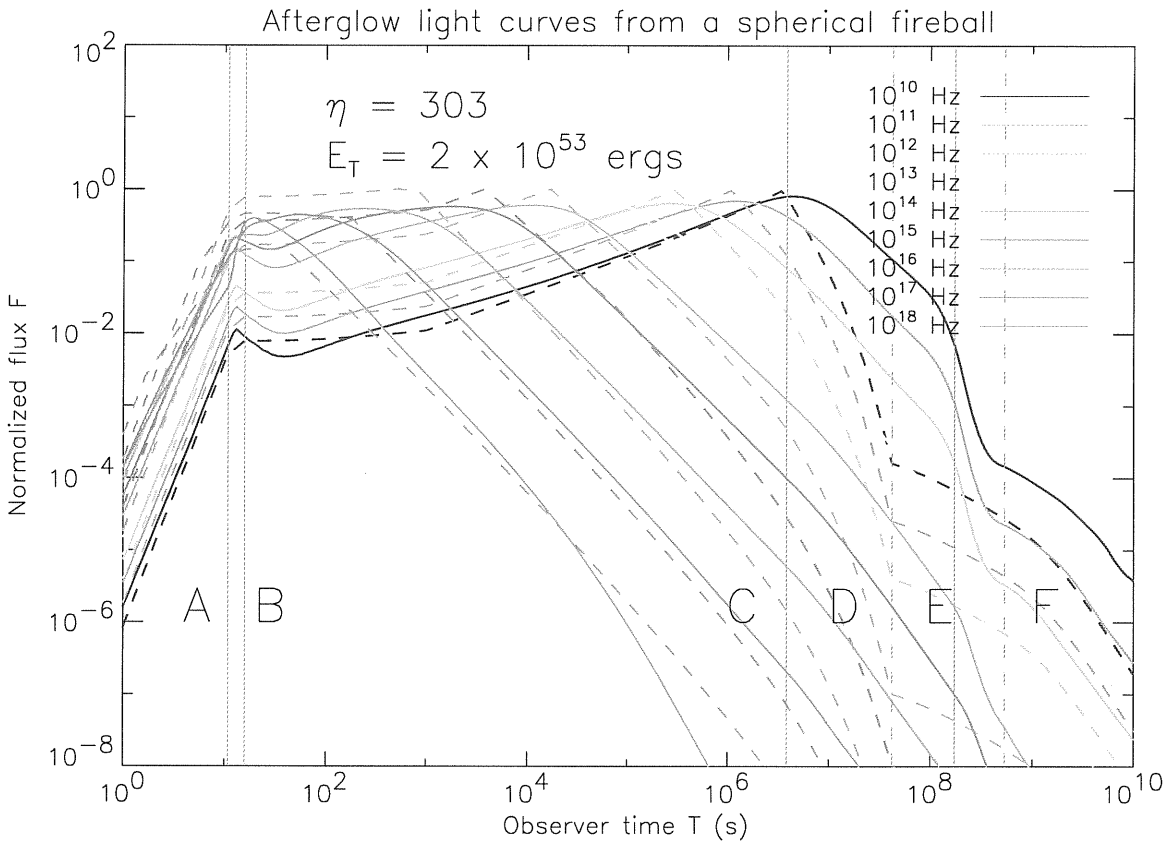

Figure 5.23: *The afterglow light curves already shown in fig.5.19 (solid curves) are now plotted together with the corresponding approximated version $F_\nu^{app}(T)$ defined by (5.15) and (5.16) that represent the contribution to observed radiation due to matter just behind the shock along the line of sight (dashed curves). In calculating the light curves approximations, the characteristic frequencies $\nu_m(T)$ and $\nu_c(T)$ have been multiplied by two in order to have the right peak superposition. As we have already seen in fig.5.6, the approximation start to fail significantly when the effect of volume integration becomes important, i.e. at the end of the Blandford & McKee stage. In this case we also see that "exact" light curves are generally more smooth and "rounded" than their approximations, with the exception of the part covering the early deceleration stage, that usually presents a sharp peak instead of the predicted flattening.*

Fig.5.22 shows the afterglow light curves with electron cooling properly accounted for from a spherical fireball with $\eta = 25$ and $E_T = 1.8 \times 10^{52}$ ergs. We can recognize the same peaking behaviour discussed in the previous section: light curves at a frequency lower than the limiting value derived from (5.25) peak during the Blandford & McKee stage or after, and all the others peak during the transient early deceleration. This is not surprising because the same line of reasoning used to justify the results obtained in that case can be applied also now. Actually, qualitative results about light curve peaks discussed in section 5.3.1 are still valid, but the estimation of the peak time for peaks in the early deceleration stage, that appears to be less rigorously constant and better approximated by $T_0(0)$ rather than by the time in the middle of the interval from $T_d(0)$ to $T_0(0)$.

The same general trend to smoothness that does not allow a simple broken power law approximation in afterglow light curves when electron cooling is taken in account, appears also in the spectra (see. **figs.5.24**, **5.25**) In **fig.5.26** it is apparent that even if spectral breaks are visible, the "exact" light curves far from the breaks are not very well approximated by power laws.

Finally I want to point out that the late exponential steepening of spectra always visible in figs.5.24 and 5.26 is not a physical spectral break, but the effect of numerical integration of the exact local comoving emissivity (3.230) with $N(\gamma_e, t')$ given by (3.214) and $< P'_{\gamma_e}(\nu') >$ given by (D.14), which has an exponential cut off at high frequencies. A finer sampling of the integration volume moves the exponential steepening of the spectra at higher frequencies but is very time consuming. Of course light curves are also affected by this problem. Using spectra of fig.5.24 it can be roughly seen at what time a monochromatic light curve in fig.5.19 is dominated by "underestimation" of the emitted radiation due to insufficient integration volume sampling. For example, the light curve at 10^{19} Hz would be "unreliable" (because the instantaneous spectrum at this frequency starts to show the numerical exponential cut off) just after about 10^4 s, so we have not shown it in fig.5.19 although its absolute peak flux level is comparable to the one at other frequencies. The light curve at 10^{18} Hz starts to be "unreliable" at about 10^5 s and so on.

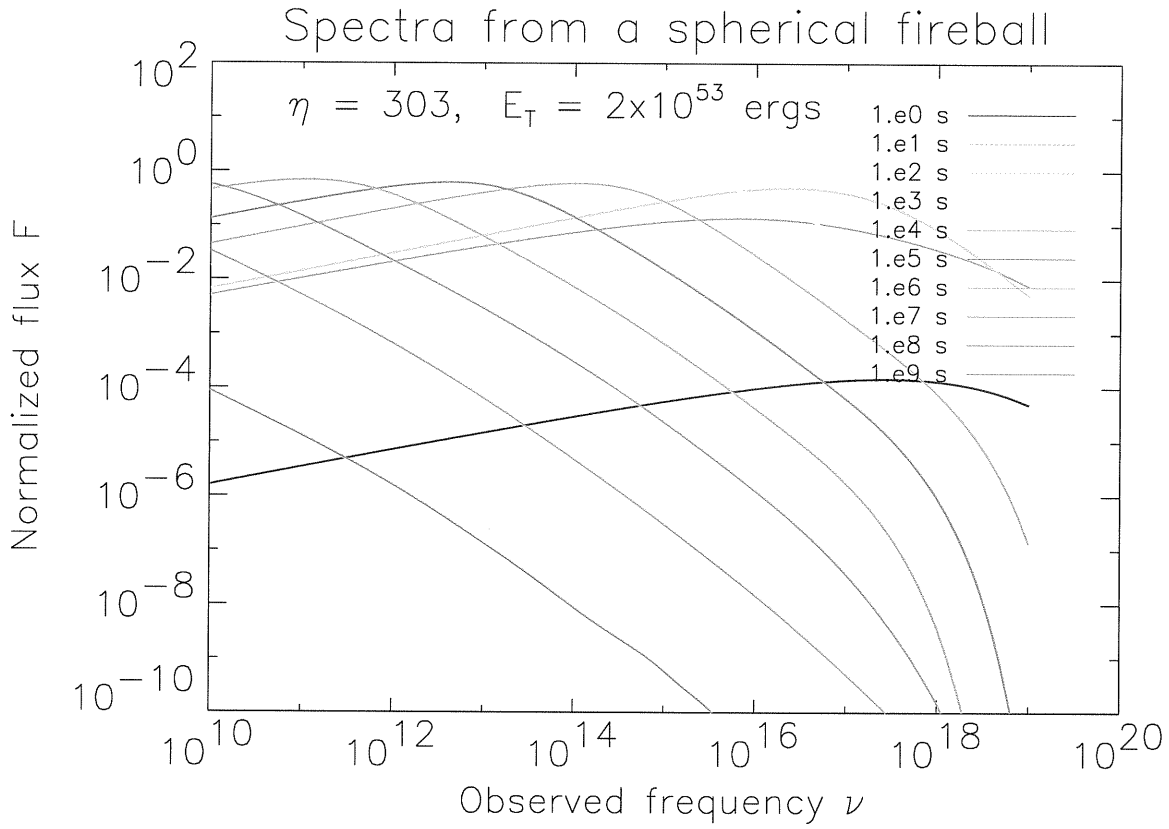

Figure 5.24: *Afterglow spectra from a spherical fireball with baryon loading parameter* $\eta = 303$ *and total energy* 2×10^{53} *ergs at different times of the observer. The calculation takes into account electron cooling. We have used the same normalization constant used for the light curves. Spectra appear to be more regular than light curves, but are anyway smoother than simple broken power laws.*

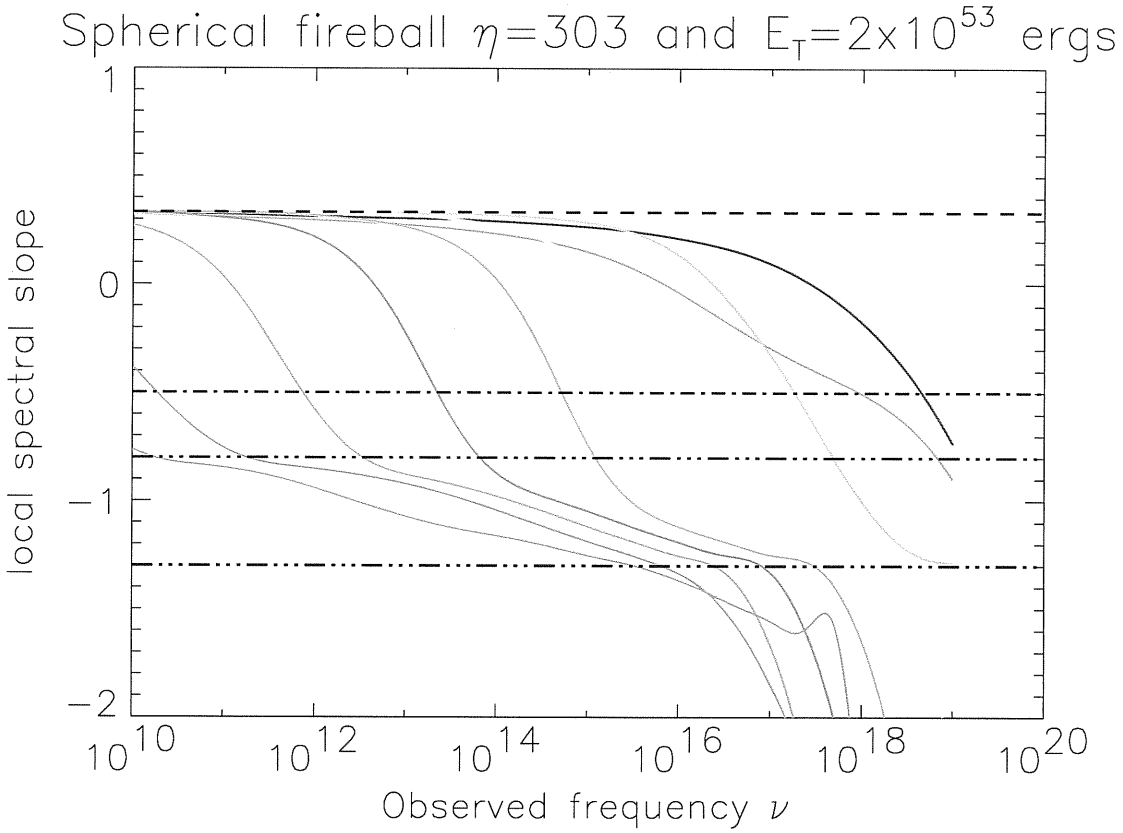

Figure 5.25: *Local spectral slopes for spectra shown in fig.5.24. Horizontal lines correspond respectively, from the top to the bottom, to the expected spectral slopes* $1/3$, $-1/2$, $-(p-1)/2$ *and* $-p/2$. *Only the rising part of the synchrotron spectrum going as* $\nu^{1/3}$ *seems to be common to most of the calculated spectra. There seems to be a trend to reach a final slope* $-p/2$, *but an exponential steepening occurs after. This exponential steepening in the local slopes corresponds to the exponential steepening in the spectra we have discussed in the text.*

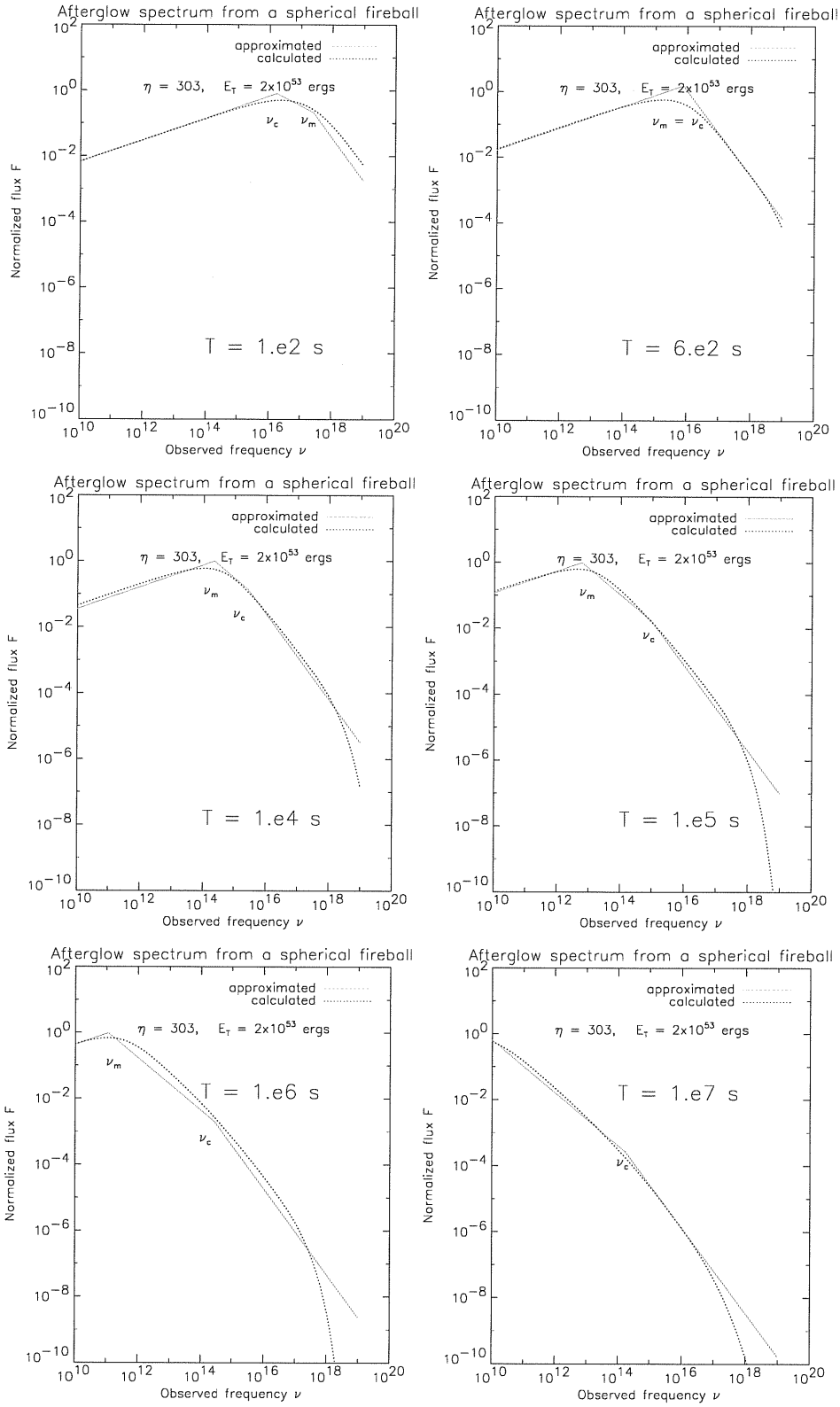

Figure 5.26: *Some of the spectra shown in fig.5.24 are plotted again together with the corresponding expected broken power laws.*

5.3.3 Conclusions

The spherical fireball afterglow calculation we make neglecting the electron cooling reproduces well the "standard" afterglows previously calculated by [Granot, Piran & Sari 1999c] on the time interval corresponding to the Blandford & McKee evolution stage and extend the model predictions to times after the GRB explosion beyond the transition to non relativistic expansion and to a large range of baryon loading parameter values (from $\eta \sim 3$ to $\eta \sim 300$) in a consistent way.

Fireballs with low baryon loading parameter/total energy generally produce higher frequency afterglows with a different peaking behaviour, the peak occurring in an evolutionary stage different from the well known self–similar Blandford & McKee stage. It can be proved that in this case the peak must always be in the transient early deceleration stage. The new family of afterglow light curve peaks is roughly identified as having a frequency independent peak time and a frequency and baryon loading parameter dependent normalized peak height. Standard afterglow peaks, on the contrary, have frequency dependent peak times and constant normalized peak heights (see equations (5.27) and (5.28)). Though we have modeled the typical stage during which the new peaks are expected to show up (the transient stage from the coasting to the Blandford & McKee stage) just to match smoothly two well known evolutionary stages, the shortness of this stage itself guarantees an uncertainty of no more than 20% on the peak time and peak height values we find.

The criterion telling us at which frequency the light curve peak start to be in the early deceleration stage once the baryon loading parameter and total energy values are set, is relation (5.25), that can be also used to calculate at which baryon loading parameter a given monochromatic light curve start to peak in the early deceleration stage, given the fireball total energy.

For high baryon loading parameter/total energy values ($\eta \gtrsim 100$, $E_T \gtrsim 10^{52}$ ergs) we do not expect to observe any light curve peak of the newly identified class. They are going to appear only at very high frequencies (out of the range of usually observed frequencies we are exploring) and, in any case, when the GRB is likely to have not ended yet. For moderately low baryon loading parameter values (for instance $\eta \sim 25$), on the contrary, we might have high frequency ($\nu \gtrsim 10^{16}$ Hz) afterglow peaks occurring in the early deceleration stage long after the GRB end, i.e. on an observable timescale depending on the fireball total energy as $E_T^{1/3}$, but, according to absolute peak flux estimation in physical units presented in fig.5.18 and equation (5.27), dimmer of more

than a factor 100 than an afterglow peak from a fireball at $\eta \sim 300$ with the same total energy. Note that a dimmer absolute peak corresponds to a globally dimmer afterglow light curve during the Blandford & McKee stage having anyway the same slope predicted by [Granot, Piran & Sari 1999c]. For the same fireball with $\eta \sim 25$ producing, for instance, a dim X–ray afterglow, optical and radio afterglows might be "regular", i.e. well described by Granot model, and with absolute peak fluxes more than 100 times greater than in the X–rays.

Thus, spherical fireballs with a standard high value of the total energy of about 10^{52} ergs but moderately low η value around 20–25, though able to produce highly variable, energetic and long GRBs as less loaded fireballs with $\eta \gtrsim 100$, might produce simultaneously "regularly" intense radio and optical afterglows and 100 times dimmer X–ray afterglows. Actually, a case does exist of optical afterglow detection without any associated X–ray afterglow detection (GRB 970100, [Frontera *et al.* 2000]). These might be explained as due to absorption.

Note that GRB and afterglow observations have not provided any direct measure of the fireball baryon loading parameter yet. The standard value $\eta \gtrsim 100$ is suggested by the lower limits on the bulk Lorentz factor of the flow in internal shocks, but not rigorously settled on.

We suggest that a low η in a spherical model may mimic the effect of X–ray absorption.

Our results about afterglow peaks from spherical fireballs, though discussed in detail just for the case of neglected electron cooling, are general and valid also if cooling effects are included in the model.

However, the main result of the most complete afterglow calculation we have performed, is that realistic treatment of the radiation process together with realistic hydrodynamical evolution of the fireball and detailed accounting for relativistic effects, makes predicted afterglows light curves and spectra very smooth and difficult to be approximated as broken power laws. Sharp breaks and well defined slopes are almost completely smoothed away, and fitting observed afterglow light curves and spectra with broken power laws might lead to unreliable estimation of the intrinsic fireball parameters. Moreover, deviations of the magnetic field distribution from equipartition are unlikely to leave any clear and precise signature on the afterglow, and adiabatic cooling as well as other second order radiation loss mechanisms are likely to affect the

afterglow less than small deviations in the fireball hydrodynamics.

We can conclude that, since a real fireball will be even more chaotic and disordered than we have supposed, the rough broken power law fitting of observed afterglow light curves and spectra currently used to estimate fireball intrinsic properties according to very simple models is doomed to become more and more difficult and less consistent and conclusive with increasing number of observations and quality of data. It is possible that many of the "observed" breaks and slopes are actually less significant than is currently believed and corresponding estimations of the fireball parameters would be affected by large errors. A more complete modeling of light curves and spectra might help in dealing with the forthcoming observational data.

Appendix A

Jump conditions at Relativistic Shock Waves

A strong ultra relativistic collisionless shock wave that propagates in a cold and uniform medium produces great heating and compression of the matter it encompasses.

From a macroscopic point of view the net result of complex microscopic phenomena acting at the boundary layer can be described as follows.

Let us call n_1, ρ_1, p_1, e_1 and $\hat{\gamma}_1$ the comoving particle density, mass density, pressure, total energy density and adiabatic index of the unshocked matter respectively. Corresponding quantities with index 2 can be defined for the newly shocked material *. Let us also call u_2 and u_1 the velocities of the shocked and the unshocked matter with respect to the lab frame. The shock velocity in the lab frame will be U and the shock Lorentz factor will be Γ.

Let us assume that the unshocked matter is cold ($e_1 \sim \rho_1 c^2 \gg p_1$) and at rest with respect to the lab frame ($u_1 = 0$) and that the shock is strong $\left(\frac{p_2}{n_2} \gg \frac{p_1}{n_1}\right)$ and ultra relativistic ($\Gamma \gg 1$).

It can be proven that under these assumptions the Lorentz factor of the shocked matter as measured in the lab frame $\gamma = 1/\sqrt{1 - u_2^2/c^2}$ (i.e. the Lorentz factor of the shocked matter motion relative to the unshocked matter, which is at rest) is quite high too, and is related to the shock Lorentz factor by the simple expression

$$\gamma \sim \frac{\Gamma}{\sqrt{2}} \tag{A.1}$$

*Note that elsewhere in the text (chapter 3) the comoving properties of the shocked material have been denoted with a prime.

As a result of the shock transit the fluid acquires a relativistic bulk motion following the blast wave front, but the shock wave travels slightly faster than the shocked fluid behind it as the amount of shocked matter is continuously increasing. This is apparent also from the estimate of the Lorentz factor of the shocked matter motion relative to the shock itself, that is $\gamma_2 \sim \sqrt{2}$ (see below for the proper definition of γ_2).

As far as the comoving particle density and energy density of the shocked fluid are concerned, the assumptions we made lead to the following simple expressions:

$$n_2 = 2\sqrt{2}n_1\Gamma \quad \leftrightarrow \quad \rho_2 = 2\sqrt{2}\rho_1\Gamma \tag{A.2}$$

$$e_2 = 2\Gamma^2\rho_1 c^2 \tag{A.3}$$

Moreover we shall have $p_2 = e_2/3$, or equivalently $\hat{\gamma}_2 = 4/3$, the shocked matter being relativistic (the typical Lorentz factor of random motions of shocked particles in the comoving frame of the shocked fluid is given by $\frac{e_2}{\rho_2 c^2} \propto \Gamma \gg 1$).

Equations (A.1), (A.2) and (A.3) represent the jump conditions at the shock for the flow, i.e. the generalization of the Rankine Hugoniot conditions for non relativistic strong shocks.

The derivation of equations (A.1), (A.2) and (A.3) can be performed as follows.

A.1 Derivation

In the reference system where the shock is at rest let us call v_1 the speed of the unshocked matter flowing towards the shock and v_2 the speed of the shocked matter flowing out of it. Then we define $\beta_1 = \frac{v_1}{c}$ and $\beta_2 = \frac{v_2}{c}$. The corresponding Lorentz factors will be γ_1 and γ_2. As the unshocked matter is at rest in the lab frame, in this new reference system we shall see it plunging on the shock at the same velocity the shock had in the lab frame, so we can assume $v_1 = U$ and $\gamma_1 = \Gamma$.

In this reference system the shock appears as a discontinuity surface for the fluid comoving properties. The jump conditions at the shock are determined by imposing the conservation laws of energy, momentum and particle number through it, i.e. the continuity of the stress energy tensor components and of the current of particles in the flow direction (for us the x direction). Then, following [Landau & Lifshitz 1987], we can write:

$$[nu^x] = 0 \leftrightarrow n_1 v_1 \gamma_1 = n_2 v_2 \gamma_2 \tag{A.4}$$

$$[T^{xx}] = [(e+p)(u^x)^2 + pc^2] = 0 \leftrightarrow (e_1 + p_1)\beta_1^2\gamma_1^2 + p_1 = (e_2 + p_2)\beta_2^2\gamma_2^2 + p_2 \tag{A.5}$$

$$[T^{0x}] = [(e+p)u^0u^x] = 0 \leftrightarrow (e_1+p_1)\beta_1\gamma_1^2 = (e_2+p_2)\beta_2\gamma_2^2 \tag{A.6}$$

These relations can be simplified by remembering that we had assumed an unshocked cold medium ($e_1 \sim \rho_1 c^2$ and $p_1 \sim 0$), an ultra relativistic shocked matter ($e_2 = 3p_2$), and an ultra relativistic shock ($\Gamma = \gamma_1 \gg 1$) but we shall use these assumptions later in the calculation.

Note that the velocity of the shocked matter with respect to the unshocked matter is

$$v_{12} = \frac{v_1 - v_2}{1 - \frac{v_1 v_2}{c^2}} \tag{A.7}$$

and the corresponding Lorentz factor is

$$\gamma_{12} = \gamma_1\gamma_2\left(1 - \beta_1\beta_2\right) \tag{A.8}$$

As the unshocked matter is at rest in the lab frame, the relative velocity of the shocked and unshocked matter is equal to the velocity of the shocked matter relative to the lab frame end we can write $v_{12} = u_2$ and $\gamma_{12} = \gamma$.

¿From equations (A.4), (A.5) and (A.6) we get, with simple algebra,

$$\beta_1 = \frac{v_1}{c} = \sqrt{\frac{(p_2 - p_1)(e_2 + p_1)}{(e_2 - e_1)(e_1 + p_2)}} \tag{A.9}$$

$$\beta_2 = \frac{v_2}{c} = \sqrt{\frac{(p_2 - p_1)(e_1 + p_2)}{(e_2 - e_1)(e_2 + p_1)}} \tag{A.10}$$

$$\beta_{12} = \frac{v_{12}}{c} = \sqrt{\frac{(p_2 - p_1)(e_2 - e_1)}{(e_1 + p_2)(e_2 + p_1)}} \tag{A.11}$$

From (A.9) we get

$$\gamma_1 = \left(1 - \frac{v_1^2}{c^2}\right)^{-1/2} = \left(\frac{(e_2 - e_1)(e_1 + p_2)}{e_1(e_2 - p_2 - e_1) + p_1(e_2 - p_2 + p_1)}\right)^{-1/2} \tag{A.12}$$

that after substituting $p_1 = 0$ and $p_2 = \frac{e_2}{3}$ becomes

$$\gamma_1 = \left(\frac{(e_2 - e_1)\left(e_1 + \frac{e_3}{3}\right)}{e_1\left(\frac{2}{3}e_2 - e_1\right)}\right)^{1/2} = \left(\frac{\left(\frac{e_2}{e_1} - 1\right)\left(1 + \frac{1}{3}\frac{e_2}{e_1}\right)}{\left(\frac{2}{3}\frac{e_2}{e_1} - 1\right)}\right)^{1/2} \tag{A.13}$$

As we want $\gamma_1 \gg 1$, the only allowed relations between e_2 and e_1 are

1. $\frac{e_2}{e_1} \sim \frac{3}{2}$,

2. $\frac{e_2}{e_1} \gg 1$.

If (1) is valid, then substituting into (A.9) and (A.10) we get

$$\beta_1 = \sqrt{\frac{p_2 e_2}{(e_2 - e_1)(e_1 + p_2)}} = \left[\frac{1}{3}\frac{\left(\frac{e_2}{e_1}\right)^2}{\left(\frac{e_2}{e_1} - 1\right)\left(1 + \frac{1}{3}\frac{e_2}{e_1}\right)}\right]^{1/2} = \left[\frac{1}{3}\frac{\frac{9}{4}}{\frac{1}{2}\frac{3}{2}}\right]^{1/2} = 1 = \beta_2$$

that is quite unacceptable.

On the other hand, if (2) is valid we get

$$\gamma_1 \sim \left[\frac{\frac{1}{3}\left(\frac{e_2}{e_1}\right)^2}{\frac{2}{3}\frac{e_2}{e_1}}\right]^{1/2} = \left[\frac{1}{2}\frac{e_2}{e_1}\right]^{1/2} \tag{A.14}$$

thus, using $e_1 \sim \rho_1 c^2$,

$$e_2 \sim 2\gamma_1^2 e_1 \sim 2\gamma_1^2 \rho_1 = 2\Gamma^2 \rho_1 c^2 \tag{A.15}$$

and equation (A.3) is proven. Moreover,

$$\beta_1 \sim 1, \quad \beta_2 = \left[\frac{1}{3}\frac{1 + \frac{1}{3}\frac{e_2}{e_1}}{\frac{e_2}{e_1} - 1}\right]^{1/2} \sim \left[\frac{1}{9}\right]^{1/2} = \frac{1}{3} \tag{A.16}$$

$$\gamma_2 \sim \left(1 - \frac{1}{9}\right)^{-1/2} = \left(\frac{9}{8}\right)^{1/2} = \frac{3}{2\sqrt{2}} \sim \sqrt{2} \tag{A.17}$$

$$\gamma = \gamma_{12} = \gamma_1\gamma_2(1 - \beta_1\beta_2) \sim \gamma_1 \frac{3}{2\sqrt{2}}\left(1 - \frac{1}{3}\right) = \frac{\gamma_1}{\sqrt{2}} \tag{A.18}$$

Finally, the relations just found imply

$$n_2 = n_1 \frac{\beta_1}{\beta_2}\frac{\gamma_1}{\gamma_2} \sim n_1\gamma_1 3\frac{2\sqrt{2}}{3} = 2\sqrt{2}\Gamma n_1 \tag{A.19}$$

as we wanted to prove.

Appendix B

Blandford & McKee Self–Similar Solution

The Blandford & McKee self–similar solution which we want to discuss here is the one describing the self–similar stage of expansion for the spherical ultra relativistic blast wave produced by a strong explosion in a cold and uniform medium.

The shocked matter flow is the spherically symmetric solution of the relativistic equations of hydrodynamics satisfying the jump conditions at the shock (A.1), (A.2) and (A.3) under the assumptions that the surrounding medium is cold and at rest relative to the lab frame and that the shock wave is strong and ultra relativistic.

Let us assume that the shock radius and Lorentz factor follows the evolution laws $R(t)$ and $\Gamma(t)$, where t is the coordinate time of the Minkowski lab frame, whose origin is the center of the explosion. $R(t)$ and $\Gamma(t)$ are clearly related by the differential equation of motion

$$\frac{dR}{dt} = c\left(1 - \frac{1}{\Gamma^2(t)}\right)^{1/2} \tag{B.1}$$

Let's assume $\Gamma(t) \propto R(t)^{-m/2}$. Under this assumption self–similar solutions for the flow surely exist and they have a simple physical meaning for some special values of $m > -1$. The case $m = 3$ corresponds, for example, to the *adiabatic* self–similar expansion while the case $m = 6$ corresponds to a *radiative* self similar expansion.

Now I illustrate the main steps required to derive the Blandford & McKee self–similar solution, and the main properties of the solution itself in the adiabatic $m = 3$ case.

As we have already done in appendix A let us call n_1, ρ_1 p_1 and $e_1 \sim \rho_1 c^2 \gg p_1$ the ambient medium properties (remind that the ambient medium is supposed to be cold,

uniform and at rest). The shocked fluid comoving properties will be $n_2(r,t)$ $\rho_2(r,t)$ $p_2(r,t)$, $e_2(r,t)$ and $\gamma(r,t)$. As we expect the shocked fluid to be relativistic, the following relations hold: $e_2(r,t) = \rho_2(r,t)\gamma(r,t)c^2$ and $p_2(r,t) = e_2(r,t)/3$. Moreover $n_2(r,t) \propto \rho_2(r,t)$.

The general relativistic equations of hydrodynamics for the ideal relativistic shocked fluid in spherical symmetry can be rewritten as follows [Blandford & McKee 1976]:

$$\frac{d}{dt}\left(p_2\gamma^4\right) = \gamma^2\frac{\partial p_2}{\partial t} \tag{B.2}$$

$$\frac{d}{dt}\ln\left(p_2^3\gamma^4\right) = -\frac{4}{r^2}\frac{\partial}{\partial r}\left(r^2\beta\right) \tag{B.3}$$

$$\frac{d}{dt}\left(\frac{p_2}{n_2^{4/3}}\right) = 0 \tag{B.4}$$

where

$$\frac{d}{dt} = \frac{\partial}{\partial t} + \beta\frac{\partial}{\partial r}, \quad \beta = \left(1 - \frac{1}{\gamma^2}\right)^{1/2} \tag{B.5}$$

The solution we are looking for must satisfy the boundary conditions

$$\gamma\left(R(t),t\right) = \frac{\Gamma(t)}{\sqrt{2}} \tag{B.6}$$

$$p_2\left(R(t),t\right) = \frac{2}{3}\Gamma^2(t)\rho_1 c^2 \tag{B.7}$$

$$n_2\left(R(t),t\right) = 2\sqrt{2}n_1\Gamma(t) \tag{B.8}$$

which correspond to the Rankine–Hugoniot conditions for a strong ultra relativistic shock discussed in the appendix A, and must be of the form $\Gamma(t) \propto R(t)^{-m/2}$. The solution will be valid if the condition $\Gamma(t) \gg 1$ is satisfied.

Following [Granot, Piran & Sari 1999a] we prefer using as similarity variable

$$\chi(r,t) = 1 + 2(m+1)\Gamma^2(t)\left(1 - \frac{r}{R(t)}\right) \tag{B.9}$$

As we want to describe the region behind the shock front, we consider $\chi \geq 1$. In order to satisfy the boundary conditions the solutions of (B.2), (B.3) and (B.4) we want must have the form

$$\gamma(t,\chi) = \frac{\Gamma(t)}{\sqrt{2}}g(\chi), \quad g(1) = 1 \tag{B.10}$$

$$p_2(t,\chi) = \frac{2}{3}\Gamma^2(t)\rho_1 c^2 f(\chi), \quad f(1) = 1 \tag{B.11}$$

$$n_2(t,\chi) = 2\sqrt{2}\Gamma^2(t) n_1 h(\chi), \quad h(1) = 1 \tag{B.12}$$

Throughout the detailed calculations required to get such solutions all expansions in $1/\Gamma(t)$ can be self–consistently truncated at the order of the first contributing term because we are working in the limit $\Gamma(t) \gg 1$. Since our similarity variable differs from the Blandford & McKee similarity variable

$$\chi_{BM}(r,t) = [1 + 2(m+1)\Gamma^2(t)]\left(1 - \frac{r}{ct}\right) \tag{B.13}$$

only by terms of order $\Gamma(t)^{-2*}$, we can safely use the self–similar solutions found by [Blandford & McKee 1976].

In their original paper Blandford & McKee find, for the case $m = 3$,

$$g(\chi) = \chi^{-1/2} \tag{B.14}$$

$$f(\chi) = \chi^{-17/12} \tag{B.15}$$

$$h(\chi) = \chi^{-5/4} \tag{B.16}$$

Remind that, in the ultra relativistic limit, the fluid total energy density is related to the pressure by the relation $p_2(t,\chi) = \frac{1}{3} p_2(t,\chi)$.

Then note that a more convenient choice of the independent variables in the Blandford & McKee solution is the set Γ, χ instead of the set t, χ.

After this change of variables we can rewrite the $m = 3$ solution as

$$\gamma(\Gamma,\chi) = \frac{\Gamma}{\sqrt{2}}\chi^{-1/2} \tag{B.17}$$

$$p_2(\Gamma,\chi) = \frac{2}{3}\Gamma^2 m_p n_1 c^2 \chi^{-17/12} \tag{B.18}$$

$$n_2(\Gamma,\chi) = 2\sqrt{2}\Gamma^2 n_1 \chi^{-5/4} \tag{B.19}$$

with

$$\chi(r,\Gamma) = 1 + 8\Gamma^2\left(1 - \frac{r}{R(\Gamma)}\right) \tag{B.20}$$

and

$$e_2(\Gamma,\chi) = \frac{1}{\hat{\gamma}_2 - 1} p_2(\Gamma,\chi) = 2\Gamma^2 m_p n_1 c^2 \chi^{-17/12} \tag{B.21}$$

Remind that the function $R(\Gamma)$ in (B.20) must be consistent with the initial assumption

$$\Gamma \propto R^{-3/2} \tag{B.22}$$

*This is because in the limit $\Gamma(t) \gg 1$ we can write as a first approximation $R(t) \sim ct - \frac{1}{2(m+1)\frac{ct}{\Gamma^2(t)}}$.

and that, once the missing proportionality constant in (B.22) is specified, the function $\Gamma(t)$ can be found as solution of the differential equation (B.1) for any given initial condition $\Gamma(t_0) = \Gamma_0$.

The proportionality constant in (B.22) can be determined by the adiabaticity condition, and this is the reason why the $m = 3$ case has been identified with the self–similar solution for the adiabatic expansion from the beginning. Actually we can calculate the total energy E_T and the total mass M_s of the flow as follows

$$E_T = \int \left[-p_2(\Gamma,\chi) + \left(p_2(\Gamma,\chi) + e_2(\Gamma,\chi) + n_2(\Gamma,\chi)\, m_p c^2\right)\gamma(\Gamma,\chi)^2\right] dV \tag{B.23}$$

$$M_s = \int m_p n_2(\Gamma,\chi)\,\gamma(\Gamma,\chi)\, dV \tag{B.24}$$

where the volume element is $dV = 4\pi r^2 dr$.

To calculate the integrals in (B.23) and (B.24) we must change integration variable from r to χ. From (B.20) we get

$$r = \frac{R(1+8\Gamma^2-\chi)}{8\Gamma^2} \tag{B.25}$$

and thus

$$dV = 4\pi\left[\frac{R(1+8\Gamma^2-\chi)}{8\Gamma^2}\right]^2 \frac{R}{8\Gamma^2} d\chi \tag{B.26}$$

and

$$E_T = \int_1^{1+8\Gamma^2} \left[-p_2(\Gamma,\chi) + \left(p_2(\Gamma,\chi) + e_2(\Gamma,\chi) + n_2(\Gamma,\chi)\, m_p c^2\right)\gamma(\Gamma,\chi)^2\right] 4\pi\left[\frac{R(1+8\Gamma^2-\chi)}{8\Gamma^2}\right]^2 \frac{R}{8\Gamma^2} d\chi \tag{B.27}$$

$$M_s = \int_1^{1+8\Gamma^2} m_p n_2(\Gamma,\chi)\,\gamma(\Gamma,\chi)\, 4\pi\left[\frac{R(1+8\Gamma^2-\chi)}{8\Gamma^2}\right]^2 \frac{R}{8\Gamma^2} d\chi \tag{B.28}$$

Since we are interested in the limit $\Gamma \gg 1$, we expand the integrands in powers of $1/\Gamma$, take the lowest order terms only and integrate between 1 and $+\infty$. The result of the integration is then

$$E_T = \frac{8}{17}\pi n_i m_p c^2 R^3 \Gamma^2 \tag{B.29}$$

$$M_s = \frac{4}{3}\pi n_i m_p R^3 \tag{B.30}$$

The total mass in the flow is exactly the total mass the shock has swept up and the the total energy in the flow (rest mass included) is proportional to $R^3\Gamma^2$. The adiabaticity

condition $E_T = constant$ reduces to

$$\Gamma = \left(\frac{17}{8} E_T \frac{1}{\pi n_i m_p c^2}\right)^{1/2} R^{-3/2} \tag{B.31}$$

that is consistent with the assumption $\Gamma \propto R^{-3/2}$.

Appendix C

Sedov Self–Similar Solution

Let us consider the spherical expanding blast wave in Newtonian physics formed in case of:

- strong explosion, i.e. instantaneous release of a large amount of energy E_T in a small volume;
- polytropic gas with adiabatic index $\hat{\gamma}$ and uniform mass density ρ_1 as surrounding medium;
- pressure behind the shock (p_2) much larger than the pressure of the undisturbed gas (p_1) in front of it, or equivalently

$$(\hat{\gamma}-1)p_2 \gg (\hat{\gamma}+1)p_1 \tag{C.1}$$

$$\frac{p_2}{p_1} \gg \frac{\hat{\gamma}+1}{\hat{\gamma}-1} \tag{C.2}$$

  (strong shock condition);
- adiabatic evolution, i.e. negligible radiation losses.

We look for self–similar solutions of the equations of classical hydrodynamics describing the shocked matter evolution.

We define the self–similarity variable

$$\xi(r,t) = r\left(\frac{\rho_1}{E_T t^2}\right)^{1/5} \tag{C.3}$$

The position $R(t)$ of the shock at a certain time t must correspond to a constant value of the self–similarity variable depending on the adiabatic index of the surrounding medium only:

$$R(t)\left(\frac{\rho_1}{E_T t^2}\right)^{1/5} = \beta(\hat{\gamma}) \tag{C.4}$$

The constant $\beta(\hat{\gamma})$ must be determined by solving the equations of motion.

Then,

$$R(t) = \beta(\hat{\gamma})\left(\frac{E_T t^2}{\rho_1}\right)^{1/5} \tag{C.5}$$

and

$$U(t) = \frac{dR}{dt} = \frac{2}{5}\frac{R}{t} = \frac{2}{5}\beta(\hat{\gamma})\left(\frac{E_T}{\rho_1 t^3}\right)^{1/5} \tag{C.6}$$

For a plane strong shock moving in uniform medium in the frame of the shock we see the unshocked material at a pressure p_1 and mass density ρ_1 flowing toward the shock with a velocity v_1 and the shocked material at a pressure p_2 and mass density ρ_2 flowing out from the shock at a velocity $v_2 < v_1$. The jump conditions across the shock are:

$$\rho_1 v_1 = \rho_2 v_2 \tag{C.7}$$

$$p_1 + \rho_1 v_1^2 = p_2 + \rho_2 v_2^2 \tag{C.8}$$

$$\varepsilon_1 + \frac{p_1}{\rho_1} + \frac{1}{2}v_1^2 = \varepsilon_2 + \frac{p_2}{\rho_2} + \frac{1}{2}v_2^2 \tag{C.9}$$

where ε_1 and ε_2 are the internal energy per unit mass for the unshocked and the shocked fluid respectively. If the shock velocity relative to the lab frame is U and the unshocked fluid is at rest in the lab frame ($u_1 = 0$) then $v_1 = U$ and the shocked fluid velocity relative to the lab frame u_2 is given by the relation $u_2 - u_1 = v_2 - v_1$. Using the jump conditions across the shock we get

$$u_2 = \frac{2v_1}{\hat{\gamma}+1} = \frac{2}{\hat{\gamma}+1}U \tag{C.10}$$

and then

$$\rho_2 = \rho_1\frac{\hat{\gamma}+1}{\hat{\gamma}-1} \tag{C.11}$$

$$p_2 = \frac{2}{\hat{\gamma}+1}\rho_1 U^2 \tag{C.12}$$

For a spherical strong shock we know $U(t)$ and we just expect that for the matter immediately behind the shock the same equations as in the plane case hold, so that

$$u_2(R(t), t) = \frac{2}{\hat{\gamma}+1}U(t) \tag{C.13}$$

$$\rho_2(R(t),t) = \rho_1 \frac{\hat{\gamma}+1}{\hat{\gamma}-1} \tag{C.14}$$

$$p_2(R(t),t) = \frac{2}{\hat{\gamma}+1}\rho_1 U^2(t) \tag{C.15}$$

However, the velocity, mass density and pressure distributions of the shocked fluid far from the shock will not be uniform, but will be self–similar.

If we use as self–similarity variable

$$\xi(r,t) = \frac{r}{R(t)} = \left(\frac{r}{\beta(\hat{\gamma})}\right)\left(\frac{\rho_1}{E_T t^2}\right)^{1/5} \tag{C.16}$$

we expect the flow behind the spherical blast wave to fit the following distribution laws

$$u_2(r,t) = \frac{2}{5}\frac{r}{t}V(\xi) \tag{C.17}$$

$$\rho_2(r,t) = \rho_1 G(\xi) \tag{C.18}$$

$$c_s^2(r,t) = \frac{\hat{\gamma}p_2(r,t)}{\rho_2(r,t)} = \frac{4}{25}\frac{r^2}{t^2}Z(\xi) \tag{C.19}$$

where the functions V, G and Z must be determined as solutions of the equations of hydrodynamics according to the boundary conditions

$$V(1) = \frac{2}{\hat{\gamma}+1} \tag{C.20}$$

$$G(1) = \frac{\hat{\gamma}+1}{\hat{\gamma}-1} \tag{C.21}$$

$$Z(1) = \frac{2}{(\hat{\gamma}+1)^2}(\hat{\gamma}-1) \tag{C.22}$$

that come from (C.13), (C.14) and (C.15).

The spherically symmetric self–similar solutions for the equations of hydrodynamics are the ones corresponding to the functions V, G and Z such that

$$\xi^5 = \left[\frac{1}{2}(\hat{\gamma}+1)V(\xi)\right]^{-2}\left\{\frac{\hat{\gamma}+1}{7-\hat{\gamma}}[5-(3\hat{\gamma}-1)V(\xi)]\right\}^{\nu_1}\left[\frac{\hat{\gamma}+1}{\hat{\gamma}-1}(\hat{\gamma}V(\xi)-1)\right]^{\nu_2} \tag{C.23}$$

with $\nu_1 = -\frac{13\hat{\gamma}^2-7\hat{\gamma}+12}{(3\hat{\gamma}-1)(2\hat{\gamma}+1)}$ and $\nu_2 = \frac{5(\hat{\gamma}-1)}{2\hat{\gamma}+1}$

$$G(\xi) = \frac{\hat{\gamma}+1}{\hat{\gamma}-1}\left[\frac{\hat{\gamma}+1}{\hat{\gamma}-1}(\hat{\gamma}V(\xi)-1)\right]^{\nu_3}\left\{\frac{\hat{\gamma}+1}{7-\hat{\gamma}}[5-(3-\hat{\gamma})V(\xi)]\right\}^{\nu_4}\left[\frac{\hat{\gamma}+1}{\hat{\gamma}-1}(1-V(\xi))\right]^{\nu_5} \tag{C.24}$$

with $\nu_3 = \frac{3}{2\hat{\gamma}+1}$, $\nu_4 = -\frac{\nu_1}{2-\hat{\gamma}}$ and $\nu_5 = -\frac{2}{2-\hat{\gamma}}$

$$Z(\xi) = \frac{\hat{\gamma}(\hat{\gamma}-1)(1-V(\xi))V^2(\xi)}{2(\hat{\gamma}V(\xi)-1)} \tag{C.25}$$

The determination of $\beta(\hat{\gamma})$ is the made by assuming the total energy conservation for the flow evolution (adiabatic flow condition). As the total initial energy is the energy of the explosion E_T, while in the following times the energy resides entirely in the shocked material and is partly kinetic and partly thermal we must impose

$$E_T = \int_0^{R(t)} \rho(r,t)\left[\frac{1}{2}v^2(r,t) + \frac{c_s^2(r,t)}{\hat{\gamma}(\hat{\gamma}-1)}\right] 4\pi r^2 dr \tag{C.26}$$

By substituting (C.17), (C.18) and (C.19) we get the following expression for the total energy of the adiabatic flow at any time after the self–similar expansion regime has started

$$E_T = \frac{16\pi}{25}\rho_1 \frac{R^5(t)}{t^2}\int_0^1 G(\xi)\left[\frac{1}{2}V^2(\xi) + \frac{Z(\xi)}{\hat{\gamma}(\hat{\gamma}-1)}\right]\xi^4 d\xi = \frac{16\pi}{25}\rho_1\frac{R^5(t)}{t^2}K(\hat{\gamma}) \tag{C.27}$$

where we have named

$$K(\hat{\gamma}) = \int_0^1 G(\xi)\left[\frac{1}{2}V^2(\xi) + \frac{Z(\xi)}{\hat{\gamma}(\hat{\gamma}-1)}\right]\xi^4 d\xi \tag{C.28}$$

¿From (C.5) we then get

$$E_T = \frac{16\pi}{25}\rho_1\frac{E_T}{\rho_1}\beta(\hat{\gamma})^5 K(\hat{\gamma}) \tag{C.29}$$

that can be inverted to give

$$\beta(\hat{\gamma}) = \left(\frac{25}{16\pi}\right)^{1/5}\left(\frac{1}{K(\hat{\gamma})}\right)^{1/5} \tag{C.30}$$

We can conclude that the shock radius and velocity follows the evolution laws

$$R(t) = \left(\frac{1}{K(\hat{\gamma})}\right)^{1/5}\left(\frac{25}{16\pi}\right)^{1/5}\left(\frac{E_T t^2}{\rho_1}\right)^{1/5} \tag{C.31}$$

and

$$U(t) = \frac{2}{5}\left(\frac{1}{K(\hat{\gamma})}\right)^{1/5}\left(\frac{25}{16\pi}\right)^{1/5}\left(\frac{E_T}{\rho_1 t^3}\right)^{1/5} \tag{C.32}$$

On the other hand, if we recall (C.6) we can write

$$\frac{R^5(t)}{t^2} = R^3(t)\left(\frac{R(t)}{t}\right)^2 = R^3(t)\left(\frac{5}{2}U(t)\right)^2 = \frac{25}{4}R^3(t)U^2(t)$$

then finally, solving equation (C.31) for E_T, we get

$$E_T = \frac{4}{3}\pi\rho_1 R^3(t)U^2(t) \times 3K(\hat{\gamma}) \tag{C.33}$$

This is the general expression for the total energy of the self–similarly expanding spherical blast wave in terms of the shock radius and velocity in the non relativistic regime. It is independent of when the self–similar behaviour starts, provided that the possible preceding expansion stages were adiabatic.

In the case $\hat{\gamma} = \frac{5}{3}$ (monatomic perfect gas), equations (C.23), ((C.24) and (C.25) become

$$\xi^5 = \left[\frac{4}{3}V(\xi)\right]^{-2}\left[\frac{5}{2} - 2V(\xi)\right]^{-82/39}\left[4\left(\frac{5}{3}V(\xi) - 1\right)\right]^{10/13} \tag{C.34}$$

$$G(\xi) = 2^{-30/13}(1 - V(\xi))^{-6}\left(\frac{5}{3}V(\xi) - 1\right)^{9/13}(5 - 4V(\xi))^{-82/13} \tag{C.35}$$

$$Z(\xi) = \frac{5}{3}\frac{(1 - V(\xi))V^2(\xi)}{5V(\xi) - 3} \tag{C.36}$$

with

$$V(1) = \frac{3}{4}, \quad G(1) = 4, \quad \text{and} \quad Z(1) = \frac{5}{16} \tag{C.37}$$

Moreover [Spitzer 1978],

$$K(5/3) = \frac{3}{8 \times 1.53} \sim 0.245 \tag{C.38}$$

and

$$\beta(5/3) = \left(\frac{25}{6\pi}1.53\right)^{1/5} \sim (2.2029)^{1/5} \tag{C.39}$$

For $\xi = 0$ equation (C.34) has the solution $V(0) = \frac{1}{\hat{\gamma}} = \frac{3}{5}$. Then we can verify that $V(1) = \frac{3}{4}$ is the solution of equation (C.34) for $\xi = 1$. In general we expect only one solution $V(\xi)$ for each possible ξ in the range [0,1]. This solution can be calculated numerically. It increases continuously from 3/5 to 3/4 when ξ grows from 0 to 1. Once $V(\xi)$ has been calculated, $G(\xi)$ and $Z(\xi)$ can be obtained from (C.35) and (C.36), then we can plot the velocity, density and pressure distributions behind the shock at a given time t.

For an easy presentation of the results, let us define the *adimensional* functions $F_{u_2}(\xi)$, $F_{\rho_2}(\xi)$, $F_{p_2}(\xi)$ and $F_{c_s^2}(\xi)$ such that

$$u_2(\xi,t) = \frac{2}{5}\frac{R(t)}{t}V(1)F_{u_2}(\xi) \tag{C.40}$$

$$\rho_2(\xi,t) = \rho_1 G(1)F_{\rho_2}(\xi) \tag{C.41}$$

$$p_2(\xi,t) = \frac{\rho_1}{\hat{\gamma}}\frac{4}{25}\frac{R^2(t)}{t^2}Z(1)G(1)F_{p_2}(\xi) \tag{C.42}$$

$$c_s^2(\xi,t) = \frac{4}{25}\frac{R^2(t)}{t^2}Z(1)F_{c_s^2}(\xi) \tag{C.43}$$

According to this definition the matter velocity, the pressure distribution and the squared sound velocity of shocked matter at a give time t are obtained through multiplication of $F_{u_2}(\xi)$, $F_{p_2}(\xi)$ and $F_{c_s^2}(\xi)$ by a t dependent factor which is a decreasing function of t. On the other hand, the density distribution of matter behind the shock does not depend on time at all.

In the case $\hat{\gamma} = 5/3$ the definitions (C.40), (C.41), (C.42) and (C.43) correspond to

$$u_2(\xi,t) = \frac{2}{5}\frac{R(t)}{t}\xi V(\xi) \quad \rightarrow \quad F_{u_2}(\xi) = \frac{4}{3}u_2(\xi,t)\frac{5}{2}\frac{t}{R(t)} = \frac{4}{3}\xi V(\xi) \tag{C.44}$$

$$\rho_2(\xi,t) = \rho_1 G(\xi) \quad \rightarrow \quad F_{\rho_2}(\xi) = \frac{\rho_2(\xi,t)}{4\rho_1} = \frac{G(\xi)}{4} \tag{C.45}$$

$$p_2(\xi,t) = \frac{3}{5}\rho_2(\xi,t)\frac{4}{25}\frac{R^2(t)}{t^2}\xi^2 Z(\xi) = \rho_1\frac{3}{5}\frac{4}{25}\frac{R^2(t)}{t^2}\xi^2 Z(\xi)G(\xi) \quad \rightarrow$$

$$F_{p_2}(\xi) = \frac{4}{5}p_2(\xi,t)\frac{5}{3}\frac{25}{4}\frac{t^2}{R^2(t)} = \frac{4}{5}\xi^2 Z(\xi)G(\xi) \tag{C.46}$$

$$c_s^2(\xi,t) = \hat{\gamma}\frac{p_2(\xi,t)}{rho_2(\xi,t)} = \frac{4}{25}\frac{R^2(t)}{t^2}\xi^2 Z(\xi) \quad \rightarrow \quad F_{c_s^2}(\xi) = \frac{16}{5}\xi^2 Z(\xi) \tag{C.47}$$

It is easily seen from equations (C.34) and (C.35) that, as $\xi \rightarrow 0$, $V(\xi)$ must tend to a constant limit and $G(\xi)$ to zero. Precisely

$$V(\xi) - \frac{3}{5} \propto \xi^{13/2}, \qquad G(\xi) \propto \xi^{9/2} \tag{C.48}$$

Then, from equation (C.36) we find that for $\xi \rightarrow 0$

$$Z(\xi) \propto \xi^{-13/2} \rightarrow \infty \tag{C.49}$$

We can conclude that for $\xi \to 0$ we expect

$$F_{u_2}(\xi) \propto \xi \to 0$$
$$F_{\rho_2}(\xi) \propto \xi^{9/2} \to 0$$
$$F_{p_2}(\xi) \propto \xi^2 \xi^{9/2} \xi^{-13/2} \to constant$$

In our calculation $F_{p_2}(\xi)$ tends to about 0.01111 for $\xi \to 0$.

On the other hand we expect

$$F_{c_s^2}(\xi) \to +\infty$$

for $\xi \to 0$.

The functions $F_{u_2}(\xi)$, $F_{\rho_2}(\xi)$, $F_{p_2}(\xi)$ and $F_{c_s^2}(\xi)$ we calculated by solving numerically equation (C.34) for $\hat{\gamma} = 5/3$ are shown in fig.C.1.

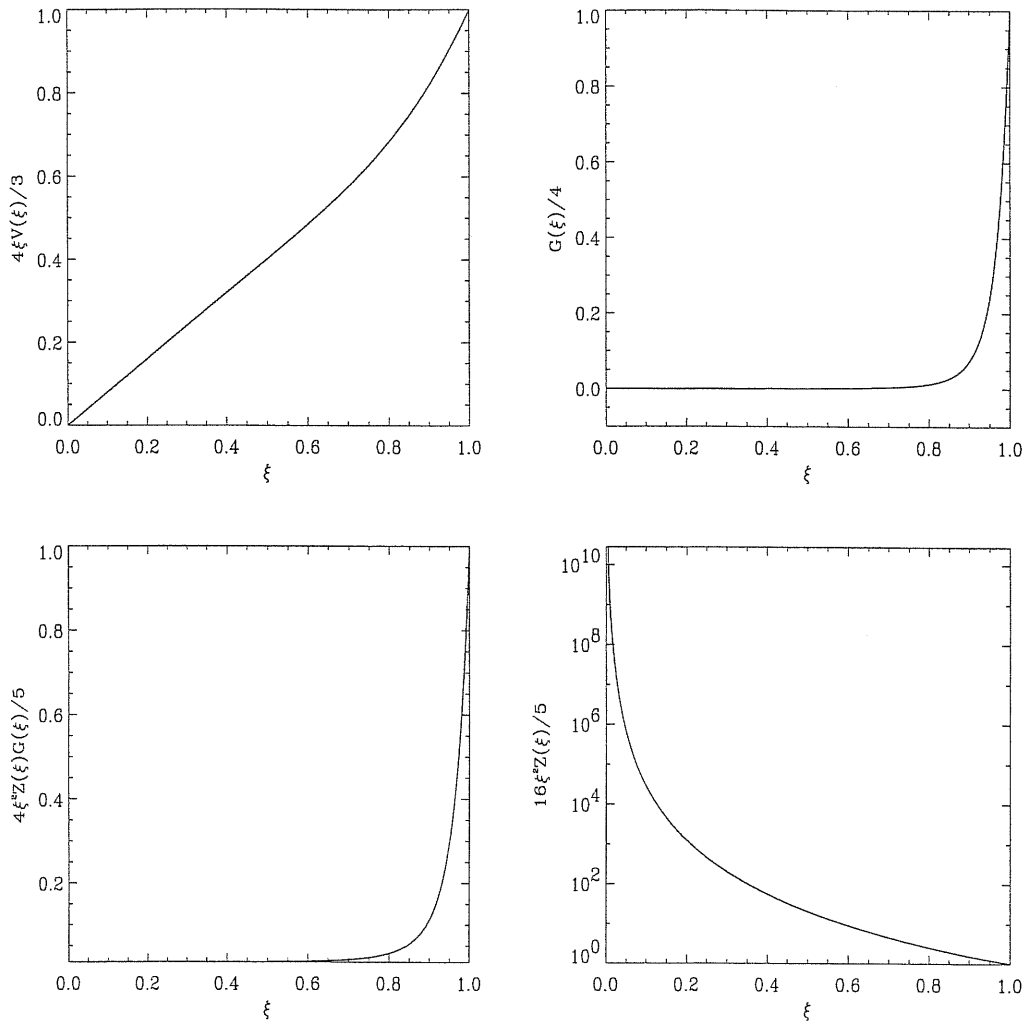

Figure C.1: *Top Left panel:* $F_{u_2}(\xi) = \frac{4}{3}\xi V(\xi)$. *Top Right panel:* $F_{\rho_2}(\xi) = \frac{G(\xi)}{4}$. *Bottom Left panel:* $F_{p_2}(\xi) = \frac{4}{5}\xi^2 Z(\xi)G(\xi)$. *Bottom Right panel:* $F_{c_s^2}(\xi) = \frac{16}{5}\xi^2 Z(\xi)$.

Appendix D

Synchrotron Radiation

I briefly summarize the well known results which can be found in any text book on radiation processes (see for example [Rybicki & Lightman 1979, Tucker 1975]) in a notation suitable for our case.

D.1 Emitted Radiation

D.1.1 .... radiation emitted by a single particle

For an electron moving in a uniform magnetic field B with a Lorentz factor γ_e and a pitch angle α the total emitted power is

$$P_{syn}(\gamma_e, \alpha) = \frac{2}{3}\left(\frac{e^2}{m_e c^2}\right)^2 c\beta_e^2\gamma_e^2 B^2 \sin^2\alpha \tag{D.1}$$

and the spectrum of emitted radiation is

$$P_{\gamma_e,\alpha}(\nu) = \sqrt{3}\frac{e^3 B}{m_e c^2}\sin\alpha F\left(\frac{\nu}{\nu_{syn}(\gamma_e,\alpha)}\right) \tag{D.2}$$

where

$$\nu_{syn}(\gamma_e,\alpha) = \frac{3}{2}\frac{eB}{2\pi m_e c}\gamma_e^2\sin\alpha = \frac{3}{4\pi}\frac{eB}{m_e c}\gamma_e^2\sin\alpha \tag{D.3}$$

and

$$F(x) = x\int_x^{+\infty} K_{\frac{5}{3}}(\xi)d\xi \tag{D.4}$$

$K_{\frac{5}{3}}(\xi)$ being the modified Bessel Fuction of order $5/3$.

It can be proved that

$$F(x) \sim \frac{4\pi}{\sqrt{3}\Gamma\left(\frac{1}{3}\right)}\left(\frac{x}{2}\right)^{1/3} \qquad x \ll 1 \tag{D.5}$$

$$F(x) \sim \left(\frac{\pi}{2}\right)^{1/2} e^{-x} x^{1/2} \qquad x \gg 1 \tag{D.6}$$

Moreover, the Spectrum reaches its maximum at

$$\nu_{peak}(\gamma_e, \alpha) = 0.29\, \nu_{syn}(\gamma_e, \alpha) \tag{D.7}$$

The modified Bessel function $F(x)$ and its asymptotics are shown in fig.D.1.

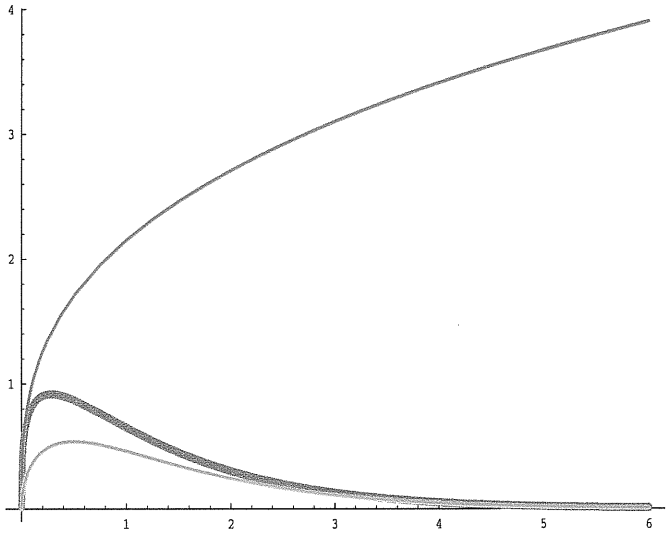

Figure D.1: *The function $F(x)$ (gray solid line) and its asymptotic expressions for $x \ll 1$ (red solid line) and $x \gg 1$ (blue solid line).*

The total emitted power (D.1) and the spectrum (D.2) refer to a finite integration time Δt short enough that the radiation loss does not affect the electron Lorentz factor, which is assumed constant. Thus we can say that (D.1) and (D.2) are instantaneous total power and spectrum emitted by the electron.

The electron Lorentz factor γ_e cannot be assumed constant any longer after a time $t_{cool}(\gamma_e, \alpha)$ such that the total energy radiated as synchrotron radiation during this time interval ($\sim P_{syn}(\gamma_e, \alpha) t_{cool}$) is comparable to the total electron energy ($\gamma_e m_e c^2$). Then we can define as the *cooling time* for a relativistic electron, the quantity

$$t_{cool}(\gamma_e, \alpha) = \frac{3}{2}\left(\frac{m_e c^2}{e^2}\right)^2 \frac{\gamma_e m_e c^2}{c\beta_e^2 \gamma_e^2 B^2 \sin^2\alpha} = \frac{3}{2}\left(\frac{m_e c^2}{e^2}\right)^2 \frac{m_e c}{\beta_e^2 \gamma_e B^2 \sin^2\alpha} \tag{D.8}$$

D.1.2 .... radiation emitted by an ensemble of monoenergetic particles

Now we assume that all the emitting electrons in a given fluid element have the same Lorentz factor $\gamma_e \gg 1$ but randomly distributed directions, i.e random pitch angles α. Let n'_e be the number density of emitting electrons in the volume element dV. The total number of electrons with pitch angle between α and $\alpha + d\alpha$ in our volume element will be $\frac{n'_e dV}{4\pi} 2\pi \sin\alpha d\alpha$. Each of these electrons will emit synchrotron radiation as described in the previous section. Assuming that emission from different electrons is not coherent we can calculate the total power and spectrum emitted by the fluid element as the sum of total power and spectrum emitted by all the electrons (this is equivalent to an integration over α of the number of electrons with pitch angle between α and $\alpha + d\alpha$ times $P_{syn}(\gamma_e, \alpha)$ or $P_{\gamma_e,\alpha}(\nu)$ respectively). Then we will divide by dV as quantities per unit volume are usually preferred when dealing with a fluid. Moreover, since the emission in the fluid comoving frame is expected to be isotropic, we can further divide by 4π to have a quantity per unit solid angle. The resulting quantities will be named emissivities.

The total emissivity of the fluid, i.e. the total power emitted per unit volume of the fluid and per unit solid angle will be $j'_{syn}(\gamma_e)$ such that

$$\begin{aligned} 4\pi j'_{syn}(\gamma_e) &= \frac{n'_e}{4\pi}\int_0^\pi P'_{syn}(\gamma_e,\alpha) 2\pi \sin\alpha \, d\alpha = \\ &= \frac{n'_e}{4\pi} 2\pi \frac{2}{3}\left(\frac{e^2}{m_e c^2}\right)^2 c\beta_e^2\gamma_e^2 B^2 \int_0^\pi \sin^3\alpha d\alpha = \\ &= n'_e \frac{1}{3} c \frac{B^2 e^4}{m_e^2 c^4}\beta_e^2\gamma_e^2 \frac{4}{3} = n'_e \frac{4}{9} c \frac{B^2 e^4}{m_e^2 c^4}\beta_e^2\gamma_e^2 = \\ &= n'_e \frac{4}{3}\sigma_T c \beta_e^2 \gamma_e^2 \frac{B^2}{8\pi} \end{aligned} \tag{D.9}$$

The average Synchrotron Frequency of all electrons will be

$$\nu'_{syn}(\gamma_e) = \frac{3}{2}\frac{eB\gamma_e^2}{m_e c}\frac{1}{2\pi}\frac{\pi}{4} = \frac{3}{16}\frac{eB\gamma_e^2}{m_e c} \tag{D.10}$$

The monochromatic emissivity of the fluid, i.e. the spectrum of the radiation emitted per unit volume of the fluid and per unit solid angle will be $j'_{\gamma_e}(\nu')$ such that:

$$\begin{aligned} 4\pi j'_{\gamma_e}(\nu') &= \frac{n'_e}{4\pi}\int_0^\pi P'_{\gamma_e,\alpha}(\nu') 2\pi \sin\alpha \, d\alpha = \\ &= \frac{n'_e}{4\pi} 2\pi\sqrt{3}\frac{e^3 B}{m_e c^2}\int_0^\pi F\left(\frac{\nu'}{\nu'_{syn}(\gamma_e,\alpha)}\right)\sin^2\alpha \, d\alpha = \end{aligned}$$

$$= n'_e \frac{\sqrt{3}}{2} \frac{e^3 B}{m_e c^2} \int_0^\pi F\left(\frac{\nu'}{\nu'_{syn}(\gamma_e, \alpha)}\right) \sin^2 \alpha \; d\alpha \tag{D.11}$$

All the primes mean that we are referring to the frame comoving with the fluid. Again the integration time $\Delta t'$ must have been chosen short enough for γ_e to be assumed constant during emission, so that (D.9) and (D.11) represent the instantaneous total and monocromatic emissivity of the fluid.

Note that if we define the average value of the single particle spectrum

$$< P'_{\gamma_e}(\nu') >= \frac{1}{4\pi} \int_0^\pi 2\pi P'_{\gamma_e,\alpha}(\nu') \sin \alpha \; d\alpha \tag{D.12}$$

we can say that

$$4\pi j'_{\gamma_e}(\nu') = n'_e < P'_{\gamma_e}(\nu') > \tag{D.13}$$

The average single particle spectrum can be expressed in the following way

$$< P'_{\gamma_e}(\nu') >= \frac{\sqrt{3} B e^3}{2 m_e c^2} \; Q\left[S\left(B, \frac{\nu'}{\gamma_e^2}\right)\right] \tag{D.14}$$

with

$$S\left(B, \frac{\nu'}{\gamma_e^2}\right) = \frac{4\pi m_e c}{3eB} \frac{\nu'}{\gamma_e^2} \tag{D.15}$$

and

$$Q[x] = \int_0^\pi F\left(\frac{x}{\sin \alpha}\right) \sin^2 \alpha d\alpha \tag{D.16}$$

The function $Q[x]$ can be calculated numerically (see fig.D.2).

The average cooling time for the electrons will be

$$t_{cool}(\gamma_e) = \frac{n'_e \gamma_e m_e c^2}{4\pi j'_{syn}(\gamma_e)} = \frac{3}{4} \frac{8\pi m_e c}{\sigma_T \beta_e^2 \gamma_e B^2} \tag{D.17}$$

D.1.3 .... radiation emitted by an ensemble of particles with a power law energy distribution

If the electron energy distribution is such that the electron population have Lorentz factors γ_e varying between $\gamma_{e,min}$ and $\gamma_{e,max} \gg \gamma_{e,min}$, and the number of electrons per unit volume with Lorentz factor between γ_e and$\gamma_e + d\gamma_e$ is

$$dn'_e = N(\gamma_e) d\gamma_e = N_e \gamma_e^{-p} d\gamma_e \tag{D.18}$$

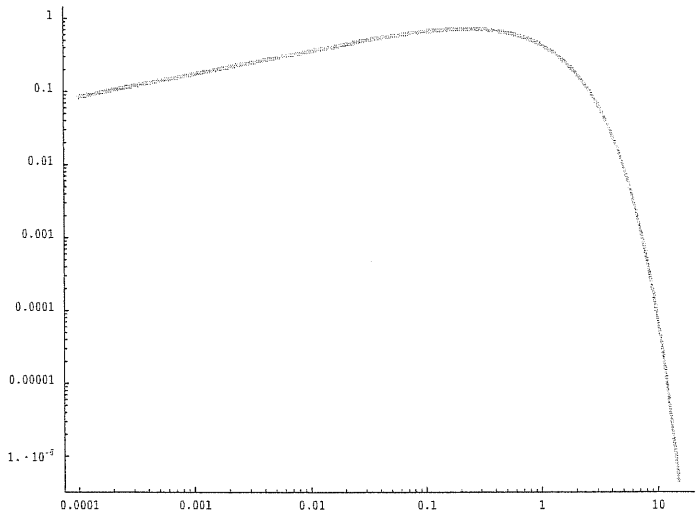

Figure D.2: *Plot of the function $Q[x]$ given by equation (D.16)*

with $p > 2$, but the electron speed directions are still randomly distributed, then we can calculate the instantaneous monochromatic emissivity of the fluid as

$$4\pi j'(\nu') = \frac{1}{4\pi}\int_0^{\pi} d\alpha 2\pi \sin\alpha \int_{\gamma_{e,min}}^{\gamma_{e,max}} d\gamma_e P'_{\gamma_e,\alpha}(\nu') N_e \gamma_e^{-p} \tag{D.19}$$

The quantity $P'_{\gamma_e,\alpha}(\nu')$ is the instantaneous spectrum of radiation emitted by a single electron of Lorentz factor γ_e and pitch angle α. So, $j'(\nu')$ is simply the sum of the instantaneous spectra emitted by every single electron in the volume element. If the integration time $\Delta t'$ is shorter than the cooling time of all electrons in our volume element, we can use expression (D.2) for $P'_{\gamma_e,\alpha}(\nu')$ and write:

$$\begin{aligned} 4\pi j'(\nu') &= \frac{N_e}{2}\frac{\sqrt{3}e^3 B}{m_e c^2}\int_0^{\pi} d\alpha \sin^2\alpha \int_{\gamma_{e,min}}^{\gamma_{e,max}} d\gamma_e F\left(\frac{\nu'}{\nu'_{syn}(\gamma_e,\alpha)}\right)\gamma_e^{-p} = \\ &= 2\pi N_e \frac{\sqrt{3}e^2}{4c}\nu'_B\left[\frac{2\nu'}{3\nu'_B}\right]^{-\frac{p-1}{2}}\int_0^{\pi} d\alpha \sin\alpha^{\frac{p+3}{2}}\int_{x_{min}(\nu',\alpha)}^{x_{max}(\nu',\alpha)} x^{\frac{p-3}{2}}F(x)dx \end{aligned} \tag{D.20}$$

with

$$\nu'_B = \frac{eB}{2\pi m_e c} \tag{D.21}$$

$$x_{min}(\nu',\alpha) = \frac{2\nu'}{3\nu_B}\frac{1}{\sin\alpha}\frac{1}{\gamma^2_{e,max}} \tag{D.22}$$

$$x_{max}(\nu',\alpha) = \frac{2\nu'}{3\nu_B}\frac{1}{\sin\alpha}\frac{1}{\gamma^2_{e,min}} \tag{D.23}$$

In order to have a reasonable approximated expression for $j'(\nu')$, note that in the limit $x_{min} \to 0$ (i.e. $\gamma_{e,max} \to +\infty$) and $x_{max} \to +\infty$ (i.e. $\nu' \to +\infty$). If we use the asymptotic expression of $F(x)$ for $x \to +\infty$ (eq.(D.6)) the right hand side in equation (D.20) becomes

$$2\pi N_e \frac{\sqrt{3}e^2}{4c}\nu'_B \left[\frac{2\nu'}{3\nu'_B}\right]^{-\frac{p-1}{2}} 2^{\frac{p-3}{2}} \frac{3p+7}{3(p+1)}\Gamma\left(\frac{3p-1}{12}\right)\Gamma\left(\frac{3p+7}{12}\right)\int_0^\pi d\alpha \sin\alpha^{\frac{p+3}{2}} \quad \text{(D.24)}$$

This must be the asymptotic behaviour of $j'(\nu')$ at very high frequencies, let us say $\nu' \gg \nu'_{syn}(\gamma_{e,min})$, except for a numerical coefficient.

On the other hand, from the asymptotic expression of $F(x)$ for $x \to 0$ (eq. (D.5)), we know that all electrons emit a spectrum $\propto \nu'^{1/3}$ at low frequencies, so also $j'(\nu')$ is expected to be $\propto \nu'^{1/3}$ at $\nu' \ll \nu'_{syn}(\gamma_{e,min})$.

Then we expect a reasonable approximation for $j'(\nu')$ in the case $\gamma_{e,max} \gg \gamma_{e,min}$ to be

$$j'_{app}(\nu') = \begin{cases} j'_{max}\left(\frac{\nu'}{\nu'_{syn}(\gamma_{e,min})}\right)^{\frac{1}{3}} & \nu' \leq \nu'_{syn}(\gamma_{e,min}) \\ j'_{max}\left(\frac{\nu'}{\nu'_{syn}(\gamma_{e,min})}\right)^{-\frac{p-1}{2}} & \nu' > \nu'_{syn}(\gamma_{e,min}) \end{cases} \quad \text{(D.25)}$$

with

$$4\pi j'_{max} \propto 2\pi N_e \frac{\sqrt{3}e^2}{4c}\nu'_B \left[\frac{\pi}{4}\gamma^2_{e,min}\right]^{-\frac{p-1}{2}} 2^{\frac{p-3}{2}} \frac{3p+7}{3(p+1)} \Gamma\left(\frac{3p-1}{12}\right)\Gamma\left(\frac{3p+7}{12}\right)\int_0^\pi d\alpha \sin\alpha^{\frac{p+3}{2}} \quad \text{(D.26)}$$

Provided that $\gamma_{e,max} \gg \gamma_{e,min}$, we can also write

$$n'_e = \int_{\gamma_{e,min}}^{\gamma_{e,max}} N_e \gamma_e^{-p} d\gamma_e \sim \frac{N_e}{p-1}\gamma_{e,min}^{-p+1}$$

from which we get

$$N_e \sim n'_e(p-1)\gamma_{e,min}^{p-1}$$

then we expect

$$4\pi j'_{max} \propto n'_e \frac{\sqrt{3}e^3 B}{4m_e c^2} \frac{2^{\frac{3p-5}{2}}}{\pi^{\frac{p-1}{2}}}(p-1)\frac{3p+7}{3(p+1)}\Gamma\left(\frac{3p-1}{12}\right)\Gamma\left(\frac{3p+7}{12}\right)\int_0^\pi d\alpha \sin\alpha^{\frac{p+3}{2}} \quad \text{(D.27)}$$

Moreover, we can note that

$$< \gamma_e >= \frac{1}{n'_e}\int_{\gamma_{e,min}}^{\gamma_{e,max}} \gamma_e N_e \gamma_e^{-p} d\gamma_e \sim \frac{p-1}{p-2}\gamma_{e,min} \quad \text{(D.28)}$$

and consequently

$$\frac{4\pi j'_{syn}(<\gamma_e>)}{\nu'_{syn}(<\gamma_e>)} = n'_e \frac{4}{9} cB^2 \frac{e^4}{m_e^2 c^4} \gamma^2_{e,min} \frac{16 m_e c}{3eB\gamma^2_{e,min}} = \\ = n'_e \frac{\sqrt{3} e^3 B}{4 m_e c^2} \left(\frac{16}{9}\right)^2 \frac{3}{\sqrt{3}} \tag{D.29}$$

So we can write

$$n'_e \frac{\sqrt{3} e^3 B}{4 m_e c^2} = \frac{4\pi j'_{syn}(<\gamma_e>)}{\nu'_{syn}(\gamma_{e,min})} \frac{\sqrt{3}}{3} \left(\frac{9}{16}\right)^2 \tag{D.30}$$

and, after a substitution of (D.30) into (D.29), we get

$$4\pi j'_{max} \propto \Xi(p) \frac{4\pi j'_{syn}(<\gamma_e>)}{\nu'_{syn}(<\gamma_e>)} \tag{D.31}$$

with

$$\Xi(p) = 9\sqrt{3} \frac{2^{\frac{3(p-7)}{2}}}{\pi^{\frac{p-1}{2}}} (p-1) \frac{(3p+7)}{(p+1)} \Gamma\left(\frac{3p-1}{12}\right) \Gamma\left(\frac{3p+7}{12}\right) \int_0^\pi d\alpha \sin\alpha^{\frac{p+3}{2}} \tag{D.32}$$

The numerical factor missing in (D.31) can be determined by fitting the exact function given by (D.20). It will be the function $\Upsilon(p)$ defined as

$$\Upsilon(p) = \frac{lim_{\nu' \to +\infty} j'(\nu')}{\Xi(p) \frac{j'_{syn}(<\gamma_e>)}{\nu'_{syn}(<\gamma_e>)}}, \qquad \gamma_{e,max} \equiv +\infty \tag{D.33}$$

Finally we can conclude that

$$4\pi j'_{max} = C(p) \frac{4(p-1)}{3p-1} \frac{4\pi j'_{syn}(<\gamma_e>)}{\nu'_{syn}(<\gamma_e>)} \tag{D.34}$$

where the coefficient

$$C(p) = \Upsilon(p)\ \Xi(p)\ \frac{3p-1}{4(p-1)} \tag{D.35}$$

is such that, for instance, $C(2.5) = 0.86$, $C(2.6) = 0.88$, $C(3) = 1$. The final form of the coefficient in (D.34) has been written this way to match with Granot's results [Granot, Piran & Sari 1999c].

The agreement between $j'(\nu')$ and $j'_{app}(\nu')$ is perfect at high frequencies far from the peak and quite good even at low frequencies. See fig.D.3

The expression (D.20) represents the instantaneous monocromatic emissivity from a power law of electrons and could actually be observed only with an integration time $\Delta t'$

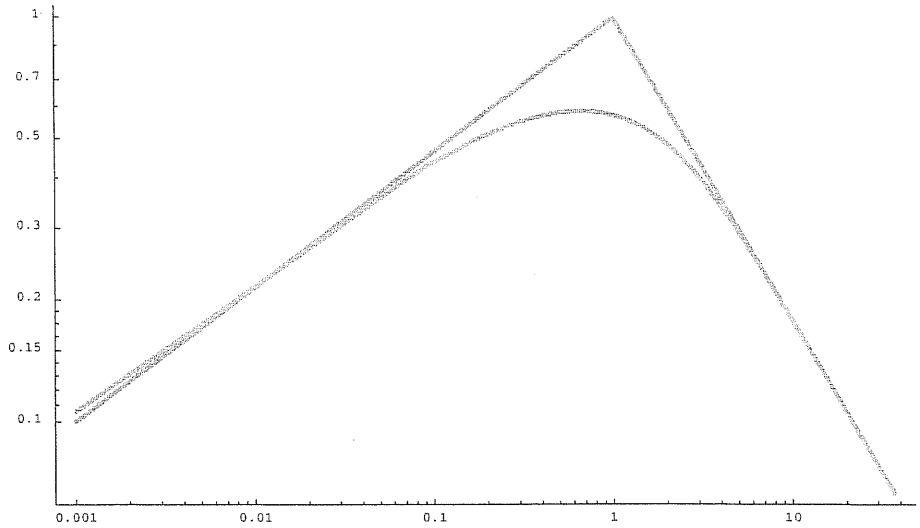

Figure D.3: *Plot of the true monochromatic emissivity due to an infinite power law of electrons as calculated through equation (D.20) and its approximated expression (D.25) with* j'_{max} *given by (D.34) in the case* $p = 2.5$. *We have used as* x *coordinate the normalized frequency* $\nu'/\nu'_{syn}(\gamma_{e,min})$ *and have normalized both functions to* j'_{max}.

shorter than the synchrotron cooling time of the highest energy electrons, $t_{cool}(\gamma_{e,max})$. The approximation (D.25) is expected to be valid only up to frequencies $\sim \nu'_{syn}(\gamma_{e,max})$. The true instantaneous monochromatic emissivity (D.20) shows an exponential cut off at frequencies $\nu' > \nu'_{syn}(\gamma_{e,max})$ (see fig.D.4).

Anyway, if we wait for a time interval $t' > t_{cool}(\gamma_{e,max})$ and no fresh electrons are supplied during this time, the highest energy electrons cool down and stop emitting. The high energy cut off of the electron power law shifts to a Lorentz factor $\gamma_{e,c} < \gamma_{e,max}$ that depends on the time t'. The cut off Lorentz factor after a time t' must be the one for which the cooling time of the electrons is exactly t', so

$$t' = t_{cool}(\gamma_{e,c}) = \frac{3}{4}\frac{8\pi m_e c}{\sigma_T \beta_{e,c}^2 \gamma_{e,c} B^2} \sim \frac{3}{4}\frac{8\pi m_e c}{\sigma_T \gamma_{e,c} B^2} \tag{D.36}$$

and consequenly

$$\gamma_{e,c}(t') = \frac{3}{4}\frac{8\pi m_e c}{\sigma_T t' B^2} \tag{D.37}$$

The *cooling Lorentz factor* $\gamma_{e,c}(t')$ can eventually become lower than $\gamma_{e,min}$ at late times, and this will change the shape of the integrated spectrum, i.e. the spectrum of the radiation emitted during all the time interval t'.

If $\gamma_{e,c}(t') > \gamma_{e,min}$, the integrated spectrum of radiation emitted during the time interval t' is due to two different sets of electrons, one made of electrons that have

not substantially changed their Lorentz factors during the time t' because their cooling time is still longer than t' (i.e. the electrons with a Lorentz factro between $\gamma_{e,min}$ and $\gamma_{e,c}(t')$), and another one made of electrons that have cooled down during the time interval t' because their cooling time was shorter than t' (i.e. the electrons with a Lorentz factor between $\gamma_{e,c}(t')$ and $\gamma_{e,max}$). Recalling the asymptotic behaviour of the function $F(x)$ at low and high values of x (see expressions (D.5) and (D.6)), we can see that the single particle integrated spectrum of an electron that does not substantially cool over the time interval t' can be approximated as a two segments law, consisting of a $\propto \nu'^{1/3}$ power law and an exponential cut off at about the synchrotron frequency. It can be shown that electrons that cool down during the time t', instead, show an integrated spectrum that can be approximated as a three segments law, the first segment $\propto \nu'^{1/3}$ up to the synchrotron frequency, the second segment $\propto \nu'^{-1/2}$ from the synchrotron frequency to the cooling frequency $\nu'_c(t') \equiv \nu'_{sync}(\gamma_{e,c}(t'))$, and a final exponential cut off. The integrated spectrum due to the whole population, i.e. the superposition of all the single particle spectra, then will be well approximated by the broken power law

$$j'_{app}(\nu') = \begin{cases} j'_{max}\left(\frac{\nu'}{\nu'_m}\right)^{\frac{1}{3}} & \nu' \leq \nu'_m \\ j'_{max}\left(\frac{\nu'}{\nu'_m}\right)^{-\frac{p-1}{2}} & \nu'_m < \nu' < \nu'_c(t') \\ j'_{max}\left(\frac{\nu'_c(t')}{\nu'_m}\right)^{-\frac{p-1}{2}}\left(\frac{\nu'}{\nu'_c(t')}\right)^{-\frac{p}{2}} & \nu'_c(t') < \nu' \end{cases} \tag{D.38}$$

where $\nu'_m \equiv \nu'_{syn}(\gamma_{e,min})$, $\nu'_c(t') \equiv \nu'_{sync}(\gamma_{e,c}(t'))$ and j'_{max} is defined as in (D.34).

If $\gamma_{e,c}(t') < \gamma_{e,min}$, all electrons have cooled down during the time interval t' and the approximated expression for the integrated spectrum will be

$$j'_{app}(\nu') = \begin{cases} j'_{max}\left(\frac{\nu'}{\nu'_c(t')}\right)^{\frac{1}{3}} & \nu' \leq \nu'_c(t') \\ j'_{max}\left(\frac{\nu'}{\nu'_c(t')}\right)^{-\frac{1}{2}} & \nu'_c(t') < \nu' < \nu'_m \\ j'_{max}\left(\frac{\nu'_m}{\nu'_c(t')}\right)^{-\frac{1}{2}}\left(\frac{\nu'}{\nu'_c}\right)^{-\frac{p}{2}} & \nu'_c < \nu' \end{cases} \tag{D.39}$$

Remember that (D.38) and (D.39) are analitic approximations for the monochromatic power emitted per unit volume and unit solid angle in the comoving frame accumulated during all the time interval t'. Detailed calculations and pictures will be shown in the following sections.

D.1.4 .... radiation emitted by an ensemble of particles with a generic energy distribution law

If the electron energy ditribution law is such that at a given time t' the number density of electrons with Lorentz factors between γ_e and $\gamma_e + d\gamma_e$ and random pitch angles

$$N(\gamma_e, t')d\gamma_e \tag{D.40}$$

then the instantaneous monocromatic emissivity of the fluid is $j'(\nu', t')$ such that

$$4\pi j'(\nu', t') = \int_{\gamma_{e,min}(t')}^{\gamma_{e,max}(t')} d\gamma_e \frac{N(\gamma_e, t')}{4\pi} \int_0^\pi d\alpha 2\pi \sin\alpha \; P'_{\gamma_e,\alpha}(\nu') \tag{D.41}$$

where, as usual, for $P'_{\gamma_e,\alpha}(\nu')$ we use expression (D.2).

A clearer espression for $j'(\nu', t')$ can be obtained substituting in (D.41) the average single particle spectrum

$$< P'_{\gamma_e}(\nu') >= \frac{1}{4\pi} \int_0^\pi 2\pi P'_{\gamma_e,\alpha}(\nu') \sin\alpha d\alpha \tag{D.42}$$

The result is

$$4\pi j'(\nu', t') = \int_{\gamma_{e,min}(t')}^{\gamma_{e,max}(t')} d\gamma_e N(\gamma_e, t') < P'_{\gamma_e}(\nu') > \tag{D.43}$$

If we know how the electron energy distribution $N(\gamma_e, t')$ evolves with time we can in principle calculate how the fluid monocromatic emissivity $j'(\nu', t')$ evolves. Note that the range $(\gamma_{e,min}(t'), \gamma_{e,max}(t'))$ of the electron energy distribution is also time dependent.

Note that in expression (D.43), the function $< P'_{\gamma_e}(\nu') >$ is known (the function Q defined in (D.16) can be calculated numerically once, and stored for future uses). Then, the expression (D.43) is the most convenient for a numerical calculation of the instantaneous comoving emissivity of a fluid element when the emitting electron energy distribution is known. And the emitting electron energy distribution $N(\gamma_e, t')$ can in principle always be calculated at any time as a solution of the particle diffusion–loss equation (see section E), thus the problem reduces to a numerical integration of known functions.

We can give some examples using the results from appendix E.

In the case of a power law distribution of electrons

$$dN_E = KE^{-p}dE \quad \text{for} \quad E > E_{min} \tag{D.44}$$

instantaneously injected in the fluid element at the time $t' = 0$ and subsequently affected only by pure synchrotron radiation losses due to the presence of a constant magnetic field B, we expect that, at the time t', electrons whose lifetime was greater than t' have cooled, while the others have simply drifted to slightly lower energies. Thus we expect a high energy cut–off in the electron distribution. Actually, the electron energy distribution evolves according to the law

$$N_E(E,t') = \begin{cases} KE^{-p}(1-aB^2Et')^{p-2} & E'_{min} < E < E'_{max} \\ 0 & E < E'_{min} \text{ or } E > E'_{max} \end{cases} \tag{D.45}$$

where $a = \frac{1}{6\pi}\frac{\sigma_T c}{(m_e c^2)^2}$,

$$E'_{min} = \frac{E_{min}}{1 + aB^2 E_{min} t'} \tag{D.46}$$

and

$$E'_{max} = \frac{1}{aB^2 t'} \tag{D.47}$$

Remember that $N(\gamma_e, t') = N_E(\gamma_e m_e c^2, t') m_e c^2$. In particular

$$N(\gamma_e, 0) = N_E(\gamma_e m_e c^2, 0) m_e c^2 = K\left(m_e c^2\right)^{1-p} \gamma_e^{-p} = N_e \gamma_e^{-p}$$

with

$$N_e = K\left(m_e c^2\right)^{1-p}$$

thus we can write

$$N(\gamma_e, t') = \begin{array}{ll} N_e\gamma_e^{-p}(1 - aB^2 m_e c^2 \gamma_e t')^{p-2} & \gamma'_{e,min} < \gamma_e < \gamma'_{e,max} \\ 0 & \gamma_e < \gamma'_{e,min} \text{ or } \gamma_e > \gamma'_{e,max} \end{array} \tag{D.48}$$

with

$$\gamma'_{e,min} = \frac{\gamma_{e,min}}{1 + aB^2 m_e c^2 \gamma_{e,min} t'}, \qquad \gamma_{e,min} = \frac{E_{min}}{m_e c^2} \tag{D.49}$$

and

$$\gamma'_{e,max} = \frac{1}{aB^2 m_e c^2 t'} \tag{D.50}$$

Note that $\gamma'_{e,max}$ is identical to $\gamma_{e,c}(t')$ given by (D.37).

So, in this case the spectrum of the emitted radiation at the time t' is

$$j'(\nu', t') = \frac{1}{4\pi} \int_{\gamma'_{e,min}}^{\gamma'_{e,max}} d\gamma_e \; N_e \gamma_e^{-p} (1 - aB^2 \gamma_e m_e c^2 t')^{\; p-2} < P'_{\gamma_e}(\nu') > \qquad \text{(D.51)}$$

This integral can be evaluated numerically. The result is shown in fig.D.4. The function (D.51) is well approximated by a broken power law growing as $\nu'^{1/3}$ up to $\nu'_m = \nu'_{sinc}(\gamma_{e,min})$, decreasing as $\nu'^{\frac{-(p-1)}{2}}$ from ν'_m to $\nu'_c = \nu'_{sinc}(\gamma'_{e,max})$, and then dropping exponentially for $nu' > \nu'_c$. The peak value is still given by (D.34).

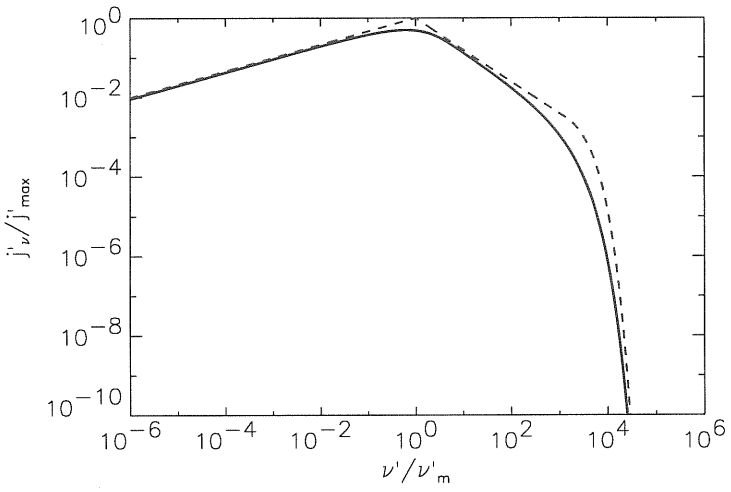

Figure D.4: *Plot of the instantaneous spectrum $j'(\nu', t')$ emitted by the electron distribution (D.48) at a fixed t' (solid line) and its analitic approximation (dashed line). Frequency is in units of ν'_m, and emissivity is normalized to j'_{max}.*

After that we can also integrate the instantaneous spectrum (D.51) over a time interval and compare the result with the approximated broken power laws (D.38) and (D.39) presented in the previous section. Results are shown in fig.D.5. We can see that after a time $t'_c = 1/am_e c^2 B^2 \gamma_{e,min}$ the integrated spectrum $\frac{1}{t'} \int_0^{t'} j'(\nu', s) ds$, initially well approximated by (D.38) changes its shape and needs to be approximated by (D.39).

D.2 Observed Radiation

We have said that a population of monoenergetic electrons moving with a Lorentz factor γ_e in a magnetic field B emits a total power per unit volume

$$P'_{tot}(\gamma_e) = 4\pi j'_{syn}(\gamma_e) = n'_e \frac{4}{3} \sigma_T c \beta_e^2 \gamma_e^2 \frac{B^2}{8\pi} \qquad \text{(D.52)}$$

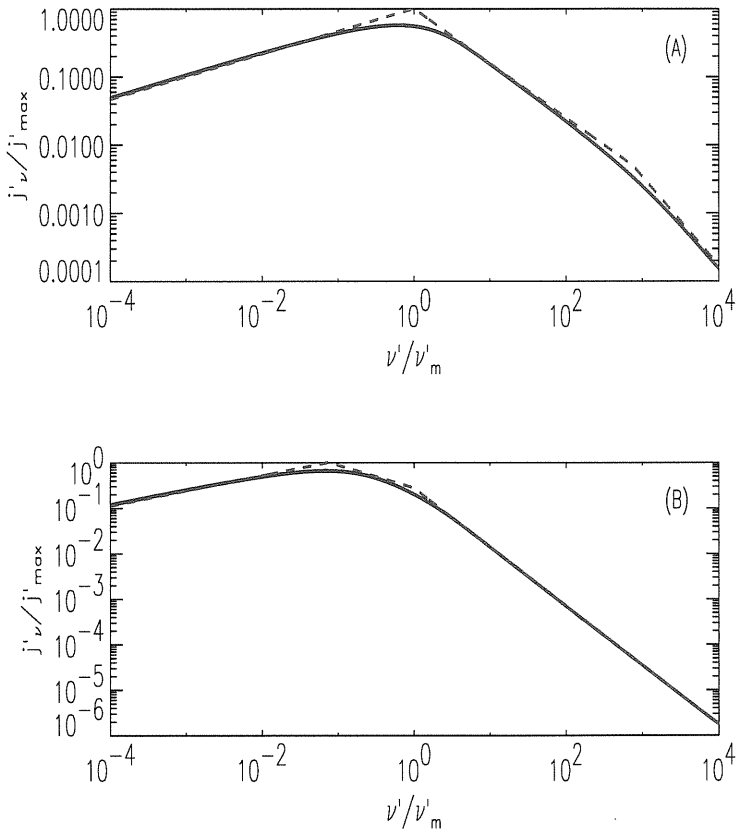

Figure D.5: *Plots of the integrated spectrum of a cooling power law of electrons* $\frac{1}{t'}\int_0^{t'} j'(\nu', s)ds$ *(solid line) and its analitic approximation* j'_{app} *(dashed line), in the two cases* $t' < t'_c$ *(upper panel) and* $t' > t'_c$ *(lower panel). Frequency is in units of* ν'_m *in the upper panel and in units of* ν'_c *in the lower panel and emissivity is always normalized to* j'_{max}.

This result is valid in the fluid comoving frame.

If the fluid is moving with respect to the lab frame at a Lorentz factor γ and in a direction forming an angle ϑ with the line of sight, it can be proved that the power observed in the lab frame is

$$P_{tot}(\gamma_e) = \frac{P'_{tot}(\gamma_e)}{\gamma^4(1-\beta\cos\vartheta)^3} \tag{D.53}$$

Moreover, if the typical frequency of emitted radiation is

$$\nu'_{syn}(\gamma_e) = \frac{3}{16}\frac{eB\gamma_e^2}{m_e c} \tag{D.54}$$

then the typical frequency of observed radiation is

$$\nu_{syn}(\gamma_e) = \frac{\nu'_{syn}(\gamma_e)}{\gamma_e(1-\beta_e\cos\vartheta)} \tag{D.55}$$

Finally, the observed electron Lorentz factor in the lab frame is $\gamma_e\gamma$.

Appendix E

The diffusion–loss equation for the electrons

Consider a fluid element of volume $V(t')$ in which relativistic electrons are injected at a rate $\mathcal{Q}(E,t')$ such that the total number of electrons with energy between E and $E+dE$ injected in the fluid element during the time interval from t' to $t'+dt'$ is $\mathcal{Q}(E,t')\,dE\,dt'$.

Each electron of energy $E = m_e c^2 \gamma_e$ in the fluid element suffers energy losses according to the law

$$-\left(\frac{dE}{dt'}\right) = b(E,t') \tag{E.1}$$

where the function $b(E,t')$ is expected to be positive.

A general expression for $b(E,t')$ including all the possible energy loss processes in a fully ionized plasma is the following:

$$b(E,t') = [A_{brems}(t') + A_{AD}(t')]\,E + [A_{sync}(t') + A_{IC}(t')]\,E^2 \tag{E.2}$$

The linear term in E accounts for Bremsstrahlung radiation and adiabatic losses, while the quadratic term accounts for Synchrotron and Inverse Compton radiation.

From standard textbooks we know that

$$A_{brems}(t') = 4\,n'(t')\,Z^2\left(\frac{e^2}{m_e^2 c^2}\right)^2 \alpha_s\,\bar{g}\,c \tag{E.3}$$

$$A_{AD}(t') = \frac{1}{3}\,(\nabla\cdot\mathbf{v})\,(t') \tag{E.4}$$

$$A_{sync}(t') = \frac{4}{3}\frac{\sigma_T c}{(m_e c^2)^2} U_{mag}(t') \tag{E.5}$$

$$A_{IC}(t') = \frac{4}{3}\frac{\sigma_T c}{(m_e c^2)^2} U_{rad}(t') \tag{E.6}$$

where Z is the atomic number of the ionized matter (made of one chemical specie only), α_s is the fine structure constant and $\bar{g} = \ln(2\gamma_e) - \frac{1}{3} \sim constant$ for $100 \lesssim \gamma_e \lesssim 10^5$. The vector field $\mathbf{v}$ represents the fluid velocity field and $n'(t')$, $U_{mag}(t')$ and $U_{rad}(t')$ are the particle number, magnetic and radiation energy densities in the fluid element.

In a very low density plasma such as the one which we are dealing with, Bremsstrahlung and Inverse Compton radiation losses are supposed to be negligible as compared to Synchrotron radiation losses and we will neglect them. The adiabatic losses (i.e. energy losses due to adiabatic expansion of the fluid element) are to be considered negligible on short timescales, but can affect the emitting electron energy on long timescales.

Regardless of what term dominates in (E.2), an electron population with an energy distribution $\mathcal{N}_E(E,t')$ such that at the time t' the total number of electrons with energy between E and $E+dE$ in the volume $V(t')$ is $\mathcal{N}_E(E,t')dE$, evolves according to the diffusion–loss equation

$$\frac{d\mathcal{N}_E}{dt'} = \frac{d}{dE}\left[b(E,t')\mathcal{N}_E(E,t')\right] + \mathcal{Q}(E,t') + \mathcal{D}\nabla^2\mathcal{N}_E(E,t') \tag{E.7}$$

where the last term represents the number of electrons with energy E that leave the fluid element by diffusion. $\mathcal{D}$ is the diffusion coefficient.

In the case of acceleration processes at shocks the injection rate can be approximated as

$$\mathcal{Q}(E,t') = \mathcal{K}E^{-p}\delta(t') \qquad E > E_{min} \tag{E.8}$$

The shock instantaneously provides a power law of electrons at $t' = 0$ and then moves away leaving the newly shocked electrons free to cool and diffuse. No fresh electrons are supplied after $t' = 0$.

If we neglect the diffusion loss term in (E.7) we can write

$$\frac{d\mathcal{N}_E}{dt'} = \frac{d}{dE}\left[b(E,t')\mathcal{N}_E(E,t')\right] + \mathcal{Q}(E,t') \tag{E.9}$$

The solution of (E.9) with electron injection rate (E.8) will depend on which term dominates in (E.2). We have already said we are interested in solutions for synchrotron dominated radiation losses with adiabatic expansion accounted for. Moreover, we will deal with a magnetic field decreasing with time.

In our case the use of equation (E.9) instead of (E.7) can be justified if the gyration radius of the injected electrons is much smaller than the fluid element size, so that electrons on average do not diffuse away from their injection site. Fig.E.1 shows the

gyration radius of the average emitting electrons compared to the fireball shock radius at the time of emission as a function of the position behind the shock along the line of sight at different observer times. It can be seen that this ratio is always small, so our assumption about the absence of electron diffusion is probably satisfied by average electrons, that are the bulk of the population. A small fraction of emitting electrons having a Lorentz factor significantly higher than the average might anyway diffuse to adjacent fluid elements, but we expect this effect to be negligible. The fact that in the

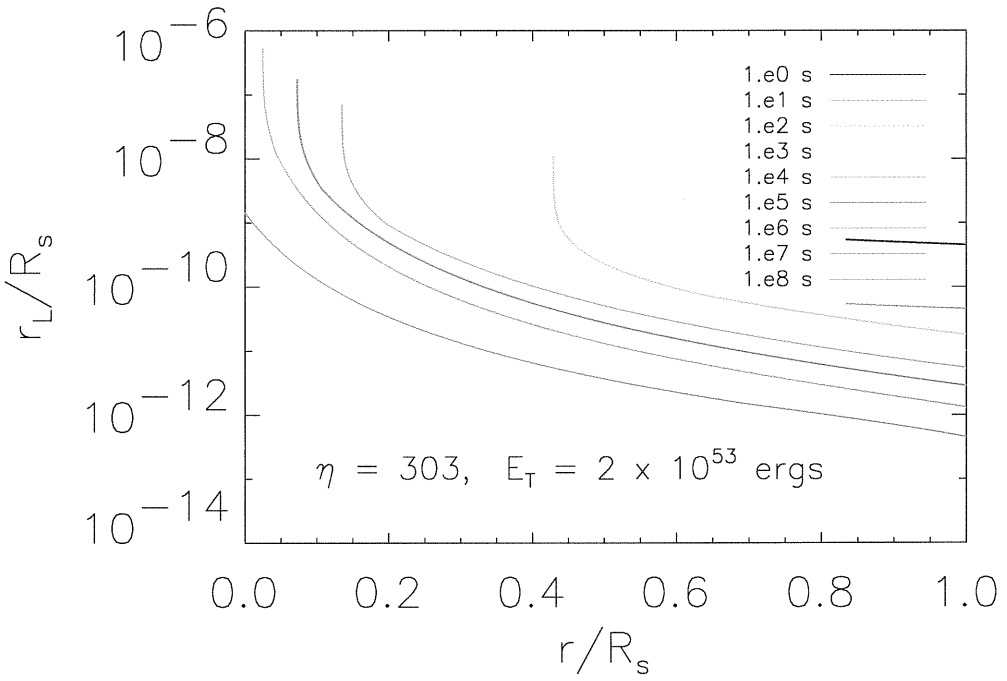

Figure E.1: *Plots of the ratio* $\frac{r_L}{R_s}$ *with* $r_L = \frac{m_e c^2}{eB}\gamma_{e,min}\beta_{e,min}$ *at the time of emission as a function of the position behind the shock along the line of sight at different observer times.*

shocked plasma we are dealing with inverse Compton radiation can be neglected, could be easily verified, for instance, calculating the ratio $\frac{A_{IC}}{A_{sync}} = \frac{U_{rad}(t')}{U_{mag}(t')} = \frac{4\pi}{c} j' \frac{8\pi}{B^2}$ at the time of emission as a function of the position behind the shock along the line of sight at different observer times. We can approximate the electron energy ditribution as a monoenergetic distribution with a lorentz factor equal to the minimum and conclude that, for negligible inverse compton contribution to the emitted radiation it should always come (see relation (D.9)): $j' \sim j'_{sync}(\gamma_{min}(t')) \sim \frac{1}{4\pi} n'_e(t') \frac{4}{3} \sigma_T c \beta_{min}(t')^2 \gamma_{min}(t')^2 U_{mag}(t')$, so that $\frac{A_{IC}}{A_{sync}} = \frac{U_{rad}(t')}{U_{mag}(t')} \sim \frac{4}{3}\sigma_T n'_e(t') \left(\gamma_{min}(t')^2 - 1\right) \ll 1$.

It can be seen in fig.E.2 that the approximated value for the ratio $\frac{A_{IC}}{A_{sync}}$ we have just calculated is always small enough to justify our assumption.

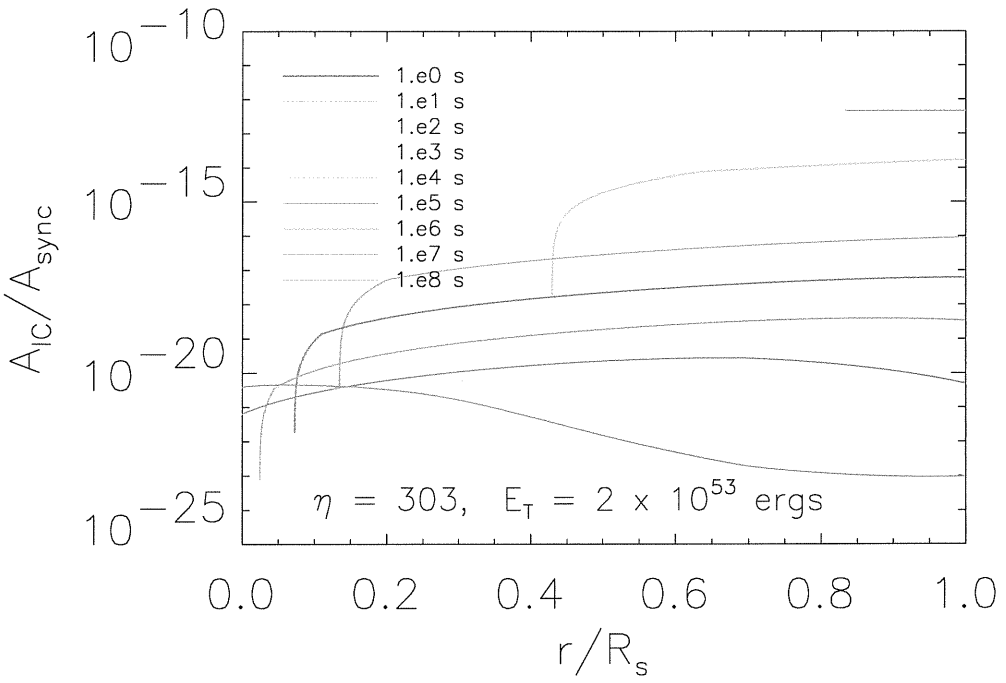

Figure E.2: *Plots for the quantity* $\frac{4}{3}\sigma_T n'_e\,(\gamma^2_{min}-1) \sim \frac{A_{IC}}{A_{sync}}$ *versus the position relative to the shock radius at different observer times.*

In the remaining part of the section we will calculate and interpret the general solution we need after solving (E.9) with the electron injection rate E.8 under different simplifying assumptions.

- If we have as dominant cooling mechanism the Synchrotron process we can write

$$b(E,t') \sim A_{sync}(t')E^2 = aB^2(t')E^2 \tag{E.10}$$

Suppose the cooling mechanism acts on the electron population on a timescale much shorter than the timescale on which the magnetic field strength varies, so that we can assume

$$B(t') = constant \tag{E.11}$$

In this case the solution of the diffusion–loss equation is simply

$$\mathcal{N}_E(E,t') = \begin{cases} \mathcal{K}E^{-p}(1-aB^2Et')^{p-2} & E'_{min} < E < E'_{max} \\ 0 & E < E'_{min} \text{ or } E > E'_{max} \end{cases} \tag{E.12}$$

where $a = \frac{4}{3}\frac{\sigma_T c}{(m_e c^2)^2}\frac{1}{8\pi}$,

$$E'_{min} = \frac{E_{min}}{1+aB^2E_{min}t'} \tag{E.13}$$

and

$$E'_{max} = \frac{1}{aB^2t'} \tag{E.14}$$

The result is that after t' seconds the electron power law shows a high energy cut–off progressively moving towards lower frequencies as time passes. The cut–off energy is the one corresponding to electrons having a lifetime for synchrotron losses ($\tau_{sync} \sim E/(dE/dt')_{sync} \sim 1/aB^2E$) as short as the time t' elapsed from the shock passage. At the same time the minimum electron energy is moving towards lower frequencies too according to the energy loss equation by synchrotron radiation for a single electron.

- If the dominant energy loss mechanism is synchrotron radiation but the magnetic field is not constant (and, for instance, decreases with time), the solution of the diffusion loss equation (E.9) with the instantaneously injected power law of electrons (E.8) is

$$\mathcal{N}_E(E,t') = \begin{cases} \frac{\mathcal{K}E^{-p}}{\left[1-aE\int_0^{t'}B(x)^2dx\right]^{2-p}} & E'_{min} < E < E'_{max} \\ 0 & E < E'_{min} \text{ or } E > E'_{max} \end{cases} \tag{E.15}$$

where

$$E'_{min} = \frac{E_{min}}{1+aE_{min}\int_0^{t'}B(x)^2dx} \tag{E.16}$$

and

$$E'_{max} = \frac{1}{a\int_0^{t'}B(x)^2dx} \tag{E.17}$$

The general behaviour of the electron energy distribution is not very different from the constant magnetic field case, except that the parameter that determines the cut off is now the average squared magnetic field over the time interval t'. In order to simplify the expressions (E.15), (E.16) and (E.17) we can define the auxiliary function

$$H^2(t') = \int_0^{t'} B(x)^2dx \tag{E.18}$$

- If the dominant energy loss mechanism is synchrotron radiation but the volume element is also expanding and the adiabatic cooling is acting too, things get more complicated.

  Suppose that the magnetic field is constant and the adiabatic cooling rate is constant too ($A_{AD} \equiv g = constant$). In this case the solution of (E.9) is

$$\mathcal{N}_E(E,t') = \begin{cases} \frac{\mathcal{K}E^{-p}e^{-gt'}}{\left[e^{-gt'} - aB^2E\frac{(1-e^{-gt'})}{g}\right]^{2-p}} & E'_{min} < E < E'_{max} \\ 0 & E < E'_{min} \text{ or } E > E'_{max} \end{cases} \tag{E.19}$$

  with

$$E'_{min} = \frac{E_{min}e^{-gt'}}{1 + aB^2E_{min}\frac{(1-e^{-gt'})}{g}} \tag{E.20}$$

  and

$$E'_{max} = \frac{e^{-gt'}}{aB^2\frac{(1-e^{-gt'})}{g}} \tag{E.21}$$

  The diffusion–loss equation solution (E.19) actually reduces to the previous one (E.12) if $gt' \ll 1$, since in this case $(1 - e^{-gt'}) \sim gt'$ and $e^{-gt'} \sim 1$.

  In solution (E.19) we have a high energy cut off of the injected power law determined by a sort of weighted magnetic field

$$H^2(t') = B^2\frac{(1-e^{-gt'})}{g} = B^2\int_0^{t'} e^{-gs}ds = \int_0^{t'} G(s)B^2ds \tag{E.22}$$

  and by a second parameter

$$G(t') = e^{-gt'} \tag{E.23}$$

  Note that a constant adiabatic cooling rate coefficient is obtained in case of spherical pure radial expansion with a fluid velocity field $v(r) \propto r$.

- In case of pure synchrotron losses with adiabatic cooling, if both the magnetic field and the adiabatic cooling rate are time dependent, the solution of the diffusion loss equation (E.9) for the instantaneously injected power law of electrons given by (E.8) will be

$$\mathcal{N}_E(E,t') = \begin{cases} \frac{\mathcal{K}E^{-p}e^{-\int_0^{t'} g(x)dx}}{\left[e^{-\int_0^{t'} g(x)dx} - aE\int_0^{t'} e^{-\int_0^{s} g(x)dx}B^2(s)ds\right]^{2-p}} & E'_{min} < E < E'_{max} \\ 0 & E < E'_{min} \text{ or } E > E'_{max} \end{cases} \tag{E.24}$$

with

$$E'_{min} = \frac{E_{min} e^{-\int_0^{t'} g(x)dx}}{1 + aE_{min} \int_0^{t'} e^{-\int_0^s g(x)dx} B^2(s)ds} \tag{E.25}$$

and

$$E'_{max} = \frac{e^{-\int_0^{t'} g(x)dx}}{a \int_0^{t'} e^{-\int_0^s g(x)dx} B^2(s)ds} \tag{E.26}$$

The solution (E.24) clearly reduces to the previous one (E.19) for g and B constant. The the integral $\int_0^{t'} g(x)dx$ must be calculated quite accurately because it is the argument of an exponential function that multiplies the whole particle distribution. On the other hand, the integral $\int_0^{t'} e^{-\int_0^s g(x)dx} B^2(s)ds$ can be calculated with low precision. A factor ten of uncertainty in its value produces only a ??% error on the particle distribution.

If we define

$$H^2(t') = \int_0^{t'} G(s)B^2(s)ds \tag{E.27}$$

and

$$G(t') = e^{-\int_0^{t'} g(x)dx} \tag{E.28}$$

we can rewrite (E.24), (E.25) and (E.26) as

$$\mathcal{N}_E(E,t') = \begin{cases} \frac{\mathcal{K}E^{-p}G(t')}{[G(t') - aEH^2(t')]^{2-p}} & E'_{min} < E < E'_{max} \\ 0 & E < E'_{min} \text{ or } E > E'_{max} \end{cases} \tag{E.29}$$

$$E'_{min} = \frac{E_{min}G(t')}{1 + aE_{min}H^2(t')} \tag{E.30}$$

and

$$E'_{max} = \frac{G(t')}{aH^2(t')} \tag{E.31}$$

We can conclude that the general solution of the diffusion–loss equation (E.29) has a quite simple structure. It can be verified that it conserves the total number of electrons, as expected. Actually we have

$$\begin{aligned} n'_e(t')V(t') &= \int_{E'_{min}}^{E'_{max}} \mathcal{N}_E(E,t')dE = \\ &= \int_{E'_{min}}^{E'_{max}} \frac{\mathcal{K}E^{-p}G(t')}{[G(t') - aEH^2(t')]^{2-p}} dE = \\ &= \frac{\mathcal{K}}{p-1} \frac{1}{E_{min}^{p-1}} = \int_{E_{min}}^{+\infty} \mathcal{K}E^{-p}dE = \\ &= \int_{E_{min}}^{+\infty} \mathcal{N}_E(E,0)dE = n'_e(0)V(0) \end{aligned} \tag{E.32}$$

Since $V(t') = 1/n'(t')$ where $n'(t')$ is the proton density, we can say that at any time t'

$$\frac{n'_e(t')}{n'(t')} = \frac{n'_e(0)}{n'(0)} = \epsilon \quad \rightarrow \quad n'_e(t') = \epsilon n'(t') \tag{E.33}$$

and that the electron energy distribution per unit volume at the time t' will be

$$N_E(E,t') = \frac{\mathcal{N}_E(E,t')}{V(t')} = \mathcal{N}_E(E,t')n'(t') \tag{E.34}$$

or equivalently

$$N_E(E,t') = \begin{cases} \frac{K(t')E^{-p}G(t')}{[G(t')-aEH^2(t')]^{2-p}} & E'_{min} < E < E'_{max} \\ 0 & E < E'_{min} \text{ or } E > E'_{max} \end{cases} \tag{E.35}$$

with

$$K(t') = \mathcal{K}n'(t') = n'_e(0)V(0)(p-1)E_{min}^{p-1}n'(t') = \frac{n'_e(0)}{n'(0)}n'(t')(p-1)E_{min}^{p-1} = \\ = \epsilon n'(t')(p-1)E_{min}^{p-1} = n'_e(t')(p-1)E_{min}^{p-1} \tag{E.36}$$

and E'_{min} and E'_{max} given by (E.25) and (E.26) respectively. The parameter $\epsilon \leq 1$ represents the number of non–thermal electrons injected in the volume at the time $t' = 0$. We will always use $\epsilon = 1$ according to the discussion in section (3.7.1).

Bibliography

[Abramowitz & Stegun 1970] *Handbook of Mathematical Functions* (nineth edition), Dover Publications, INC, New York (1970)

[Aloy *et al* 2000] ApJ **521**, L119

[Andersen *et al* 1999] Science **283**, 2075

[Andersen, Hjorth *et al* 2000] A&A **364**, L54

[Akerlof *et al.* 1999] Nature **398**, 400

[Band *et al* 1993] ApJ **413**, 281

[Bath *et al.* 1992] Nature **359**, 217

[Berger, Diercks *et al.* 2001] ApJ **556**, 556

[Berger, Sari *et al.* 2000] ApJ **545**, 56

[Bhargavi & Cowsik 2000] ApJ **545**, L77

[Blandford & McKee 1976] The Physics of Fluids **19 (8)**, 1130

[Blandford & Znajek 1977] MNRAS **179**, 433

[Bloom *et al.* 1999] Nature **401**, 453

[Bloom, Kulkarni & Djorgovski 2002] Astronomical Journal, March 2002, in press

[Boella *et al.* 1997] A&A Suppl. Ser. **122**, 299

[Bradt & Smith 1999] A&A Suppl. Ser. **138**, 423

[Briggs *et al.* 1996] ApJ **459**, 40

[Castro-Tirado, Zapatero-Osorio *et al.* 1999] Science **283**, 2069

[Castro-Tirado *et al.* 1998] Science **279**, 1011

[Castro-Tirado & Gorosabel 1999] A&A Suppl. Ser. **138**, 449

[Castro-Tirado *et al.* 2001] A&A **370**, 398; astro–ph/0102177

[Chevalier & Li 1999] ApJ **520**, L29

[Chevalier & Li 2000] ApJ **536**, 195

[Chevalier & Li 2000] ApJ **536**, 195; astro–ph/9908272

[Costa *et al.* 1997] Nature **387**, 783

[Costa *et al.* 1998] Adv. Space. Res. **22 (7)**, 1129

[Costa 1999] AIP Conf. Proc. 5th Huntsville Symposium on Gamma–ray bursts

[Covino, Lazzati *et al.* 1999] A& A **348**, L1

[Crider 1997] ApJ **479**, L39

[Dai & Lu 1999] ApJ **519**, L155

[Dai & Lu 2001] A&A **367**, 501

[Dal Fiume & Amati 2000] A&A **355**, 454

[Djorgovski *et al.* 1997] Nature **387**, 876

[Djorgovski, Frail *et al.* 2001] ApJ, submitted (2001); astro–ph/0107539

[Draine & McKee 1993] Ann. Rev. A&A **31**, 373

[Eichler, Livio, Piran & Schramm 1989] Nature **340**, 126

[Esin & Blandford 2000] ApJ **534**, L151

[Fenimore, Epstein & Ho 1993] A&A Suppl. Ser. **97**, 59

[Fenimore & Ramirez–Ruiz 2002] ApJ submitted. astro–ph/0004176

[Fishman 1981] Astrophys. Space Sci. **75**, 125

[Fishman 1995] PASP **107**, 1145

[Fishman 1999] A&A Suppl. Ser. **138**, 395

[Fishman *et al.* 1993] A&A Suppl. Ser. **97**, 17

[Fishman *et al.* 1994] ApJ Suppl. Ser. **92**, 229

[Fishman & Meegan 1995] ARA&A **33**, 415

[Ford 1995] ApJ **439**, 307

[Ford & Band 1996] ApJ **473**, 1013

[Frail *et al.* 1997] Nature **389**, 261

[Frail *et al* 1999] Proc. of the 5th Huntsville Gamma-Ray Burst Symposium; astro–ph/9912171

[Frail *et al.* 2001] ApJ **562**, L55; astro–ph/0102282

[Frail, Kulkarni *et al* 1999] ApJ **525**, L81

[Frail, Waxman & Kulkarni 2000] ApJ in press

[Frontera 1998] in: M. S. Potgieter, B. C. Raubenheimer, & D. J. van der Wait (eds.), 25th International Cosmic Ray Conference, Vol. 8, (World Scientific: Singapore), p. 307; astro-ph/9802157

[Frontera *et al.* 2000] ApJ Suppl. Ser. **127**, 59

[Fruchter, Krolik & Rhoads 2001] ApJ 563, 597; astro–ph/0106343

[Fruchter, Thorsett *et al.* 1999] ApJ **519**, L13

[Fynbo, Gorosabel *et al.* 2001] A&A **373**, 796; astro–ph/0102158

[Fynbo, Jensen *et al.* 2001] A&A **369**, 373

[Galama, Briggs *et al.* 1999] Nature **398**, 394

[Galama *et al.* 1998] ApJ **497**, L13

[Galama *et al.* 1998] Nature **395**, 670

[Galama *et al.* 2000] ApJ **536**, 185

[Galama & Wijers 2001] ApJ **549**, L209

[Gallant, Achterberg & Kirk 1999a] A&A Suppl. Ser. **138**, 549

[Gallant, Achterberg & Kirk 1999b] MNRAS **305**, L6

[Garnavich, Loeb & Stanek 2000] ApJ **544**, L11

[Giblin *et al.* 1999] ApJ **524**, L47

[Goodman 1986] ApJ **308**, L47

[Goodman 1997] New Astronomy **2 (5)**, 449

[Granot, Piran & Sari 1999a] ApJ **513 (2)**, 679

[Granot, Piran & Sari 1999b] ApJ **527**, 236

[Granot, Piran & Sari 1999c] A&A Suppl. Ser. **138**, 541

[Granot , Piran & Sari 2000] ApJ **534**, L163

[Granot & Sari 2002] ApJ **568**, 820

[Groot *et al.* 1997] IAU Circ. 6584

[Gorosabel *et al.* 1998] A&A **335**, L5

[Gruzinov & Waxman 1999] ApJ **511**, 852

[Guilbert, Fabian & Rees 1983] MNRAS **205**, 593

[Hakkila *et al.* 1994] ApJ **422**, 659

[Halpern *et al.* 1999] ApJ **517**, L105

[Halpern, Kemp, Piran & Bershady 1999] ApJ **517**, L105

[Halpern, Uglesich *et al.* 1999] ApJ **543**, 697

[Harrison, Bloom & Frail 1999] ApJ **523**, L121

[Harrison, Yost *et al.* 2001] ApJ **559**, 123; astro–ph/0103377

[Hjorth *et al.* 2000] ApJ **534**, L147 & ApJ **539**, L75 (erratum)

[Holland *et al.* 2001] A&A **371**, 52; astro–ph/0103058

[Huang, Dai & Lu 2000] A&A **355**, L43

[Israel, Marconi *et al.* 1999] A&A **348**, L5

[Jensen, Fynbo *et al.* 2001] A&A **370**, 909

[Jaunsen, Hjorth *et al.* 2001] ApJ **546**, 127

[Katz 1994] ApJ **432**, L107

[Klebesadel, Strong, & Olson 1973] ApJ **182** L85

[Klose *et al.* 2000] ApJ **545**, 271

[Krolik & Pier 1991] ApJ **373**, 277

[Kulkarni *et al.* 1998] Nature **393**, 35

[Kulkarni *et al.* 1999] Nature **398**, 389

[Kulkarni *et al.* 2000] Proc. of the 5th Huntsville Gamma–Ray Burst Symposium; astro–ph/0002168

[Kumar & Panaitescu 2000] ApJ **541**, L9

[Kumar & Piran 2000a] ApJ **535**, 152

[Kumar & Piran 2000] ApJ **532**, 286

[Kuulkers, Antonelli *et al.* 2000] ApJ **538**, 638

[Lamb 2001] Proc. of the Conf. *Gamma-Ray Bursts in the Afterglow Era: 2nd Workshop*, eds. F. Frontera, E. Costa, J. Hjorth, ESO Astrophysics Symposia, Berlin: Springer Verlag, in press (2001); astro-ph/0107551

[Lamb, Castander & Reichart 1999] A&A Suppl. Ser. **138**, 479

[Landau & Lifshitz 1987] *Fluid Mechanics*, Pergamon Press, Oxford 1987

[Lazzati, Covino & Ghisellini 2001] MNRAS submitted; astro–ph/0011443

[Lazzati *et al.* 2001] A&A **378**, 996

[Lee, Tucker *et al.* 2001] ApJ in press; astro-ph/0104201

[Li & Chevalier 2001] ApJ **551**, 940

[Livio & Waxman 2000] ApJ **538**, 187

[Lloyd–Ronning & Ramirez–Ruiz 2002] ApJ submitted

[Loeb & Perna 1998] ApJ **495**, 597

[Longair 1981] *High Energy Astrophysics*, Cambridge University Press, Cambridge 1981

[MacFadyen & Woosley 1999] ApJ **524**, 262

[MacFayden, Woosley & Heger 2001] ApJ **550**, 410

[Masetti, Bartolini *et al.* 2000] A&A **359**, L23

[Masetti, Palazzi *et al.* 2001] A&A **374**, 382

[Meegan 1998] Adv. Space Res. **22 (7)**, 1065

[Meegan *et al.* 1992] Nature **355**, 143

[Meegan *et al.* 1995] ApJ **446**, L15

[Mészáros 1997] Rev. Mod. Astron **10**, 127

[Mészáros 2000] Nucl. Phys. Proc. Suppl. **80**, 63; astro–ph/9904038

[Metzger *et al.* 1997] Nature **387**, 878

[Mészáros, Laguna & Rees 1993] ApJ **415** 181

[Mészáros & Rees 1999] MNRAS **306 (3)**, L39

[Mészáros, Rees & Papathanassiou 1994] ApJ **483** 181

[Mészáros & Rees 1997] ApJ **476**, 232

[Mészáros, Rees & Wijers 1998] ApJ **499**, 301

[Moderski, Sikora & Bulik 2000] ApJ **529**, 151

[Norris, Marani & Bonnell 2000] ApJ **534**, 248

[Norris 2002] ApJ submitted. astro–ph/0201503

[Paczyńsky 1986] ApJ **308**, L43

[Paczyńsky 1987] ApJ **317**, L51

[Paczyński 1998] ApJ **494**, L45

[Palazzi, Pian *et al.* 1998] A&A **336**, L95

[Panaitescu 2001] ApJ **556**, 1002

[Panaitescu & Kumar 2001a] ApJ **554**, 667; astro–ph/0010257

[Panaitescu & Kumar 2001b] ApJ **571**, in press; astro–ph/0109124

[Panaitescu & Mészáros 1997] ApJ **482**, 942

[Panaitescu & Mészáros 1999] ApJ **526**, 707

[Panaitescu, Mészáros & Rees 1998] ApJ **503**, L314

[Panaitescu, Wen, Laguna & Mészáros 1997] ApJ **482** 942 (1997)

[Pedersen *et al.* 1998] ApJ **496**, 311

[Pian 2001] Chapter for the book *Supernovae and Gamma-Ray Bursters*, edited by K. W. Weiler, Springer-Verlag Press (2001); astro–ph/0110051

[Pian, Soffitta *et al.* 2001] A&A **372**, 456

[Piran 1997] in: J. N. Bahcall & J. P. Ostriker (eds.), *Unsolved Problems in Astrophysics* (Princeton University Press: Princeton), p. 343

[Piran 1999] Physics Reports **314**, 575; astro–ph/9810256

[Piran 1999a] Physics Reports **333**, 529; astro–ph/9907392

[Piro, Garmire *et al.* 2001] ApJ **558**, 442; astro-ph/0103306

[Preece 2000] ApJ Suppl. Ser. **126**, 19

[Price, Harrison *et al.* 2001] ApJ **549**, L7

[Price, Kulkarni *et al.* 2002] ApJ Letters submitted, astro-ph/0201399

[Prilutskii & Usov 1975] Astrophys. Space Sci. **34**, 395

[Protheroe 1998] astro-ph/9812055

[Ramaprakash, Kulkarni *et al.* 1998] Nature **393**, 43

[Ramirez-Ruiz & Lloyd-Ronning 2002] New Astronomy submitted. astro-/ph0203447

[Rees 1998] in: A. V. Olinto, J. A. Frieman, & D. N. Schramm (eds.), Proc. 18th Texas Symposium on Relativistic Astrophysics (World Scientific: Singapore), p. 34

[Rees 1999] A&A Suppl. Ser. **138**, 491

[Rees & Mészáros 1992] MNRAS **258**, 41P

[Rees & Mészáros 1994] ApJ **430** L93 (1994)

[Reichart 1999] ApJ **521**, L111

[Reichart 2001] ApJ **553**, 235

[Rhoads 1999] ApJ **525**, 737

[Rhoads & Fruchter 2001] ApJ **546**, 117

[Rol, Wijers *et al.* 2000] ApJ **544**, 707

[Rossi *et al.* 2002] MNRAS **332**, 945; astro-ph/0112083

[Rybicki & Lightman 1979] *Radiative Processes in Astrophysics*, John Wiley & Sons, New York 1979

[Sari 1997] ApJ **489**, L37

[Sari & Esin 2001] ApJ **548** 787 (2001)

[Sari, Narayan & Piran 1996] ApJ **473**, 204 (1996)

[Sari & Piran 1995] ApJ **455** L143 (1995)

[Sari & Piran 1999a] ApJ **520**, 641

[Sari & Piran 1999b] ApJ **517 (2)**, L109

[Sari, Piran & Halpern 1999] ApJ **519**, L17

[Sari, Piran & Narayan 1998] ApJ **497** L17

[Scalo & Wheeler 2001] ApJ **562**, 664; astro-ph/0105369

[Schmidt 1999] ApJ **523**, L117

[Schwartz, Thomsen, Bame & Stansberry 1988] J. Geophys. Res. **93 (12)**, 923

[Sedov 1959] *Similarity and Dimensional Methods in Mechanics*, Academic Press, New York 1959

[Smette, Fruchter *et al.* 2001] ApJ **556**, 70

[Smith *et al.* 1999] A&A **347**, 92

[Sokolov *et al.* 2001] Proceedings of The Second Rome GRB Workshop, ed: N. Masetti. Springer

[Spitzer 1978] *Physical Processes in the Interstellar Medium*, Wiley, New York 1978

[Stanek, Garnavich *et al.* 1999] ApJ **522**, L39

[Stanek, Garnavich *et al.* 2001] ApJ **563**, 592; astro–ph/0104329

[Stecklum, Fischer *et al.* 2001] Proc. 20th Texas Symposium on Relativistic Astrophysics, eds. J. C. Wheeler and H. Martel, in press (2001); astro-ph/0103120

[Stern & Svensson 1996] ApJ **469**, L109

[Strong, Klebesadel, & Olson 1974] ApJ **188** L1

[Taylor, Bloom *et al.* 2000] ApJ **537**, L17

[Tegmark *et al.* 1996a] ApJ **466**, 757

[Tegmark *et al.* 1996b] ApJ **468**, 214

[Tucker 1975] *Radiation Processes in Astrophysics*, The MIT Press, Cambridge 1975

[Usov & Chibisov 1975] Sov. Astron. **19**, 115

[van der Bergh 1983] Astrophys. Space Sci. **97**, 385

[van Paradijs *et al.* 1997] Nature **386**, 686

[Vreeswijk, Galama *et al.* 1999] ApJ **523**, 171

[Vrba *et al.* 2000] ApJ **528**, 254

[Waxman & Draine 2000] ApJ **537**, 796

[Waxman, Kulkarni & Frail 1998] ApJ **497**, 288

[Wijers & Galama 1999] ApJ **523**, 177

[Wijers, Rees, & Mészáros 1997] MNRAS **288**, L51

[Wijers, Vreeswijk *et al* 1999] ApJ **523**, L33

[Woods & Loeb 1995] ApJ **383**, 292

[Zand, Kuiper *et al.* 2001] ApJ in press; astro–ph/0104362

[Zhang & Mészáros 2001] ApJ **552**, L35

[Zharikov *et al.* 1998] A&A **337**, 356